A Tribometer with Programmable Motion and Load to Investigate the Influence of Molecular Structure on Wear of Orthopaedic Polyethylene

Alastair Scott Kilgour

A thesis submitted for the degree of Doctor of Philosophy

The University of Edinburgh

December 2009

Acknowledgements

Firstly, I would like to thank my supervisor Dr. Alistair Elfick for introducing me to the exciting field of tribology and to his patient ear during our many discussions. His guidance is thoroughly appreciated.

I would also like to thank Rabah, Andy, Bryony, Kim and Martin all of whom I was lucky enough to share an office with during my studies at Edinburgh University.

My deepest thanks to Dr. Jane Blackford, who as an undergraduate introduced me to the field of materials science and has since been a mentor, unknowingly or otherwise.

I would also like to express my appreciation to Dr. Chris Jeffree for his expert operation of the FE-SEM.

A mention must be made to Mr Bobby Hogg and the technical staff in the University of Edinburgh workshop, providing advice and skills without which my designs would have never left the paper.

For my time in the University of California Berkeley I would like to thank Prof. Lisa Pruitt and her group for making my stay so enjoyable and educational. It was difficult returning to sunny Scotland. This was made possible through the Royal Society of Edinburgh, Lessells Scholarship for which I am eternally grateful.

Finally, I would like to thank my Family and friends for their continued support and encouragement, without which this thesis would not have been possible.

Abstract

Total hip arthroplasty commonly involves a hard metallic/ceramic femoral ball component articulating against an acetabular ultra-high molecular weight polyethylene (UHMWPE) counter-bearing. A novel six-station, wear tribometer, featuring programmable load and motion, was designed to further the investigation into wear, sub-surface plasticity and debris generation of UHMWPE. This thesis describes the pin-on-plate device, its validation and subsequent use to assess unirradiated (-PE) and gamma-irradiated highly crosslinked (+PE) UHMWPE wear behaviour.

With the emphasis on dynamic loading and a closer gait matched open wear path, the tribometer improves on the clinical relevance of pin-on-plate testing. There is a requirement for this type of machine in order to investigate the directional dependence of wear and debris generation of UHMWPE more accurately, where "simplified" tribometers (adequate for constant load/constant velocity and constant load/sinusoidal velocity work) are not capable or suitable. For the first time in orthopaedic pin-on-plate studies, tests were conducted using an advanced dynamic load synchronised to a more physiologically accurate elliptical motion path.

To validate the machine, three orthopaedic polymers of clinical relevance; Polytetrafluroethylene, Polyacetal, and UHMWPE were subjected to linear-reciprocating (LR) and novel elliptical motion paths under a Paul-type load profile. All three polymers showed higher wear factors under elliptical motion, by up to 2 orders of magnitude, agreeing well with explanted values. The UHMWPE elliptical wear factor was comparable to that reported for clinical, where $k_{elliptical} = 1.56 \times 10^{-6}$ mm^3/Nm.

In the crosslinked study, the mean steady state wear of -PE and +PE groups under linear reciprocating motion was not significantly different. However, under elliptical motion, crosslinking reduced UHMWPE wear by up to 92% when compared to the unirradiated group.

In –PE pins worn under LR motion and in +PE pins subjected to both motion paths a sub-surface damage zone with reduced crystallinity and increased strain was measured using Raman spectroscopy. This was attributed to large strain accumulation in the slower wearing surfaces providing a mechanism for de-crystallisation. The discovery of such a near-surface layer is in good agreement with critical strain wear models. In disagreement, however, we found the sliding induced layer to extend to greater depths than previous reported.

Contents

LIST OF FIGURES

LIST OF TABLES

NOMENCLATURE

+PE	100kGy crosslinked UHMWPE used within
ΔH	Enthalpy of fusion (J/kg)
ΔT	Change in temperature (K)
A_{slide}	Secondary sliding direction of the wear path
A_{pin}	Cross sectional area of the test pin
a	Apparent contact area (mm^2)
A_c	Heat transfer area (m^2)
AR	Wear path aspect ratio
B	Flux density
B_{slide}	Primary sliding direction of the wear path
CFM	Cubic feet per minute
cp	Specific heat capacity (J/kgK)
DCM	Direct compression molded
Delrin®	DuPont trade name for Polyacetal
DSC	Differential scanning calorimetry
d	Laser spot diameter (µm)
E	Young's Modulus (GPa)
EHL	Elastohydrodynamic lubrication
F	Friction force (N)
FDA	US Food and Drug Administration
FE-SEM	Field-emission scanning electron microscopy
FWHM	Full width at half maximum
H	Material hardness
I	Current measured in amperes (A)
I_{second}	Second moment of area (mm^4)
ID	Inner diameter (mm)
In vitro	A biological process made to occur in a laboratory or other controlled experimental environment rather than within a living organism or natural setting
In vivo	A biological process occurring or made to occur within a living organism or natural setting
J_{total}	Total inertia of the ball screw system
K	Thermal conductivity (W/mK)
k	Wear factor (mm^3/Nm)
L	Length of the coil
L_{pin}	Length of the test pin
Load profile	Load exerted down on the polymer pin during one complete slide track
LR	Linear reciprocating wear path
m	Mass of the chamber base (kg)
M	Maximum bending moment (Nmm)
M_c	Average molecular weight between crosslinks (g/mol)

N	Normal load (N)
n	Molecular weight between crosslink sites
NCS	Newborn calf serum
OD	Outer diameter (mm)
-PE	Unirradiated UHMWPE
Pitch	Pitch of the ball-screw thread
POD	Pin-on-disc tribometer
POP	Pin-on-plate tribometer
PSU	Power supply unit
PTFE	Polytetrafluoroethylene
Q	Wear volume per unit sliding distance
Q_{heat}	Energy input (W)
R_1	Femoral ball radius
r_1	Perpendicular distance between input force and fulcrum
r_2	Perpendicular distance between output force and fulcrum
rms	root mean square
S	Swelling ratio
S.D	Standard deviation
SEM	Scanning electron microscopy
Slide track	Wear path traced on the metal counterface by the surface of the polymer pin
T	Torque
t	Cycle time (s)
THA	Total hip arthroplasty
THR	Total hip replacement
TKR	Total knee replacement
UHMWPE	Ultra-high molecular weight polyethylene
V	Wear volume (mm^3)
V_1	Molar volume of xylene (cm^3/mol)
v_2	Volume fraction of polymer in a swollen gel
$v(t)$	Instantaneous sliding velocity at cycle time t (mm/s)
Vac	Electricity supply using alternating current
V_{av}	Average sliding velocity over a sliding move (mm/s)
Vdc	Electricity supply using direct current
V_s	Raman scattering volume (μm^3)
W	Weight loss due to wear (mg)
W_F	Final weight of worn pin (mg)
W_G	Weight gain of control pin (mg)
W_I	Initial weight of pin (mg)
w	Angular velocity (rad/s)
XLPE	Highly crosslinked polyethylene

X_1	Flory-Huggins interaction parameter
X_c	Crosslink density (mol/cm^3)
x	Sliding distance (m)
y	Distance from neutral axis to outer most fibre (mm)
ρ_s	Density of the polymer (g/cm^3)
σ	Bending Stress (MPa)
σ_{nom}	Nominal contact stress (MPa)
σ_{UTS}	Ultimate tensile strength (MPa)
ε_{UTS}	Ultimate strain to failure
$\varnothing$	Diameter (mm)
$\propto$	Proportional
α	Angular acceleration of the ball screw
μ	Coefficient of friction
η	Ball screw efficiency
θ	Maximum cross-shear angle (radians)
θ_{arm}	Angle through which the loading arm rotates
ΔW_A	Work to rupture molecules and generate wear debris in the secondary direction

1 Introduction

The majority of today's hip replacements still resemble the artificial hip developed by Sir John Charnley in the 1960's[1]. Throughout its relatively short history total hip replacement (THR) has alleviated pain and restored mobility to millions of patients whom previously suffered through rheumatoid, or osteo-, arthritis; two of the most common forms of arthritis.

THR is the most common of all the big-joint (hip, knee, shoulder) orthopaedic procedures. The current "gold-standard" has been continuously refined over the past three decades, yet conceptually it remains the same; a hard metal ball component articulates against a low friction polymer counterface. The polymer in question is ultra-high molecular weight polyethylene (UHMWPE), which forms an extremely effective acetabular bearing insert. Unfortunately, the discovery that UHMWPE micron and sub-micron particles, a consequence of wear, induce a pathogenic response in the tissue supporting the implant which leads to late-stage failure is a reminder that prosthetic treatments remain imperfect. Not infrequently, the patient will require the primary prostheses to be replaced, but revision surgery into the joint area is accompanied by elevated risks and costs. Revision procedures add increased complication to both surgeon and patient, as well as using far more healthcare resources than the initial procedure[2]. There is then, a need to better understand the origins of UHMWPE wear, in order to benefit the patient through prolonging the useful operating lifetime of prostheses and reducing the expenditure of the health-care provider.

To assess the degree of wear and debris production, tribological assessments are performed (tribology, from the Greek, *Tribos*, for rubbing). Laboratory wear studies evaluate a material's resistance to wear and the volume, size and shape of debris produced. These parameters are known to be important in determining the magnitude and severity of the failure response. Wear studies often start with simplified pin-on-plate tests and then, if the material shows significant promise, more complex full joint simulators are used to better approximate the physiological conditions found in the hip joint.

Many wear-reducing treatments have been proposed for UHMWPE, all with the aim of increasing the longevity of the metal-on-polymer bearing couple. Some, such as Hylamer®, a highly-crystalline UHMWPE, were heralded with the promise of increased operating lifetime. Nevertheless, despite the FDA confirming Hylamer® to be at least substantially equivalent to conventional material (UHMWPE gamma irradiated with a minimum dose of 25kGy), the grade

was abandoned shortly after its introduction having fallen out of favour with surgeons. Crosslinking the polymer is believed to be the most successful wear-reducing treatment of UHMWPE. This is by no means a recent development, but refinements in the crosslinking process have led to its growing reputation as the successor to conventional UHMWPE. Crosslinked UHMWPE improves on the wear performance of conventional UHMWPE under both hip joint and to a lesser extent knee joint motion. However, with each orthopaedic manufacturer preferring their own treatment technique, often based on in-house wear studies, the role of crosslinking in the wear process, although crucial, is not completely understood.

Operating and environmental conditions in the body are severe with cyclic loading and complex wear paths increasing the difficulty in approximating *in vivo* wear in the laboratory. Historical pin-on-plate studies conducted on uni-directional or linear-reciprocating (LR) sliding machines have proven inadequate in representing UHMWPE wear. This may be attributed to the simplified sliding arrangement causing highly divergent wear rates when compared to clinical studies. These basic machines are a reminder that laboratory testing conditions have considerable impact on polymer wear and care should be taken, especially when investigating newer materials which lack clinical experience for comparison and verification. The generally accepted paradigm, that the wear performance of polyethylene is intimately related to the sliding conditions, means that contemporary tribometers should offer increased tribological flexibility to reflect the growing understanding of UHMWPE wear.

To date, few studies have attempted to link microstructural modification and wear rate of unirradiated and crosslinked orthopaedic polyethylene. We postulate that a tribometer capable of more accurately replicating the *in vivo* molecular reorientation of UHMWPE will facilitate a more complete understanding of the precise origins of wear and the role of crosslinking. In future, the suitability of novel biomaterials may be assessed in an environment more physiologically representative, but without the expense and complication of hip simulators.

In response to areas seen as limitations in contemporary tribometer designs, this thesis describes the development of a simplified, desktop, wear testing machine to better approximate the clinical tribological conditions. Once established, such a machine may provide valuable insight into the effects of physiological loads and motions on wear rate and microstructural development. Better insight will increase our understanding of wear to more closely predict the morphological progression of UHMWPE *in vivo*.

A summary of key objectives follows:

i. In order to generate realistic *in vivo* UHMWPE wear, a novel tribometer will be designed and built. The machine should be capable of imposing more physiologically accurate slide tracks and loading profiles than previous pin-on-plate machines over large numbers of cycles.

ii. To commission and validate the clinical relevance of the wear tester, three polymers of historical significance in the development of THR will be worn. The wear rates will be compared to those from clinical data.

iii. The directional dependence of UHMWPE wear will be investigated using both an historical LR and more advanced elliptical slide track. These will be used to distinguish tribological surface behaviour and resulting wear rates and wear factors.

iv. The application of non-destructive analysis techniques has seldom been used in pin-on-plate wear studies. The development of Raman spectroscopy offers the ability to measure near surface crystallinity and molecular structure, allowing the structural modification of UHMWPE at the worn surface to be monitored in response to sliding motion.

v. To investigate the role of crosslinking in the wear of UHMWPE, two different grades of polymer will be tested. Both non-crosslinked (-PE) and highly crosslinked (+PE) material will be subject to LR and multi-directional motion. Microstructural surface and sub-surface development in both grades will be characterised using a variety of techniques including, swelling tests, Raman spectroscopy and scanning electron microscopy.

2 Literature Review

Summary

Within the hip joint cavity, cartilage lines the top of the articulating surfaces and in conjunction with healthy synovial joint fluid provides painless, low friction operation during normal joint motion. Degradation and thinning of the cartilage and a decrease in synovial fluid viscosity is a condition referred to as arthritis. Arthritis can cause excruciating pain during even mundane tasks such as walking, sitting and standing up. To remedy such conditions patients may seek replacement surgery. Replacement joints may fail due to wear and damage associated with inherently harsh conditions found in the body; a combination of cyclic stresses, fatigue, corrosion and sliding wear.

It is of merit to screen candidate biomaterial behaviour and develop an understanding of current materials in an effort to extend the useful operational lifetime of the prosthetic joint. Wear behaviour of joint materials is assessed through laboratory studies (*in vitro* studies), conducted on both explanted/retrieval specimens and test samples prepared specifically, often taking simplified geometrical form. Retrieval (*ex vivo*) and experimental studies provide important insights into wear mechanisms of candidate and current acetabular cup materials. Pin-on-disc (POD) and pin-on-plate (POP) tribometers have historically been used as useful laboratory pre-screening tools because they are simple, cost-effective and provide opportunities for studying basic wear mechanisms through precise control of testing conditions and variables. Nevertheless, wear rates of components within the body may vary considerably due to the myriad of conditions between individuals. Therefore, wear data describing the behaviour of bearing materials should be treated with caution; particularly when data comes from simple test machines. *In vitro* pin-on-plate wear behaviour should be seen as indicative of that *in vivo* and not predictive. More reliable estimation of *in vivo* wear rates may be derived from joint simulator testing.

To date, few studies have attempted to link microstructural evolution and wear rate of unirradiated and irradiated orthopaedic polyethylene. Such information could improve understanding of the role of crosslinking on wear reduction and debris morphology under sliding wear.

2.1 Overview of Chapter

This chapter introduces the primary cause for patient discomfort during joint articulation and presents one remedy involving orthopaedic surgery; damaged natural bearing surfaces are replaced with low-wearing artificial materials. In the majority of cases the bearing material combination consists of a hard metallic or ceramic ball component articulating against a low wear UHMWPE socket[3]. Unfortunately, for reasons discussed in Section 2.3, the bio-compatibility of bulk UHMWPE is compromised in its particulate debris form which is released during wear. Much research is concerned with methods to reduce the amount of wear debris generated at the articulating surface in the hope of extending the useful operating lifetime of the prosthesis.

2.2 Load Bearing Synovial Joints

2.2.1 Natural Joints

All bones in the human skeleton, apart from the hyoid bone in the neck, are connected to each other through joints. This provides the flexible framework in which we move, work and play. There are nine different types of joint in the skeleton, of which the ball-and-socket type is the most flexible. Descriptions of the hip and knee joint will be the focus of the following section.

The hip joint is classed as a ball-and-socket type, where the proximal end of the femur bone, the femoral head, sits within the spherical cavity of the acetabulum (Figure 2-1). The ball-in-socket arrangement allows flexion-extension, abduction-adduction and internal-external rotation of the femur. Enclosed within the cavity, or joint space, synovial fluid acts to minimise friction and protect the articulating cartilage surfaces.

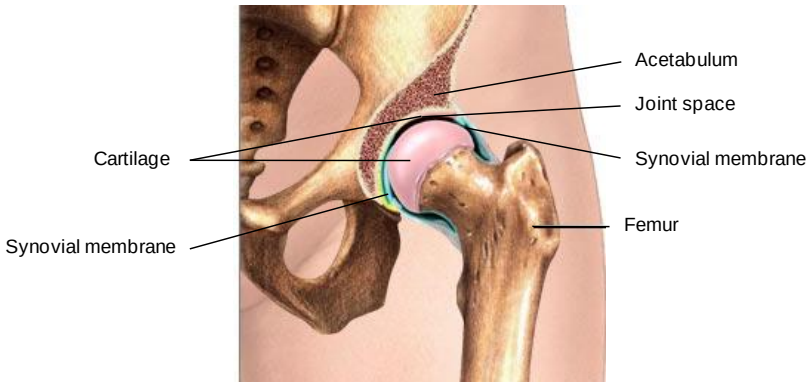

Figure 2-1: Illustration of the ball-and-socket hip joint[1].

[1] From The National Library of Medicine, USA.

There has been a plethora of work done into understanding the roles cartilage and synovial fluid play in the smooth operation of the joint. In healthy diarthrodial joints, articular cartilage covers the surface of opposing bony contacts which would otherwise be exposed to bone-on-bone wear. Cartilage, unlike the bone underneath contains no nerve fibres, hence, healthy cartilage ensures painless operation of the joint. It is this layer of fibrous tissue, the bearing surface, which is subject to sliding and rolling motion.

In load-bearing joints the joint space surrounding and enclosing the contacting surfaces and within the cartilage itself are fluid-filled. Interstitial synovial fluid may flow to the surface of the cartilage in response to load bearing[4]. This results in natural bearing surfaces partially protected by newly introduced fluid in the contact region aiding longevity. In addition, synovial fluid contains constituents which are thought to be effective boundary lubricants such as lubricin, hyaluronic acid, and surface active phospholipids[5]. Synovial fluid also supplies surrounding tissue with nutrients as well as removing catabolic products

Rheological studies on synovial fluid show increasing shear rates drastically reduce fluid viscosity[6]. As such, synovial fluid is described as a non-Newtonian fluid, displaying shear-thinning behaviour. Furthermore, Cooke *et al.* found that for given shear rates, samples of synovial fluid extracted from diseased joints consistently showed lower viscosity than those samples extracted from healthy joints.

To illustrate the extraordinarily low coefficient of friction, Charnley measured the coefficient of friction of a human knee joint, finding the average coefficient of friction was approximately three times lower than the coefficient for ice sliding on ice; 0.01 vs. 0.03[7].

Many engineering lubrication regimes have been proposed to explain the complex and significant role of synovial fluid on joint longevity. Over the past four decades research has indicated that synovial joints experience boundary, fluid film, squeeze-film, and mixed lubrication modes dictated by the individual patient and instant in the load and motion cycle. Further description of lubrication regimes is covered in Section 2.2.2.1.

Early analytical studies on resultant hip joint forces and moments calculated double-peak type load curves as seen in Figure 2-2[8]. This is representative of the “heel-down”, “stance phase”, “toe-off” and “swing” cycle of typical gait. Paul calculated hip joint loading during walking to be a maximum five-fold that of patient mass. Hence an 80kg patient may exert up to 4kN of load through the joint during walking. Similar dynamic load profiles have since been published from

in vivo experimental data gathered from modified hip implants that include strain gauges to measure force[9]. A typical walking pace of 4km/h was shown to result in a gait cycle of approximately 1 second (Figure 2-3). Here, the maximum load is almost four-fold that of the patient's body weight occurring under the "heel-strike". The stance phase accounts for approximately 50% of the load cycle.

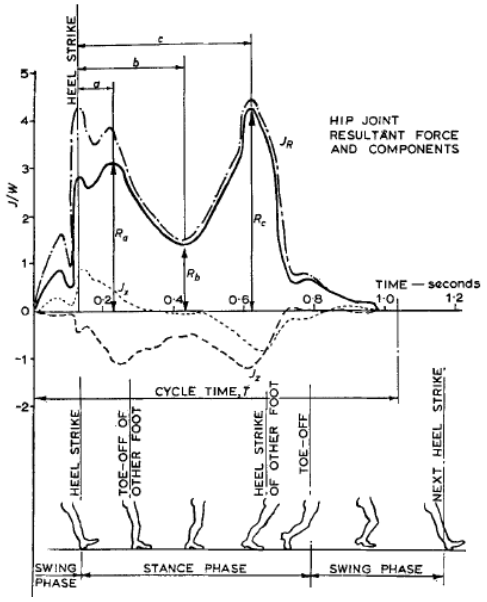

Figure 2-2: Dynamic loading of the hip joint during walking[8].

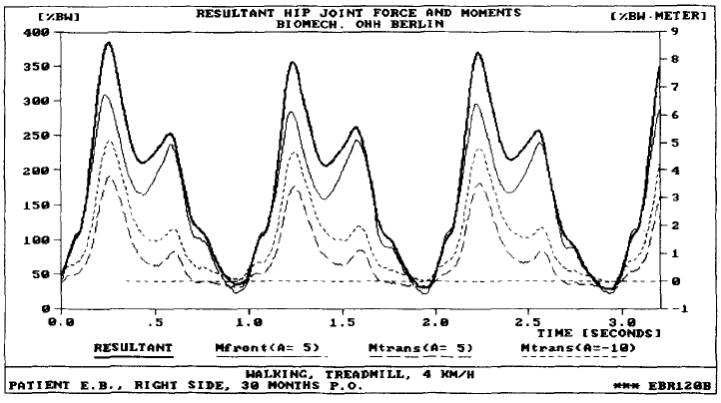

Figure 2-3: Hip joint loading from experimental studies[9].

The knee joint is described as a hinge joint, but unlike the elbow joint (the primary skeletal hinge joint) which restricts movement to one degree of freedom, the knee joint also allows the foot to rotate. Therefore, movement in the knee is a combination of rolling and gliding/sliding. A total

knee replacement (TKR) will typically involve the resurfacing of the femoral condyles with a highly polished metal component which articulates on a UHMWPE liner secured at the proximal end of the tibia (Figure 2-4).

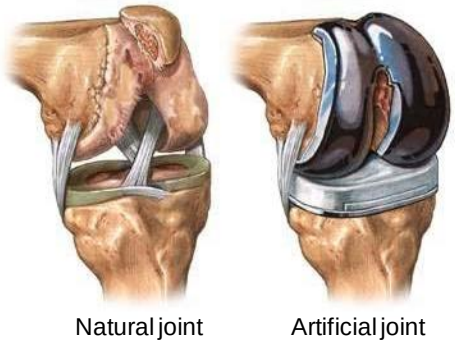

Figure 2-4: Illustration of the knee joint showing the metal femoral component articulating on the UHMWPE tibial tray[2].

Contact conditions in the knee can be more severe than in the hip joint. The apparent contact area, consisting of two femoral condyles sliding and rolling against the tibial tray, is smaller than the hemispherical cavity associated with the conformal contact of the ball and socket joint (Figure 2-5). Contact stresses in the knee can be up to eight-fold those found in the hip joint.

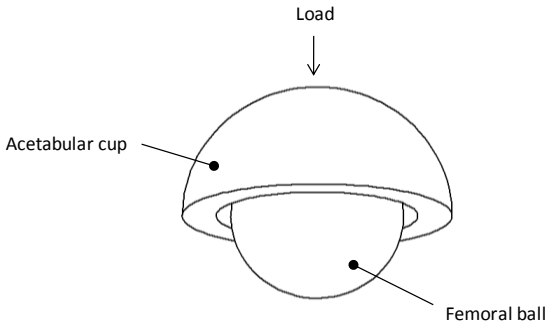

Figure 2-5: Geometry of two bodies with one convex (ball) and one concave (socket) in contact.

To a first approximation, the contact stress, a result of the acetabular cup loaded against the femoral head, can be calculated by dividing the load by the curved surface area of a hemisphere with a radius equal to that of the femoral ball. The nominal stress, σ_{nom}, for an 80kg patient, exerting 4kN of load through a 32mm diameter ball would result in a mean nominal contact stress of 3.2MPa.

[2] From The National Library of Medicine, USA.

$$\sigma_{nom} = \frac{N}{2\pi {R_1}^2}$$

Equation 2-1: Nominal contact stress where N is the applied load and R_1 is the radius of the femoral ball.

More complicated direct measurements, using calibrated piezo-resistive transducers implanted in arrays within femoral head cartilage show under a joint load of 2.7kN, a mean contact stress and maximum peak contact stress of 2.9MPa and 8.8MPa respectively, sites of maximum local stress were found within the general region of the acetabular dome[10].

Motion in the knee joint is associated with rolling and sliding, most prominent in the flexion-extension direction (forward and back). In contrast, motion in the hip joint consists of more open type wear paths, associated with sliding in both the flexion-extension and abduction-adduction (left and right) axes. Sliding motion of the hip joint is described further in Section 2.6.5.

2.2.2 The Polymer and Metal Artificial Joint

Hip and knee replacements have made a considerable impact on the quality of life of millions of people. The 2005 revenue for hip implants in Europe was valued at $1,400,000,000, contributing to around 30% of total procedures worldwide[11]. Patients seek orthopaedic surgery when non-inflammatory degenerative joint disease such as osteoarthritis or inflammatory degenerative joint disease such as rheumatoid arthritis, cause degrading changes in the articular cartilage and joint space. The result can often be painful bone-on-bone contact which is debilitating to the patient.

A hugely successful procedure, total hip arthroplasty will typically involve the surgeon replacing the two “worn-out” surfaces (the femoral head on the proximal femur side and the acetabulum in the pelvic bone) with two synthetic load-bearing materials (Figure 2-6). The polymer cup and metal ball combination was inspired by the reportedly high friction of early metal cup and metal ball designs. The softer polymer surface was thought to offer lower resistance to sliding and rotational articulation.

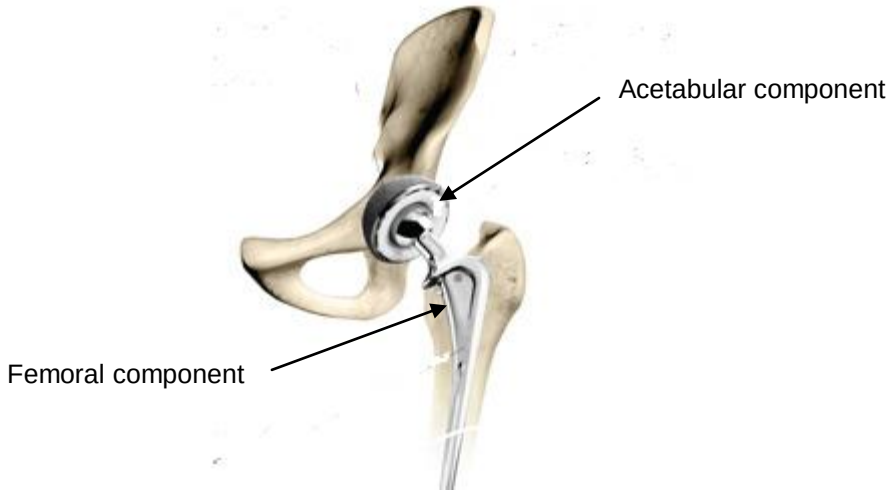

Figure 2-6: In the majority of THR, a hard metallic or ceramic ball articulates against a low wear UHMWPE socket[3].

First generation metal-on-metal prosthesis, such as the McKee-Farrar and Müller prostheses (where both bearing surfaces were made from cobalt chrome molybdenum) suffered from high friction and inconsistent manufacturing tolerances. High friction and the resultant large torques at the component-bone interface were suggested to account for the high rates of fixation failure[12]. The move to metal-on-plastic articulation was proposed to reduce the frictional torque transmitted to the fixation interface, aiding longevity. Indeed, Unsworth showed on a hip joint pendulum machine that the frictional torque on a McKee-Farrar joint was a maximum six-fold that of the frictional torque from a Charnley metal-on-polymer joint under dry sliding conditions. The maximum difference between the two joints occurred when both joints were loaded with a maximum static load of 1.5kN[13]. This behaviour was attributed to the UHMWPE having a lower shear-strength at the metal-polymer interface than the metal-on-metal junctions, reducing the size of the frictional force. Secondly due to geometric effects, the Charnley metal-on-polymer joint was designed with a smaller femoral head diameter, reducing the frictional torque (*T)* of the joint (Figure 2-7).

[3] From www.jointreplacement.com.

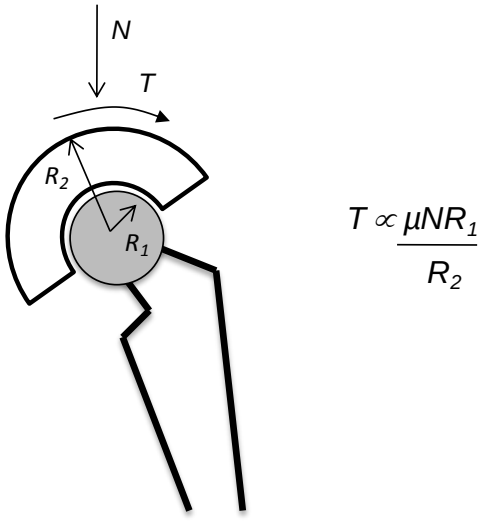

Figure 2-7: Resistive torque of a joint where; N is he applied load; T is the torque; R_1 radius of the femoral ball; R_2 radius to acetabular/bone interface.

2.2.2.1 Joint Lubrication

When operating in the body, the joint replacement benefits from the lubrication of the synovial fluid. In an effort to more accurately represent *in vivo* behaviour, laboratory studies on wear of orthopaedic components often include a readily available bovine serum lubricant to act as the synovial fluid medium.

The use of lubricating fluid to reduce wear and friction is commonly observed in engineering practice; oil to lubricate motor engines is a prominent example. For surfaces which appear to undergo dry sliding, often intermediate surface effects may influence the nature of sliding; most solid bodies in contact have on their surfaces a substance which shares little tribological resemblance to that of the bulk material e.g. an oxide layer, moisture or contaminants.

In these cases it is not the interfacial shear strength of the bulk materials at the contacting asperities which need be overcome to generate sliding, but rather the interfacial shear strength of the intermediate fluid or contaminant. In general, most solid bodies are separated by very thin and difficult to observe films in the order of 1-100μm thickness[14]. The thickness of the fluid film relative to the surface roughness of the two sliding surfaces may be used to describe the lubrication regime.

A film thickness which is of sufficient size to completely separate two sliding surfaces achieves a state called fluid-film lubrication[15]. This situation may be produced through external pressurisation of the lubricant, or hydrostatic lubrication. In the case of natural, and artificial,

joints this is not observed. In contrast, hydrodynamic lubrication is created by the motion of the bearing. For complete hydrodynamic separation, opposing surfaces must be inclined to one another. Trapped fluid within the contact becomes pressurised, eventually forcing the bearing surfaces apart into a state of fluid-film lubrication. Fluid-film is desirable. Surfaces completely separated during sliding undergo very low material wear. Hydrodynamic lubrication as a regime found in natural joints was first proposed by MacConaill[16]. In this study it was noted that opposing cartilaginous joint surfaces had differing curvature, akin to inclined surfaces, such that synovial fluid could get trapped and pressurized to form a thick fluid film. This theory would account for the low wear, low friction and long life of natural joints.

However, Charnley later argued that the reciprocating motion of the joint would interrupt the film, along with the inherent slow sliding velocities and high loads found in the joint[7]. According to hydrodynamic theory, at zero velocity, the thickness of the fluid film is zero. Therefore, the start/stop nature of hip motion must introduce non-hydrodynamic conditions resulting in partial cartilage-cartilage rubbing. Charnley suggested that hydrodynamic lubrication was invalid due to its dependence upon geometry and fluid viscosity rather than material and fluid behaviour. As such, it could not accurately represent the complex biological lubricating system in cartilaginous joints.

To account for low joint wear and friction a boundary lubrication regime was proposed[7]. For boundary lubrication to occur the lubricant, or constituents thereof adsorb to one of the contacting surfaces forming a protective layer (Figure 2-8). This molecular mechanism is described in detail by Bowden and Tabor[17]. Rubbing surfaces are protected and separated by monolayer films absorbed onto the surface by physical or chemical bonding. More specifically surface-active phospholipids (SAPL) have been proposed to chemisorb to the cartilage surface providing the very low friction mechanism under large physiological loads and slow sliding speeds[18].

For bearing surfaces which have appreciable motion in the perpendicular direction squeeze-film lubrication can result. Under compression, trapped fluid in the joint space becomes pressurised before flowing away from of the loaded contact, Figure 2-8iii. The pressurised fluid squeeze-film aids bearing wear under dynamic loading.

For natural joints the unusual properties of cartilage give rise to two alternative proposed lubrication mechanisms. McCutchen suggests that spongy cartilage could exude fluid (“weep

fluid") into the contact region under load to provide increased protective film thickness at the localised contact[4]. Walker *et al*. imply that under load, water is absorbed into the cartilage leaving a concentrated synovial fluid on the cartilage surface acting in the contact zone[19]. The concentrated fluid was thought to be more effective in reducing wear and friction. This mechanism was called "Boosted Lubrication".

Finally, in bearing conditions where the pressurised fluid in the contact zone may be large enough to elastically deform the surfaces, elastohydrodynamic lubrication (EHL) has been developed[20]. EHL is a form of hydrodynamic lubrication where both elastic deformation of the bearing surface and changes in lubricant viscosity with pressure can not be ignored in film thickness development. For lubricated contact involving polymers with low elastic moduli, EHL is referred to as soft-EHL. It seems likely that synovial joints will undergo soft-EHL at some point in the load and motion cycle due to the compliance of articular cartilage. However, synovial fluid has been shown to be isoviscous, or viscosity independent of applied pressure[6], which does not satisfy the general equations of EHL. As such, a lubrication regime described by more precise EHL film thickness equations called isoviscous-elastic are used to approximate the minimum film thickness in joints[21].

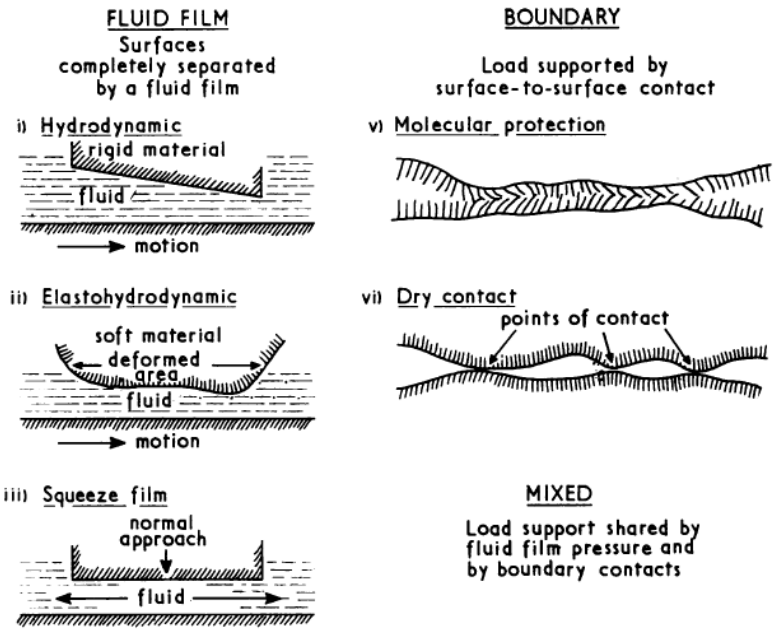

Figure 2-8: Types of lubrication regimes between two surfaces loaded together[19].

The predicted lubricating film thickness is compared to the surface roughness of the bearing surfaces to indicate the amount of asperity contact and severity of wear. EHL has been used to model UHMWPE cup and metal wear in the hip joint. The resulting thickness of lubricant film was found insufficient to separate polymer-on-metal bearing surfaces *in vivo*, resulting in the load being supported by both the lubricant and the higher asperities of the bearing[22].

In the situation where film thickness falls such that the compressive load across the bearing is supported jointly by the fluid and solid body asperity contacts, a mixed-lubrication regime is experienced. Asperity-asperity contacts provide the origins of adhesive and abrasive wear mechanisms, where both interfacial and cohesive wear of the polymer will constitute the frictional force and energy dissipation at the sliding interface.

Considering the historical proposals for joint lubrication it seems likely that natural joint lubrication will consist, to some degree of all the above mechanisms and furthermore there will be contact between both prosthetic surfaces operating *in vivo*. Despite a mixed-lubrication regime it is believed that little or no transfer film occurs between the UHMWPE cup and the femoral ball when articulating *in vivo*[23-25]. It has been suggested that proteins in natural synovial fluid adhere to the metal[7, 26] or ceramic[27] surface acting as boundary lubricants preventing adhesion.

2.2.2.2 In vitro Lubricants

In vitro wear studies have shown the type of lubricant to have a large effect on the wear of both PTFE and UHMWPE. Pin-on-plate studies have shown a build up of transfer film from both dry sliding and when water or saline solutions are used as lubricating mediums[23, 24, 28]. This has been attributed to the smooth molecular profiles of both polymers permitting unobstructed movement between molecules. The result is a reduction in the cohesive strength of the polymer allowing transfer to the metal counterface[29]. Transfer of UHMWPE onto explanted femoral heads is not reported in the literature. Unlike synovial fluid, it is generally acknowledged that water and saline solutions do not possess sufficient boundary lubricant properties to prevent transfer of polymer to metal. Therefore, dry and water based sliding are thought to induce modes of wear not representative of *in vivo*; a lubricant containing proteins is more appropriate.

Furthermore, simulator studies have compared wear debris from serum and other lubricants and concluded that the size and morphology of debris recovered under serum lubricated conditions is comparable to particles recovered from periprosthetic tissue at revision[25]. In brief, sliding in a

bovine serum lubricant produced polyethylene particles sub-micron in size, akin to those particles retrieved from surrounding joint tissue. To further corroborate the use of serum, no transfer film was observed on the metal femoral components, in a similar fashion to those surfaces imaged from explanted joints. In stark contrast under water based sliding, large 2-3mm flake like particles were observed along with traces of polyethylene transfer films on the metal counterfaces.

Denatured proteins found in serum after exposure to heating, cyclic vibration, and shearing from wear studies have been shown to be corrosive to UHMWPE[30]. Chandrasekaran *et al*. proposed that proteins trapped in the contact region were deformed through a combination of the normal loading and sliding action. The deformed molecule denatures releasing free radicals resulting in increased reactivity. The absorption of these free radicals into the near-surface of UHMWPE may cause chain scission or the rupture of molecular bonds, promoting the production of wear debris and susceptibility to wear.

A reduction in the wear rates of both conventional and crosslinked UHMWPE material with increasing protein concentration has been reported[31, 32]. The opposite wear behaviour is found of PTFE, higher wear rates were found to coincide with increasing protein concentration[33, 34]. The protein concentration of human synovial fluid extracted from healthy joints is approximately 18-20mg/ml[35].

The constituents of newborn calf serum used as a lubricating medium have also been shown to affect the wear of UHMWPE. Studies investigating the extent of protein composition (i.e. albumin to globulin ratio) have shown γ-globulin to enhance serum decomposition[34] and cause increased UHMWPE wear rates[30]. In brief, as the ratio of albumin to globulin increased, wear rates for both PTFE[33] and UHMWPE decreased[31].

2.2.3 What Makes a Successful Prosthetic Bearing Material?

Materials which form the two bearing counterparts must first and foremost be able to accommodate the range of forces imposed by patients of different size, without deforming to an appreciable extent. Gross deformation of the components would lead to pain and prosthetic revision. Structural integrity of the polymer acetabular cup must remain intact over a range of dynamic stress conditions. Mechanical stresses and strains are induced through cyclic loading and sliding of the joint. Furthermore the polymer should be tough. A tough material is one which can dissipate large amounts of strain energy without failure.

Once structural integrity and toughness have been established the focus falls upon wear rate, debris generation and coefficient of friction at the articulating surface. These must be acceptably low for a range of different tribological/physiological conditions to improve the component service lifetime. Friction is described as the surfaces resistance to relative motion; high friction may result in excessive wear and energy loss, too little friction may result in meagre grip and inefficient traction. According to the non-interacting two-term model developed by Briscoe and Tabor[36], friction at the polymer-metal interface is attributed to frictional energy dissipated by both adhesive surface interactions and sub-surface ploughing and abrasive interactions. A simpler definition of friction is described in Amonton's first law, discussed in greater detail within Section 2.6.1.

In general, if the counter surface is smooth, then wear may result from adhesive forces forming a transfer film as the cohesive strength of the softer material is overcome. This process involves the surface layers and is termed an interfacial wear process. A rough counter surface will increase the abrasive action acting to a significant depth beneath the polymer surface. The extent of this ploughing and plastic deformation is categorised as cohesive wear. The transition between the two zones is illustrated in Figure 2-9, extracted from a recent review by Briscoe and Sinha[37].

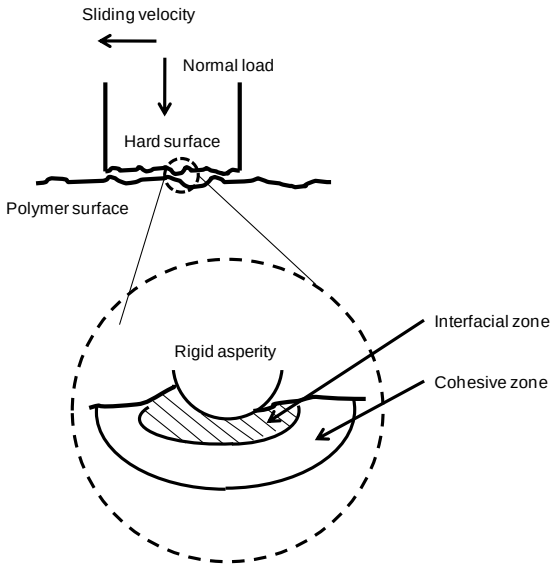

Figure 2-9: Two term model of friction[37]. Frictional energy at the sliding interface is dissipated by both adhesive surface interactions (interfacial zone) and abrasive sub-surface ploughing interactions (cohesive zone).

Wear rate and debris generation is perhaps a more subtle relationship in the physiological environment than in other "mechanical" systems. The UHMWPE cup may have sufficiently low

wear; in that the component will not "wear through" but debris released from the surface is known to be a precursor to a biological response called osteolysis. The development of osteolysis is expanded upon in Section 2.3.1. A good prosthetic bearing material should offer structural stability, toughness, low friction, low wear and minimal surface degradation under sliding.

Polymers are more compliant than metals and are characterised by their lower yield and ultimate strengths, but increased strain to failure (Table 2-1). As a result, nearly all contact deformation, plasticity and fatigue under loading and sliding occurs within the surface and sub-surface of the polymer component[38]. The hard metal/ceramic counterface has a strong influence over the dominant polymer wear mechanism and is discussed at greater depth in Section 2.4.2.

	PTFE	Polyacetal	UHMWPE	Cobalt-Chrome
Molecular weight (10^6 g/mol)	1-10	0.02-0.09	2-6	-
Density (g/cm^3)	2.17	1.42	0.927-0.944	8.3
Yield strength (MPa)	9	66-83	19	448-941
Tensile strength (MPa)	20.7-34.5	67-69	27	655-1277
Modulus of elasticity (GPa)	0.4-0.55	2.8-3.6	0.69-1	210
Elongation at break (%)	200-400	17-75	300	4-14
Poisson's ratio	0.46	0.35	0.46	-
Crystallinity (%)	93-98	60-77	39-75	-
Melting Point (°C)	327	172-184	138-147	-

Table 2-1: Mechanical properties from ASTM F75 for orthopaedic cobalt chrome and ASTM F-648 for fabricated UHMWPE.

In brief, rough metal counterfaces promote abrasive wear; ploughing, tearing and micro-cutting of the bulk polymer as hard metal asperities plough through the softer polymer to a significant depth. In contrast, polymers sliding on smooth metal surfaces are susceptible to adhesive wear mechanisms and fatigue on the surface and sub-surface. In the absence of boundary lubrication adhesion leads to polymer transfer onto the counterface. Transfer films alter the intended sliding materials and can be stable and low wearing, or unstable increasing polymer wear. Metal components, such as the femoral head, are polished to a very smooth surface finish in an effort to prevent damaging abrasive wear and favour slower, high cycle fatigue-type wear mechanisms within the polymer.

To add to the complex nature of acetabular cup wear, UHMWPE will typically exhibit elastic behaviour at low temperatures and high rates of strain and viscous behaviour at high temperatures and low rates of strain. A polymer that acts in this manner is termed visco-elastic[39].

This further complicates the relationship between applied load, strain rate, surface stress and shear stress beneath the UHMWPE surface. In addition, the magnitude of the coefficient of friction at the polymer surface can vary a sizable amount with the conditions of sliding[40], being dependent on the lubricating medium and sliding motion.

2.3 Why Research is Needed

2.3.1 Osteolysis

All materials considered for human implantation are subject to extensive biocompatibility and biostability studies. Testament to this is the excellent short to medium-term clinical performance of UHMWPE cups combined with metallic or alumina ceramic femoral components. However, despite the rigorous clinical trials, the long-term performance of the UHMWPE acetabular cup and counterbearing is compromised by aseptic loosening of the components.

During articulation thousands of micron and sub-micron sized UHMWPE wear particles are released from the surface with each step. These particles may cause a pathogenic response in surrounding periprosthetic tissue, leading to bone resorption at the component-bone interface and have been linked to the high rates of late-stage failure after some 10-15 years *in vivo*[41, 42]. The failure mode is not "wearing-out" of the acetabular component but rather wear-mediated osteolysis causing loss of bony support around the implant[43]. Aseptic loosening can result in micro-motion and joint instability, making joint revision surgery a necessity. Revision surgery can be technically challenging and the operational lifetime of revised components often being much shorter than the primary implant. The increasing trend towards the use in young active patients places yet greater tribological demands on these bearings.

A variety of debris shapes and sizes have been reported using scanning electron microscopy and particle size analysis. The majority of wear particles are known to be around the sub-micron scale[44, 45]. Polyethylene particles retrieved from periprosthetic tissue and worn acetabular cups have been imaged as both spheroids, similar in size to the nodular sub-units observed in the unconsolidated resin[46], and larger more elongated particles up to 10μm in length[47].

The body's immune system will respond to any foreign material introduced into the body[11]. In response to micron sized UHMWPE particles, a cascade of responses are triggered leading to new cell recruitment to the joint area (Figure 2-10). UHMWPE particles are phagocytosed by macrophages in the periprosthetic tissue, which release pro-inflammatory cytokines causing an imbalance in the osteoblast (bone depositing cell) and osteoclast (bone resorbing cell) levels[48]. Small phagocytosible particles 0.5-1.0μm are more active than large particles[49]. The amount of particulate debris may be reduced by reducing the volumetric wear of the UHMWPE component.

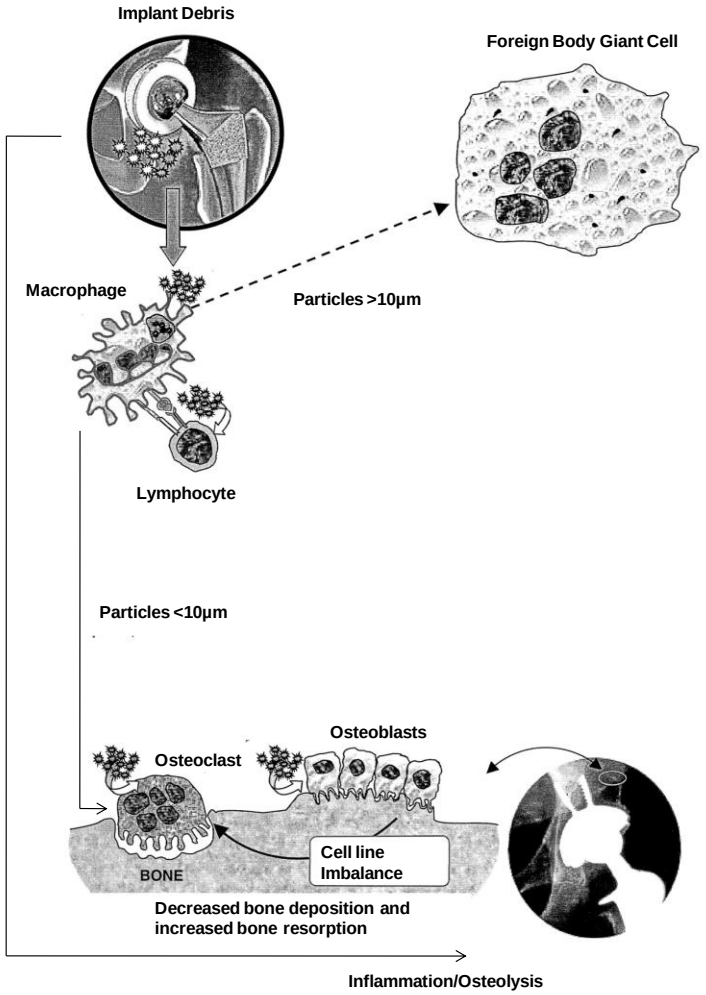

Figure 2-10: Postulated biological mechanisms of UHMWPE particle activated macrophage induced osteolysis[11].

2.4 How are Wear Mechanisms Described?

2.4.1 Tribology of Artificial Joints

The Oxford Dictionary defines tribology as the study of surfaces in relative motion. Wear, friction and lubrication are all constituents of tribology and are used to describe and understand surface behaviour of bearings and other moving mechanical systems. The study of tribology was brought to the British government's attention through the "*Jost*" report[50]. Compiled after observing industrial practice, the report emphasised the large number of machine breakdowns due to high wear, high friction and insufficient bearing lubrication. The report estimated huge amounts of money were being lost to wear, friction and lubrication.

The study of tribology can also be applied to the natural environment. The term "Biotribology" was introduced in 1973 by Dowson and Wright to account for wear, friction and lubrication in biological systems such as natural or artificial joints[51]. More recently, Dowson relates the load bearing joint to plain mechanical bearings using the following analogy; bone corresponds to the hard metal backing, articular cartilage to the softer lining of low friction bearing material and synovial joint fluid to the bearing lubricant[52].

2.4.2 Describing Wear

Wear in total hip arthroplasty can be considered as the loss of material from one or more surfaces due to relative motion. The literature is full of reported wear data, but in almost all cases it is material and situation specific. The unpredictable nature of wear is concisely summarised by Burwell and Strang[53] who wrote,

> "The lack of any empirical laws of wear makes it impossible to define any wear coefficient in the sense that Coulomb's first law enables us to define a coefficient of friction, or Newton's law defines a coefficient of viscosity, or Hooke's law a Young's modulus".

Wear of prosthetic components can take place in several locations; for example articulation between intended bearing surfaces, such as the femoral head inside the acetabular cup, or articulation between two non-bearing surfaces, such as the back of the polymer cup on the metallic backing. Wear is classified according to four principal mechanisms; adhesion, abrasion, fatigue and corrosion. Each mechanism is summarised in the following short sections. It should be noted that each is not a distinct route to debris production; rather that more than one mode

will often be responsible for surface degeneration and wear. Further discussion of UHMWPE wear is dealt with in Section 2.7.

2.4.2.1 Adhesion

When two nominally flat surfaces approach, initial contact occurs at the tips of the highest asperities. The actual area of surface contact is dictated by the deformation of these asperities under load and is called the real contact area. Stresses at these junctions will be locally higher than the nominal far-field stress and asperity deformation will be either elastic (recoverable deformation) or plastic (permanent deformation)[54]. Upon sliding, adhesive wear will occur if the molecular forces of attraction between contacting asperities is greater than either cohesive strength of the individual materials. Under such conditions transfer and material removal will occur from the weaker surface and deposit on the stronger surface (Figure 2-11). In the case of polymer-on-metal sliding, loss of polymer due to adhesion results in a transfer film.

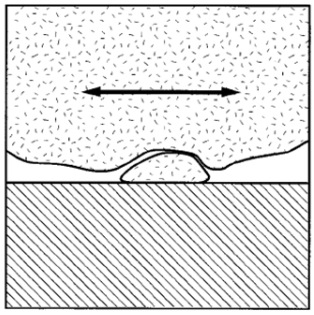

Figure 2-11: Adhesive wear[55]. Molecular forces of attraction between the sliding bodies are greater than either cohesive strength of the bearing surfaces, leading to a loss of material from one surface to another.

Under water lubricated sliding conditions UHMWPE forms a transfer layer against the corresponding metal surface[56]. The transfer occurs when the adhesive force between metal and polymer is greater than the cohesive strength of the UHMWPE. This tribological event causes what was originally polymer-on-metal sliding to become polymer-on-polymer, although the inherent nature of the transfer film can make it fragile and prone to breaking up, causing the bearing couple to revert back to polymer-on-metal[23]. Under such conditions the process of polymer transfer is cyclic.

The molecular chain profile determines the ability of the polymer to form either a very thin stable transfer-film or unstable lumpy transfer during dry sliding. Polymers with side branching are known to produce unstable lumpy transfer on metal counter surfaces during dry sliding[38]. For

example, PTFE has a “smooth” molecular profile (described at greater length in Section 4.2.2) and as such thin transfer films adhere to a glass substrate.

2.4.2.2 Abrasion and Toughness

Abrasive wear occurs between surfaces with different levels of hardness and is described as “wear by displacement of material caused by hard particles or protuberances”[57]. Asperities on the surface of the harder material plough material away from the softer surface (Figure 2-12). In THR the mode of wear is particularly pertinent to the severity of wear in the softer UHMWPE by the harder metallic or ceramic surface.

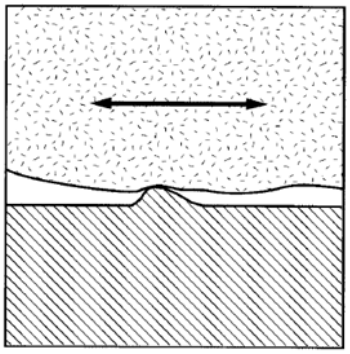

Figure 2-12: Abrasive wear [55]. The harder material surface will remove material from the softer surface through a process of abrasion and ploughing.

The degree of roughness, to a first approximation, is typically represented by the arithmetic surface roughness (R_a) which is described as the deviation of surface peaks and troughs about a mean surface line (Figure 2-13). However, arithmetic surface roughness on its own is not sufficient to characterise surface texture. The skewness of the amplitude distribution about the mean centre line (R_{sk}) can be used to describe the symmetry or asymmetry of peaks and troughs. Zero skew describes a surface with equal weight of peaks and troughs. A surface with negative skew indicates a higher proportion of troughs to peaks (less potential for abrasive damage) and positive skew implies the surface is dominated by peak imperfections with more potential for abrasive wear.

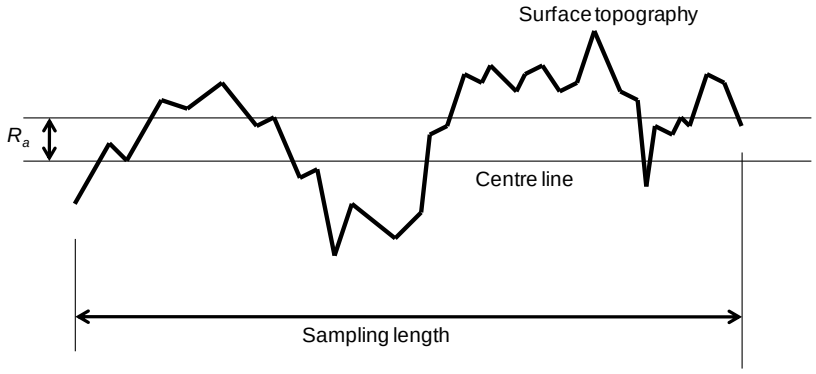

Figure 2-13: Arithmetic surface roughness (R_a)[4].

Laboratory studies on simplified pin-on-disc tribometers have shown higher polymer wear rates on surfaces with increasing roughness[58]. Early studies would involve the polymer pin being statically loaded onto rotating discs with varying sizes of abrasive particles embedded on the disc surface. Abrasive particles penetrate the softer polymer and produce wear debris by shear or micro-cutting, or by low cycle fatigue. These experiments linked the ability of a polymer to resist abrasive wear according to toughness, or energy required to rupture the material[59]. This finding, called the Ratner-Lancaster relationship, correlates polymer wear rate to be inversely proportional to the toughness or product of the stress and strain at tensile break (Equation 2-2); where V is the wear volume, σ_{UTS} is the ultimate tensile strength and ε_{UTS} strain to failure of the polymer. Because this relationship relies on bulk properties rather than surface properties, it is often summarised as the cohesive part of the two-term interfacial and cohesive model[36] described in Section 2.2.3.

$$V \propto \frac{1}{\sigma_{UTS}\varepsilon_{UTS}}$$

Equation 2-2: Ratner and Lancaster found the wear volume to be proportional to the reciprocal of the mechanical properties at tensile break.

More recent multi-directional pin-on-plate studies have confirmed the dependence of UHMWPE wear on counterface surface roughness. Cobalt-chrome plates with larger arithmetic mean surface roughness's were associated with increased UHMWPE wear[60]. Nevertheless there remains uncertainty as to the effects of surface roughness *in vivo*[61]. Elfick *et al.* conducted a retrieval study of forty-two pairs of femoral and acetabular components. No significant

[4] From the Zygo NewView 100 user manual (pg 3-53).

correlation was observed between UHMWPE clinical wear factor and femoral head arithmetic surface roughness.

2.4.2.3 Third body

Third body wear is a form of abrasive wear in which particles of a material not initially associated with surface articulation become trapped in the contact zone[62] (Figure 2-14). In the context of a cemented femoral component articulating against UHMWPE, 3rd body particles could be a result of PMMA (bone cement) particles becoming trapped within the two articulating bearing surfaces [63].

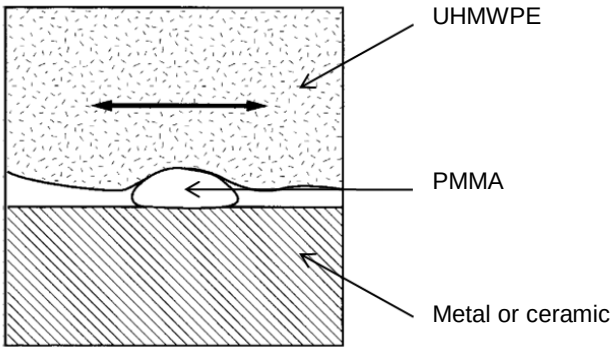

Figure 2-14: Third body wear[55]. Material not initially associated with the bearing couple may get trapped causing a form of accelerated abrasive wear.

Third body wear can damage both the metal and polymer bearing surfaces. A recent retrieval study of hydroxyapatite coated UHMWPE cups articulating against porous coated anatomical (PCA) stem combinations were revised due to severe osteolysis and loss of bone support. Hydroxyapatite surfaces, typically with grain sizes of 125-250μm were hot-pressed into the backside surface of the acetabular cups to encourage osseointegration between the component and supporting bone[64]. However, after 9 to 14 years post-implantation, examination under a scanning electron microscopy revealed that hydroxyapatite particles had migrated into the joint space and were embedded within the UHMWPE bearing surface. As a result, severe abrasion and scratching was observed on both the UHMWPE and metal surfaces.

2.4.2.4 Fatigue

Fatigue is a cyclic process usually involving fluctuating contact stresses below the material yield stress (high cycle fatigue) or stresses above the yield point (low cycle fatigue). The process is an accumulative mechanism where one stress and strain cycle would not normally be enough to

cause crack propagation or failure. Over many cycles the fatigue limit of the material may be exceeded resulting in the release of wear particles.

Under a mixed-lubrication and boundary regime, UHMWPE and counterface contact will occur between the larger surface asperities. At these local contacts, stresses exceeding polymer yield will result in microscopic plastic deformation and tearing. As such, polymer debris production has been treated as a low cycle plastic-strain driven fatigue process [65].

2.4.2.5 The Archard Wear Equation

The real area of contact between two surfaces is generally much smaller than the apparent contact area. Using a mathematical model, Archard introduced a theory of adhesive wear based on the concept of real contacts under plastic deformation[66]. To a first approximation, Archard found the real contact area between two surfaces to be proportional to the applied load. Upon further derivation the wear volume of a sliding couple was found to be proportional to the normal load and sliding distance and inversely proportional to the material hardness of the softer surface. This is represented mathematically in the Archard equation seen in Equation 2-3: where Q is the wear rate (volume per unit sliding), K is a dimensionless wear coefficient, N is the compressive force and H is the hardness of the softer material in sliding contact. The equation assumes that changes in load do not cause significant changes in any other sliding variable such as surface temperature. The wear equation was confirmed empirically through metal-on-metal dry sliding experiments; good agreement was found under steady-state sliding conditions.

$$Q = \frac{KN}{H}$$

Equation 2-3: The Archard equation.

Hardness in metals accurately describes the ease of plastic flow. However, the visco-elastic properties inherent in polymers make the definition less succinct. In the context of polymer adhesive wear, it is possible to replace the dimensionless wear coefficient and ambiguous hardness parameter with a dimensional wear factor, k and re-write the Archard wear equation (Equation 2-4):

$$V = kNx$$

Equation 2-4: The Archard equation for polymer sliding wear.

Where V is the wear volume (mm^3), k is the wear factor (mm^3/Nm), N is the applied normal load (Newton's) and x is the sliding distance (m). The equation implies that if the dimensional wear factor is constant, that is once the surface conditions during sliding attain steady-state, the wear volume is directly proportional to sliding distance and applied load. The wear factor term represents the probability of generating a wear particle and is often adopted as a way of communicating the probability that UHMWPE debris will be released from the articulating joint surface.

2.4.3 Representing Wear

Polymer wear is typically plotted on a graph of wear volume vs. sliding distance/no. of cycles (Figure 2-15). A period of accelerated wear at the beginning of such sliding experiments is often observed and is referred to as "wearing-in" or "bedding-in", attributed to the initially rough and irregular surfaces being worn down to smoother, lower wearing contacts. Upon "bedding-in" the more conformal surfaces may undergo a slower steady-state wear rate.

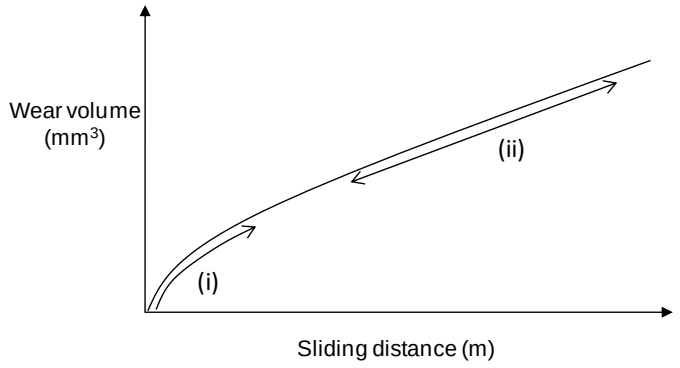

Figure 2-15: Wear graph schematic showing; (i) accelerated wear-in period; (ii) wear volume is proportional to sliding distance under steady-state conditions.

To image worn UHMWPE surfaces, scanning electron microscopy is traditionally used[67, 68]. Such topographic studies indicate the type and extent of the wear mechanisms acting under sliding. Abrasive wear may be revealed by the extent of ploughing and scratching on the surface. A burnished surface appearance may indicate an adhesive dominant wear regime. Electron microscopy images are used to show surface features on the micron/millimetre length scales. The discovery of acidic etching to reveal the crystalline structure in polyethylene[69] has led to more recent studies using both topographic and microstructural images to reveal the extent of near-surface deformation and wear on the nano/micron scale[70-72].

2.4.4 Surface Roughness Measurement

Wear and friction at the moving interface are of fundamental influence to the final surface texture and appearance after sliding. These characteristics are formed from a series of peaks and valleys that vary in height and spacing, possessing properties that are a result of the way the surface was produced or worn. Roughness parameters are usually measured with a contacting profilometer or non-contacting white light interferometer.

2.4.4.1 Contact

A surface measuring instrument relies on contact with the surface and typically consists of a stylus with a small tip, where the surface is measured by passing the stylus across the surface. As the stylus moves up and down in response to surface undulations, changes in height are recorded and plotted. The stylus tip diameter dictates the spatial resolution and limits the size of the smallest features to be recorded. Data is represented in a two-dimensional line scan, requiring a series of scans to produce three-dimensional information. On soft surfaces which could be damaged or influenced by the passing stylus, a casting can be taken to accurately reproduce the surface and, once cured is used under the stylus.

Castings of soft hip and knee cartilage have been used in conjunction with contact profilometry. The mean centre line roughness of cartilage taken from patients with osteoarthritis was found to be a minimum R_a 0.75µm, with a maximum, R_a 5µm[19]. In comparison, the UHMWPE acetabular cup is typically machine finished to R_a 0.1-2.5µm and the metal femoral head, R_a 0.005-0.025µm.

2.4.4.2 Non-contact

Non-contact interferometry instruments use the principle of constructive and de-constructive white light interference to produce surface information. Because this technique no longer relies on the stylus of a contact machine, immediate three-dimensional information is attained without the tip profile limiting the smallest resolvable feature. Instead, the size of the x and y scan area and spatial resolution is dependent on the magnification of the objective used to focus on the surface. Higher magnification increases the scan resolution and allows smaller surface features to be resolved.

Elfick *et al.* used a x400 magnification objective to scan 180x135µm areas on worn femoral components, giving a resolution of 0.56µm/pixel[61]. This setup is capable of differentiating finer surface undulations than those studies carried out on a contact measurement machine with, for

example, a stylus diameter of 12.5μm[71]. The larger tip may distort the true surface profile by broadening peaks and narrowing valleys[73].

2.5 Ultra-high Molecular Weight Polyethylene

UHMWPE has characteristics of notably high abrasion resistance, high impact strength, low friction, low density, excellent toughness, relative ease of fabrication, biocompatibility, and bio stability. As with any semi-crystalline polymer, these properties are inextricably linked to its chemical structure, molecular weight, crystalline organisation and thermal history[39].

2.5.1 UHMWPE Ultrastructure

UHMWPE is a linear polyethylene consisting of numerous repeating units of ethylene $(C_2H_2)_n$. A molecular chain segment is seen in Figure 2-16, where the carbon backbone forms a stable all-trans zig-zag configuration. All-trans isomerism refers to the orientation of bonds about the backbone chain resulting in the lowest energy, most stable chain conformation. Within each molecule atoms are bound by strong covalent bonds. Neighbouring molecules are bound by weaker van der Waals forces.

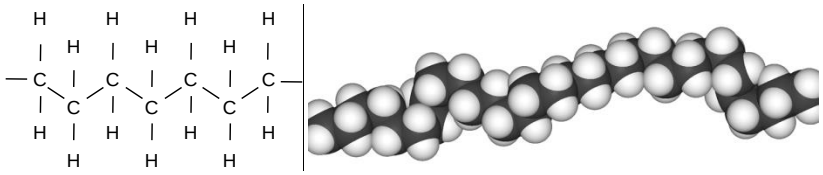

Figure 2-16: Polyethylene chain segment[5].

Polyethylene is referred to as a semi-crystalline polymer based on its ability to partially crystallise from the melt. Figure 2-17 shows the simplest semi-crystalline two-phase model of polyethylene[74]. Upon cooling from the melt a proportion of linear molecules fold in a close-packed regular manner forming ordered domains known as crystalline lamellae. The remaining molecules are dis-ordered and tangled in amorphous domains, where a proportion of chains may bond with multiple neighbouring crystal structures.

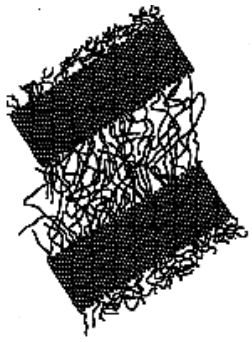

Figure 2-17: Two adjacent chain folded lamellae and interlamellar amorphous material[75].

[5] From http://plastics-engineering.blogspot.com

The regular folded chains pack into an orthorhombic crystal structure with lattice parameters a=0.741nm; b=0.493nm and c=0.254nm[76] (Figure 2-18). The main chain axis is oriented perpendicular to the top and bottom crystal surfaces according to the chain folded model[74]. UHMWPE lamellae are typically 10-50nm in thickness and 1µm in length[77]. However, due to the high molecular chain weights in UHMWPE, a chain with an average molecular weight of 6 x 10^6 g/mol can be up to 27µm in length[6], greatly exceeding the thickness of individual crystal lamella. To account for this, the long-chain molecules are proposed to fold back and forth within each crystal structure such that the backbone axis is perpendicular to the top and bottom fold surfaces. Molecules are held in the unit cell arrangement by secondary van der Waals bonds.

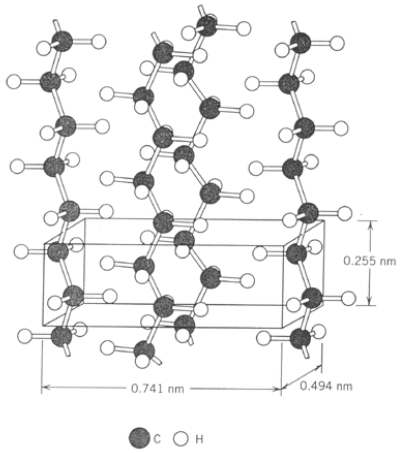

Figure 2-18: Perspective view of the orthorhombic crystal structure of a polyethylene unit cell where; a = 0.741nm; b = 0.493nm; c = 0.254nm[76].

Crystal lamellae are separated and joined by dis-ordered chain molecules or amorphous material[78]. Amorphous chains which connect one or more crystal lamella are called tie-molecules.

---

[6]In the planar zigzag configuration bond lengths and angles along the carbon-carbon backbone are shown below:

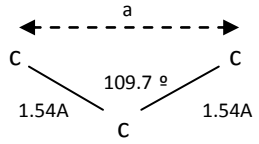

Using the cosine rule $a^2 = b^2 + c^2 - 2bc * cosA$, a = 0.252nm. Therefore, UHMWPE with a molecular weight of 6x10^6 g/mol may have up to 214,286 carbon atoms, equivalent to an extended chain length of 27µm.

The mechanical properties of UHMWPE depend in part on the ratio of crystalline to amorphous material. Tensile tests show unirradiated UHMWPE with higher crystallinity has reduced mechanical properties such as ultimate strength and strain to failure, but assumes a larger modulus of elasticity and improved resistance to fatigue crack propagation[79]. This can be attributed to the crystal lamellae being significantly stiffer than surrounding amorphous material. Hence, UHMWPE with a higher crystallinity will have a greater modulus of elasticity and yield stress.

2.5.2 Polymerisation to Powder

UHMWPE is polymerised from ethylene gas in the presence of hydrogen and a titanium tetra chloride catalyst at high temperatures. The process is called Ziegler-Natta polymerisation. The end product is a fine white powder with a mean particle size of approximately 140μm[77]. Only two average molecular chain weights are polymerised into orthopaedic grade powder, $2x10^6$g/mol and $6x10^6$g/mol. Both are an order of magnitude greater than the nearest long-chain polyethylene, that of high-density polyethylene. The microstructure created through thermal and pressure treatments during polymerisation is temporary; subsequent consolidation into bulk material, post-manufacture sterilisation method and heat-treatment will dictate the final microstructural form, wear resistance and mechanical behaviour[80].

2.5.3 Powder to Consolidated Form

Processing UHMWPE from powder into bulk material commonly occurs through three manufacturing methods; ram extrusion, compression moulding and direct compression moulding (Table 2-2). Regardless of consolidation route, UHMWPE must meet or exceed the ASTM F-648 requirements listed in Table 2-1.

	Processing technique		
Consolidation method	Ram extruded	Compression moulded	Direct compression moulded (DCM)
Bulk form	Bars or Rods	Sheet	Net-shaped component
Final manufacturing step	Machining	Machining	Little or none

Table 2-2: UHMWPE is commonly processed through one of three techniques; ram extrusion, compression moulding or direct compression moulding[81].

Ram extrusion is the process of heating and compressing UHMWPE powder through a circular die. The powder is compressed and forms a rod or bar of similar cross-sectional area to the die dimensions. The consolidated material is drawn through the die to create an extrusion or length

of UHMWPE bar. Typical bar diameters are approximately 50mm. Once cooled, the bar is fed into an automatic lathe where it is machined into the acetabular shape and finished into the final component.

Compression moulding refers to a process of compressing the unconsolidated powder into thick sheets in a large press. Typical UHMWPE sheet sizes are 1x2m, with thicknesses between 30–80mm. The consolidated sheets are sectioned into smaller sizes and machined into the finished components.

Direct compression moulding (DCM) creates a finished component straight from the mould. Powder is placed into a mould of the exact acetabular cup dimensions, heated and pressed to form the finished shape. The bearing surfaces formed are already that of implant quality finish requiring little or no final machining.

The influence of consolidation method on wear performance is of interest to orthopaedic manufacturers wishing to maximise the longevity of their bearing components. In particular, comparisons between the wear resistance of DCM and ram extruded components have been well reported. In one *in vitro* study, DCM UHMWPE tibial components were found to be more wear resistant than machined compression moulded stock following 4 million test cycles[82]. However, the compression moulded stock was consolidated from GUR1050 material and the DCM components from 1900H stock. Although both grades have similar molecular weights they were produced from powders with different particle morphology. Starting powder morphology has been suggested to be linked to wear observed *in vivo*[46, 83]. Hence differences in wear behaviour observed in the Benson *et al.* study may not be solely attributed to consolidation method.

Bankston *et al*. evaluated the clinical wear rates of UHMWPE acetabular liners fabricated from ram extruded bar and DCM[84]. In this study the starting material was identical. Radiographic evaluation was performed to assess the linear wear of each acetabular component. After a follow-up period of 5-9 years a significant difference emerged between the wear rates of the two groups. DCM components had a mean linear penetration rate of 0.05mm/yr, lower than the ram extruded group which had a mean wear rate of 0.11mm/yr. To further corroborate this finding, a more recent study compared the clinical wear rates of 63 surgically retrieved acetabular components; 19 consolidated using DCM, the remaining cups machined from ram extruded bar stock[85]. The machined components were found to wear significantly more, a 2.3 fold increase

over the moulded components. Those cups belonging to the DCM cohort were found to be better consolidated with fewer fusion defects when imaged under a scanning electron microscope.

Microstructural variation as a function of depth within ram extruded and compression moulded material has also been investigated[86]. Microstructural disparity between material close to the die or compression walls and material within the middle of the stock was observed using x-ray scattering. This variation was attributed to the applied shear stresses exerted on the melt material in contact with the die walls or compression platens. However, in both manufacturing material groups crystallographic texture variation was low compared to that induced by large scale plastic deformation.

2.5.4 Manufacturing

Three different grades of resin are produced for implant manufacture. Two are supplied by Ticona (Bayport, TX, USA, and Oberhausen, Germany) with the nomenclature, 1050 and 1020. A third, 1900H is produced by Montell (Wilmington, DE, USA). The Montell resin code has remained unchanged despite modifications in production during the last three decades. The Ticona numbering system is more readily explained[77]. The first digit refers to its use; all Ticona resins produced for orthopaedic implants have a first digit of 1. The second digit, 0, indicates the absence of calcium stearate. Ticona resins no longer have added calcium stearate so this digit remains 0. The third digit is correlated to the average molecular weight of the resin, for example, 1050 has a higher average molecular weight than 1020. Finally, the fourth digit is a Ticona internal code designation.

2.5.5 Sterilisation Techniques

UHMWPE components are sterilised to eradicate bacterial or viral agents which would otherwise be implanted into the body along with the component. Infection of any kind may result in early revision and with it the chances of long term survivorship. The sterilisation technique must be effective without degrading the properties of the implantable material. The simplest method of sterilising is to expose the device or component to high temperatures using steam or dry heat[87]. These methods can reach temperatures up to 180°C making them unsuitable in the sterilisation of UHMWPE which has a melting temperature nearer 140°C.

UHMWPE was traditionally sterilised by Charnley using a 25kGy dose of gamma irradiation in air[81]. This method was discontinued in the mid-1980's over concern that irradiation in an

oxygen-rich environment compromised the wear performance and mechanical properties in a continuous degenerative process called oxidation embrittlement.

Oxidation of UHMWPE is a chemical process that results from chain scission and free-radical formation. The high energy irradiation source ruptures a proportion of covalent bonds leaving behind a population of free radicals. Free radicals are charged ions which are capable of subsequently forming new bonds. In air, the resulting carbon free-radicals become free to react with oxygen, causing a reduction in molecular weight, mechanical properties, toughness and resistance to delamination wear[88, 89]. Furthermore, UHMWPE irradiated in an oxygen-rich environment is known to continually degrade during shelf storage and *in vivo* use. A study of seventy-three gamma sterilised in air knee implants revealed a mean wear rate of 0.9mm/yr for those components with a shelf life of at least four years increasing to 1.6mm/yr for those with a shelf life of at least five years[88].

Chain scission and corresponding reduction in molecular weight has been linked to increased crystallinity and decreased strain to failure reducing the toughness of the material[90]. The increase in crystallinity may be attributed to the higher mobility associated with shorter molecular chains, more able to fold into crystalline lamellae.

Under certain conditions, polymers with reduced toughness have been shown to offer lower resistance to abrasive wear (Section 2.4.2.2). To minimise the harmful effects of oxidation, the current industry standard is to sterilise UHMWPE components with gamma irradiation in an inert oxygen-reduced environment or sterilise without radiation using ethylene oxide or gas plasma[77].

2.5.6 Crosslinking

Irradiation and subsequent chain scission in an inert environment is more likely to lead to crosslinking than oxidation. Crosslinks are covalent bonds that link adjacent UHMWPE chains. Historically, orthopaedic polyethylene has always been crosslinked; an unintentional artefact of early sterilisation methods, but these methods also produced significant levels of free radicals forming unintentional carbonyl bonds (Section 2.5.5).

Modern polymer grades are intentionally processed to enhance the crosslink levels and crosslink density in an effort to improve the wear resistance of UHMWPE in certain applications. The relationship between crosslinking and wear is further described in Section 2.7.2. Crosslinking

can be achieved by subjecting the polymer to higher doses of radiation than those levels normally considered for sterilisation purposes for a discrete period of time.

Conventional UHMWPE implants may see sterilisation radiation doses between 25 to 40kGy (2.5Mrad to 4Mrad), while crosslinked materials receive elevated doses between 50 to 100kGy (5Mrad to 10Mrad)[81]. The higher energy doses rupture a greater number of chains producing a larger population of free-radicals. In the inert environment the free-radicals bond together to form crosslinks between neighbouring chains. Crosslinks stiffen the polymer network and limit chain movement. This can be seen schematically in Figure 2-19.

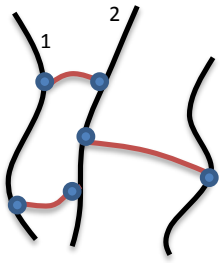

Figure 2-19: Crosslinking in the amorphous domain; movement between chains 1 and 2 is limited due to additional post-irradiated crosslink bonding (shown in red).

Not all free-radicals are available to form additional C-C bonds. Residual free-radicals that become trapped in the ordered crystalline domains do not recombine and may subsequently react with diffused oxygen post-operatively. These residual free radicals are responsible for long-term oxidation embrittlement and continuous material degradation throughout the component lifetime.

To reduce the amount of oxidation embrittlement, crosslinked UHMWPE components are thermally treated in one of two methods; post-irradiation below-melt anneal or post-irradiated above-melt anneal. During these thermal treatments the molecular chains have more energy to reconfigure and recombine trapped free radicals. Below melt annealing is used to maintain the original irradiation microstructure. In a retrieval study comparing the oxidative states of below and above melt annealed acetabular cups, those having previously been subjected to an above-melt anneal treatment showed no measurable change in oxidation. Cups which were below-melt annealed were found with varying elevated oxidation levels and embrittled regions[91].

Above-melt annealing is thought to recombine a greater number of trapped free-radicals; this is likely to be attributed to the dissolution of the crystalline phase freeing a greater number of radicals for further crosslinking. Due to the higher temperatures inherent in the above-melt treatment the original crystallinity is lost during cooling from the melt. The result is the

formation of a lower crystallinity microstructure, a consequence of the newly formed crosslinks restricting chain mobility and folding. Lower crystallinity cross-linked material may experience a decrease in fatigue crack propagation resistance and mechanical properties when compared to conventional material[92, 93]. A decrease in mechanical properties such as ultimate tensile strain and elastic modulus may increase the susceptibility of the polymer to abrasive wear[59].

Figure 2-20 summarises the current crosslinking and sterilisation methods that originate from 1050 bar stock[94]. Cold Irradiated Subsequent Melt (CISM) refers to the process of irradiating at room temperature then annealing above the melt temperature. Cold Irradiated Annealed Non-melt (CIAN) refers to the process of irradiation at room temperature followed by a below melt anneal. Finally, manufacturers which electron beam irradiate at elevated temperatures followed by above melt annealing refer to the process as Warm Irradiated Adiabatic Melting (WIAM). Irradiation is carried out on heated components to increase chain mobility and promote cross-linking. The adiabatic term refers to the increase in bulk temperature of the polymer component due to the energy associated with the electron beam irradiation. This has been reported to be up to 10ºC±1ºC[95].

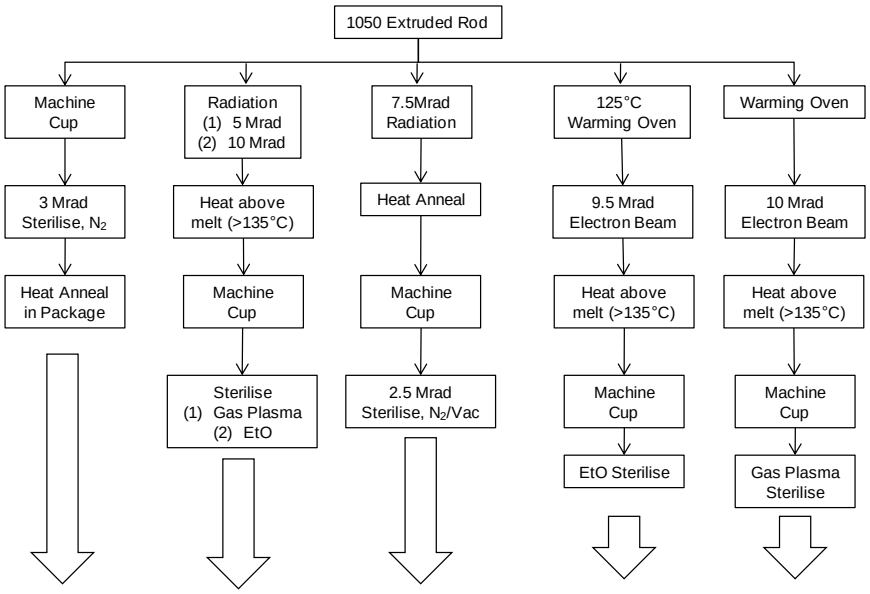

Process Name	**Heat Stabilised**	**CISM** (Cold Irradiated Subsequent Melt)	**CIAN** (Cold irradiated Annealed Non-melt)	**WIAM** (Warm Irradiated Adiabatic melting)	**WISM** (Warm Irradiated Subsequent Melt)
Product Name	Duration™	(1) Marathon™ (2) XLPE™	Crossfire™	Durasul™	Longevity™
Company	Stryker Howmedica Osteonics	(1) Depuy/J and J (2) Smith and Nephew	Stryker Howmedica Osteonics	Sulzer	Zimmer

Figure 2-20: The five crosslinking methods originating from 1050 extruded stock[94].

2.6 How are Joints and Materials Tested?

2.6.1 Introduction to Wear Studies

A tribometer is used to determine the resistance to motion and amount of wear that occurs between sliding surfaces. Resistance to sliding motion is described by a coefficient of friction. Defined by Amontons in 1699, it is the constant of proportionality between the applied normal force compressing two surfaces together and the resultant frictional force resisting motion (Equation 2-5); where F is the friction force, μ is the coefficient of friction and N is the normal reaction. The coefficient of friction is most commonly determined experimentally by loading one surface onto a counter-surface under precise load and applying movement between the surfaces.

$$F = \mu N$$

Equation 2-5: Amonton's first law of friction.

In vitro studies on the wear performance of candidate bearing materials for prosthetic joints are conducted on both full joint simulators and pin-on-plate wear machines. Full joint simulators model simplified anatomical positions and movements, using prosthetic implants to closely model the convex-concave contact found *in vivo*. Such screening devices are used to assess the bearing performance of prosthetic implants seeking FDA approval. The pin-on-plate machine offers a cost-effective alternative, using test samples with simplified geometry worn under less complicated sliding motions and loading conditions. These machines are often used to assess distinct tribological aspects of a bearing couple. A brief comparison between joint simulators and pin-on-plate machines can be seen in Table 2-3.

Wear model (contact geometry)	Schematic	Advantages	Disadvantages
Full joint (convex-on-concave)	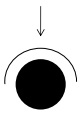	Close anatomical motions and loads	Cost of machine and samples. Time associated with setup and wear measurements.
Pin-on-plate (flat-on-flat)	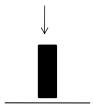	Cost effective, Study specific design/materials, Identify grossly unsuitable materials	Material wear can be motion dependent. Simplicity can limit clinical relevance

Table 2-3: Brief comparison between full joint and pin-on-flat screening devices.

2.6.2 The Pin-on-Flat Machine

The perceived role of pin-on-flat wear testers in orthopaedic research has been to rank material combinations in terms of their efficacy as bearing couples[24, 28, 96-99]. Materials which show good performance (low friction, low wear, good abrasive resistance), in these preliminary investigations will then be studied further on full joint simulators.

Pin-on-flat studies are often conducted on simple asymmetric wear-testing machines, where two sliding bodies are designed to undergo different wear rates. Most often, a faster wearing pin is loaded onto a rotating or reciprocating plate[54]. Typical motions employed by these machines are either uni-direction (pin-on-disc) or linear-reciprocating (pin-on-plate type).

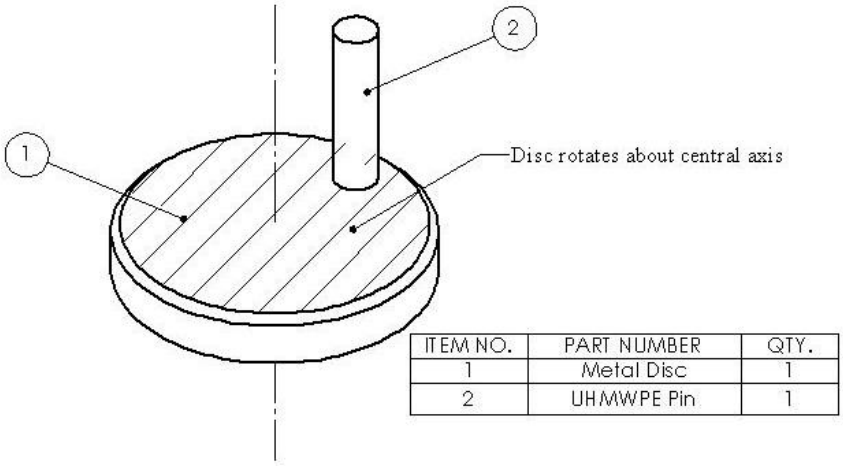

Figure 2-21: Pin-on-disc schematic; a test pin is loaded under constant force onto a rotating disc of constant velocity. The pin describes a circular path over the disc surface.

The conventional pin-on-disk layout used in orthopaedic studies consists of an UHMWPE pin statically loaded onto a rotating metal disc (Figure 2-21). The machine's simple kinematics produce constant sliding velocity which, although simple to maintain, may promote dissimilar lubricating conditions to those found in the joint. Under constant velocity, pressurised fluid in the contact zone may sufficiently separate the bearing surfaces preventing asperity-asperity contact. The hydrodynamic nature of this lubricating regime may cause unusually low, misleading, polymer wear rates.

A more realistic motion is that generated from a linear-reciprocating machine (Figure 2-22), where the start/stop nature of the joint is thought to play an important role in the abrasive/adhesive type wear mechanisms of implanted materials[24]. The back and forth motion-

type is more suited to the kinematic start/stop nature of the natural joint. Furthermore, because relative velocity is required to draw in and pressurise fluid to cause a separation effect, fluid film lubrication is disrupted at the extremes of sliding stroke resulting in surface interactions.

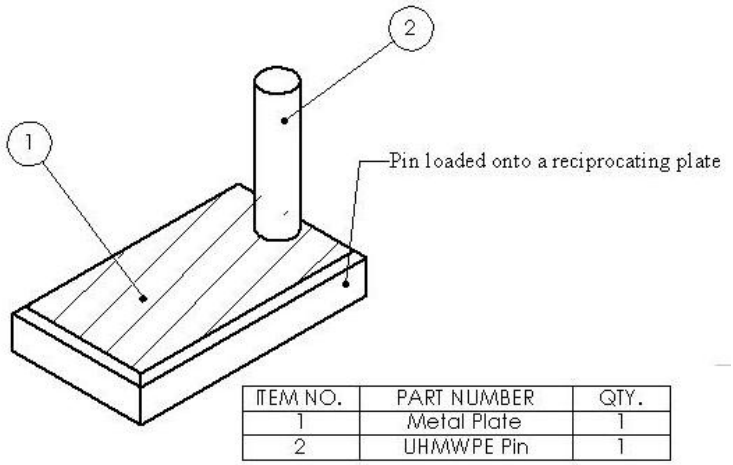

Figure 2-22: Pin-on-plate schematic; the pin, loaded onto a reciprocating plate, describes a linear "back and forth" wear path over the plate surface.

2.6.3 Pin-on-Flat Orthopaedic Wear Studies

In 1958 Sir John Charnley redesigned the metal-on-metal total hip replacement in order to reduce the frictional torque thought to be responsible for the high number of metal-on-metal joint failures. The novel polymer-on-metal bearing couple consisted of a small metal femoral ball articulating against a polymer cup. Torque transferred to the bone-implant interface was reduced (Figure 2-7) which was believed to increase joint longevity. The initial polymer, polytetrafluroethylene (PTFE), was known to exhibit low friction under sliding and offer good biocompatibility. However, PTFE had a poor wear performance, often failing clinically within a few years[1]. To gain confidence in the wear performance of bearing components, Charnley began to conduct accelerated wear studies on potential materials prior to implantation.

The history of orthopaedic pin-on-flat studies may be divided around the discovery that UHMWPE appears to strain harden and become more wear resistant under simple sliding motion. This finding is reported to have occurred in 1996[100, 101]. Section 2.6.3.1 attempts to describe a number of tribometers used between 1960-1996 and Section 2.6.3.3 reflects on those machines used in studies from 1996 onwards.

2.6.3.1 Simple Motion Machines

The first tribometer for screening candidate acetabular cup materials was a linear-reciprocating machine built in 1960 by Sir John Charnley's technician Harry Craven. The device consisted of four individual test chambers mounted on a linear reciprocating base driven by a crank arm and electric motor. Each polymer pin was statically loaded and worn against a corresponding metallic plate. The sliding distance, equivalent to the stroke length of the crank arm was approximately 25mm. Each 6.25mm diameter polymer pin was mounted perpendicular to the plate movement and loaded into contact with a nominal contact pressure of 5MPa. Wear tests on both PTFE and UHMWPE were conducted within an aqueous (saline) lubricant. The saline environment was thought to represent a harsh wear environment for the polymers. The height of each pin was recorded continuously during each test by a dial test indicator. A reduction in pin height was attributed to polymer wear and from this, volumetric wear rate could be calculated.

By 1968, the positive attributes of a thermoplastic polymer socket were readily recognised; low friction, high strength-to-weight ratio, sufficient stiffness and elasticity to provide damping under cyclic loading and relative ease of manufacture. Generic wear test machines would be used to screen potential prosthetic joint materials[102]. Amstutz used a LFW-1 tribometer built by Dow Corning, where a curved polymer block was machined to conform to an oscillating steel bar. A constant load and mineral oil provided a simple wear model for assessing candidate acetabular cup materials. Because the machine was not designed for wear testing orthopaedic joint materials, the wear model (specimen geometry, load, motion patterns, and lubricant) bared little resemblance to clinical conditions.

McKellop *et al.* addressed the issue of the generic wear tester by designing a 12-station linear reciprocating machine specifically for testing materials for use in prosthetic joints[24]. Some limitations of the Dow Corning LFW-1 were solved. For example, the difficult to machine curved polymer block specimens were replaced by simple polymer pins and the ability to wear test 12 samples increased the statistical confidence in polymer wear rates. The introduction of a simple specimen holder and chamber assembly allowed test specimens to be removed at intermediate intervals. The machine was also able to record lubricant temperature and compensate for fluid evaporation by automatic top-up using de-ionised water. This maintained a constant lubricant level and protein concentration in serum lubricated tests. Friction at the pin/plate interface was inferred by strain gauges attached to the pin holder. Creep of the polymer pins under constant load was found to be many times larger than the contribution of wear to

overall height loss. Where Craven and Amstutz calculated wear from physical change, McKellop *et al*. used gravimetric analysis to record polymer wear; samples were weighed before and after sliding with mass loss attributed to wear. Nevertheless, weight gain due to polymer fluid absorption was found to intermittently cause a net increase in the weight of the pins. To compensate for weight gain, additional control pins were soaked in lubricant and used to standardise the amount of fluid absorbed. Mass loss in the worn specimens was found after removing the weight gain of the soak-control specimens. Sliding tests were conducted in blood serum, saline solution and distilled water, where friction and wear processes were found to be dependent on the type of lubricating medium. Sliding in blood serum produced worn surfaces that resembled those on explanted prosthesis, preventing a UHMWPE transfer film.

Rostoker and Galante used a one-station uni-directional pin-on-disc wear tester to investigate the relationship between applied load and UHMWPE wear[98]. Pin wear was calculated through dimensional changes, however, pins were pre-loaded under static load and height loss recorded until creep became negligible prior to sliding. Sliding studies were conducted in a water-based lubricant and for the first time the machine offered control over lubricant temperature, where all tests were conducted at 37°C.

In 1982, Rose and Cimino, designed and built a hemispherical-on-flat uni-directional pin-on-disk tribometer[103]. In these tests, a rounded metal pin was statically loaded onto an UHMWPE disk (Figure 2-23). Contact geometries and loads were chosen to produce pseudo-Hertzian contact stresses, approximate to those found in the hip joint. Sliding was conducted in a bovine serum lubricant which was left at ambient temperature, 21°C prior to testing. Neither the tribometer nor testing protocol accounted for fluid absorption with soak-control discs nor were samples subject to pre-loading prior to testing to minimise creep. Instead, lubricant was collected and the wear debris filtered and weighed to approximate the amount of polymer wear. This novel measurement protocol proved challenging and is rarely used as the sole method to calculate wear in contemporary research laboratories.

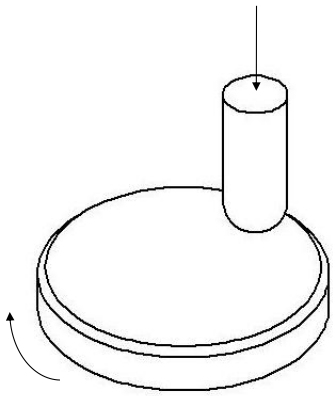

Figure 2-23: Hemispherical pin loaded onto a rotating disc of constant velocity. The contact geometry can be used to approximate contact stresses and areas using a method derived by Hertz.

Using a similar tribological arrangement to Rose and Cimino, Wright *et al*. used a Stanmore Mk-2 pin-on-disc machine where a hemispherical metal face was statically loaded, by the addition of weights of known mass, onto a rotating polymer disc[99]. The machine was designed with the ability to contra-rotate the pin specimen against the rotating polymer disc; pin and plate rotation was unsynchronised. Four test stations allowed wear to be investigated under four different lubricating conditions simultaneously. At 100h intervals discs were removed, washed, dried, weighed and surface measurements were recorded using contact profilometry. To account for fluid absorption, a control disc was stored in test lubricant and weighed alongside the worn disc at each interval. Despite the soak-control disk, occasionally a weight gain was recorded, where the minimum weight change was determined by the accuracy of the balance used, 0.2mg. The effect of lubricant, pin rotation, magnitude of applied load, relative velocities and polymer disc storage in various environments were all investigated. Under rotating pin and plate kinematics, characteristic wear traits similar to those seen on explanted UHMWPE acetabular cups were observed; wear track profiles were reportedly smooth and a reduced transfer of polymer onto the metal pins was observed.

2.6.3.2 The Strain Hardening Phenomenon

Despite the advances in tribometer design and reports of similar clinical wear features between studies in Section 2.6.3.1 and retrieved acetabular cups, the one degree of freedom motion machines, adequate for constant load/constant velocity and constant load/sinusoidal velocity work prove inadequate in representing UHMWPE clinical wear rates and wear factors. It is now commonly accepted that simple sliding kinematics produce wear factors up to two orders of magnitude lower than clinical data[104-106]. Similar discrepancies in wear data are not observed using hip simulator machines despite the growing number of different designs in use[107]. The less complex wear screening devices are thought to re-orientate UHMWPE molecules parallel to the direction of sliding to extremes uncommon with *in vivo*[101]. The restructuring produces an UHMWPE worn surface that is stronger and more wear resistant in the direction of sliding. The phenomenon is known as strain hardening[108]. This molecular orientation may be thought of in a similar manner to the molecular alignment of polyethylene under tension, an analogy discussed at greater length in Section 2.7.1.

The discovery of microstructural alignment in response to the quasi-linear motion of early wear screening devices and the consequent strain hardening offered an explanation for the divergent wear rates produced in early pin-on-plate studies when compared to considerable *in vivo* wear rates[109]. An example of microstructural alignment in worn UHMWPE imaged during this investigation is seen in Figure 2-24.

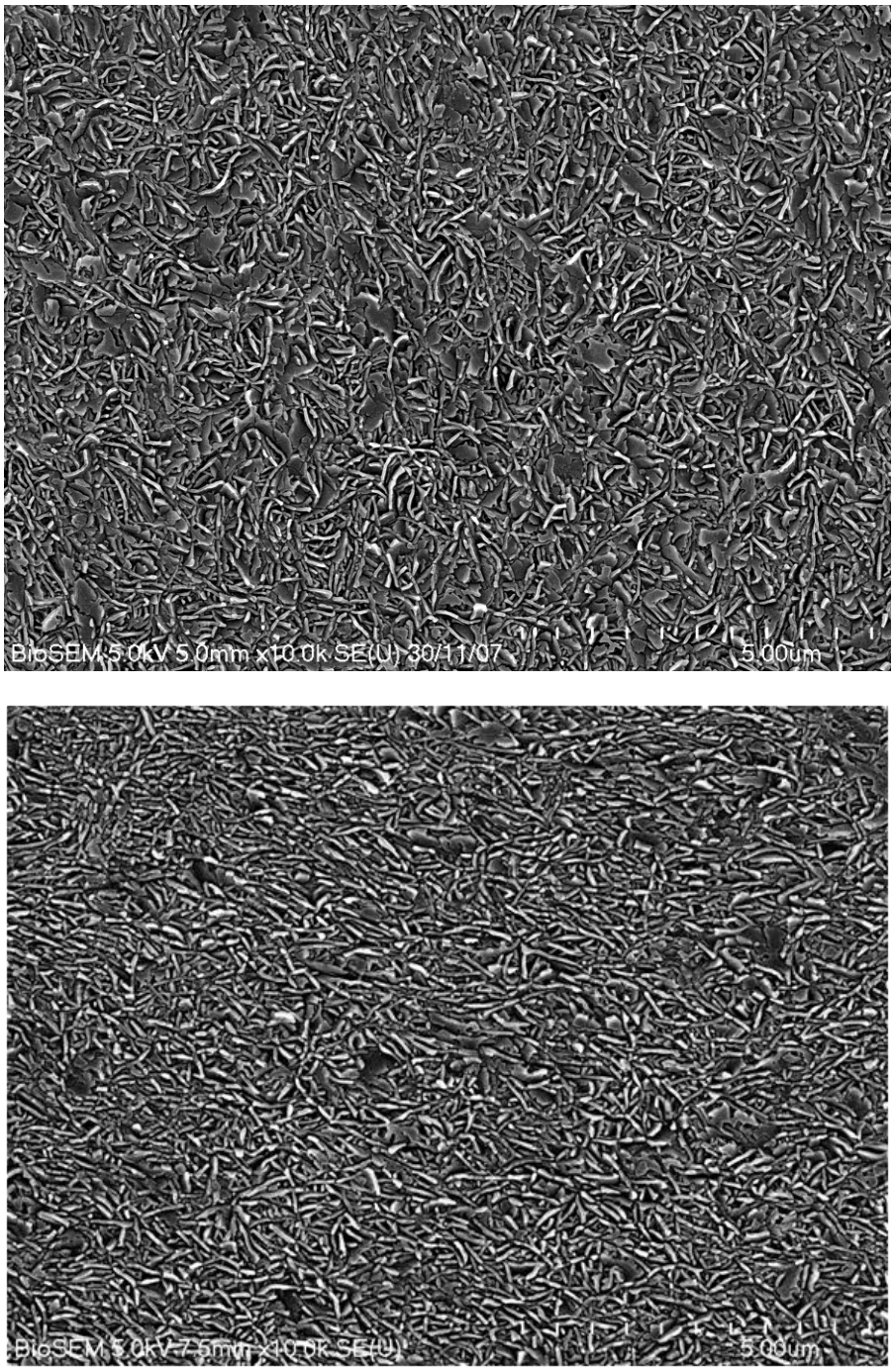

Figure 2-24: FE-SEM micrograph of (above); etched +PE unworn control material, and (below); etched +PE following three million load and linear reciprocating motion cycles. Note the preferred orientation in the principal, left to right, sliding direction.

Early anisotropic wear behaviour of polyethylene was first noted by Pooley and Tabor who found wear of HDPE to be highly influenced by the degree of slide paths crossing on the worn surface[29]. A similar observation in orthopaedic UHMWPE sliding led to the term "crossed shear" to explain the relationship between UHMWPE acetabular cup wear and multi-directional motion[100]. By considering two adjacent quasi-rectangular wear paths traced on the femoral head during gait it is possible to appreciate the cross-shear phenomenon, Figure 2-25.

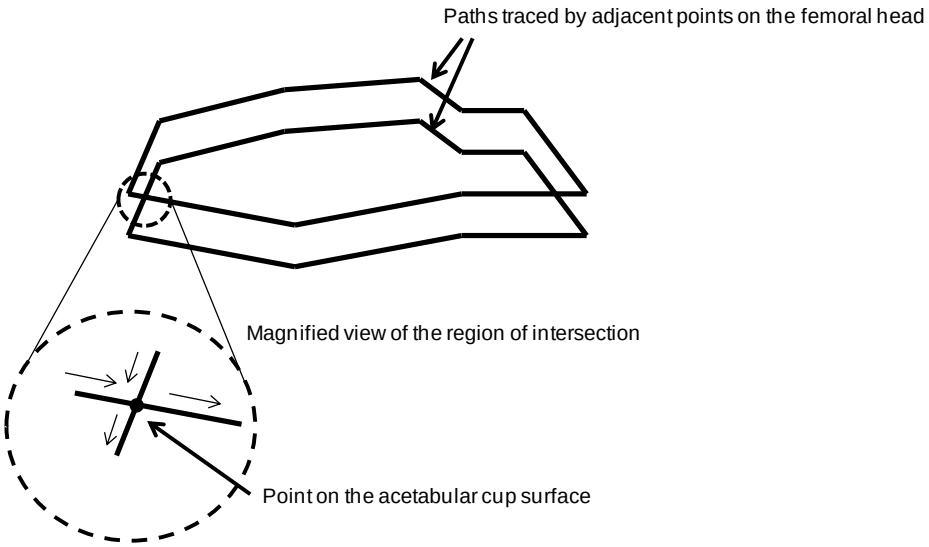

Figure 2-25: Multi-directional shear acts at the intersection of surface "crossing" paths[100].

To account for the accelerated wear within the body, Wang *et al*. propose that UHMWPE undergoes an orientation softening phenomenon in response to the complex multi-direction motion within the hip joint[110]. In brief, orientation softening suggests that UHMWPE molecules align in the primary wear direction, producing a surface with greater wear potential under perpendicular motion, or cross-shear motion. The orientation-softening model accounts for the directional dependence of the wear track whereby UHMWPE strain-hardens in the primary flexion/extension direction (producing very low wear rates under linear-reciprocating motion) and in doing so increases the susceptibility to wear in a direction perpendicular to this, corresponding to the adduction/abduction direction (explaining higher *in vivo* wear rates).

To further this observation, a theoretical wear model based on the effective frictional work concept was introduced[111]. Known as the unified theory of wear it expands on the orientation softening model by attempting to simplify the complex wear mechanisms occurring on the polyethylene surface.

Consider a rectangular wear path of sides length A_{slide} and B_{slide} (Figure 2-26) where $A_{slide}<B_{slide}$ such that B_{slide} defines the principle direction in which the molecules are known to orientate. Increased wear resistance or strengthening in the principal direction results in weakening or increased susceptibility to wear in the perpendicular direction. Wang suggests wear in the B_{slide} direction is negligible and therefore the work done to generate a wear particle in this direction can be neglected. As such, only the frictional work in direction A_{slide} should be considered responsible in producing wear.

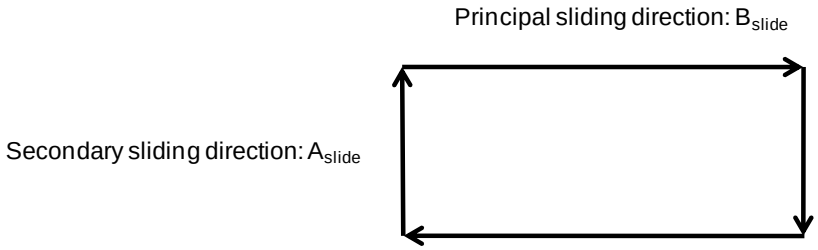

Figure 2-26: Simplified rectangular wear path showing; B_{slide}, the principal sliding direction; A_{slide}, the cross shear direction.

The frictional work associated with the rupturing of molecules and debris generation in the A_{slide} direction can be derived from the concept of energy and work done (Equation 2-6):

$$\Delta W_A = \frac{2\mu N v}{w}\left(\theta - \frac{sin(2\theta)}{2}\right)$$

Equation 2-6: Theoretical frictional work released per cycle in the perpendicular direction.

Where, μ is the coefficient of friction, N is the applied normal load, v is the velocity, w is the angular velocity and θ is the maximum cross-shear angle. The total volume of wear debris per cycle is found by dividing the frictional work by the work required to produce a unit volume of wear debris, or expressed another way, the volume of wear debris is proportional to the friction coefficient, the normal load and the sliding distance per cycle in the effective work direction (Equation 2-7).

$$V \propto \mu N(2A_{slide})$$

Equation 2-7: Expression for wear rate per sliding cycle.

Recall that the wear factor is found by dividing the wear volume by the product of the normal load and sliding distance, then:

$$k \propto \frac{\mu N(2A_{slide})}{N(2A_{slide}+2B_{slide})} \propto \frac{A_{slide}}{A_{slide}+B_{slide}}$$

Equation 2-8: Wear factor proportional to the crossing path motion.

In an effort to assess the accuracy of this model five rectangular wear tracks (5x5mm, 4x6mm, 3x7mm, 2x8mm, 1x9mm) and a linear track (0x10mm) were programmed into an AMTI OrthoPOD multi-station pin-on-disc machine[112]. Discrepancies over the wear rates predicted by the model suggest that some of the underlying assumptions maybe overly simplified[47, 112]. Nevertheless, the discovery of microstructural alignment in retrieved acetabular cups[44] and simulator-tested components[108] indicates the possibility that molecular orientation may occur in the ball and socket joint. If Wang's wear model is to be believed then such alignment would leave the UHMWPE surface more susceptible to wear in directions that cross the aligned structure. To exploit this characteristic wear behaviour in such a way as the human gait does on implanted polyethylene acetabular cups, desktop tribometers should exert some form of multi-directional motion at the sliding interface.

2.6.3.3 Multi-directional Motion Machines

Contemporary asymmetric pin-on-plate wear-testers generate sliding motions using two degrees of freedom (Table 2-4). With the importance of multi-directional motion acknowledged, existing designs would often be adapted into configuration 1 by rotating the pin against the reciprocation of the test plate to produce multi-directional motion (Figure 2-27)[105, 113, 114].

Configuration	Description	Degrees of freedom (translations/rotations)	
		Plate	Pin
1	Pin rotates/oscillates. Plate reciprocates	1	1
2	Plate translates in two axes Pin completely fixed.	2	0

Table 2-4: Two of the most common experimental sliding arrangements in contemporary multi-directional motion machines.

These machines are capable of producing conventional UHMWPE wear data in what is considered the clinical range, assessed through linear penetration rates and wear factor comparisons to clinical data[1, 115-117]. However, the rotating/oscillating pin-on-reciprocating plate machines produce highly diverse sliding paths, introducing complicated shear vector variation across the pin surface.

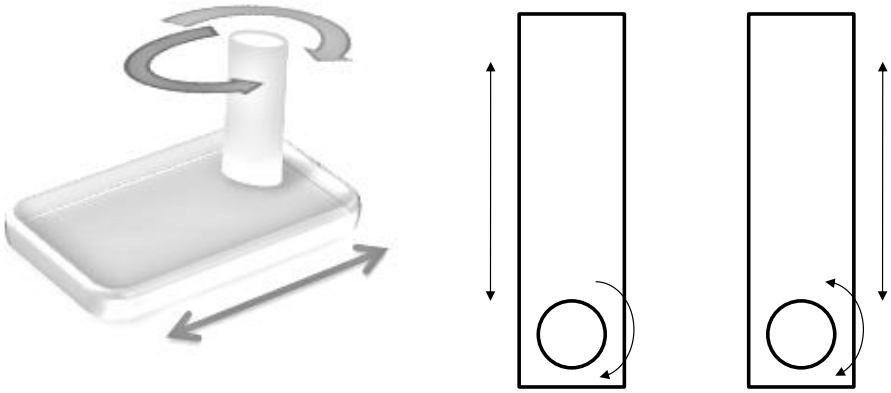

Figure 2-27: Simple multi-directional motion.

Such complexity has been suggested to be key to the success of producing clinically relevant wear data[105]. The mechanics of these machines generate wear paths that vary continuously along the radius of the face of the pin, much like the variation simulated to occur across the surface of a femoral head during *in vivo* articulation. Each point across the hemispherical surface will travel through a path possessing a different degree of cross-shear and aspect ratio. The aspect ratio of a siding path is defined as the ratio between the lengths of the primary and secondary

axes. For example, those points on the pin surface nearer the centre of rotation will travel in a more linear fashion, be subjected to limited multi-directionality and trace paths of higher aspect ratios (Figure 2-28).

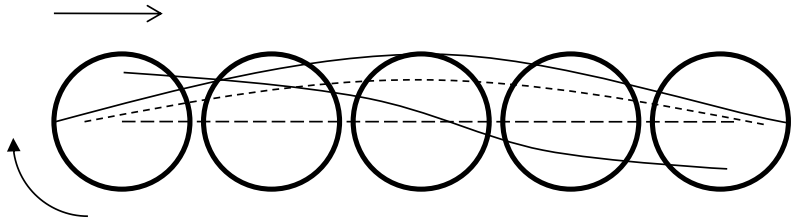

Figure 2-28: Four different paths traced at points on a rotating pin during one half cycle[105].

Adapted tribometers may achieve wear factors close to clinical but the nature of the sliding impedes any investigation into microstructural change during wear. Microstructural analysis is facilitated by adopting, or designing tribometers which exert uniform shear vectors across the pin surface. More recent machines are based around configuration 2 (Table 2-4), using two translations of the lower bearing surface, or plate, to produce sliding motion. In keeping the pin stationary, the whole pin surface is exposed to the same sliding motion and friction forces remain constant across the pin diameter resulting in a uniform tribological condition.

An early machine designed to exert uniform slide tracks across the pin face was the circularly translating pin-on-disc (CTPOD) tribometer[106]. The uniform slide path was thought to offer a more controlled approach to wear testing than adapted rotating pin machines. The pin remained stationary relative to a circularly translating plate ensuring each point on the pin surface travelled through the same circular wear path per cycle. The CTPOD wear experiments were conducted using a 10mm diameter slide path.

More recently, wear testers capable of rectangular wear paths have been used to introduce a secondary motion perpendicular to the principal motion axis. The rectangular motion path was asserted to better approximate the quasi-rectangular cross-shear motion uncovered from slide track simulations[100]. A 2-axis stepper driven system was built and applied by Bragdon *et al.* to offer a simple approximation of the sliding path and load experienced by a representative point on the femoral head[104]. The two translations introduced identical shear vectors at the sliding interface creating a uniform tribological condition. A motion control system controlled the two slides mounted orthogonally, producing a 10x5mm rectangular path (Figure 2-29). A double-peak, Paul-type load curve[8] was applied through use of hydraulics onto six 8mm diameter test pins.

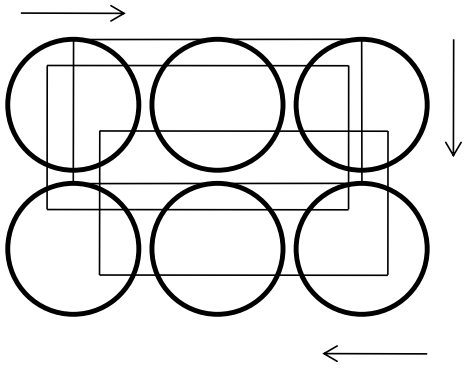

Figure 2-29: Sliding paths at points on the pin surface during rectangular motion. Crossing points are suggested to produce a condition of "cross-shear".

The AMTI OrthoPOD is one of few commercially available multi-directional tribometers used in orthopaedic wear studies[118]. The machine is capable of wear testing six pins which are secured in the upper head and loaded onto six individual test plates. Motion paths are generated through a combination of upper head rotation and disc holder rotation (i.e. the rotation of the disk specimens and the rotation of the eccentrically mounted pins). Straight line sliding paths between the pin and plate require the pin to rotate relative to the disk[119]. Test pins are no longer subjected to uniform shear vectors such as the CTPOD or two translation machines, but are instead subjected to tribological conditions more similar to those of the adapted oscillating pin-on-translating plate.

Current pin-on-plate machines employ either two rotations[112], two translations[104, 120], or a combination[105, 113], to achieve "cross-shear",[121] (Table 2-5). It is generally accepted that a desk-top tribometer capable of generating multi-directional motion is necessary to generate realistic UHMWPE wear rates and wear mechanisms. Even still, many tribological differences exist between *in vivo* and pin-on-flat machines. These disparities make pin-on-flat machines best suited to simple wear ranking of materials and wear relationship studies. To more accurately conduct either type of investigation, some form of multi-directional motion is required at the pin/plate interface. Multi-directional motion machines have produced UHMWPE wear factors well-matched to clinical, calling into scrutiny the relevance of wear data collected from simple uni-directional or linear-reciprocating machines. Despite this, some contemporary studies are still conducted on simple uni-directional pin-on-disc machines. Klapperich *et al.* and Zhou *et al.* have both used a uni-directional tribometer to investigate the effects of contact stress[71] and crosslinking[122] on UHMWPE wear rate.

Group	Motions	Polymer material	Pin diameter (mm)	Apparent contact area (mm^2)	Load curve	Peak Stress/Nominal stress (MPa)	Motion	Sliding speed mm/s	Frequency (Hz)
Boston 2001[104]	Two translations	Nonirradiated UHMWPE 4150	9.00	63.62	Double peak	4.8/~	Rectangular 5mmx10mm	60.00	2.00
Durham 2000[105]	Reciprocating / Translating	Gamma irradiated UHMWPE	5.00	19.63	Constant	~/2.04	Stroke 26mm, pin rotates	52.00	1.00
Harvard Medical school, Boston 2003[112]	Two rotations	GUR 1050 UHMWPE	9.00	63.62	Constant	~/3	Rectangular 1mmx9mm	20.00	1.00
Helsinki 100 station 2005[123]	Translating, pin stationary	Gamma irradiated UHMWPE	9.00	63.62	Constant	1.10	Circular, diameter 10mm	31.40	1.00
Helsinki 12 station 1998[106]	Translating, pin stationary	2.5Mrad gamma irradiated GUR 415 UHMWPE	3mm chamfered at 60°	7.07	Constant	10.00	Circular, diameter 10mm	32.00	1.02
Leeds 2006[113]	Reciprocating / Translating	10MRad gamma irradiated GUR 1050 UHMWPE	8.00	50.27	Constant	~/3.2	Stroke 28mm, pin rotation 60°	-	-

Table 2-5: Summary of contemporary pin-on-plate tribometers.

2.6.4 The Measurement of Wear

Wear in asymmetrical polymer pin-on-metallic/ceramic disc/plate wear tests involves the loss of material from the softer pin as it is worn against the harder counter-surface. Historically, pin wear has been calculated by one of three methods summarised in Table 2-6.

Method	Pros	Cons
Debris collection	Not susceptible to creep or dimensional changes	Difficult; lengthy protocol; accuracy of collection and filtration
Gravimetric analysis	Simple method, relatively quick to record individual samples	Affected by fluid absorption; require additional loaded soak-control specimens
Height loss	Simple method; quick to record individual samples	Dimensional changes other than from wear (such as creep) may introduce errors

Table 2-6: Historical wear methods used in asymmetrical pin-on-plate studies.

Contemporary pin-on-plate wear measurement is often made using a gravimetric method. Wear of the test pin is defined as the weight loss with respect to the initial weight, accounting for any weight gain due to fluid uptake (Equation 2-9):

$$W = W_I - W_F + W_G$$

Equation 2-9: Gravimetric weight loss accounting for fluid absorption.

*w*here W is the weight loss due to wear, W_I the initial pin weight, W_F the final pin weight and W_G the weight gain of the load-soak pin. Specimens that are subjected to load but remain stationary are known as "load-soak" pins. As demonstrated in Equation 2-9, load-soak specimens are in-part responsible for the final mass loss of the worn specimens. Because UHMWPE under load has been shown to absorb a greater amount of fluid than unloaded control specimens[124] the inclusion of a load soak-control is important for accurate wear measurement.

Mean linear wear rate is often presented when discussing and evaluating polymer wear against a flat plate. This value can be calculated by dividing the volume lost (mm^3) by the original cross-sectional area (mm^2) of the test pin.

2.6.5 Motion of the Hip Joint

The plastic socket used in ball-in-socket total hip joints is subject to a range of multi-directional motion and loading. Three-dimensional computer simulations illustrate the variation in sliding paths traced across the femoral surface during a single gait cycle[100, 125, 126]. The general form of the slide paths have been described as quasi-rectangular[100] or quasi-

elliptical[110], where each study shows a breadth of aspect ratios and sliding distances (Figure 2-30).

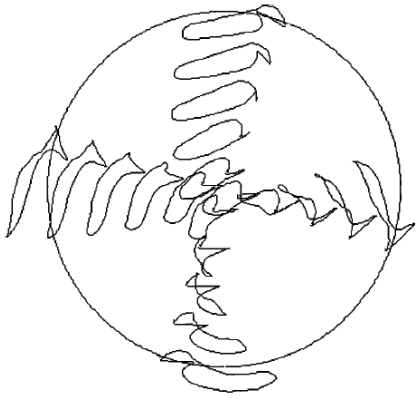

Figure 2-30: View of paths traced by 20 points on the femoral head. The spherical ball has been projected onto a flat surface for clarity[125].

More recently, this has been compared to wear tracks generated from contemporary hip simulators[107, 126]. Saikko and Calonius found discrepancies between simulated wear tracks and those from dynamic gait analysis. The differences in hip simulator wear paths may go some way to explain the range of experimental wear rates reported from different hip simulator machines[107].

Despite the range of complex motion and load waveforms adopted by research groups using hip simulators, those simulators running simplified square-wave load profiles and 2-axis motion paths in the presence of a protein-containing lubricant have been shown to produce wear rates comparable to *in vivo*[127].

To corroborate gait simulation studies, three-dimensional gait analysis has been collected from patients using video motion analysis. Davey *et al*. conducted gait analysis on seven patients due for revision of a Charnley-type primary hip replacement[128]. The principal reasons for revision were either wear of the UHMWPE cup or osteolysis. Twenty selected points on each acetabular cup were traced before revision resulting in an average aspect ratio of 3.33, ranging from 2.08±0.93 to a maximum of 5.36±1.59. The aspect ratio of the wear loci was defined as the length of the longest line joining two points on the wear path divided by the longest line joining two points perpendicular to the primary line. For example, the aspect ratio for a circular path is 1. Lower aspect ratios represent wider, more open paths as opposed to higher aspect ratios which signify a closer resemblance to linear reciprocating motion. Using transmission electron microscopy and polarised Fourier-transform infra-red spectroscopy (FTIR) no significant lamellae alignment was observed in the explanted cups

for those patients with average aspect ratios that lay within the quoted limits of "normal" gait, AR, 2.9-4.3[129].

Computer simulated sliding distances from a 32mm joint-size fall between 11-25mm per cycle[100]. Specific sliding distance depends on the position traced on the femoral head. Longer sliding distances are found around the periphery of the cup with smaller slide tracks computed nearer the pole of the cup[125]. The average sliding distance per cycle has been linked to femoral head diameter[110]. To a first approximation, the average sliding distance per cycle of the ball in socket is approximately two-thirds that of the diameter. Hence the average sliding distance of a 32mm diameter ball and cup would be 21.3mm. This is in good agreement with the 19.4mm average sliding distance reported in the Ramamurti *et al.* study[100].

2.7 Crosslinking and Wear Resistance

Crosslinking is known to increase the wear resistance of the UHMWPE acetabular cup. The same wear benefit is not afforded when UHMWPE is used as a tibial component. Wear of highly crosslinked material is commonly compared and set in context to the wear of conventional material through the ability of each to undergo molecular orientation in response to sliding motion and the ease of debris release from the worn surface.

Let us recall from Section 2.6.3.2 the ability of UHMWPE to undergo molecular alignment in response to simplified uni-directional and linear reciprocating sliding. This is thought to induce a strain hardening behaviour within the sub-surface, accounting for the low wear factors under simplified motion when compared to higher clinical wear rates[70, 110]. To further explain the restructuring phenomenon and the contribution of crosslinking to wear resistance, it is important to understand the types of deformation mechanism that may occur in the worn near-surface UHMWPE.

2.7.1 Microstructural Deformation Mechanisms

An appreciation of microstructural behaviour and reorientation under uni-axial load may be used to increase our understanding of UHMWPE wear under sliding. First let us consider the deformation mechanisms that occur in semi-crystalline polyethylene under uni-axial tension or plane-strain compression[75, 130-133]. Such studies are commonly conducted using X-ray diffraction to analyse microstructural reorientation and texture development.

Plasticity induced deformation behaviour of polyethylene is described through intralamellar (crystalline) and interlamellar (amorphous) mechanisms. It is commonly agreed that the less resistant, less stiff amorphous mechanisms occur before more resistant crystalline slip deformation schemes. A brief review of these mechanisms is described below.

Within the amorphous disordered domain three deformation modes are proposed to act[75, 132]. The first, interlamellar shear (Figure 2-31a), describes the movement of crystalline lamellae sliding past one another in response to a shear force until such critical deformation that the once unstrained and disordered tie molecules approach the limits of chain unfolding and some degree of order. The second mechanism, interlamellar separation, describes the increasing separation distance between lamellar in response to an applied force (Figure 2-31b). The resistance to deformation may depend on the number and distribution of taut tie molecules between neighbouring lamellae. Interlamellar separation may introduce density changes in the material as cavities caused by the separation appear. The third and final mechanism, lamellar stack rotation, describes the rotation of a group of lamellae under load in response to distortion caused by the impeding deformation (Figure 2-31c).

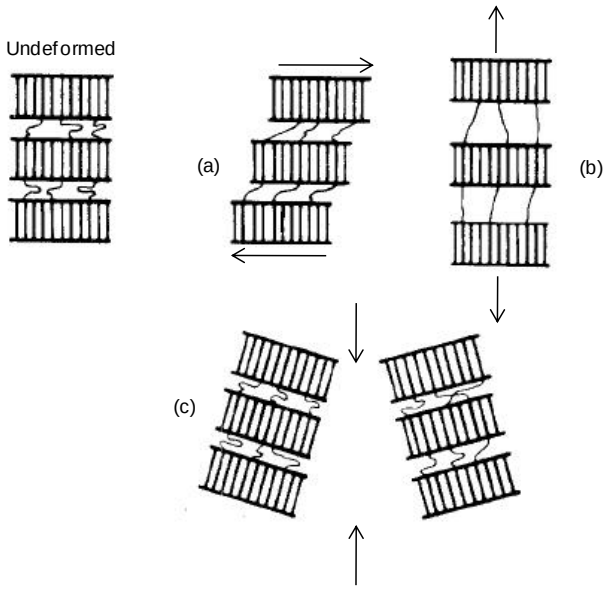

Figure 2-31: Models of deformation in amorphous regions; (a) interlamellar shear; (b) interlamellar separation; (c) stack rotation[132].

Tensile[133] and compressive[134] uni-axial loading tests show crystal lamella are able to align in the principal flow direction under large plastic strain. Li *et al*. used X-ray diffraction patterns to determine texture evolution in HDPE dogbone specimens, comparing the texture of the material held under various true strain levels between 0–2.1. At strains within the elastic limit of the stress-strain curve, crystalline lamellae and their orientation remained unchanged, supporting the hypothesis that elastic deformation is mainly confined to the less deformation resistant amorphous domains[75]. At large strain levels three distinct preferred orientations were apparent; Firstly, the c-axis of the unit cell was found to align with the sample extension direction with the a axis and b-axis lying in the plane perpendicular to the extension direction; Secondly, crystal orientation whose c-axis, b-axis, and a-axis were about 25, 65, and 90° to the extension direction, and; Thirdly, crystal orientation where the b-axis of the unit cell was aligned along the extension direction.

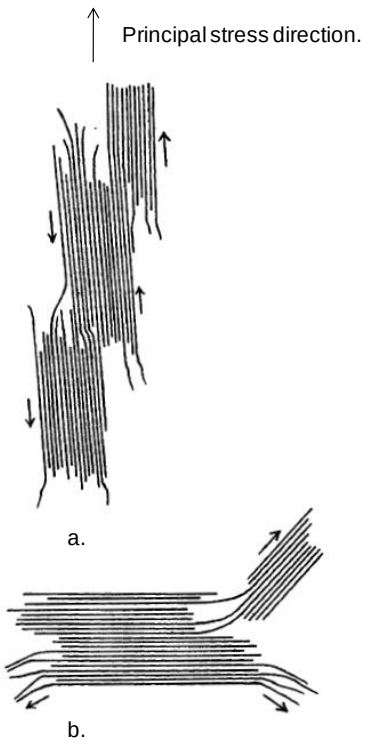

Figure 2-32: Deformation of crystal lamellar may depend on their orientation with respect to the principal stress; (a) plastic deformation includes crystallographic slip through shear; (b) transverse slip causes rupture of the crystal. Both mechanisms may lead to fragmentation[76].

Bartczak *et al*. further postulate that under large levels of strain both amorphous and crystalline components undergo similar reorientation in the flow direction and share the basis of resulting primary slip mechanisms[131]. In plane-strain compression of HDPE with initially no preferred orientation, small regions of ordered amorphous domains within the bulk disordered domains were found using X-ray diffraction. Under large-strain deformation larger amorphous domains were found to orientate with chain backbones re-organised in the flow compression direction, where elongation was attributed to gliding of neighbouring chain segments in the ordered amorphous domains along their chain axes. The resistance to shear induced alignment was found greater in the crystalline components than the amorphous components (7.2MPa vs. 5MPa), therefore early deformation is thought to localise in amorphous domains as interlamellar shear and separation. When the early stages of interlamellar shear can no longer continue, due to the stretching out of the disordered tie molecules forming a new ordered amorphous phase, the less easily deformable crystalline component may begin to deform by chain slip (Figure 2-32a) and transverse slip (Figure 2-32b). Further deformation is possible though the re-arrangement of crystalline lamellae resulting in possible stretching, thickening, rotation or fragmentation of these lamellae. Upon fragmentation, the crystal-amorphous boundaries may undergo extensive re-structuring. Tie-

link segments on the boundary may either be re-incorporated into the fragmented lamellae or segments of crystalline material may be rejected into the ordered amorphous component.

2.7.2 Wear Resistance

For applications in orthopaedics crosslinking of UHMWPE, through either gamma irradiation or electron beam radiation in an inert environment, has been shown to reduce wear in pin-on-plate tests[113, 135], hip simulator studies[136], and preliminary short-term radiograph follow-up studies[137, 138]. Irradiation doses used commercially range from 50kGy to 105kGy. More recent *in vitro* studies on irradiation and wear resistance continue the early work of Dumbleton *et al.*[139] using high-dose gamma irradiation in air to induce chain scission, free radical formation and subsequent crosslinking. Tests were conducted on a simple ring-on-disc machine. In comparison to unirradiated material, an increase in coefficient of friction and wear rate was associated with the irradiated specimens. Findings were attributed to newly created crosslinks preventing the formation of a stable transfer-film on the metal counterface. These wear tests were, however, conducted in the absence of lubrication.

Recent hypotheses for the apparent increase in wear resistance of polyethylene after crosslinking are based on theories of retardation in the re-orientation of crystalline lamellar in response to friction forces. Cross-links occur in the amorphous region where chains become entangled with one another and are close enough for new bonds to be created. The additional crosslinks may enhance the resistance to plastic flow, lamellae separation and lamellae alignment at the articulating surface resulting in better wear resistance.

Tie-molecules within the inter-crystalline amorphous domains are thought to offer increased resistance to reorientation[70, 135, 136]. Wear of an UHMWPE acetabular cup occurs mostly on the surface, a result of micro-adhesion and abrasive wear mechanisms[44]. Under repeated cyclic loading and frictional stresses at the articulating surface, an anisotropic and orientated layer develops in response to strain accumulation[140]. The complex, cross-shearing motion paths found in the hip joint are a result of abduction/adduction and internal/external rotation about the flexion/extension path. Debris produced in response to multi-directional motion on a strain hardened surface is released through fracture[140] and rupture[111] of material drawn out of the surface as particles are incrementally enlarged and released[47]. As a result of crosslinking, the addition of increased carbon-carbon covalent bonds between the amorphous molecules is thought to retard chain movement and produce a worn surface more resistant to fibular pull-out[136, 141].

Frictional strain has also been proposed to produce a near-surface plasticity zone[70]. This sub-surface zone, a precursor to wear, has been shown to occur on crosslinked specimens albeit to a smaller depth beneath the surface. This suggests the transfer of strain through inter-lamellae communication is more confined in crosslinked material. However, multi-axial loading tests revealed more pronounced orientation in highly crosslinked polyethylene's over their conventional counterparts, especially in higher molecular weight samples, adding to uncertainty as to the role of tie-molecules and interlamellar communication[142]. It has been reported that crosslinking does not prevent microstructural mobility[143], but the contribution of such a polymer network to the wear resistance under cyclic loading and shear stresses is still not clear.

To date there have been few pin-on-plate studies on orthopaedic grade crosslinked UHMWPE[72, 113, 135, 144], and fewer still on microstructural characterisation. Zhou *et al*. reported on microstructural disparity between unmodified and 100kGy gamma irradiated UHMWPE[72]. Wear tests were conducted on a reciprocating pin-on-disk machine, the polymer pin loaded in a constant manner onto a reciprocating cobalt chrome disc. Under average nominal contact pressures between 20-30MPa they attributed a fourfold increase in wear resistance of the crosslinked material to greater resistance to plastic flow.

Tests conducted on motion machines with limited cross-shear angles, more representative of knee motion have reported marginal differences in wear rates as function of radiation dose[143]. Further studies on this material have been conducted on machines which produce limited translation and rotation[113, 144]; polymer test pins are loaded under constant force onto a reciprocating test plate, or counter-bearing. In such cases the pin rotates via drive gears to operate in synchronisation with the oscillating plate. The nature of the rotating pin inherently creates non-uniform tribological conditions across the wear surface. Each point on an increasing radius from the pin centre will experience a different wear path, creating a complex worn surface. This tribological setup is more suitable for wear ranking bearing couples under constant load and sinusoidal velocity, than used to probe microstructural development. A well designed pin-on-plate tribometer has the potential to offer in-sight into fundamental wear mechanisms under controlled conditions.

3 Tribometer Design

Summary

An attempt to describe the design considerations and development of a novel pin-on-plate tribometer are presented in Chapter 3. The top-level assembly has been divided into sub-assemblies according to purpose, with each being discussed in a sub-chapter.

The machine has been designed and built in accordance with the appropriate standard; ASTM F732-00 (2006). This standard outlines the clinical relevance of developing a pin-on-plate tribometer used for orthopaedic wear testing. Simplified pin-on-plate tribometers are the mainstay of researchers worldwide who require a cost effective, flexible wear machine. However, unlike conventional pin-on-plate devices which commonly statically load a UHMWPE pin against a metallic rotating disc or sliding plate, this design incorporates programmable dynamic loading and motion profiles. There is a requirement for this type of rig in order to investigate UHMWPE wear under conditions where the "simplified" tribometers (adequate for constant load/constant velocity and constant load/sinusoidal velocity work) are not capable or suitable.

The six-station tribometer provides translation along two axes and loading in a third axis. Four stations are subject to identical load and motion profiles. Two "load-only" stations provide control specimens to account for polymer fluid absorption during gravimetric analysis. Each bearing couple is immersed in an individual lubricant chamber, where the bulk lubricant temperature can be controlled or left to ambient. Translation of the motion stations is achieved through a ball-screw mechanical system, converting rotary motion of a stepper motor to linear translation of the chamber. A torque safety factor applied to each motor ensures accurate, repeatable and reliable motion.

3.1 What Makes a Successful Tribometer?

To be fit for purpose a tribometer must be capable of accurately imposing the desired load and motion for a specified number of cycles. Such a machine will reliably wear test samples in a controlled manner according to parameters set by the user. Design, form and function of the machine are dictated by a combination of parameters such as sample geometry, relative motion, loading and lubricating medium. In the context of orthopaedic pin-on-plate design, important features are listed in Table 3-1.

Parameter	Record	Comment
Motion	Sliding distances, velocities and shapes	Sliding distances are used in wear calculations. Velocity influences the degree of heat generation and lubrication regime. Motion paths indicate the degree of cross-shear and complexity.
Load	Load profile	Load is used in wear calculations. Nominal contact stress determines clinical relevance. Profile repeatability should be monitored under dynamic applications.
Test duration	Cycle time and number	Required to clinically match motion and sliding distance with patient activity.
Operating temperature	Temperature and time to reach steady state	Real-time monitoring allows temperature changes and initial time to reach steady-state to be recorded.
Lubricant maintenance	-	Lubricant top-up should be controlled to prevent dry-sliding and fluctuating protein concentration.

Table 3-1: Potential variables to control and record during wear testing.

The design motivation behind the Edinburgh tribometer was to better simulate loading and sliding conditions found in the hip joint in comparison to contemporary pin-on-plate wear machines. The best qualities of a pin-on-plate machine would remain; short preparation time, simple specimen geometry and reliable operation. To more closely approximate tribological conditions of the hip joint, physiological loads, nominal stresses, velocities and sliding distances were used to provide a design envelope within which the machine should operate. Important features of the design include:

- Closer tribological match to clinical environment
- Programmable dynamic loading
- Programmable motion paths
- Uniform shear vectors across the pin surface
- User friendly control and operation
- Adaptable to simulate various joints

All computer aided design (CAD) work was carried out using Solid Edge V15. Solid and wireframe CAD models of the top-level assembly are seen in Figure 3-1. Before manufacture, draft drawings were released to the University's chemical engineering

machine-shop where they underwent a thorough design review. Once the drawings were finalised, these components were machined and assembled in the engineering department over a period of two years. Free-issue components, such as actuators, linear slides, control boards, PSU's and solenoid valves were specified and assembled by the author. Final assembly of the six individual lubricant chambers is photographed in Figure 3-2, where four chambers are subject to load and motion (Figure 3-3). Details of the machines operation is kept brief, for full start-up procedures the reader is referred to Appendix 1: Tribometer Start-up Protocol.

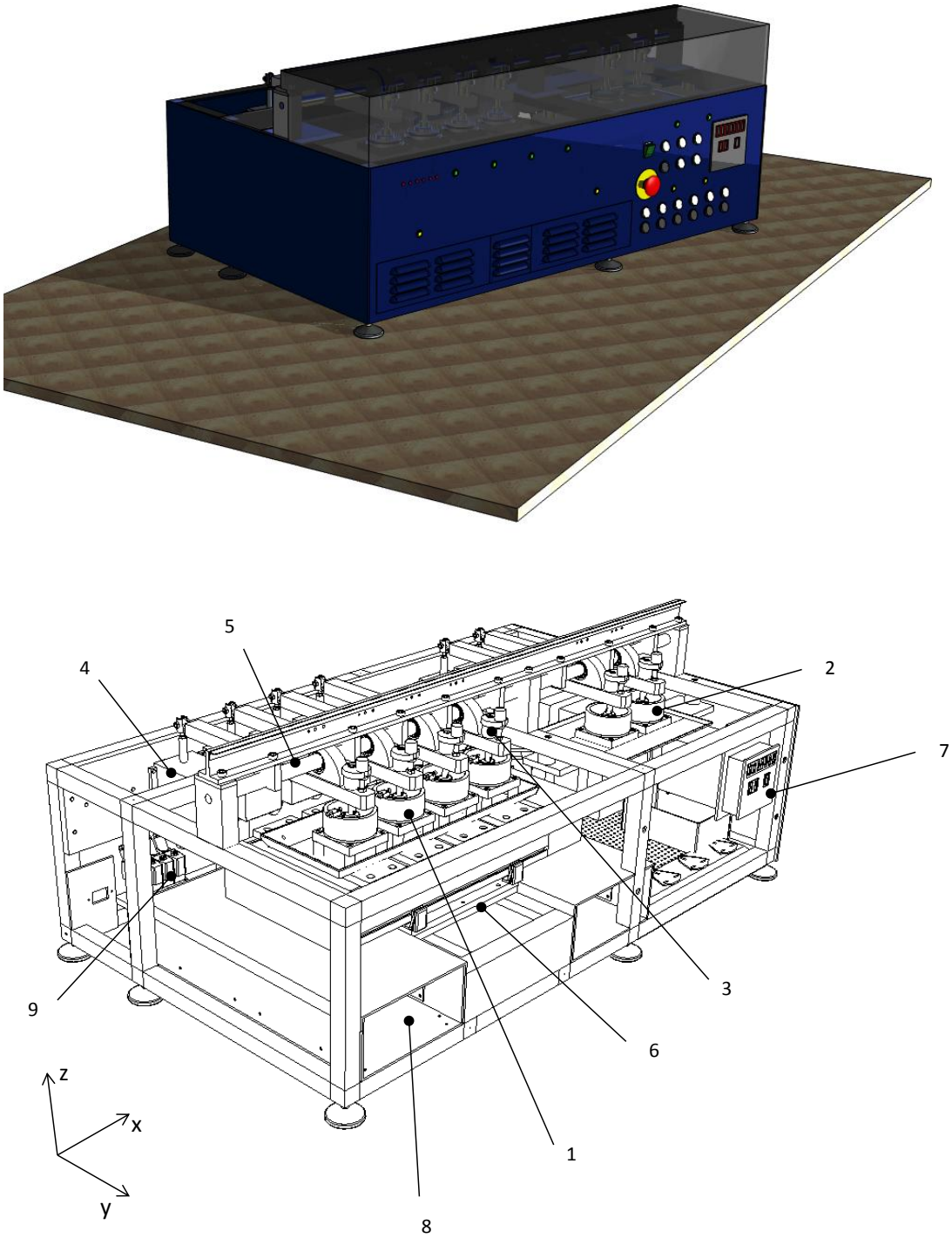

Figure 3-1: CAD images showing above; a solid body model, below; wireframe schematic; 1 Four load and motion test stations; 2 Two load soak stations; 3 Test pin holder; 4 Six electric coil actuators; 5 Bearing shaft; 6 Orthogonally mounted linear slides; 7 Individual station temperature control; 8 Cooling ducts for electric PSU's; 9 Solenoid valves for de-ionised water top up.

Figure 3-2: The six-station wear test device; shown with the dust cover lid open exposing the four load and motion stations and two load only stations.

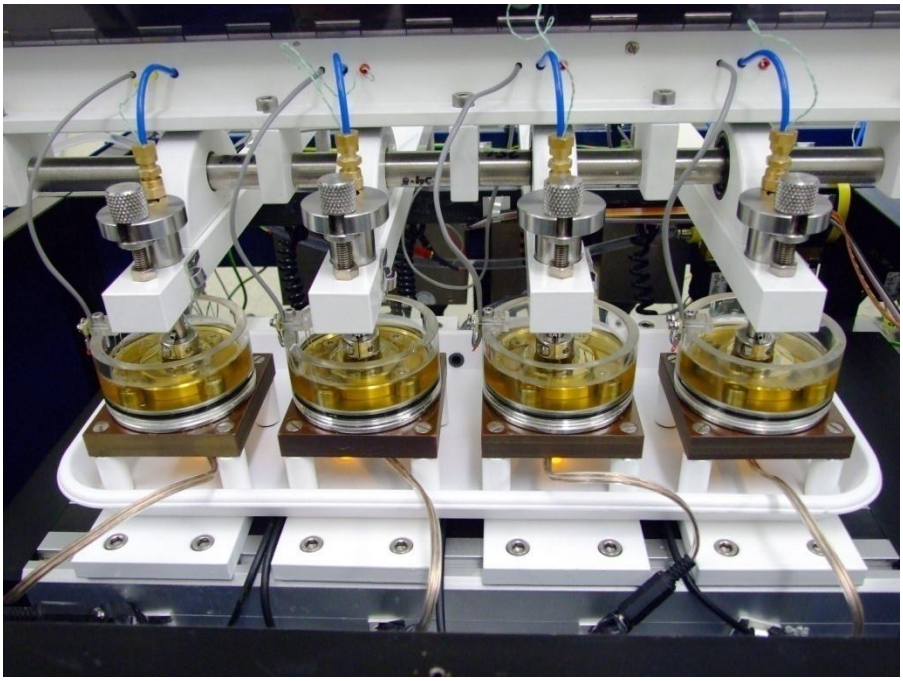

Figure 3-3: Detailed view of the four load and motion stations. Each chamber is supported by four columns providing future capacity to mount strain gauges or install a 3-axis load cell beneath each chamber. The load cell would provide friction and continuous load measurement. Heating resistors, mounted on the underside of each stainless steel base provide necessary energy to heat chamber lubricant.

3.2 The Motion Control Table

Key motion features of the machine include:

- X and Y motion constrained in the horizontal plane
- X and Y interpolation to allow complex motion
- PC user interface
- Two axis computer controlled motion system

A straightforward approach to motion control allowed both simple and more complicated motion paths to be described. Two linear slides mounted orthogonally created a two-dimensional co-ordinate system. A solid-body and wireframe schematic of the arrangement can be seen in Figure 3-4. Each linear slide was manufactured from an extruded aluminium rectangular cross-section within which a ball-screw runs the length of the body and drives a carriage. A ball-screw is a mechanical device used to convert rotary motion of a motor into precision linear motion. Each ball-screw is turned via a motor which in turn drives the carriage either forward or backward according to the rotary direction of the motor shaft. The length of translation is dependent on the number of screw rotations.

Through the orthogonal arrangement, the lower carriage may translate along one axis and the upper carriage may translate independently along a perpendicular axis. Coordinate interpolation between both carriages provided a two-dimensional motion space of length equal to the travel of the slide.

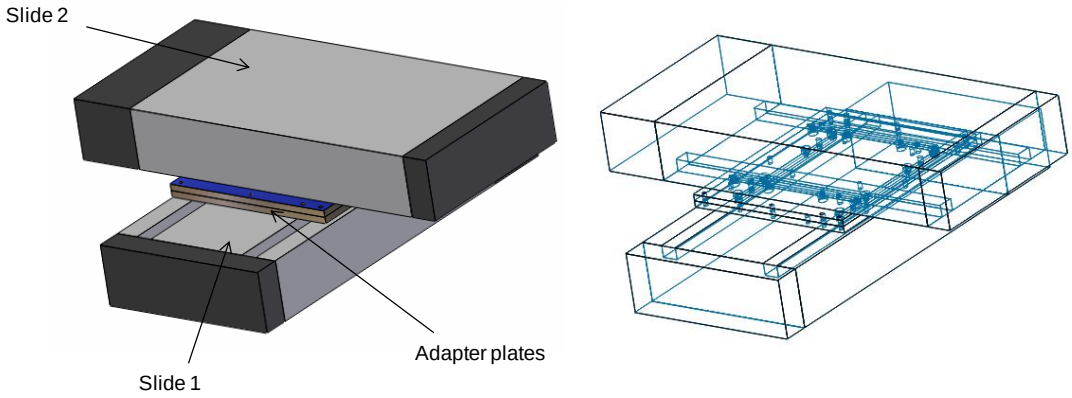

Figure 3-4: Orthogonally mounted; linear slides at 90degrees created a two-dimensional motion envelope along the x and y axes.

Slide travel is determined by the length of the ball-screw and size of carriage. Both were specified in order to satisfy the sliding distance recommended by the ASTM for pin-on-flat studies[145]; a mean polymer siding distance of 50mm per cycle. Under linear-reciprocating motion i.e. where only one axis is used, this would equate to a stroke length of 25mm. Isel

LF5 linear slides with an extruded body length of 300mm permitted a maximum sliding distance of 110mm.

There are two common methods to generate linear slide movement; servo-motors under closed-loop control, and stepper motors under open-loop control. Closed-loop systems rely on feedback from the output to determine the next input move, for example encoders continuously monitor actual move positions, compare these to the desired position and make corrections accordingly. Continuous comparison between actual position and desired position ensure closed loop servo-motor systems are very accurate. However, closed–loop systems are expensive due to the additional feedback control and sensing components. A comparison between servo and stepper motors is seen in Table 3-2.

Stepper Motor	Brushless Servo Motor
Simple to operate and maintain due to lack of feedback control	Harder to install and maintain due to greater number of parts
No feedback means system can drift without means of correction	Closed-loop control allows motor to correct its position
Cheaper for the same torque requirement than brushless servo	Expensive, control is typically analog which along with the feedback circuit is more costly
Usually specified with a torque safety margin to prevent loss of position	Can be driven closer to maximum torque and at higher speeds
Always full current passing through windings regardless of load	Will only consume current on demand

Table 3-2: The pros and cons of motor selection should be considered when designing a motion control system.

Linear slides in the current tribometer rely on cheaper more robust open-loop stepper motors. Open-loop refers to systems which convert input signals to output signals without feedback. Therefore, once a translation move is initiated, no corrections based on external influence are possible. Such systems rely on accurate and appropriately specified components to achieve repeatable and reliable operation.

A stepper motor rotates through a process of energising and de-energising coils mounted around the circumference of the motor body or stator. Permanent magnets on the rotor try to align with any electric coils that are energised. To do this the rotor will turn a discrete distance until this state is achieved. Once this occurs the next pair of coils in the motor body are energised, causing the rotor to rotate once again. Energising and de-energising subsequent pairs of coils around the motor body in quick succession causes the rotor to turn continuously; discrete steps merge into continuous rotation.

The position of the rotor within the stator can be easily lost if the acceleration and velocity limits of the motor are exceeded or overloaded. Under such circumstances the motor will skip steps. The error between the actual position and desired position will continuously

increase if the motor continues to miss steps. Such a situation is called drift, resulting in slide migration. Without feedback there is no way of sensing real-time system drift.

To minimise drift, a stepper motor with a sufficient torque safety margin was specified. The safety margin was calculated by dividing the rated motor torque by the theoretical resistive system torque. System torque was calculated from the sum of torques, T_{load}, required to move the maximum mass (Equation 3-1), the torque required to overcome friction, $T_{friction}$, within the system (Equation 3-2) and the torque required to accelerate the total mass (Equation 3-3); where N, is the normal load, p*itch* refers to the ball-screw thread, μ_{screw} is the screw coefficient of friction, η is the slide efficiency, J_{total} is the inertia of the system and α is angular acceleration of the ball screw. The maximum theoretical torque to overcome was 0.52Nm, where a full derivation can be seen in Appendix 2: Torque Calculations. The closest largest standard motor size was 1.6Nm, providing ample torque and a safety margin of 3.1.

$$T_{load} = \frac{NPitch}{2\pi\eta}$$

Equation 3-1: The torque required to translate a normal load, N.

$$T_{friction} = \frac{NPitch\mu_{screw}}{2\pi\eta}$$

Equation 3-2: The torque required to overcome friction in the ball-screw.

$$T_{accelerate} = J_{total}\alpha$$

Equation 3-3: The torque required to accelerate the applied load.

Factors that affect slide performance include resolution, accuracy and repeatability. The type of motor and thread pitch of the ball-screw determine the linear resolution of the moving carriage. The smallest discrete angular rotation of the motor results in the smallest change in linear distance along the axis. Higher resolution allowed the carriage to be controlled more precisely. The step angle and smallest discrete move of each stepper motor was 1.8°, taking 200 steps to complete one revolution. The pitch of the ball-screw was 5mm. Therefore, for one complete motor revolution the carriage translated 5mm and for one step the slide translated 0.025mm.

Repeatability is referred to as the maximum deviation about a target position when approaching that position multiple times. In a wear test application each slide approaches the same position thousands of times. Small deviation errors multiplied during typically uninterrupted periods of 250,000 thousand cycles would cause gradual but significant

migration of the wear path. According to the manufacturer's specifications, the LF5 slides were repeatable to ±0.02mm per cycle.

A stepper drive unit controlled the step and direction of each stepper motor. Two stepper drives were needed, one for each axis. Drive units supplied the necessary power to the motors and controlled the direction and angular velocity of the motor shaft. The maximum current per phase of each motor was rated at 4.10A. Each drive unit supplied sufficient current such that full motor torque could be reached without exceeding the maximum motor rating. Excess current would cause overheating. From drive theory, optimum performance is obtained when the current rating of the motor is ~1-1.5 fold the drive rating. A drive unit capable of supplying between 2.05A-4.10A was specified. A Parker XL25 stepper drive supplied an output of 3.5A rms per phase and a motor supply voltage between 48-80Vdc. A summary of motor and slide specifications can be seen in Table 3-3.

Description	Motion system
Positioning system	Linear slide
Mechanism	Ball-screw
Repeatability	±0.02mm
Slide range	110mm
Stepper motor torque	1.6Nm
System torque to overcome	0.5Nm
Current per phase	2.85A - 4.10A
Step angle (deg)	1.8
Ball-screw pitch	5mm
Resolution	0.025mm

Table 3-3: Motion control specifications.

Each drive unit had a mains input, a connector for the motor cable, and a communication port to link to an external coordinator. The external coordinator provided system intelligence and converted user commands to equivalent step and direction signals output in the form of slide translation. Such a device controls axis moves and interpolates between multi-axis moves to achieve complex slide tracks. A Trio Motion MC206 coordinator was programmed through computer software, and converted the programming language, Trio BASIC, into signals read by the stepper drives (Figure 3-5).

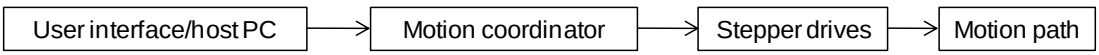

Figure 3-5: Progression of steps from motion programme to execution of move.

A MathCAD workbook was written to verify slide performance against the ASTM recommended cycle time of 1 Hz. The workbook calculated the average velocity of the slide and time taken to complete one half cycle over a stroke length of 25mm. Instantaneous

velocity *v(t)*, average velocity over the move V_{av}, acceleration *a(t)* and time taken, *t* are plotted in Figure 3-6. The acceleration and deceleration (450mm/s^2) and maximum velocity (77mm/s) were extracted from the motion programme. The linear reciprocating half cycle was completed in 0.49seconds, or one cycle in 0.98seconds which was in good agreement with the ASTM.

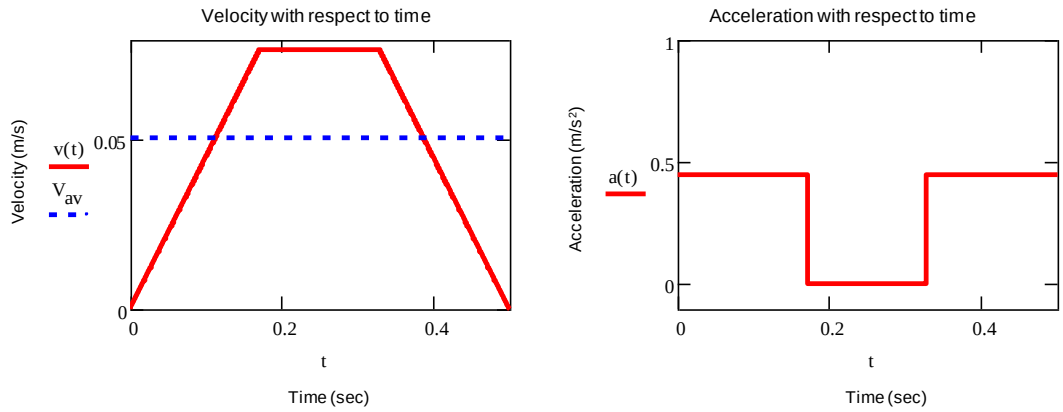

Figure 3-6: MathCAD plots; trapezoidal velocity and square-wave acceleration profiles of the slide during one half cycle of a LR move (sliding distance 25mm) where; v(t) is the time dependent velocity of the slide; V_{av} is the average velocity and; a(t) is the time dependent acceleration of the slide.

3.3 The Loading Module

Each test pin was loaded independently by an electric coil actuator and loading arm (Figure 3-7). The loading module was capable of executing a specified number of cycles, where the dynamic load output on each pin produced nominal contact stresses in the physiological range. The lever mechanism acted to magnify the output forces such that the actuator remained within its safe duty cycle. The duty cycle was specified as either the maximum continuous operating time or maximum time at full load before the module must be switched off.

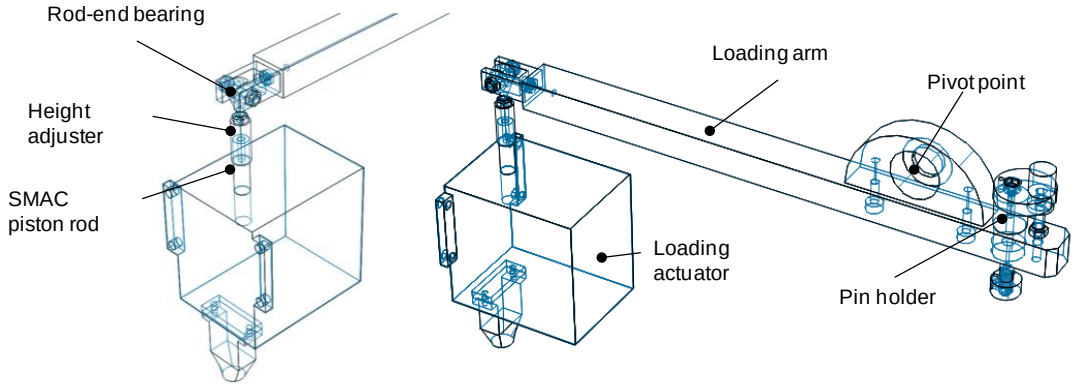

Figure 3-7: One loading module sub-assembly; consists of an electric actuator supplied by SMAC, a custom rod-end bearing which acts to transfer motion through 90degrees, a powder coated aluminium loading arm and bearing housing to pivot about and a pin holder. The angle of the loading arm can be adjusted about the horizontal through a threaded screw connector above the actuator rod or more simply at the pin holder.

Two pin loading arrangements were initially considered, direct loading and indirect loading. Direct loading describes an arrangement in which the loading force is applied directly from the actuator onto the pin (Figure 3-8a). Indirect loading describes the use of a lever mechanism to load the pin (Figure 3-8b). To assess the suitability of a ball-screw actuator used in a direct layout the theoretical stroke length was calculated. The extension of the rod actuator was assumed equivalent to the compression of the pin under load. An UHMWPE pin, 20mm in length and 5mm in diameter was used. Pin compression was dependent on pin stiffness which was calculated from the Young's Modulus of UHMWPE, E, the pin cross sectional area, A_{pin} and the length of the pin, L_{pin} (Equation 3-4).

$$k_{stiffness} = \frac{EA_{pin}}{L_{pin}}$$

Equation 3-4: Stiffness of a simple pin is proportional to its Young's modulus, E, and cross sectional area A_{pin}.

Pin compression was calculated by dividing the normal force, N, with the stiffness (Equation 3-5).

$$\delta_x = \frac{N}{k_{stiffness}}$$

Equation 3-5: Deflection of an UHMWPE pin under compressive loading.

The UHMWPE pin would theoretically compress 0.1mm under an applied force of 100N, equivalent to a nominal contact stress of 5MPa. The corresponding stroke length of an actuator mounted directly above the pin would therefore be 0.1mm under identical contact conditions. The short stroke length ruled out a ball-screw type loading actuator; limited rotation of the ball screw would restrict screw lubrication and cause unacceptable localised wear on the small section of screw being repetitively used.

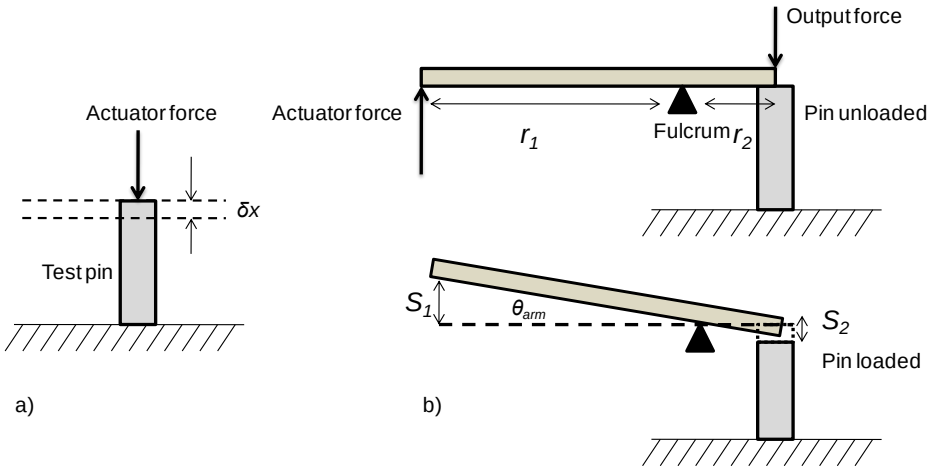

Figure 3-8: a) Direct loading of a test pin; b) Indirect loading through a class 1 lever, with r_1 the perpendicular distance between input force and fulcrum, and r_2 the perpendicular distance between output force and fulcrum.

To increase the stroke length, loading was modelled using a class 1 lever mechanism (Figure 3-8b). A class 1 level is such that the fulcrum is located between the input and output forces, but closer to the output. In this arrangement the actuator would load one end, causing the lever to rotate about the fulcrum loading the pin beneath. For small angles of θ_{arm}, actuator extension S_1 approximates to pin compression, S_2 as seen in Equation 3-6.

$$S_1 = \left(\frac{S_2}{r_2}\right) r_1$$

Equation 3-6: For small angles of θ_{arm}, vertical displacements S_1 and S_2 have the following geometric relationship.

To impose a nominal contact stress of 5MPa on a UHMWPE pin, the theoretical stroke (S_1) of an actuator mounted indirectly was 0.49mm, where r_1 was 290mm and r_2 was 60mm. To produce larger stroke lengths, the length of the lever mechanism would exceed the physical restrictions imposed upon a desktop sized wear testing machine.

To prevent mechanical wear under short stroke applications, pneumatic actuators can be used. Unlike ball-screw actuators, air-driven pistons do not rely on mechanical interference to exert force. Pneumatic loading has previously been used in a contemporary pin-on-plate machine, where a UHMWPE pin was loaded under a simplified dynamic square-wave load profile[104]. Pneumatics are clean and inexpensive but difficult to control and programme.

A more appropriate device is an electric coil actuator. The electric coil actuator is neither limited by the mechanical action of a ball-screw nor hampered by poor programmability and resolution associated with air-driven pistons. In an electric coil actuator a piston rides on a linear bearing carriage which slides on a linear guide rail. A copper coil is mounted on the piston. This coil rides inside a magnet assembly. When current flows in the coil, a reaction force is produced causing the piston to slide along the guide. By controlling the size of current passing through the coil, the output force can be controlled according to the application of Faraday's law, and Fleming's rule (Equation 3-7). Where B is the strength of the magnet assembly, L is the length of the coil, and I is the current flowing through the coil. The relationship between force and current remains proportional provided excess energy is not lost through heat.

$$F = BLI$$

Equation 3-7: Faraday's Law of current and force.

The electric coil actuators in the Edinburgh machine were supplied by SMAC[146]. These units were programmable with respect to force, position, and velocity. A closed-loop feedback system maintained the programmed load cycle throughout the duration of each test. The most appropriate SMAC unit (LAL-95-15) had a specified maximum force output of 84N and a 40% duty cycle (max load 40% of cycle time, or 40% of max load for the full cycle time).

	Direct	**Class 1 mechanism**
Max force from actuator (N)	~84	~84
Max force on pin (N)	~84	~400
40% of max load -full cycle time (N)	~34	~160

Table 3-4: Direct and indirect SMAC force comparison.

The maximum constant nominal load that could be applied from this actuator was 40% of 84N or 34N (Table 3-4). Over a 5mm diameter pin this equated to a nominal contact stress of 1.68MPa, below the ASTM recommended static contact stress of 3.54MPa. To achieve the ASTM contact stress a static 70.8N load was needed. To increase the output from the actuator the class 1 lever mechanism was revisited. Output forces were magnified according to the ratio of the perpendicular distance between the input force and fulcrum (R_1) and the

output force and fulcrum (R_2) (Figure 3-8b). Small actuator forces were magnified to that of physiological contact stresses on the pin surface. This allowed the electric servos to continuously operate well within their duty cycle preventing overheating. Physical dimensions of the lever mechanism were such that a 20N force at the actuator end was magnified to approximately 100N at the pin-plate interface. This was equivalent to a nominal contact stress of 5MPa.

The pivot location, x, was 80mm perpendicular to the sliding contact (Figure 3-9). Sliding friction forces would result in a torque to act about point A which may have caused uneven surface wear. To reduce moments about A, distance x was minimised and double-row bearings were installed at the pivot point. Two rows of ball bearings increased the bearing-shaft contact area making the module more resistant to off-axis moments. The loading module was designed to minimise or restrict all other degrees of freedom except the rotation of the loading arm about the pivot point.

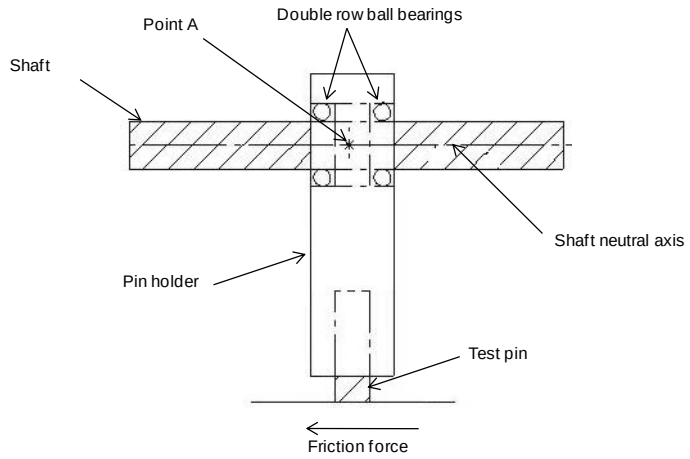

Figure 3-9: The pivot point, A, and pin/plate interface lie on separate planes. Friction at the sliding interface may induce a torque to act about the pivot point. To counteract its effects, double row bearings were used to maximise bearing contact against the main shaft.

The six actuators were programmed through one PC and controlled independently by six PID controllers. Each LAC-1 feedback controller converted commands from the PC into current which was then output as force. The current parameter could be sent back to the PC to be stored or plotted. One disadvantage of this arrangement was that the PC could only receive data from one controller at a time. Therefore, to receive data from six actuators a custom communication splitter was designed and built in-house. Output forces were controlled by the size of current passing through the actuator coils. Current was calibrated to force using a 0.1kN load cell mounted directly underneath each test-pin. Force output curves can be seen in Figure 3-10 and were used to programme the dynamic load profile. There was a linear response between current and output force. Unfortunately, this response was specific to each

actuator; the same input current command given to all six units would produce six different output forces. To reduce this variation, gradients and intercept points were calculated and stored in the register of each loading controller. For a given input command, each actuator compensated according to its individual calibration curve producing a similar output response. The output curves of the four loading actuators used in the load and motion stations before and after calibration are seen in Figure 3-10.

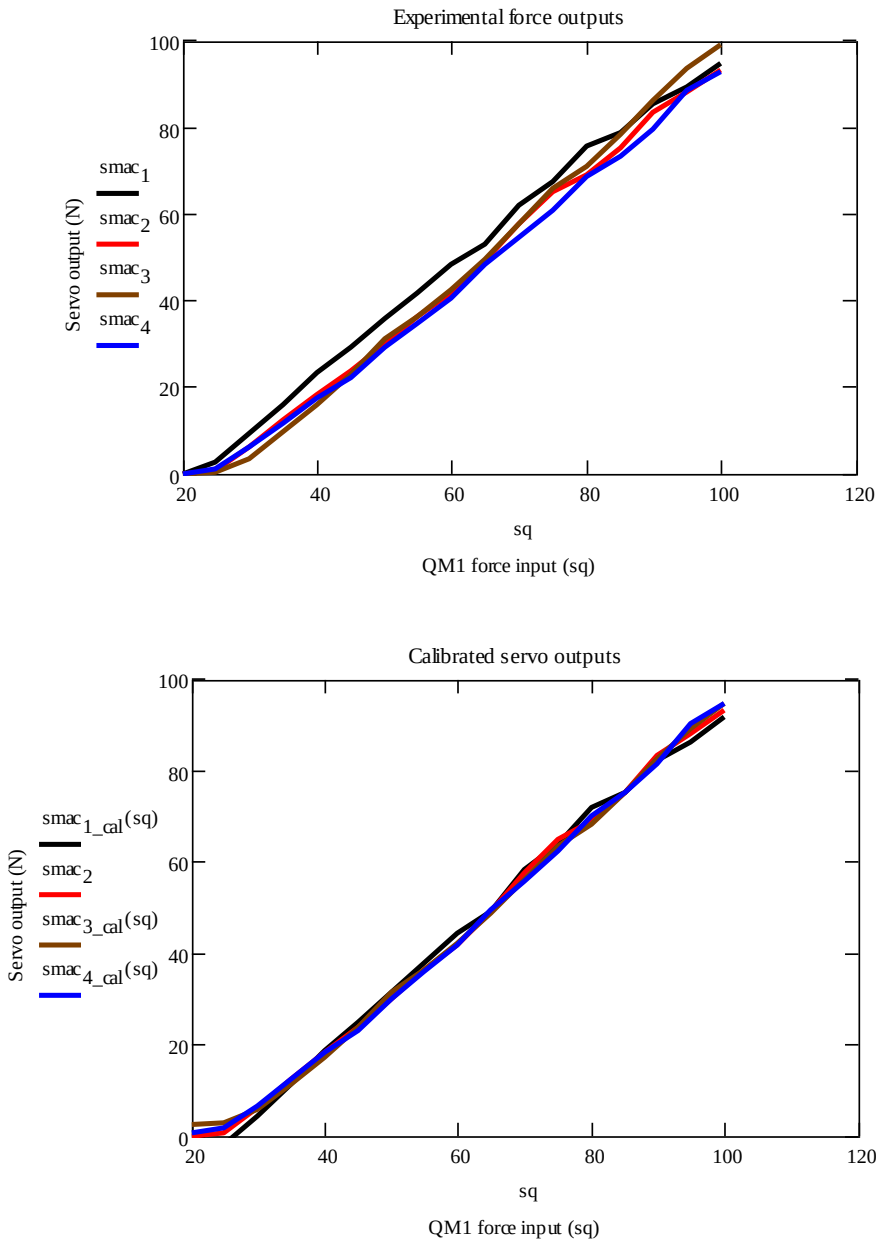

Figure 3-10: Top; uncalibrated force curves for the four load and motion stations, Bottom; once calibrated the outputs show closer grouping across a range of input (QM1) values.

The loading cycle from each unit was recorded periodically throughout each test and remained consistently within 7% of its initial cycle. On average the loading cycles output across the six units remained within 3.2% during testing. Forces and nominal contact stresses at the pin-plate interface were calculated for each actuator using MathCAD scripts (Appendix 3: Load Profile Calculations), where values from all six stations are summarised in Table 3-5.

	Mean stress per cycle (MPa)	Mean stress per stance phase (MPa)	Heel-Strike (MPa)	Relative min (MPa)	Toe-off (MPa)
Actuator 1	1.96	2.89	4.50	2.32	2.94
Actuator 2	1.90	2.99	4.47	2.37	3.01
Actuator 3	1.81	2.93	4.39	2.28	2.89
Actuator 4	1.85	2.95	4.43	2.18	2.99
Actuator 5	1.92	2.99	4.47	2.56	2.12
Actuator 6	1.92	2.98	4.47	2.50	2.05
Mean	1.88	2.94	4.45	2.29	2.96
S.D	0.06	0.04	0.05	0.08	0.05

Table 3-5: The six station actuator loading values. The actuator force is divided by the cross-section of the test pin to convert readings into stress.

Each electric coil actuator required its own switch mode transformer to convert 240Vac mains supply into a 48Vdc, 4A supply. The transformers used in the tribometer were capable of delivering up to 4.64A when air cooled with an 18CFM fan. Under natural convection cooling, the maximum current of these units was rated at 2.1A. Despite the loading arm cantilever arrangement reducing the amount of current drawn by the actuator under peak load conditions, each PSU was mounted in a cooling duct which channelled air over the power supplies, further cooling the units and increasing their current capacity. Two aluminium ducts were mounted along each side of the lower linear slide, underneath the top slide. Three PSU's were mounted in each duct (Figure 3-11). At the rear of each cooling duct a 12Vdc, 26CFM fan draws cool air in from ambient surroundings. A removable aluminium lid ensured all the components remained dust free, and sealed from potential lubricant spills above.

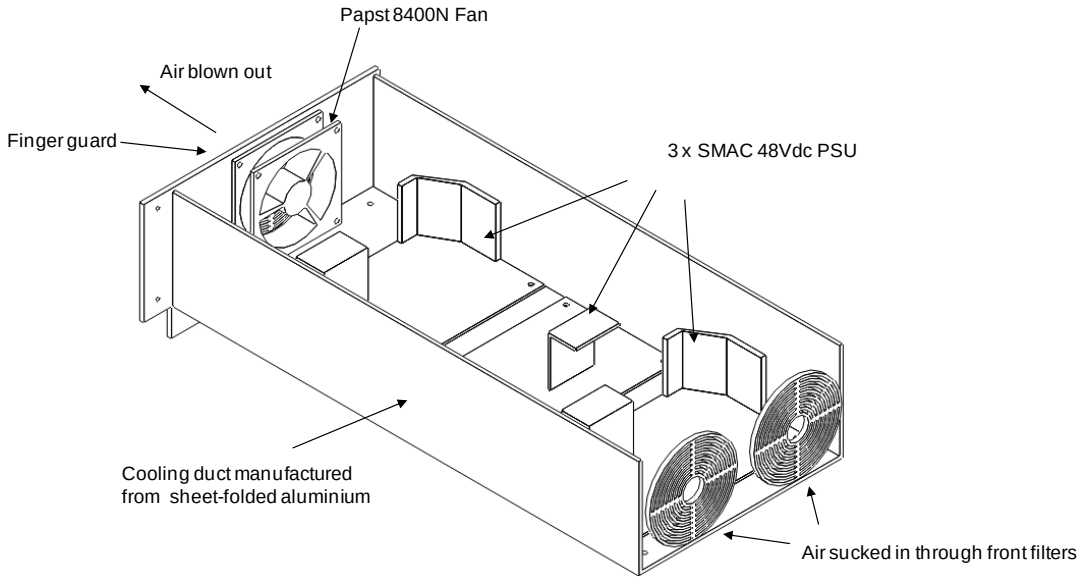

Figure 3-11: Schematic of the right cooling duct. Three power supplies were mounted adjacent to one another. To aid circulation and increase their current handling capacity a fan draws cool air in from the front, before expelling it out of the rear of the machine.

3.4 The Bearing Shaft

The six loading modules pivot about an EN58E 304 stainless steel shaft. The shaft was mounted on top of the chassis and was 1000mm in length. It was supported and clamped in three positions; at both ends and in-between stations four and five seen in Figure 3-12. Spacers were used to fix the spanwise positions of the loading arms along the length of the shaft. Stainless steel was chosen for its stiffness, fatigue resistance and corrosion resistant properties.

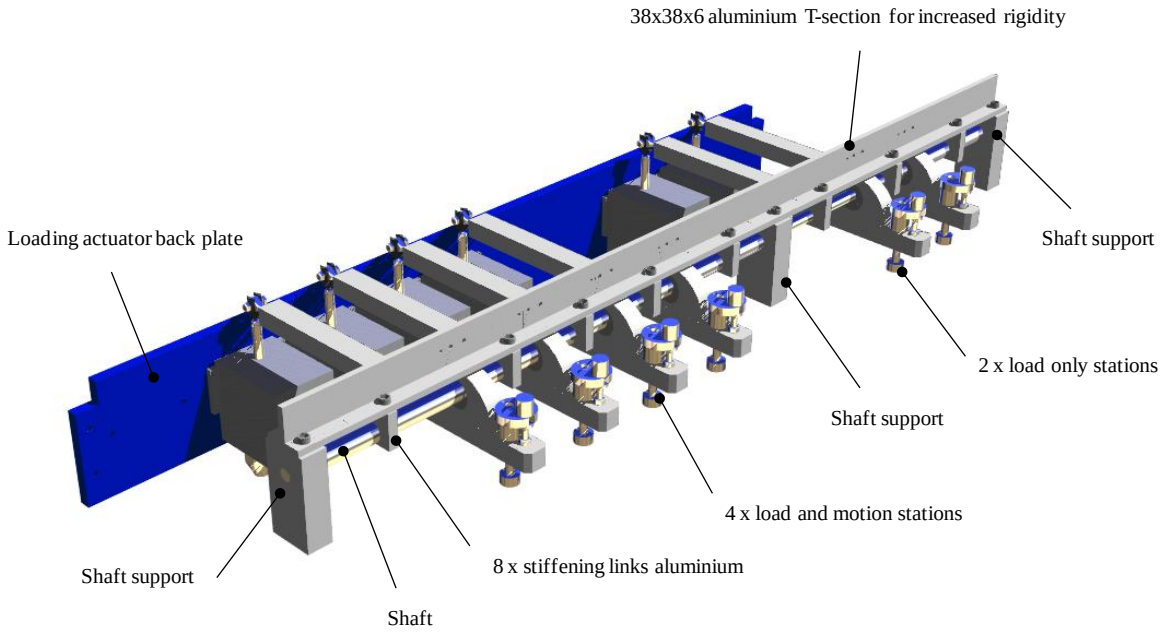

Figure 3-12: The loading assembly, showing the four load and motion stations and two load only stations divided by a third shaft-support block. All actuators were bolted to an aluminium, powder-coated blue, back plate. The T-section channel can be seen running above the length of the shaft. This increased the stiffness inherent in the design.

Stresses and deflections are imposed upon the shaft due to the static weight of each loading module (aluminium loading arms, ball-bearings and aluminium bearing housings) and the reaction forces exerted on the shaft from the pin-plate interface during dynamic loading. Significant shaft deflection may result in inconsistent loading of the test pins, high bending stresses and the potential mechanism for fatigue failure. Deflection is dependent upon the size and position of loads to be supported, the span length over which the loads act, shaft boundary conditions, material stiffness and the second moment of area of the load-bearing member. To minimise deflection the unsupported span length was designed to be as short as possible. The greatest unsupported span would be the width of the tribometer i.e. 1000mm; to shorten this, a third intermediate support was installed part-way along the shaft between stations four and five, see Figure 3-12. The shaft was clamped at all three supports such that

a bending moment was created under load. The support bending moment further reduced shaft deflection.

The theoretical maximum bending moment, longitudinal stresses and deflections with respect to shaft diameter were calculated from bending theory and differential equation of flexure (Appendix 4: Main Shaft Design Calculations). Stresses and deflections were calculated as a function of spanwise position and maximum slope. A conservative approach was taken where all calculations were applied to the longest unsupported span. Each loading module was represented as a point load along the span length and rated at the maximum 100N. The bending moment was used to calculate the local maximum longitudinal stress according to Equation 3-8: where M is the maximum bending moment, y the radius of the shaft, I_{seond} is the second moment of area and σ is the maximum tensile or compressive bending stress. The local maximum stress, σ, was directly compared to the yield stress of 304 stainless steel and a factor of safety (FOS) calculated. Differential equation of flexure was evaluated and integrated once to give the slope and twice to give deflection along its length.

$$\sigma = \frac{My}{I_{second}}$$

Equation 3-8: Beam bending theory.

Theoretical maximum deflection of the 12mm diameter stainless steel shaft was 4.31mm, during which a maximum bending stress of 197MPa developed. Despite the stress remaining below yield (197MPa<214MPa) the large deflection was unsatisfactory. This was greatly reduced to 228μm by adding a 38x38x6mm extruded aluminium t-section mounted above the shaft. The t-section increased the second moment of area (I_{second}) of the load-bearing shaft, decreasing the longitudinal stress according to Equation 3-8 and increasing the rigidity. A larger diameter shaft was considered but not implemented due to the undesirable increase in size and weight of bearings and associated shaft components. During normal operation resultant stresses remain well below yield ensuring the shaft operates in the elastic domain. Under such cyclic stress conditions, the fatigue strength of the shaft can be approximated by the endurance limit. This describes operating conditions under which fatigue failure does not usually occur and is commonly referred to as $1x10^8$ cycles[147].

3.5 The Test Chamber

There are six individual test chambers which permit sliding studies to be carried out in user-controlled, physiologically relevant test environments. The modular design forms a sealed unit to enable lubricated sliding, the stainless steel base acts as a heat sink allowing lubricant to be heated above ambient and test plates can be re-inserted in an orientation specific manner. An exploded schematic is seen in Figure 3-13 and a summary of the key features include:

- Constructed from inert and corrosive resistance materials
- Physical dimensions accommodate a range of physiological sliding distances and counter-bearing test plates
- Sealed for lubricated sliding
- Temperature controlled
- Optimised heat transfer properties for efficient minimal heating times and accurate temperature control
- Automatic lubricant evaporation compensation
- Test plates easily removed and re-inserted in an orientation specific manner
- Modular for ease of cleaning and maintenance

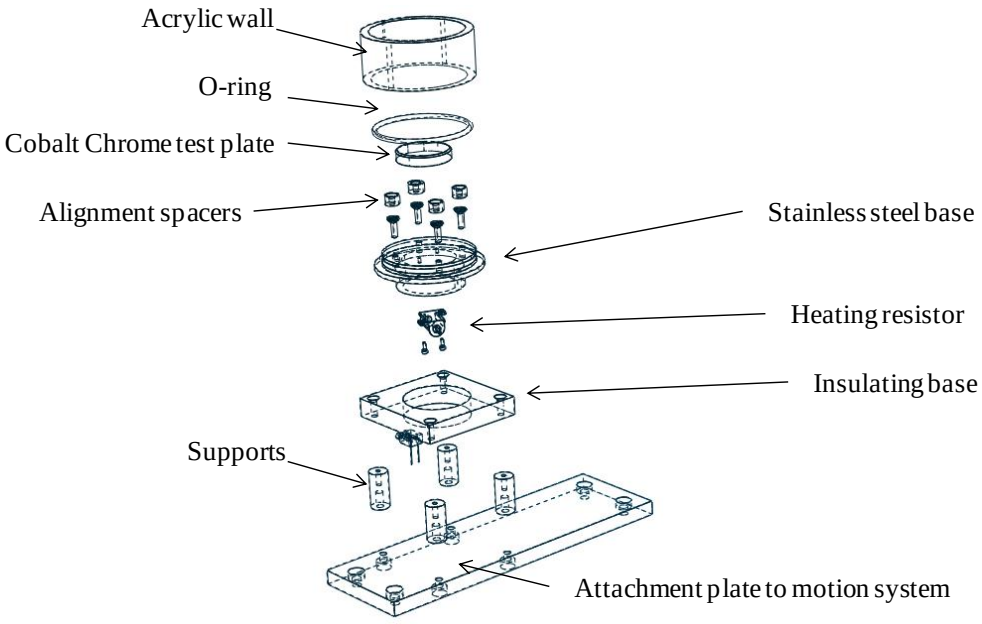

Figure 3-13: Exploded view of the modular chamber assembly. Five different materials were specified to optimise the design functionality; acrylic, nitrile rubber, 304 stainless, nylon and aluminium.

According to the ASTM for pin-on-flat studies, test lubricant should be controlled at 37ºC and completely submerge the sliding surfaces. To calculate the volume of lubricant required per chamber, the volume occupied by the test plate was subtracted from the volume of the

chamber. In the current study test plates were supplied by Smith and Nephew Inc. and measured 36mm in diameter, and 6.35mm thick, occupying a volume of 6110 mm^3. The inner diameter of the acrylic chamber wall was 60mm. Therefore, to submerge the plate beneath 3mm of lubricant required that each chamber be filled to a depth of 9.35mm. The resulting volume of fluid required per chamber was then calculated to be 19337mm^3 or 20ml.

To maintain 20ml of fluid at 37°C an aluminium wire-wound 10W resister was mounted to the underside of each chamber base. Current was passed through the resistor coils causing the resistor housing to heat up. Heat was transferred by conduction to the chamber base which acted in the manner of a heat-sink, conducting heat to the lubricant medium above. To increase system responsiveness and reduce the heat transfer distance between resistor body and lubricant, the resistor was mounted into a 25mm counter-bore, recessed on the underside of the chamber base giving a reduced effective base thickness of 4mm.

The energy required to increase the fluid and base temperature by 1 Kelvin is dependent on the mass and specific heat capacity of the base and lubricant. For example, the heat required to raise the chamber base by 1 Kelvin is seen in Equation 3-9:

$$Q_{heat} = cpm$$

Equation 3-9: Heat energy required to raise the temperature of a body by 1 Kelvin.

where Q is the energy input (Watts), cp is the specific heat capacity of the base (J/kg/K), and m is the mass of the base. The total energy required to raise the temperature by ΔT then becomes:

$$Q_{\Delta T} = Q_{\ heat}\, \Delta T$$

Equation 3-10: Total energy required to raise the temperature by ΔKelvin.

To raise the temperature of the stainless steel base and fluid from ambient (21°C) to 37°C required ~7357Joules. This was calculated assuming the thermal properties of 304 stainless steel and water. Each 10W aluminium wire-wound resistor draws 400mA, at a voltage of 12.92V when all six chambers are heating up (Table 3-6).

	Heating Circuit
PSU rating (V)	15
PSU rating (A)	4
Heating resistor (V)	12.92
Resistor current (mA)	400
Power per chamber (W)	5.2
Total power required (W)	31
Max current drawn (A)	2.4

Table 3-6: Electrical demands of the heating circuit.

The power output of each resistor was calculated by multiplying the voltage with the current, producing 5.2Watts, delivering 7357Joules in approximately 23minutes. This agrees well with the experimental heating curve seen in Figure 3-14, taking 20ml of test lubricant approximately 28 minutes to settle at body temperature.

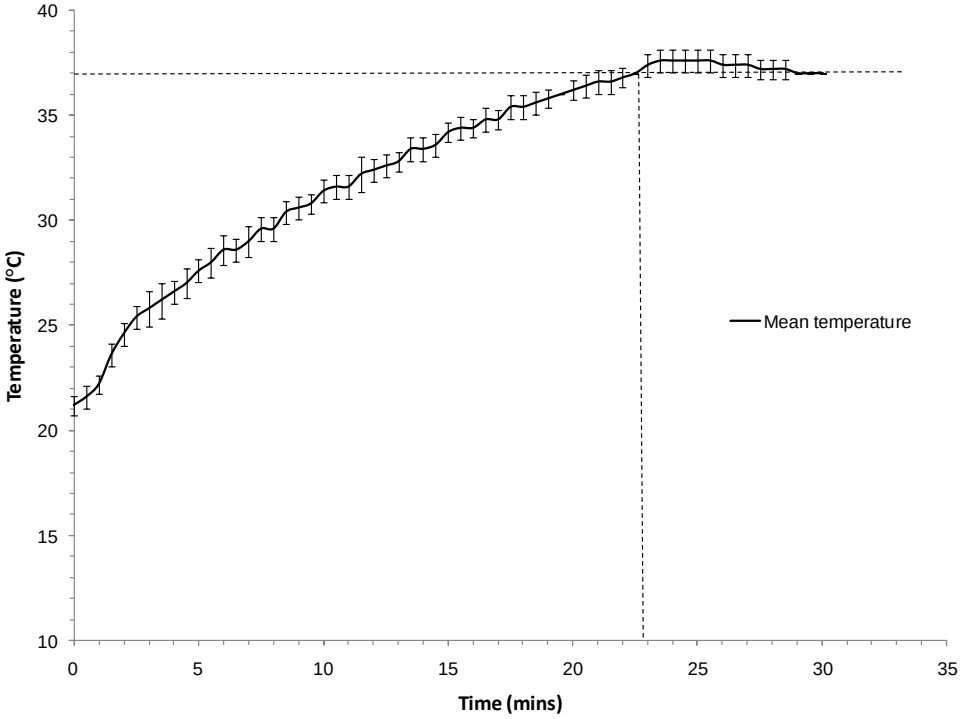

Figure 3-14: Real-time temperature profile from start-up; error bars represent standard deviation (n=6). The temperature of the lubricant overshoots 37ºC by ~1ºC after ~23minutes then settles at the set-point temperature after ~28minutes.

To further investigate the thermal responsiveness and limitations of the materials used in the modular design a two-dimensional model was analysed using heat transfer software (FEMLAB). The classical heat transfer partial differential equation and time-dependant solver were used. An external sub-domain encompassing the chamber assembly was given the properties of air and the resistor provided the only source of heat. The sub-domain divisions are seen in Figure 3-15. An aluminium chamber base was used to distinguish geometric limitations in the stainless steel base design. For example, it was found that the effective base thickness could be far greater in aluminium, highlighting the need to design a counter-bore to seat the resistor closer to the lubricant in the final stainless design. Maximising the capacity of the heating resistor was found to compensate for the decreased thermal conductivity associated with stainless steel in comparison to aluminium[148]. Figure 3-16 is an example of the heat transfer ability of the two materials, where for a given effective base thickness the aluminium material delivers a more uniform distribution of heat.

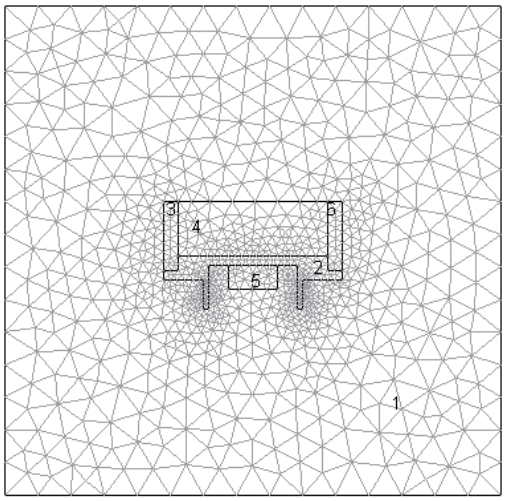

Figure 3-15: Meshing of the sub-domains used in the heat transfer model with material properties: 1-air; 2-aluminium/stainless steel; 3/5-acrylic; 4-test lubricant; 5-aluminium heat source.

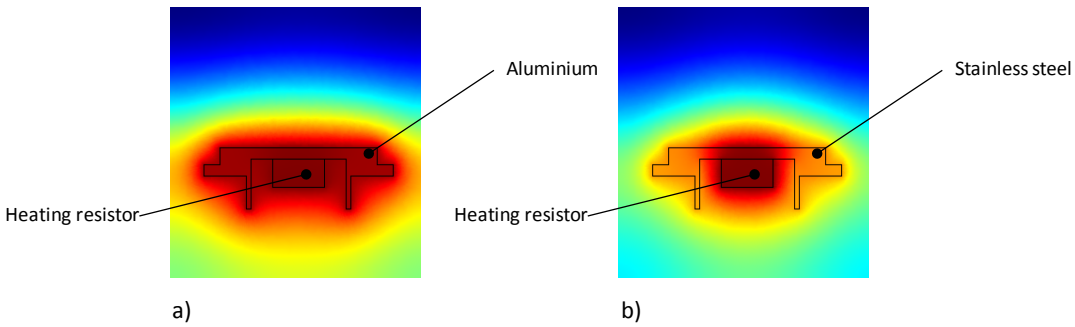

Figure 3-16: 2D heat distribution after 600 seconds through an a) aluminium base; b) stainless steel base. The colour scale remains identical in both models. Note the uniform distribution through aluminium, consistent with the greater thermal conductivity of this material.

Each chamber sits securely on a nylon base which was supported on four aluminium pillars. The pillars were designed such that strain gauges or a three-axis load cell could be installed at a later date to measure friction force. The nylon plates were designed to thermally isolate each chamber, minimising the thermal inertia and increasing the thermal responsiveness of the system. A locating pin in the chamber base and locating hole in the nylon base ensured the chamber was limited to being mounted in only one repeatable orientation. To further minimise heat loss, chamber walls were designed from acrylic pipe which has very poor heat transfer properties (Table 3-7). An o-ring was used to securely seal the chamber walls to the base. The modular design allowed each component to be removed for thorough cleaning.

Material	Thermal Conductivity (W/mK)
Acrylic (PMMA)	0.17 - 0.25
Nylon 6,6 (Tufnol)	0.24
Stainless steel 316	16.2
Aluminium alloy 2024	190

Table 3-7: Thermal conductivity values[148].

3.5.1 The Test Plate

Each test plate was fixed to the surface of the chamber base with four stainless steel spacers, tightened with stainless steel socket head counter-sink screws. Three of the spacers were Ø9.5mm in diameter and the fourth was Ø10.5mm. A small flat, machined at a tangent on the side of each CoCrMo plate located next to the larger spacer. This provided a method of ensuring each plate could be reinserted consistently (Figure 3-17). The depth of the spacers was such that they remained sub-flush with the surface of the test plate. This protected the spacers from the sliding test pin and pin holder, yet provided maximum contact to securely hold the plate in position.

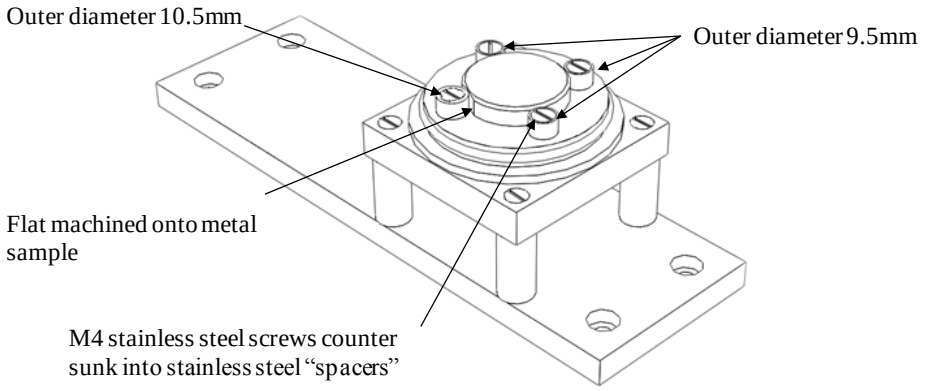

Figure 3-17: Each test plate was secured to the chamber base by four stainless spacers. One spacer was machined slightly larger in diameter, limiting the orientation of the CoCrMo plate to sit correctly when its flat edge was positioned tangential to the larger spacer.

3.5.2 Temperature Control

A six-channel PID (Proportional-Integral-Derivative) controller was used to independently control the bulk lubricant temperature within each chamber. The PID controller works by comparing the actual temperature to the user controlled set-point value. The controller attempts to minimise the difference and settle at the user defined value (Figure 3-18). Closed-loop PID algorithms are highly accurate and very stable. Within each chamber a type-K thermocouple sensed the temperature of the lubricant and relayed this to the controller. Type-K were selected due to their ease of use, suitable reading error (±1°C), and flexibility in offering a wide range of positioning and mounting arrangements.

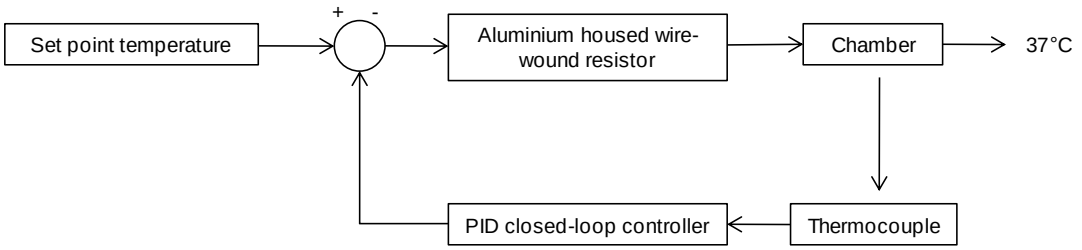

Figure 3-18: Proportional-Integral-Derivative temperature control loop.

Should the lubricant temperature in any of the chambers fall below the set-point value a heating circuit was activated. The controller closed a solid-state relay associated with the cooler chamber allowing current to flow to the resistor. The resistor generated heat which was conducted through the chamber base to the lubricant. A temperature rise was registered by the thermocouple and fed back to the controller. When the thermocouple reading approached the desired temperature the controller opened the solid-state relay cutting off the power to the resistor and hence heat supply to the chamber. This discrete opening and closing of the relays allowed each chamber to remain at 37ºC±1ºC.

The maximum load placed on the heating power supply was at the start of each test interval. During this period all six resistors draw maximum current to heat the lubricant from ambient to body temperature. The maximum current drawn by each resistor was 400mA, at 12.92V. Therefore, the current drawn by six resistors simultaneously was approximately 2.4A. To ensure the power supply was never overloaded a 15V, 4A unit was installed.

3.5.3 Lubricant Maintenance

During testing intervals, water in the dilute newborn calf serum lubricant would evaporate. Evaporation left un-monitored would result in an increase in lubricant protein concentration and a drop in lubricant volume. A significant drop in lubricant level may cause physiologically inappropriate dry sliding [24] and changes in protein concentration have been shown to affect UHMWPE wear rates from both pin-on-plate studies[149] and hip simulator studies[143]. To maintain consistency of the lubricant constituents and level, each chamber was independently “topped-up” with de-ionised water.

The real-time sensing circuit consisted of two platinum sensor probes (0.5mm diameter, Alfa Aesar) mounted in each chamber, where probe length determined the nominal lubricant level. The system was controlled by a 12Vdc relay integrated on a PCB fluid-level board which changed state in response to current flowing between the probes. Test lubricant acted as the conductive medium, restricting current to flow between the probes only when they were in contact with the fluid (Figure 3-19). If the passage of current was broken i.e. if the

lubricant level was not sufficient to make contact with the probes, the relay switched a 24Vdc voltage supply opening a solenoid valve. The open valve allowed de-ionised water to enter the chamber increasing the level of lubricant in that chamber. When the volume of fluid reached a level that caused electrical contact between the probes, the relay closed the valve preventing further de-ionised water from filling the chamber.

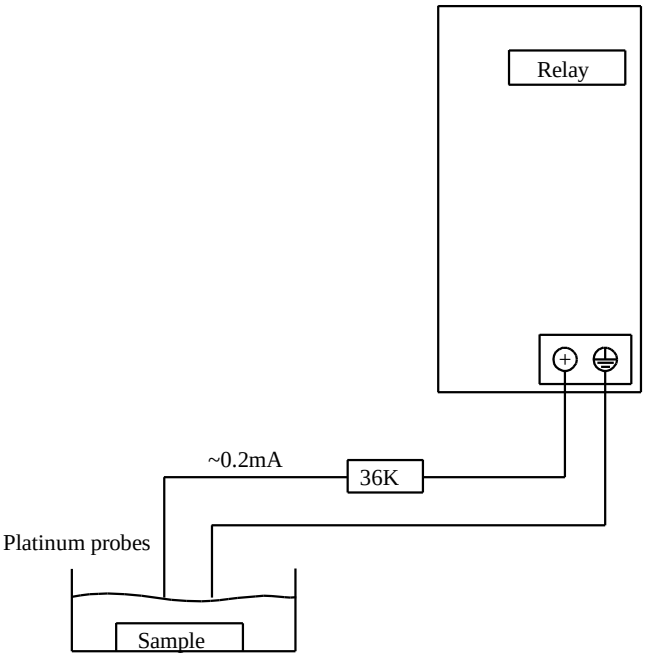

Figure 3-19: The lubricant level sensing circuit works on the principle of continuous current flow. If the lubricant level falls below the two probes, the circuit is broken and solenoid valves (not shown) open to disperse de-ionised water, re-filling the chamber until current flow resumes.

Six 24Vdc, 200mA, solenoid valves[7] were grouped and mounted onto one four-way manifold (Figure 3-20) and one two-way manifold. The manifold allowed multiple solenoids to work from one inlet supply. The four-way manifold delivered de-ionised water to the four load and motion chambers and the two-way manifold to the two load-only stations. Standard mild steel manifold fittings were retro-fitted with stainless steel components.

[7] Burkert, 6011 Miniature solenoid valve – with a sub-base connection

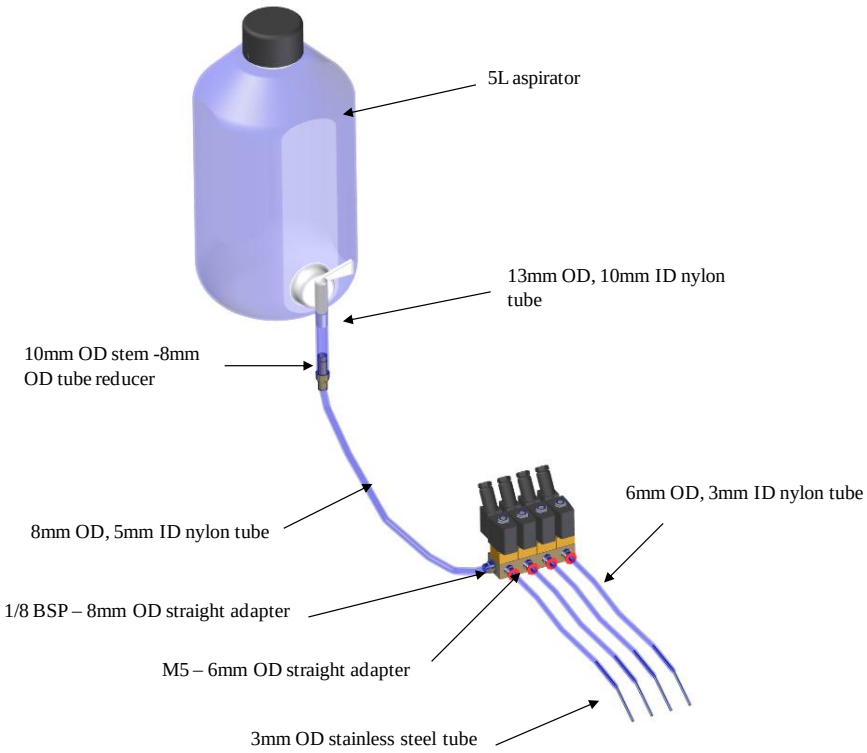

Figure 3-20: The de-ionised water "top-up" system, showing the four-way manifold with valves. The two-way "load-only" manifold has been excluded for simplicity. To prevent contamination, all standard steel valve caps and glands were re-issued in stainless steel.

The de-ionised water supply was stored in two 5L bottles. Each bottle was mounted above the rig, relying on hydrostatic pressure to gravity-feed water into each chamber. With the solenoid valve shut a stagnation point up-stream allowed hydrostatic pressure to build. The hydrostatic pressure was approximated as the density of fluid multiplied by the vertical height the fluid flowed multiplied by gravity. A water supply pressure of approximately 2646Pa, where 1 bar is equal to 1 x 10^5 Pa, produced a supply pressure of 0.03 bar per chamber. In comparison, each valve was rated at 0-21bar. The low supply pressure exerted little demand on the valves, tube fixings and seals, maximising the operational life of the fluid level system.

The current that passes between the two chemically inert platinum probes and lubricant creates an electrolytic cell. In an electrolytic cell, electrons are absorbed or released by ions in the solution and additional ionic compounds can be formed. To prevent physiologically irrelevant contamination of the original Ringer's/NCS protein solution, the current passing through the sensing circuit was minimised in two ways. Firstly, by increasing the resistance of the circuit and secondly, by adding a timer to periodically turn off the circuit.

The increased resistance reduced the size of the current flowing through the circuit. This resulted in fewer electrons passing through the cell, minimising the rate of reduction (electrons gained) at the cathode and oxidation rate (electrons lost) at the anode. The potential difference across the probes when not in contact with the lubricant was 11.90Vdc. This dropped to 7Vdc and 0.8mA upon completion of the circuit, giving a nominal circuit resistance of 8,750Ohms. To reduce the current even further, a 36,000Ohm resistor was added in series with the probe sensing circuit, taking the total resistance to 44,750Ohms. Using Ohms law and an assumed voltage drop of 7Vdc, the current was predicted to decrease to a value of 7/44.8=156μA. The actual value was measured at 210μA under a voltage drop of 11Vdc, agreeing well with the theoretical approximation.

To periodically switch the sensing circuit on and off, an asymmetrical timer was installed between the on/off switches and fluid control boards. The timer was controlled by pulse and pause settings to configure when and for how long the circuit should energise. By setting the circuit to energise intermittently for ten seconds every hour, the duty cycle of the circuit was reduced. Ten seconds was empirically found to be sufficient time to compensate for any fluid evaporation which may have occurred within the hour the system was idle. The user could bypass the timer to revert back to continuous sensing if required.

3.6 The Pin Holder

The modular specimen holder is constructed from 304 grade stainless steel and is designed to hold a 5mm diameter pin. Each 20mm long pin, when seated properly protrudes 2mm clear of the holder. The sleeved design stiffens the pin and helps to ensure a constant contact area during sliding. Without the stainless steel sleeve, friction forces during sliding would theoretically cause the small diameter pins to bend, or laterally deflect up to ±1.26mm (Figure 3-21) (Appendix 5: Pin Deflection). As a consequence, contact stresses and sliding distances would vary across the deflected surface, dictated by the amount of curvature and which areas of the pin remained in contact under lateral deflection.

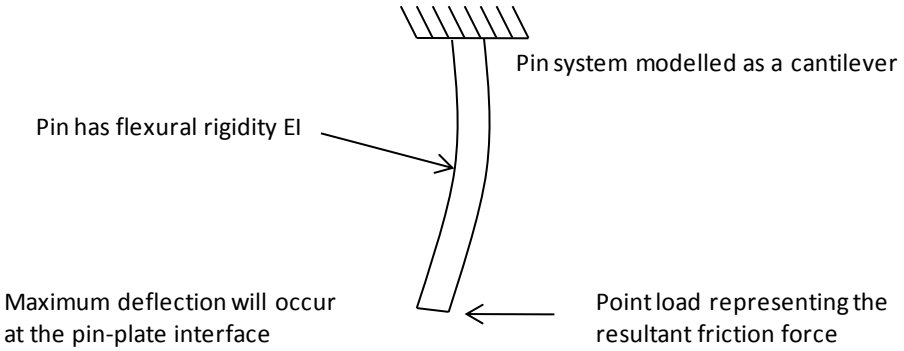

Figure 3-21: Exaggerated schematic; the pin-on-plate sliding interface is replaced by a point load representing the frictional force. To calculate tip deflection the pin was approximated as a cantilever.

Pins with larger diameters are stiffer but require larger normal loads to achieve physiological stress levels; a consequence of the larger nominal contact areas. Further attributes associated with the larger diameter include reports of lubrication starvation and trapped wear debris within the contact zone, suggested to cause misleading UHMWPE wear behaviour[71, 150, 151].

A chamfered or truncated pin maintains the stiffness of a larger diameter pin and improves the likelihood of a uniform lubrication regime across a smaller contact area. However the chamfer will inherently cause an increase in contact area as the pin is worn. Under static load this would cause a decrease in nominal contact pressure over time potentially changing the tribological sliding conditions.

To minimise pin deflection in smaller diameter pins, metal housings have previously been used where half the pin diameter protrudes from the sleeve[151]. The purpose of the sleeve was to increase the stability of the pin under normal and lateral forces generated at the pin/plate interface by providing additional stiffness. A summary of contemporary test pins is seen in Table 3-8.

Shape	Group[reference]	Dimensions (mm)	Apparent contact area (mm^2)	Load regime	Stress (MPa)
	Boston 2001[104]	Diameter 9 Length 15	63.62	Double peak Max load 310N	Peak stress 4.8
	Durham 2000[105]	Diameter 5 Length 20	19.63	Constant 40N	Nominal stress 2.04
	Edinburgh 2008	Diameter 5 Length 20	19.63	Double peak Peak 1 90N Peak 2 59N	Average nominal stress 2.0
	Harvard 2003[112]	Diameter 9 Length 20	63.62	Constant 192N	Nominal stress 3.0
	Helsinki 1998[106]	Diameter 9 Chamfer 60° Initial diameter 3mm	7.07	Constant 70.7N	Initial nominal stress 10.0
	Helsinki 2005[123]	Diameter 9 Length 12	63.62	Constant 70.7N	Nominal contact stress 1.1
	Leeds 2006[113]	Diameter 12 Chamfer 45° Initial diameter 8	50.27	Constant 160N	Nominal contact stress 3.2
	New York 2001[151]	8-23mm Metal housing	50.2-415	Constant 1200N	Nominal contact stress 2.8-23.9

Table 3-8: Contemporary polymer test pins. Not to scale.

UHMWPE pins were evaluated against a failure buckling criterion under a maximum heel-strike contact stress of 5.01MPa (100N load). The pin was treated as a free column and Euler buckling theory applied. The critical buckling force without the metal sleeve was calculated to be 131N (Appendix 6: Pin Buckling). The sleeved pin design resists both buckling and lateral deflection under the range of physiologically relevant nominal forces.

A stainless steel dowel placed through each polymer pin located into a vertical slot machined in the stainless steel sleeve. This arrangement ensured correct pin orientation upon re-insertion. Within the body of the pin holder an internal bore was machined to allow the water supply and temperature sensors to reach unobtrusively into each chamber. An exploded schematic of the sub-assembly is seen in Figure 3-22.

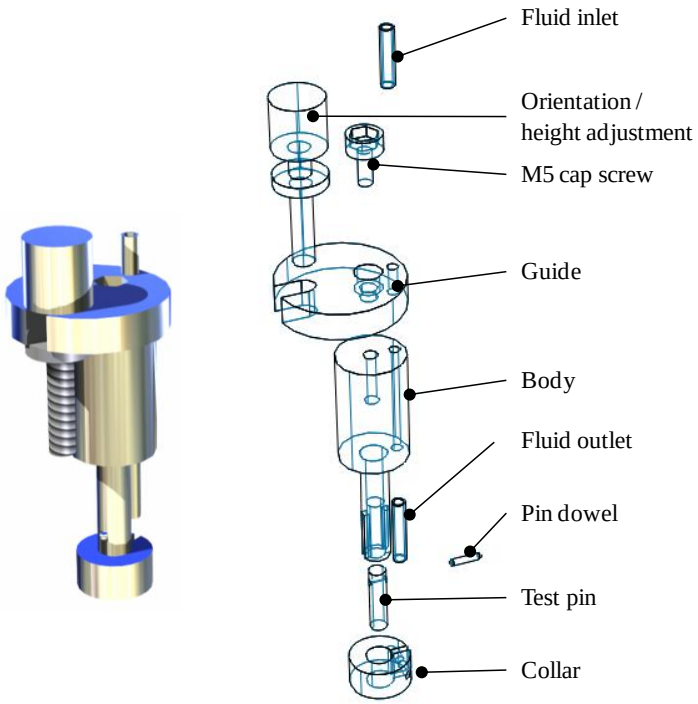

Figure 3-22: Exploded view of the test pin holder. All the modular components were designed from 304 stainless bar stock. This allowed the machining to be carried out on a single lathe, greatly simplifying the manufacturing process.

Each pin holder located into a bore in the end of the loading arm (Figure 3-1). This ensured location repeatability in the x-y plane. A sliding fit tolerance between the holder and loading arm allowed the holder to be adjusted in the z axis to accommodate for linear height changes following pin wear. In summary, each pin holder was adjustable in the z-direction but constrained against translation and/or rotation in the x-y axes. The height adjustment screw also acted to locate the pin holder in an orientation specific manner prior to testing.

3.7 The Chassis

A steel frame was constructed from 25mm x 25mm square extruded box section (Figure 3-23). The chassis was designed to accommodate the size and sliding range of the linear slides, stepper drives, test chambers, electric actuators and PID controllers. Footprint dimensions are 1000mm x 300mm x 475mm (w x h x d) to ensure "table-top" use. Width was determined by the size and number of test stations, height was determined by the stacked linear slides and chamber dimensions and depth was dictated by the length of the loading arms used to magnify actuator output forces. To mount the temperature controller, stepper drives and actuator controllers within the frame, aluminium plates were designed and fixed to the framework with socket-head cap screws. All aluminium parts (including the loading arms, bearing housings and shaft supports) were powder coated to offer increased corrosion resistance. All electrical components were earthed through the frame. The chassis was mounted on eight anti-vibration feet.

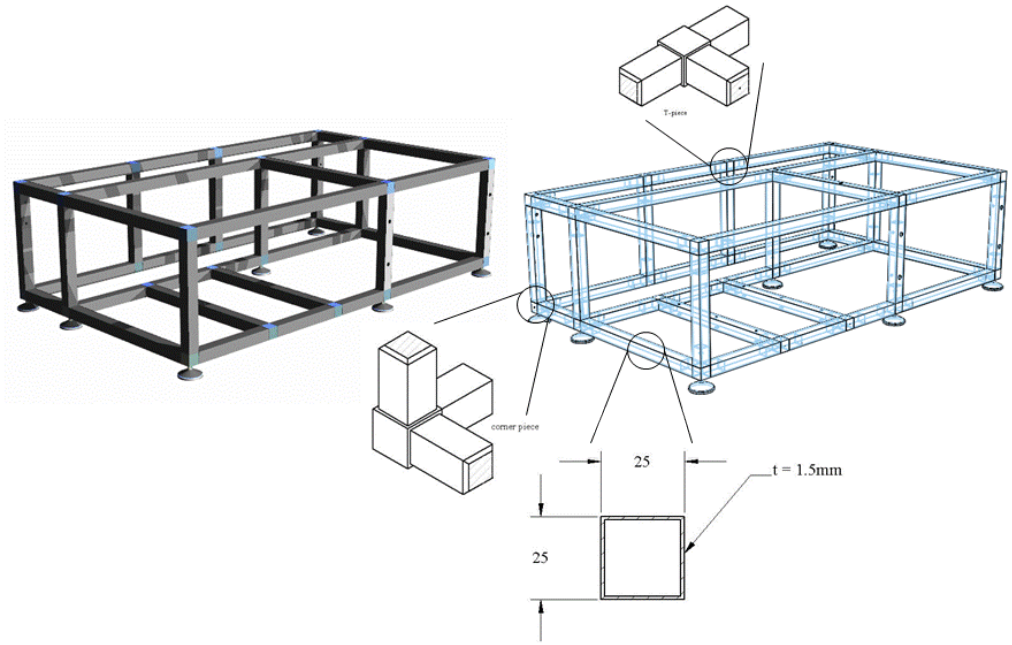

Figure 3-23: Frame assembly; steel tubing was cut to size and adjoining members were held together using a selection of connecting pieces. The structure was carefully designed to accommodate all of the tribometer's components, incorporate a non-obstructive space sufficient for maximum slide translation in the x and y axes, yet remain as compact as possible.

3.8 Synchronisation

The tribometer was computer controlled, communicating with motion, load and temperature components via RS-232. Motion and loading cycles were synchronised and run at 1Hz. The motion software initiated a trigger at the beginning of each cycle which the loading actuators responded to. The number and period of the loading and motion cycles were recorded on the PC and used to stop the machine following a discrete number of user cycles. Figure 3-24 shows the simplified communication pathways between the main components.

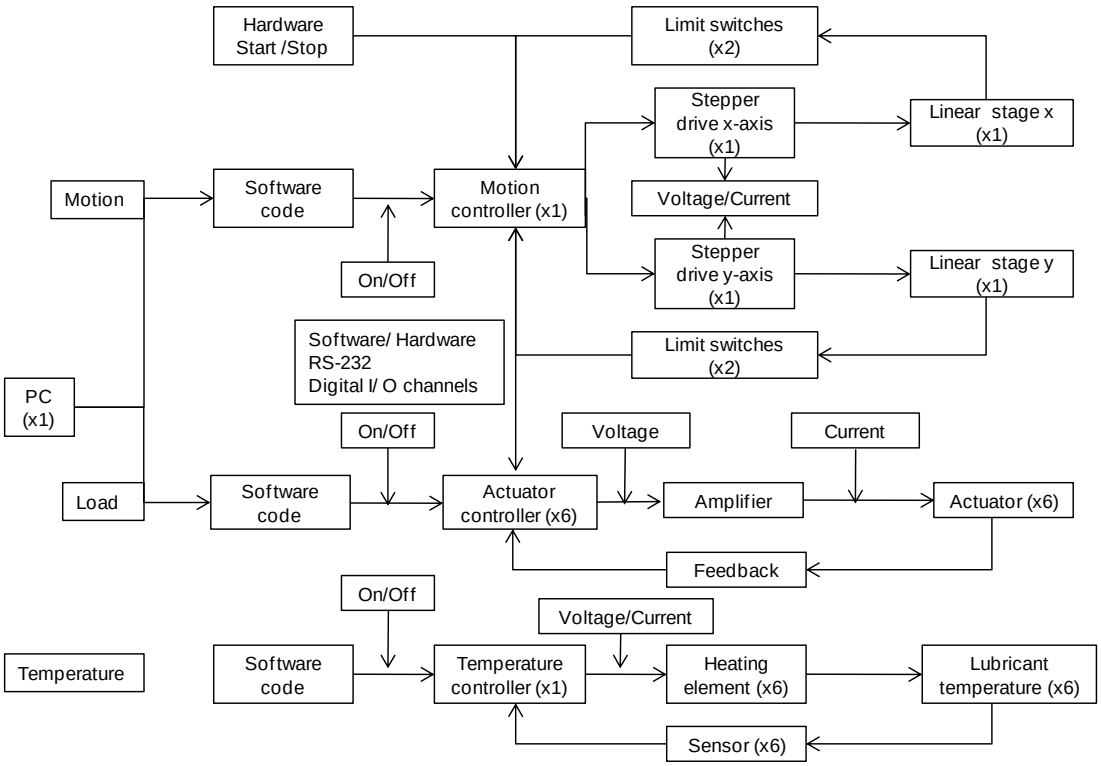

Figure 3-24: Diagram of the main component pathways. Load, motion and temperature were configured by the PC. Communication through both hardware and software relayed this information to be finally output at the pin/plate interface.

4 Materials and Methods

Summary

The clinical relevance of the tribometer wear model (the combination of applied dynamic load, sliding motion, and lubricant) was confirmed in a validation study. Three orthopaedic polymers of historical note were wear tested; polytetrafluoroethylene, polyacetal, and UHMWPE. Each polymer was worn under linear-reciprocating and elliptical motion paths.

A subsequent crosslinked study compared the wear behaviour of unirradiated (-PE) and highly crosslinked (+PE) UHMWPE. Structural integrity of the unirradiated and crosslinked material was investigated in a swell-test study. From this, crosslink density was approximated using Flory-Rehner theory.

Field emission scanning electron microscopy was used to qualitatively evaluate morphological features of worn surfaces. Additionally, SEM of potassium permanganate etched UHMWPE surfaces revealed the extent of sub-surface, wear-induced lamellae reorientation.

The use of non-destructive Raman spectroscopy was first confirmed with crystallinity measurements from conventional differential scanning calorimetry before being used to characterise the worn surfaces of –PE and +PE. A polymer laminate study quantified the scattering volume of the Raman system. This allowed the sub-surface microstructure to be investigated in accordance with the depth resolution of the system.

4.1 Overview

The use of the tribometer may be divided into two studies; a validation study and a highly crosslinked study. All materials and methods used throughout the course of work are presented within this chapter. For complete experimental protocols the reader is referred to the appendices.

4.2 The Tribological Interface

4.2.1 Cobalt Chrome Molybdenum Alloy

Twelve cobalt chrome molybdenum alloy plates (28% chromium, 6% molybdenum) were provided by Smith and Nephew Inc. Each plate was 36mm in diameter and 6.35mm thick. Six of the twelve plates arrived pre-polished to Smith and Nephew orthopaedic quality finish. White light interferometry (Zygo, NewView 100) confirmed the surface finish of the "as-polished" plates. A x40 objective was used, giving a true magnification of x400 and a system resolution of ±0.5μm in the x and y-direction and ±0.3nm in the z-direction (topography). Each image consisted of nine scans averaged to maximise the signal to noise ratio, where each image covered a surface area of 176μm and 134μm (x and y direction). Ten scans (n) were randomly taken on the surface of each plate. For all images form error was corrected through software plane removal. This compensates for tilt of the plates inherent in the equipment setup, improving the ability to display surface irregularities and making a slanted surface appear flat. The arithmetic mean surface roughness, S_a, for the six plates can be seen in Table 4-1. Range is defined as the maximum value minus the minimum value.

	Plate 1	Plate 2	Plate 3	Plate 4	Plate 5	Plate 6
Mean (μm)	0.002	0.0015	0.002	0.002	0.002	0.0014
Std Dev (μm)	0	0.00051	0	0	0	0.0002
Range (μm)	0.001	0.0014	0.001	0.001	0.001	0.0005
n	10	10	10	10	10	10

Table 4-1: Mean arithmetic surface roughness (S_a) of plates supplied by Smith and Nephew Inc.

The mean surface finish across all plates (±S.D) was S_a 0.002μm ± 0.00012μm. This is an order of magnitude lower than the counter-bearing roughness of most previous pin-on-plate studies (Table 4-2), but agrees well with the unworn femoral head finish reported from a retrieval study by Elfick *et al.*[61].

Group	Study	Surface roughness (µm)	Method of measurement
Bragdon *et al*.[104]	Pin-on-plate	Cobalt chrome R_a 0.05 µm	Non-contact laser stylus (Focodyne 250)
Elfick *et al*.[61]	PCA retrieval study (*ex vivo*)	Cobalt chrome Unworn median S_a 0.00305 µm Worn median S_a 0.01035 µm	Non-contact optical profilometer (Zygo NewView 100)
Galvin *et al*.[113]	Pin-on-plate	High nitrogen stainless steel R_a ~0.01 µm	Contact, diamond stylus
Joyce *et al*.[105]	Pin-on-plate	316 stainless steel R_a 0.05 µm	Non-contact optical profilometer (Zygo NewView 100)
Saikko *et al*.[106]	Pin-on-plate	316L stainless steel R_a 0.004-0.005µm	Contact, (RTH Talysurf)
Saikko *et al*.[123]	Pin-on-plate	Cobalt chrome R_a 0.01-0.02 µm	Contact (Taylor Hobson Surtronic 3+ diamond stylus)
Turell *et al*.[112]	Pin-on-plate	Cobalt chrome R_a 0.015 µm	Information unavailable

Table 4-2: Roughness comparison of contemporary pin-on-plate metal surfaces and explanted femoral head finish.

In addition to the mean arithmetic surface roughness of the plates, the skewness parameter (Section 2.4.2.2) was recorded. General consensus for a good bearing surface is one that possesses negative skew, such that the potential for abrasive damage is minimised. The average skewness (S_{sk}) across all six plates (n=60, ±S.D) was -0.26±0.43, indicating a close symmetry about the average surface centreline. A typical Smith and Nephew Inc. polished plate with corresponding line profile plots is seen in Figure 4-1.

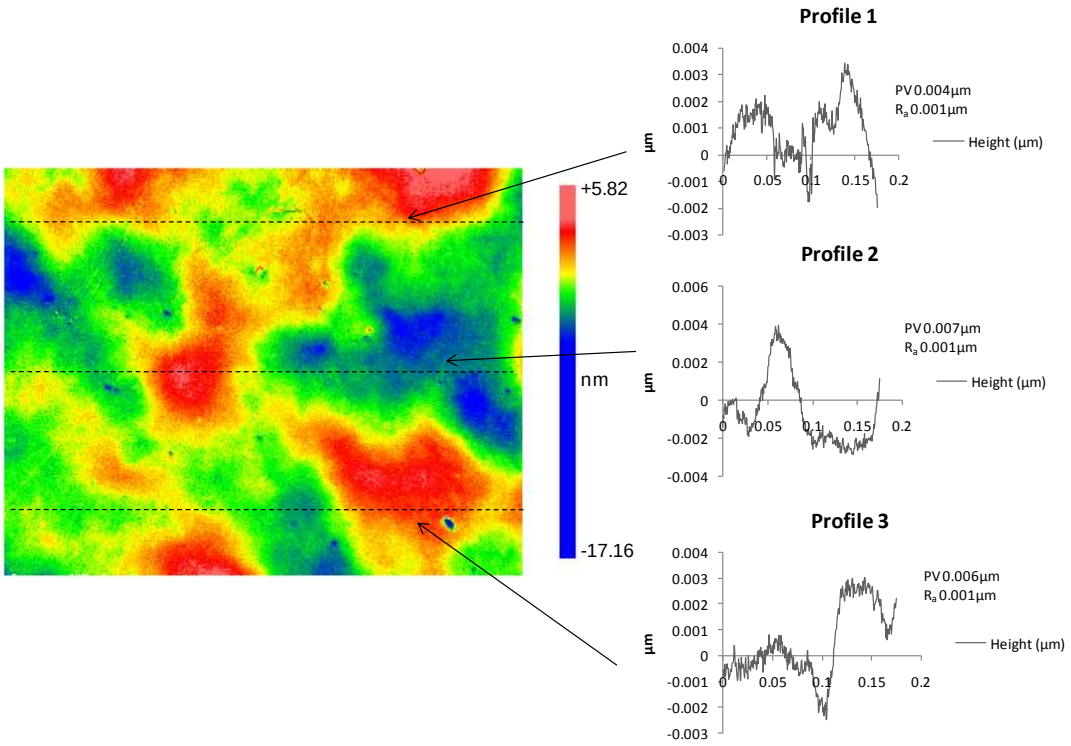

Figure 4-1: Contour plot of a Smith and Nephew Inc. CoCrMo orthopaedic surface finish complete with three profile plots; scan area 176µm x 134µm.

Prior to each new wear study plates were re-polished in-house. The initial polishing method followed a five-step protocol (Table 4-3), proposed by the Buehler materials preparation laboratory[152].

Pad	Abrasive size	Time (mins)
Abrasive discs	P240-P400	Until plane
Cloth	9µm diamond suspension	5
Cloth	3µm diamond suspension	5
Cloth	1µm diamond suspension	3
Microcloth	0.05µm colloidal silica suspension	2-3

Table 4-3: Five-Step Buehler polishing procedure for cobalt.

Early in-house polished surfaces were marred by evidence of pitting and/or grain pull-out. The 0.05µm colloidal suspension appeared to agitate the surface, removing carbides under light-abrasive polishing. Evidence of their absence was apparent by pitting, approximately 100nm in depth (Figure 4-2). These features were clearly visible under the x400 magnification of the Zygo which posted surface texture parameters in support of grain pullout; a large standard deviation about the mean arithmetic surface roughness and significant negative skew.

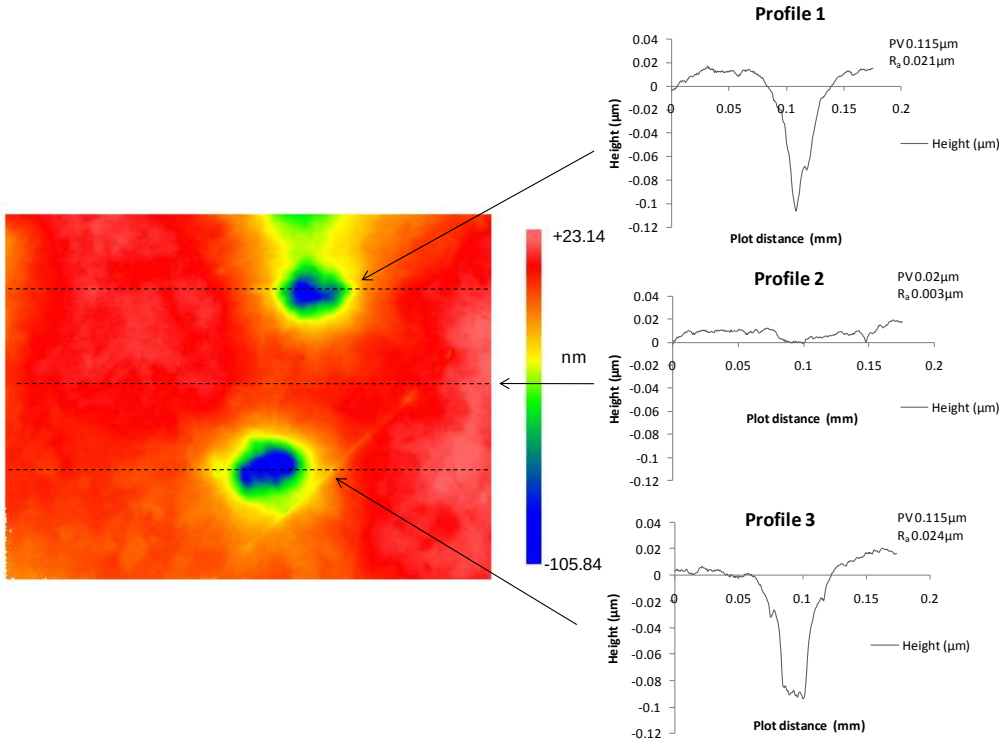

Figure 4-2: Contour plot of an initial in-house polished CoCrMo surface showing carbide sites previously removed during the 0.05µm polishing step; scan area 176µm x 134µm. Three line plots of interest indicate the pitting sites to have a depth ~100nm.

The Buehler protocol was adapted such that final polishing was completed with the 1µm suspension. This produced a surface free from pitting with centreline surface roughness's similar to the initial Smith and Nephew Inc. clinical finish (Table 4-4).

	Final polish 0.05µm	Final polish 1µm	Smith and Nephew
Range (µm)	0.0420	0.0006	0.0010
Mean (µm)	0.0150	0.0015	0.0020
S.D (µm)	0.0160	0.0002	0.0002
n	6	12	10

Table 4-4: Arithmetic surface roughness comparing final in-house polishing methods to that of Smith and Nephew Inc. Final polishing with a 1µm suspension showed good agreement.

An optical image of an in-house polished plate and interferometry plot with corresponding histogram is seen in Figure 4-3. The histogram is composed of the total number of pixels taken during the scan and their elevation with respect to the mean centre line. The frequency distribution of data points can be approximated by a normal distribution, supporting a surface skewness close to symmetry, S_{sk} -0.34±0.14. This is in good agreement with the pre-polished Smith and Nephew plates (S_{sk} -0.26±0.43).

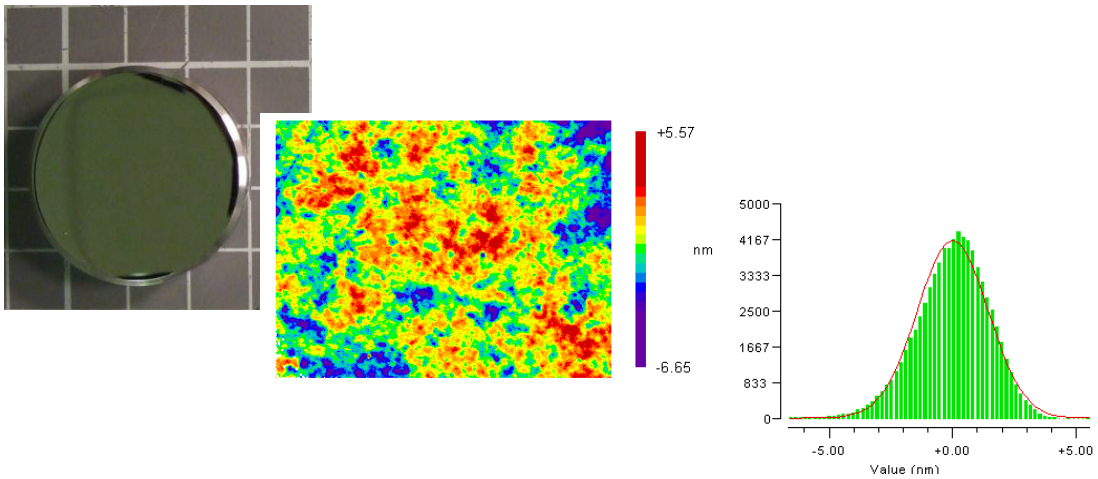

Figure 4-3: In-house plate surface finish; optical image grid size 10x10mm, Zygo contour plot 176µm x 134µm and histogram plot with superimposed normal distribution curve.

4.2.2 Polytetrafluoroethylene

Polytetrafluoroethylene (PTFE) is a semi-crystalline polymer consisting of linear carbon-carbon backbone chains onto which fluorine atoms are covalently bonded. The simple chain structure is comparable to polyethylene. Rather than the zig-zag chain conformation of the repeating ethylene monomer (Figure 2-16), PTFE assumes a regular helix conformation (Figure 4-4) with the fluorine atoms running around the carbon backbone[153]. Limited side branching and smooth helical profile are often used to explain the low coefficient of friction and high wear under sliding[154, 155].

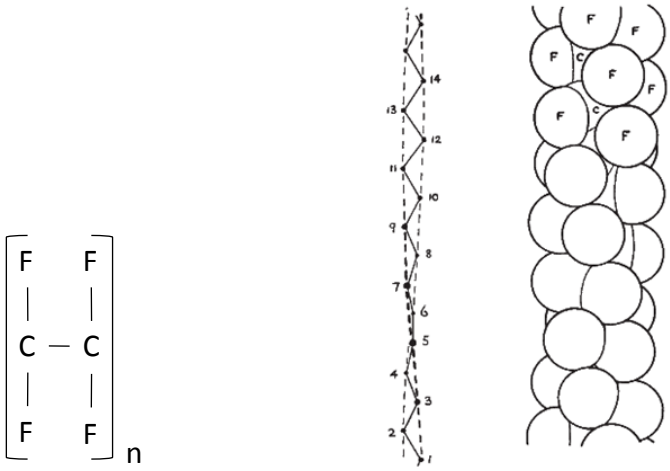

Figure 4-4: Left, monomer unit of Polytetrafluoroethylene; Right, helical conformation found in PTFE; at room temperature there are 15 $–CF_2-$ units present in seven turns of the chain[153].

The unusual low friction properties of PTFE have made it a very successful plain bearing in many applications. However, in the majority of commercial applications, fillers, such as glass or carbon fibers are added to form a PTFE composite material with low friction and more acceptable lower wear behaviour[36].

4.2.3 Polyacetal

Polyacetal, also known as polyoxymethylene, was first synthesised by DuPont scientists in 1952 and given the trade name, Delrin®. The monomer unit is seen in Figure 4-5. It is a semi-crystalline thermo-plastic, with a backbone structure similar to both polytetrafluroethylene and polyethylene.

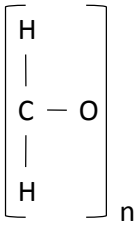

Figure 4-5: Monomer unit of polyacetal.

Polyacetal was first suggested as a load-bearing polymer due to its superior creep-resistance and hardness over UHMWPE[156]. Such attributes arise from the shorter carbon-oxygen bond (0.143μm) allowing the molecules to pack more tightly together[39]. For comparison, the carbon-carbon backbone bond found in polyethylene is longer, 0.154μm.

Recall from the Archard wear equation (Equation 2-3) the dependence of wear on hardness; to a first approximation, wear is thought to be inversely proportional to hardness, although it is understood that this is material and sliding specific. Should this relationship apply to the tribological conditions of the hip joint then the properties of polyacetal were thought to minimise sliding wear and offer more resistance to third-body abrasive wear arising from cement or bone fragments.

Since its introduction, polyacetal has been used to form the bearing component in several different joint replacements such as the convex femoral component in an all polymer total knee replacement and the acetabular cup in total hip replacement (THR). Modern artificial bearing surfaces no longer use polyacetal. Further discussion on its abandonment is found in Section 6.2.2. For the current study, white Delrin homopolymer (M_w 140,000g/mol) was supplied in 20mm diameter bar (RS Supplies, England) and turned on a manual lathe to pins 5mm in diameter and 20mm in length.

4.2.4 UHMWPE

Two groups of UHMWPE material were supplied by Smith and Nephew Inc. The resin in both groups was Ticona GUR1050 grade, consolidated by ram extrusion into 2" bar stock. The first group (-PE) consisted of unirradiated stock, machined into pins of 5mm diameter and parted-off in 20mm lengths.

The second group (+PE) were subject to the CISM process (Section 2.5.6) where UHMWPE underwent a gamma irradiation dose of 100kGy at room temperature and a post-irradiation above melt stabilisation process at 150°C. The highly crosslinked bar stock was then machined into pins of 5mm diameter and parted-off in 20mm lengths.

Tool marks remnant of the machining process can be seen in Figure 4-6. These were evident regardless of material group and were not removed prior to testing. The decision to wear test directly on the machined surface was thought to better approximate the wear-in of machined ram extruded and compression molded components. However, in some studies pin surfaces are microtomed prior to testing to remove the near-surface zone of damaged material[157]. The damaged zone is thought to contain residual stresses imparted during the machining process.

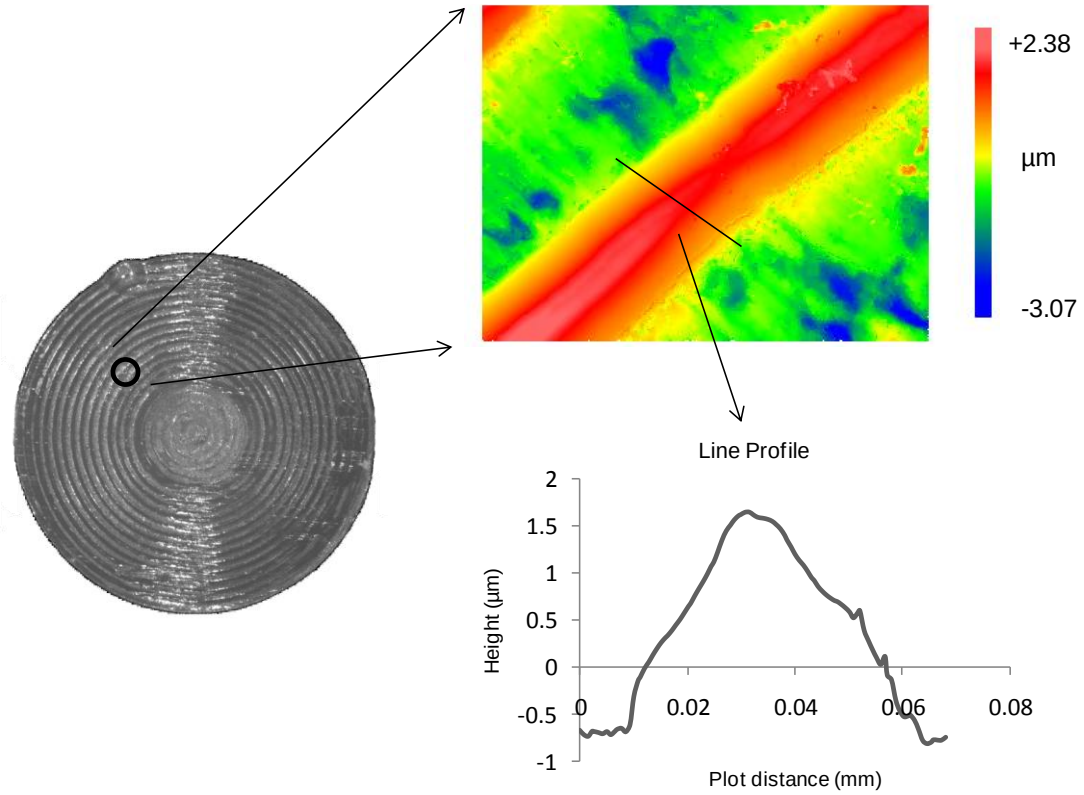

Figure 4-6: An optical image of the unworn pin surface with clearly defined concentric machining marks. The contour plot and corresponding line scan indicates these features to have an amplitude ~1.5µm; scan area 176µm x 134µm.

4.2.5 Tribological Conditions

It is worth noting that prior to the results reported in Chapter 5, trial wear tests were run with PTFE pins. These early studies provided an opportunity to troubleshoot the machine and optimise motion and load programmes. The following section describes the final test conditions to which all polymer pins were worn.

A double peak Paul-type load curve[8, 9] with a peak 1 and peak 2 of 90N and 59N was applied, corresponding to an average apparent contact pressure of 4.5MPa and 2.9MPa during the stance phase (Appendix 7: Load Profile Program). The average load per cycle, calculated by integrating under the load curve was 38N±1.6N. Motion and loading cycles were synchronised and run at 1Hz, the heel strike occurring just after the point of maximum flexion, as seen in Figure 4-7. The swing phase was programmed to account for 50% of each cycle. The ASTM F732-00 (2006) on satisfactory clinical wear testing recommends a peak contact stress between 2MPa and 10MPa, and an average nominal contact stress of 3.54MPa. Our mean contact stress of 1.9MPa is lower than the ASTM standard but similar in magnitude to Joyce *et al.*[105] and higher than Saikko[123] who used a value of 1.1MPa, suggesting that contact pressures in the hip may be lower than the ASTM indicates. Two stationary loaded pins accounted for fluid absorption.

Pin-on-plate work conducted in the presence of serum has been found to consistently produce worn surfaces more representative of those from explanted components[28]. Test lubricant used herein consisted of newborn calf serum (Harlan Sera lab) diluted with Ringer's solution to a protein concentration of 28g/l; Ringer's was used to preserve the ionic composition of the serum which was thought important for protein adsorption kinetics[158]. To inhibit bacterial growth, 0.2wt% sodium azide was added. All pin-on-plate stations were lubricated independently and lubricant was changed at each downtime. The serum was kept at 37˚C ± 2˚C through PID control.

Some researchers suggest that calcium phosphate may precipitate onto the metal bearing surface, causing a roughening effect and accelerating the wear of UHMWPE[26, 108]. To minimise this speculated damage mechanism they add ethylenediaminetetraacetic acid (EDTA), to bind the calcium in solution. EDTA was not used in the Edinburgh study. Regular renewal of the lubricating serum was thought more beneficial than to add the anti-chelating agent which may alter the protein adsorption kinetics.

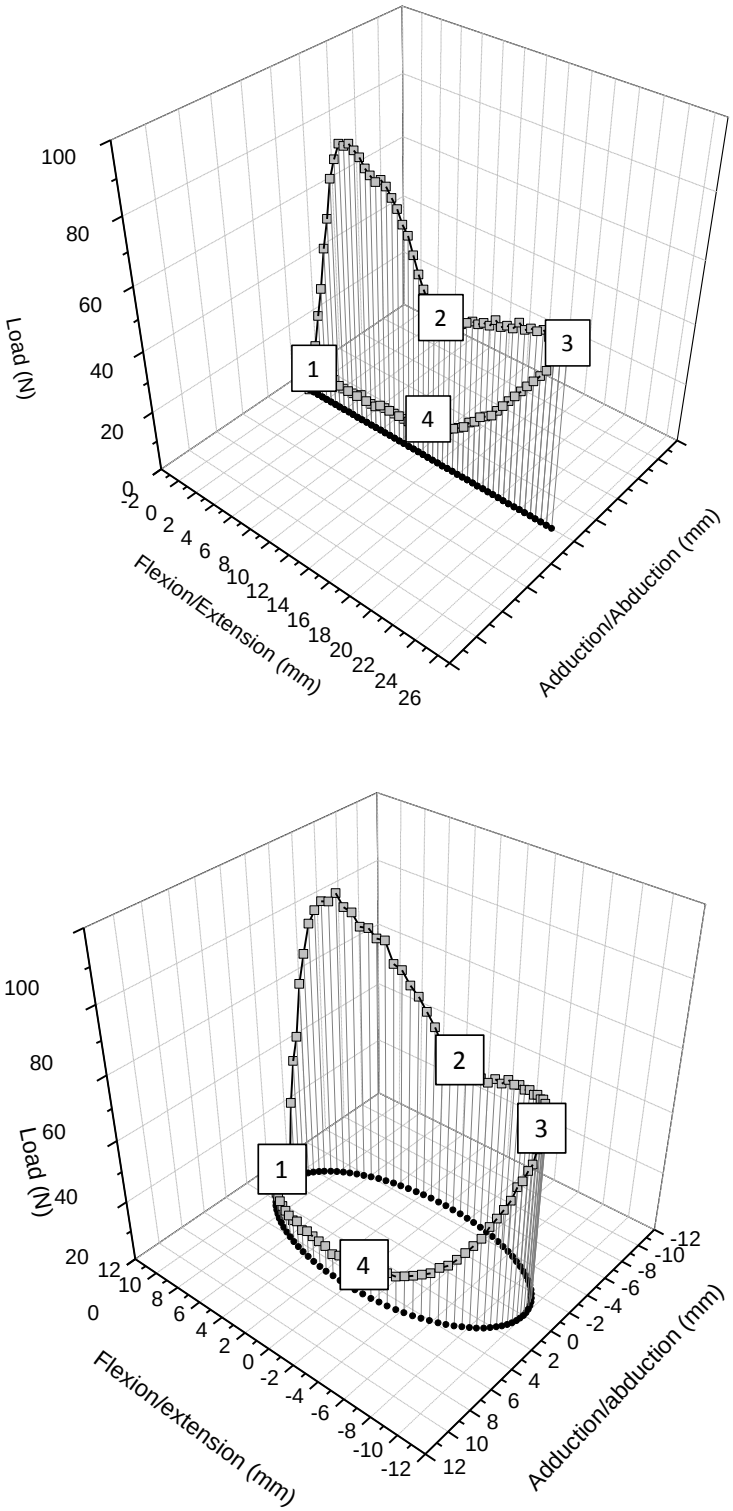

Figure 4-7: Synchronised dynamic load with; (above) linear-reciprocating motion; (below) elliptical motion. Where; 1 heel strike; 2 stance phase; 3 toe-off; 4 swing phase.

Two slide paths were chosen; a historical linear-reciprocating and contemporary elliptical motion path. Wear paths were programmed to approximate the length of those found from gait analysis[100, 125]. The elliptical path was applied to better approximate the complex quasi-elliptical wear paths simulated to occur *in vivo*[110].

Simple linear-reciprocating motion was achieved by programming the bottom slide to trace a reciprocating stroke of 25mm (Appendix 8: Linear Motion). The motion controller coordinated the move, implementing a standard trapezoidal motion profile (Figure 3-6). This consisted of a 0.17sec (450mm/s^2) acceleration period, 0.16sec (77mm/s) constant velocity period and a 0.17sec (450mm/s^2) deceleration period, taking 0.99seconds to complete one cycle. The average sliding velocity per cycle was 50.65mm/s.

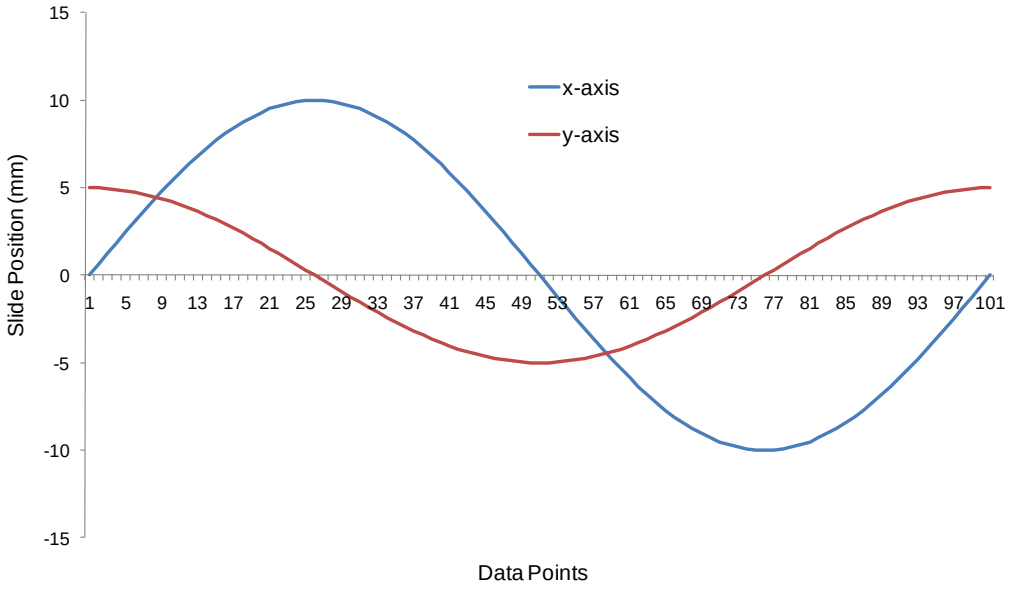

Figure 4-8: Linear slide positions during the elliptical motion cycle; a sine wave with double the amplitude of a cosine wave produced an elliptical wear path with aspect ratio, 2.

The elliptical path was achieved by programming and synchronising a sine wave on the primary axis with a cosine wave on the secondary axis (Appendix 9: Elliptical Motion). Figure 4-8 shows these waveforms, the amplitude of each wave corresponding to the total axis sliding distance divided by two. Primary and secondary linear axes moves of 20mm and 10mm produced an elliptical motion path with an AR of 2. The total length of the elliptical path was approximately 49.67mm. The start-up cycle consisted of a 0.11sec (450mm/s^2) acceleration phase followed by a resultant 50mm/s constant velocity, completing each cycle at a frequency of 1Hz. A "merge" motion command was used to produce continuous sliding between elliptical cycles.

Discretised slip velocities of the linear-reciprocating and elliptical cycles are seen in Figure 4-9. Slip velocity vectors are plotted using the direction and average speed of a point every 40ms throughout the cycle. They serve to highlight the dependence of sliding vectors at the pin-plate interface on motion behaviour. Under linear-reciprocating motion, the slip velocity vectors overlap one another along the principal sliding. To simplify Figure 4-9, only the largest velocity vectors are plotted; 77mm/s back and forth superimposed onto the y-axis.

Under elliptical motion, the discretised slip velocities are shown more clearly. The slip velocities can be multiplied by the discretised time interval to give the discretised displacement, which when plotted sequentially, one after the other (vectors 1-25) form the simplified elliptical wear path constructed from 25 incremental straight lines.

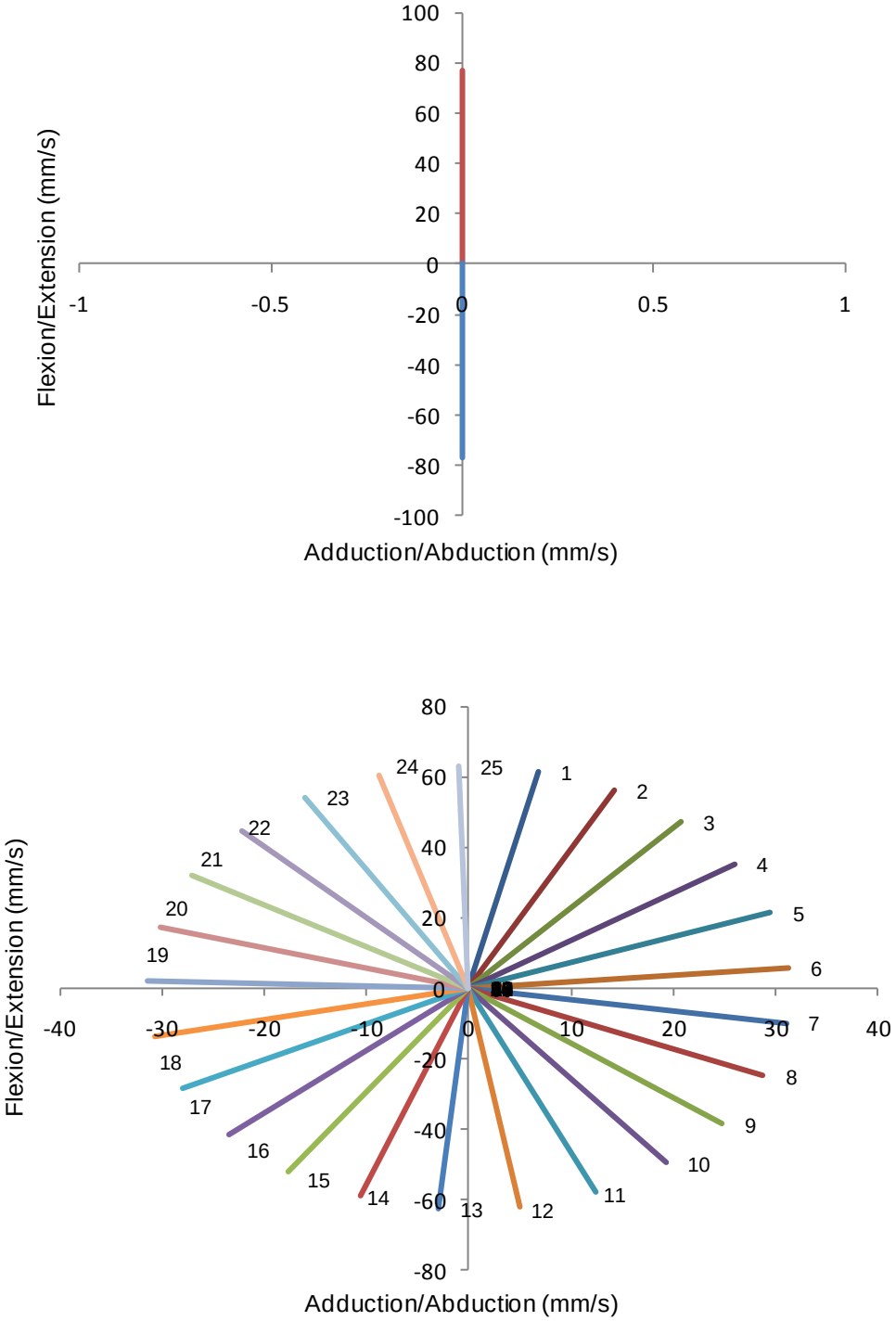

Figure 4-9: Discretised slip velocity vectors for: (above), the maximum linear-reciprocating slip velocity; and, (below) elliptical velocity vectors discretised every 40ms and plotted 1-25.

4.2.6 The Wear Tests

To validate the machine, three orthopaedic polymers of clinical relevance were tested. Four polymer test pins of each material, polytetrafluoroethylene (PTFE), polyacetal (POM), and UHMWPE were subjected to linear reciprocating and multi-directional elliptical motion. The counter-bearings for all tests consisted of medical grade cobalt chrome alloy plates, polished (Buehler, Alpha) to an average femoral implant finish[117] of better than R_a 0.01μm (Zygo, NV100). To account for fluid absorption, two load-soak control pins from each material were loaded in an identical manner to the worn pins. In a second study, +PE pins were worn under the same linear-reciprocating and elliptical motion paths. Sliding parameters for all tests are summarised in Table 4-5.

Material	**Polytetrafluoroethylene**		**Polyacetal**		**-PE**		**+PE**	
Test	Linear	Elliptical	Linear	Elliptical	Linear	Elliptical	Linear	Elliptical
Duration (km)	4	4	51	51	150	150	150	150
Cycles (10^6)	0.8	0.8	1.02	1.02	3	3	3	3
Stroke length (mm)	25.00	-	25.00	-	25.00	-	25.00	-
Cycle circumference (mm)	-	49.67	-	49.67	-	49.67	-	49.67
Av sliding speed (mm/s)	50.65	50.17	50.65	50.17	50.65	50.17	50.65	50.17

Table 4-5: Polymer wear test parameters, where –PE remained unirradiated and +PE had been 100kGy irradiated.

4.3 Raman Spectroscopy

Raman spectroscopy falls within the umbrella of vibrational spectroscopy. Chemical information specific to the sample is deduced from the type of bond vibrations observed under excitation from incident light of specific wavelength. In brief, when light interacts with a molecular bond, photons are scattered. A small percentage of these photons gains or loses a small amount of energy equal to the vibrational energy of the bond. The degrees of freedom associated with each bond in a molecule are discrete (i.e. stretching, twisting and bending are well defined) therefore the detected vibrational energy shift can be used to "fingerprint" a molecule. A molecule may be defined by several different bonds causing several different energy shifts, or Raman shifts to be detected. These are shown on a spectrum, where each peak corresponds to a bond vibration. Raman spectroscopy may be used to infer information about polymer crystallinity, residual strain, degree of oxidation and molecular orientation.

4.3.1 A Crystallinity Study

Crystallinity of UHMWPE is often used to characterise the bulk microstructure. The crystalline domains are commonly found to contribute between 50-70% of the bulk material. Changes in crystallinity ratio (ratio of crystalline to amorphous material) can signify changes in mechanical behaviour[159] and wear resistance[70]. Crystallinity is conventionally determined through thermal analysis using differential scanning calorimetry (DSC). Alternatively, polyethylene crystallinity can be determined through Raman spectroscopy[160-162], see Section 4.4.3. Before Raman could be used with confidence, the technique was verified against the more common DSC in a validation study.

DSC is commonly used to characterise the peak melting temperature and crystallinity of a polymer. A sample scan involves two pans, one containing the sample and an empty control. The DSC heats or cools both pans at a steady programmed heating/cooling rate comparing the energy flow (J/kg) between them. Variation in energy flow arises from the sample phase transitions. For example, the melting transition is an endothermic process requiring heat energy. This energy is called the enthalpy of fusion, shown as negative heat flow in the DSC thermogram (Figure 4-10).

Peak melting temperature and broadness of the melting endotherm (heat of fusion) are indicative of the crystallinity, size and size distribution of crystalline lamellae in UHMWPE. A narrow melting peak at high temperature indicates a sample with a near-uniform distribution of large crystal lamellae.

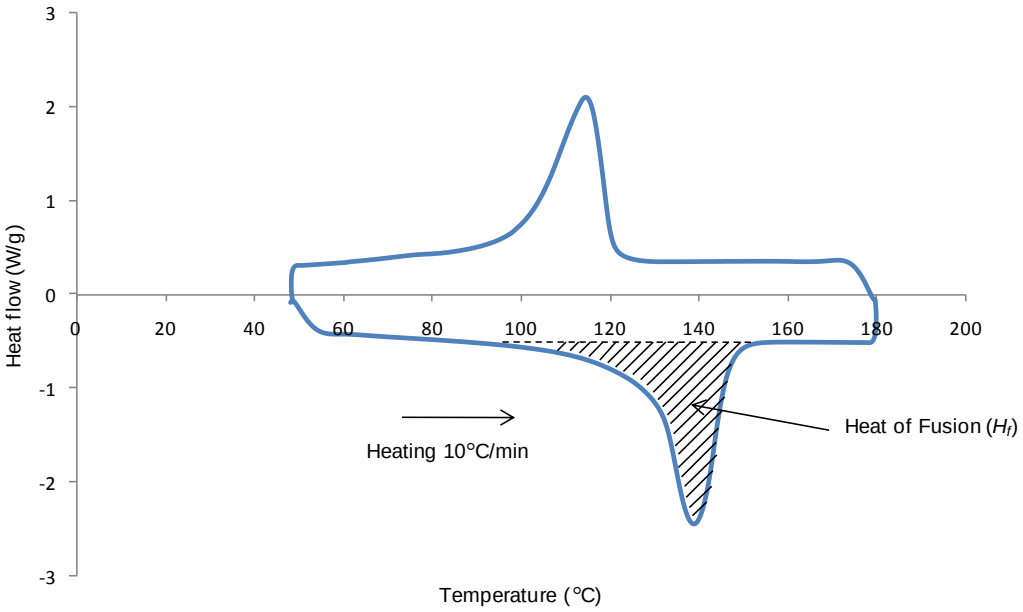

Figure 4-10: DSC endotherm of UHMWPE where endothermic heat flow is shown as negative. The melting transition (hatched domain) requires heat energy input, known as the enthalpy of fusion.

The amount of energy required to change the physical state of UHMWPE from solid to melt is proportional to the percentage crystallinity. The recorded sample enthalpy (ΔH) is compared to that of a polyethylene crystal (assumed to be 100% crystalline) and a ratio between crystalline and amorphous domains can be calculated according to the method of Wunderlich and Cormier[163] (Equation 4-1): where ΔH is the heat of fusion; the amount of thermal energy which must be absorbed or evolved for 1 mole of a substance to change states from a solid to a liquid or vice versa.

$$\%Crystallinity = \frac{\Delta H}{293J/kg}$$

Equation 4-1: Polyethylene crystallinity calculated according to the enthalpy of fusion.

The instrument (Perkin-Elmer Pyris 1) was calibrated using a high purity sample of indium, an element with a specific melting temperature and melting enthalpy. Results from the calibration scan were compared to the indium standard values and the machine adjusted accordingly. Three polyethylene types were analysed, two low density polymer powders (M_w 4,000g/mol and 35,000g/mol) and conventional 1020 UHMWPE (M_w ~$2x10^{-6}$g/mol). Samples were sectioned, weighed (samples <10mg) and placed into small aluminium pans. Three separate scans were run on each polymer, where each thermal scan consisted of one heating and cooling cycle between 50°C and 180°C at a heating rate of 10°C/min. Phase transitions were plotted on a computer displaying the thermal energy in and out of the

sample pan to maintain the programmed heating rate. Polymer crystallinity was calculated according to Equation 4-1 and compared to values calculated using Raman spectroscopy (Equation 4-6).

4.3.2 A Polymer Laminate Study

To characterise the scattering volume of the Renishaw inVia Raman microscope, polymer laminate samples were constructed. Delrin sections (10-28µm thickness) were placed on PMMA and the percentage of scattered PMMA signal with respect to Delrin thickness was recorded. The thickness of Delrin through which no PMMA peaks were recorded was noted as the minimum scattering depth.

Delrin layers were prepared using a microtome (Reichert-Jung Ultracut E) with glass knife and water trough. Sections were picked from the trough and placed onto 3mm thick PMMA blocks. Each laminate composite was left to dry in a dust-free environment before being analysed. A schematic of the method is seen in Figure 4-11.

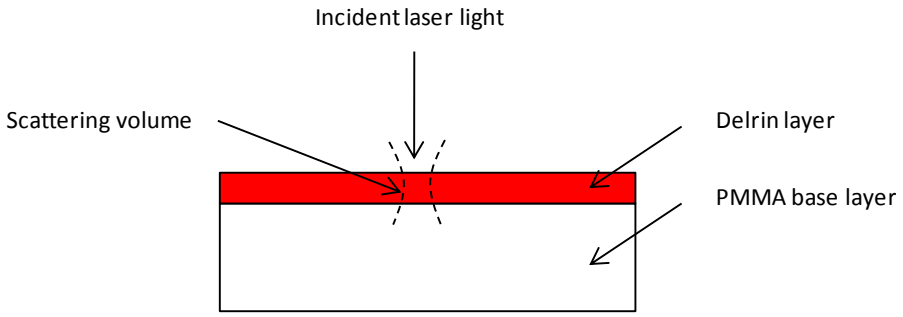

Figure 4-11: Schematic of the polymer laminate test arrangement; Delrin layers of thickness 10-28µm were placed on a PMMA substrate. The Raman laser was focused on the Delrin surface and the proportion of PMMA signal detected was used to approximate the scattering volume of the Raman microscope.

The 785nm excitation laser beam was focused on the top Delrin surface through x20 and x50 objectives. A microscope (Leica) was used to collect the backscattered light in both standard and pseudo-confocal mode. Spectra were collected and compared to that of pure PMMA. Peaks specific to PMMA were noted until the depth of the Delrin was sufficient to completely occupy the scattering volume. This thickness described the scattering resolution of the system. For sub-surface studies, the resolution equated to the smallest increment the objective had to move to ensure new material was probed.

4.4 Measurements

4.4.1 Gravimetric Analysis

Polymer wear was assessed through gravimetric analysis according to Equation 2-9, using a Mettler Toledo XS205 balance with a resolution of ± 0.001mg. Polymer wear factors were calculated according to Equation 2-4. For all tests, the minimum number of wear measurements subsequent to the initial measurement exceeded the ASTM minimum of four. At each downtime, both worn and load-soak pins were washed in an ultrasonic bath in a 1% weight aqueous solution of the detergent Neutracon for 15 minutes, rinsed in an ultrasonic bath filled with de-ionised water and finally dried with lint free tissue[145]. The cobalt chrome plates received similar treatment. Pins were then air-dried in a dust free environment for 30minutes before being weighed. The order in which the pins were weighed was rotated sequentially to ensure the effects of drying had minimal influence on the results. Detailed cleaning protocols are found in Appendix 10: Pin and plate cleaning protocols.

To a first approximation, the number of cycles between gravimetric measurements for each polymer was back-calculated using literature wear factors, the maximum theoretical pin wear volume, average load per cycle and cycle sliding distance.

First consider the wear factors, PTFE is reported to have a clinical value of $3x10^{-5}mm^3/Nm$[164] and conventional UHMWPE a clinical wear factor of $2x10^{-6}mm^3/Nm$[116]. As discussed extensively in Section 3.6, the pin holder design and specimen length limit the amount of pin wear to 2mm. Polymer wear above this threshold would result in stainless steel (the pin holder) wearing undesirably against cobalt chrome (the test plate). The wear volume to cause metal-on-metal sliding is the maximum wear/pin that can be produced from the tribometer and is found by multiplying the pin cross-sectional area by the maximum linear height loss. A maximum theoretical wear volume of $40mm^3$ was calculated ($2 \times \pi 5^2/4$). Such an approximation ignores the effects of polymer creep which might accelerate the onset of metal-on-metal sliding. The theoretical maximum sliding distance, *x*, to prevent metal-on-metal sliding can be approximated from rearranging the Archard wear relationship (Equation 2-4), where, *V* is the wear volume ($40mm^3$), *N* is the average force per cycle (38±1.6N) and *k* is the reported clinical wear factor for the polymer under test (mm^3/Nm).

Should the tribometer produce clinical wear factors, the maximum polymer-on-metal sliding distances for PTFE and UHMWPE were 26.5km and 476km respectively. Actual sliding distances were kept much lower due to the considerable period of time needed to test to these distances, see Table 4-5.

4.4.2 A Crosslink Density Study

Highly-crosslinked UHMWPE was introduced in hip replacements due to its observed decrease in wear (Section 2.7.3). Unfortunately, crosslinking can have detrimental effects on other material properties; crosslinked material may experience a decrease in fatigue crack propagation resistance and in mechanical properties such as ultimate tensile strain and elastic modulus compared to conventional material[92, 93]. Because of these conflicting attributes, the degree of crosslinking is an important property to quantify when developing polymer components.

Elevated crosslink density levels were characterised through swelling experiments according to the ASTM standard for the determination of swell ratio[165]. The swelling ratio, described as the volume of a swollen polymer network divided by the volume of the original unswollen network, indicates the maximum amount of liquid that can be absorbed by a polymer[166].

When UHMWPE is submerged in solvent, the number of crosslinks, or crosslink density, determines the ability of the polymer to either dissolve or absorb the solvent and swell. A more highly crosslinked material will have greater structural integrity and be less prone to dissolution. Hence, swell ratio can be used as a measure of the degree of crosslinking and average molecular weight between crosslinks[167]. A high swell ratio indicates a low crosslink density and a low swell ratio indicates a high crosslink density[111, 136, 168].

The Flory-Rehner equation[167] describes swelling of crosslinked polymers as a function of the Flory-Huggins interaction parameter between the polymer unit and the solvent, X_1, the molar volume of the solvent, V_1, (for xylene 136 cm^3/mole), and the molecular weight between crosslink sites, n.

$$-[ln(1-v_2)+X_1v_2^2] = V_1n\left[v_2^{\frac{1}{3}}-\frac{v_2}{2}\right]$$

Equation 4-2: The Flory-Rehner equation.

Where the swell ratio, S, is the reciprocal of the volume fraction of polymer in the swollen gel, v_2:

$$S = \frac{1}{v_2}$$

Equation 4-3: Swelling ratio.

Substituting Equation 4-3 into Equation 4-2, the crosslink density, X_c (mole/cm^3), can be expressed in terms of the swell ratio as seen in Equation 4-4:

$$X_c = -\frac{ln(1 - S^{-1}) + S^{-1} + X_1 S^{-2}}{V_1 S^{-1/3}}$$

Equation 4-4: Polymer network crosslink density.

The average molecular weight between crosslinks M_c (g/mole) can be calculated where ρ_s is the density of the polymer and X_c is the crosslink density (Equation 4-5).

$$M_c = \frac{\rho_s}{X_c}$$

Equation 4-5: Average molecular weight between crosslinks.

Swelling tests were performed on three specimens (n=3) from both the -PE and +PE groups. Samples cut to approximately 0.05-0.1g were weighed and placed in sheet steel mesh, folded to create a cage. The cage, complete with polymer, was immersed in xylene and left for 24h at 110ºC. Specimens were then removed, dried with lint free tissue to remove excess surface solvent and weighed in the swollen state. Swollen samples were finally left to dry in a vacuum oven, using a dry ice trap to collect the evaporated solvent, until mass equilibrium was reached. Dried samples were weighed to assess the amount of remaining polymer. The cage was particularly useful in containing unirradiated material which showed a greater affinity for dissolution. Crosslink density was calculated according to Equation 4-4.

4.4.3 Crystallinity

Raman spectroscopy was used to measure the crystallinity of UHMWPE. The advantages that Raman spectroscopy offers for the characterisation of UHMWPE crystallinity are threefold. Firstly it is non destructive, with the ability to probe areas of the sample surface, creating a map of data points across the sample. Secondly, it allows intermediate measurements to be gathered or depth profiling to be conducted. Thirdly, it requires little sample preparation. The technique has been used to calculate surface and sub-surface crystallinity of sectioned UHMWPE acetabular cups[169-172].

The internal Raman vibrational band structure of polyethylene is well studied; the 1416cm^{-1} band is associated with CH_2 bending in the orthorhombic crystal phase and the 1296cm^{-1} and broader second peak around 1303cm^{-1} is associated with amorphous CH_2 twisting vibrations[160, 162]. The bond vibration specific to UHMWPE is seen in Figure 4-12.

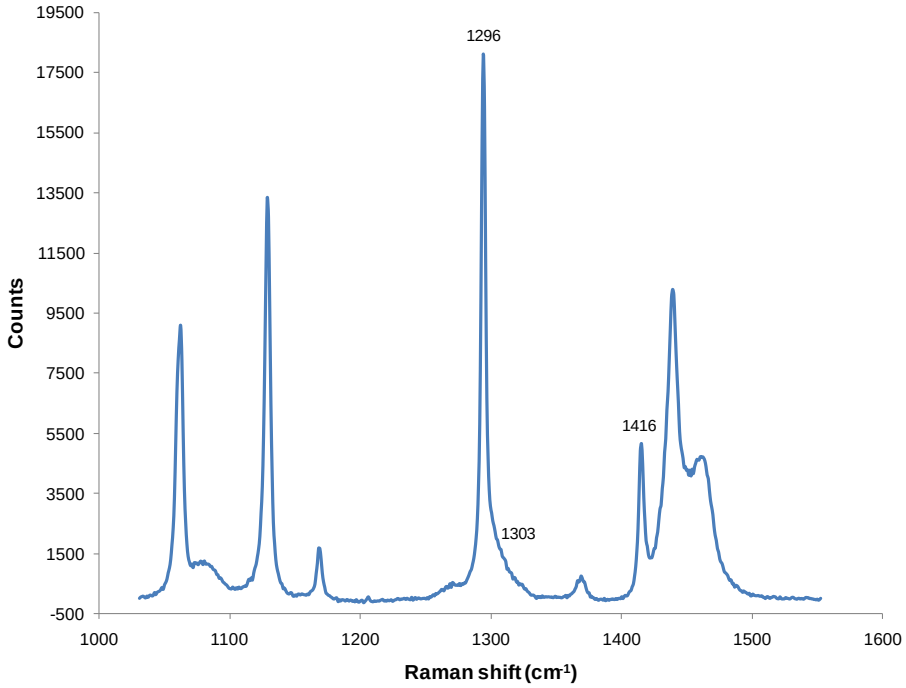

Figure 4-12: Vibrational band structure of UHMWPE taken using the inVia Raman microscope; normal mode, 10% laser power, 10sec acquisition time, x50 objective. Baseline removed and offset for clarity.

The ratio of these band intensities is indicative of polyethylene crystallinity (Equation 4-6) [162].

$$\%Crystallinity = \frac{I_{1416}}{[(I_{1296} + I_{1303})0.46]}$$

Equation 4-6: Raman bands used to calculate polyethylene crystallinity according to Strobl and Hagedorn[162].

Intensity of the Raman peaks was calculated using InVia Wire® curve fitting software. This automated routine uses Gaussian-Lorentzian curves to closely approximate the actual spectra. To converge on the broader shoulder at 1303cm^{-1} the profile was approximated using two Gaussian-Lorentzian curves; one directly under the 1296cm^{-1} peak and one offset to skew the final peak profile.

A Renishaw InVia system was used to measure Raman spectra of control, load-soak, worn unirradiated and worn highly crosslinked UHMWPE pins at room temperature. A schematic of the inverted arrangement is seen in Figure 4-13. Excitation of Raman bands was achieved by a 785nm, ~30mW laser, focused through a x50 objective. The system was configured as follows: spectra frequency range, 800-1700cm^{-1}, spectra resolution, 3cm^{-1}, acquisition time, 10secs and number of repeats, 6. Spectra were gathered in confocal mode to minimise the scattering volume. The depth resolution or scattering volume of the system was experimentally found to be less than 10µm (see Section 5.3.2). Depth profiling was

performed by focusing the laser beam at increasing depth beneath the surface. Ten scans were taken at each depth. Scattering volume (V_s) was approximated as a cylinder of length (L) ~ 10µm, with a cross-section equal to the focused laser spot (d) ~1µm,

$$V_s = \left(\frac{\pi d^2}{4}\right) L = 7.85\mu m^3$$

Equation 4-7: Raman scattering volume.

On each pin and at each scanning depth (surface, sub 12.5µm, sub 25µm and sub 37.5µm), 10 spectra were recorded. Therefore the volume of material from each pin contributing to the crystallinity calculation per depth was ~78 µm^3. The average scattering volume from four worn pins was ~314 µm^3 per depth. UHMWPE lamellae are typically on the order of 50nm x 1µm, depth and length respectively. The ten scans performed will therefore include a substantial population of crystals in an effort to statistically represent the bulk material.

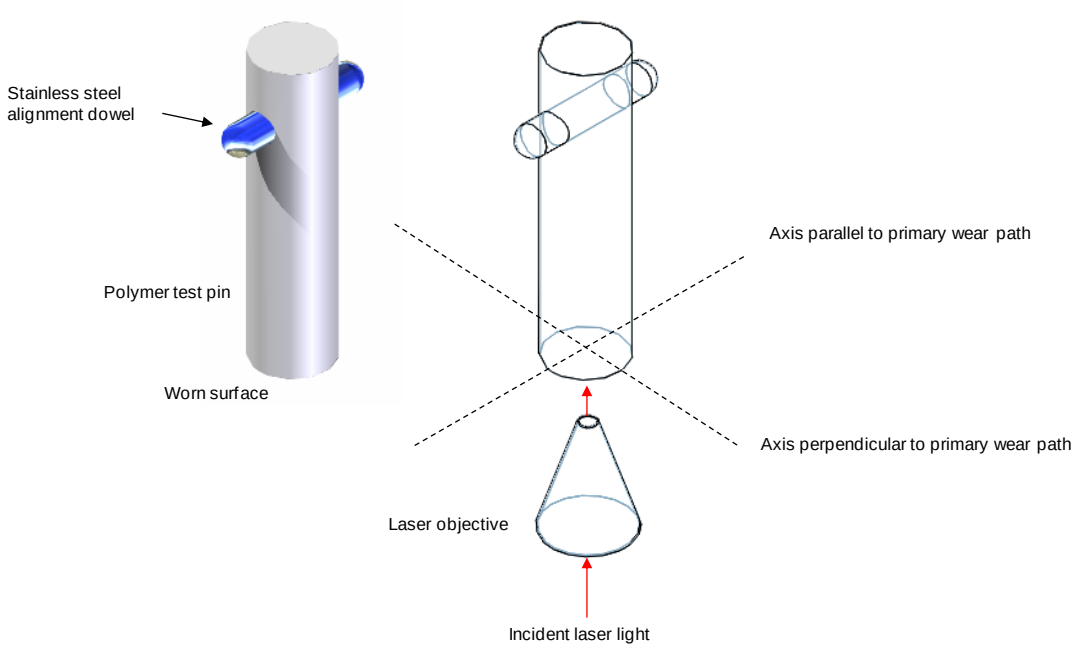

Figure 4-13: Schematic of the test pin mounting arrangement in the inverted Raman microscope.

4.4.4 Residual Strain

Plastic deformation of surface asperities in response to load and frictional sliding are thought to cause strain accumulation in the near-surface UHMWPE material. Sufficient levels of strain, to cause a critical level of damage may promote the release of wear debris[65]. In practise, damage in the near-surface of UHMWPE is difficult to quantitively measure.

Peak broadening of the Raman spectra has recently been used to relate applied load and residual strain within UHMWPE tensile test specimens[173, 174]. Kyomoto *et al.*, used

UHMWPE dog bone specimens, uniaxially strained in tension to precise levels until failure (0%-break), to investigate the peak broadening phenomenon[173]. An increase in the full width at half maximum (FWHM) of the Raman band located around 1129cm^{-1} (symmetric C-C stretch mode) was found to be proportional to the level of applied strain and independent of crosslink density; increased levels of strain produced peak broadening in all samples regardless of irradiation dose (for gamma irradiation doses tested, 25-100kGy).

To confirm the findings of Kyomoto *et al.*, a preliminary study was conducted using conventional GUR1050 UHMWPE machined into tensile test dog bone specimens (ASTM type IV). The specimens were strained at a rate of 5mm/min while subject to room temperature compressed air jet cooling in the Medical and Polymers Laboratory, Berkeley, USA.

Raman spectroscopy (1129cm^{-1} peak broadening) was performed on material cut from the gauge section of unstrained (but machined) controls, and gauge sections previously strained to 400% and failure (~500% engineering strain). Raman work was conducted in the Orthopaedic Engineering Laboratory, Edinburgh. Test specimens were stored frozen where possible.

FWHM ~1129cm^{-1} peak broadening was found to coincide with increasing levels of uniaxial strain; control, 5.19±0.10cm^{-1}; 400% strain, 5.73±0.12cm^{-1}, and at break, 5.83±0.01cm^{-1} (Figure 4-14). Unfortunately the numbers of samples tested were insufficient to make pronounced observations, however the peak-broadening trend appeared consistent with Kyomoto *et al.*.

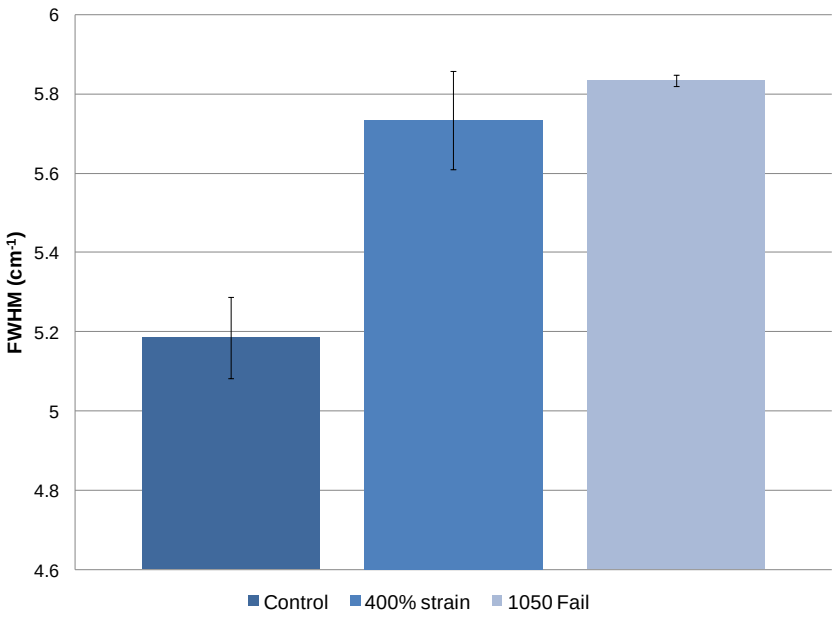

Figure 4-14: Mean full width at half maximum (~1129cm^{-1}) values of gauge GUR1050 strained specimens, where error bars represent one standard deviation.

Raman peak broadening was subsequently measured on worn surfaces and sub-surfaces of unirradiated and highly crosslinked UHMWPE pins. Broadening was compared to that of the load-soak pins and control material. Control surfaces were microtomed (Reichert-Jung Ultracut E) to minimise the effects of residual damage inherent in post-machined material.

4.4.5 The Scanning Electron Microscope

Imaging polyethylene microstructure is complex due to the small length scales associated with the regions of interest and the difficulty in imaging contrast between amorphous and crystalline domains. Conventional techniques such as optical microscopy are not sufficient. These techniques image only the surface of the bulk material, often with no contrast between domains. However, the ability to view the polyethylene microstructure serves to complement and support non-destructive Raman spectroscopy, enhancing the breadth of analysis available.

For the qualitative assessment of surface topography and to gain insight into the friction oriented response of crystalline lamellae scanning electron microscopy (SEM) was used. An SEM pilot study of etched UHMWPE samples was carried out in the School of Geosciences, using a Philips L30CP SEM. Unfortunately, this machine proved poor at providing good quality images of the UHMWPE microstructure (Figure 4-15). Instead, the School of Biological Sciences' field emission scanning electron microscopy (FE-SEM Hitachi S-5000) was used. The field emission microscope was capable of imaging with improved spatial

resolution, resolving finer surface details at higher magnification (magn.). UHMWPE images were taken with a range of magnifications up to x40k magn., although at x20k magn. the smallest length dimension of the crystalline lamellae (range 10-100nm) was easily resolvable on etched surfaces (Figure 4-16).

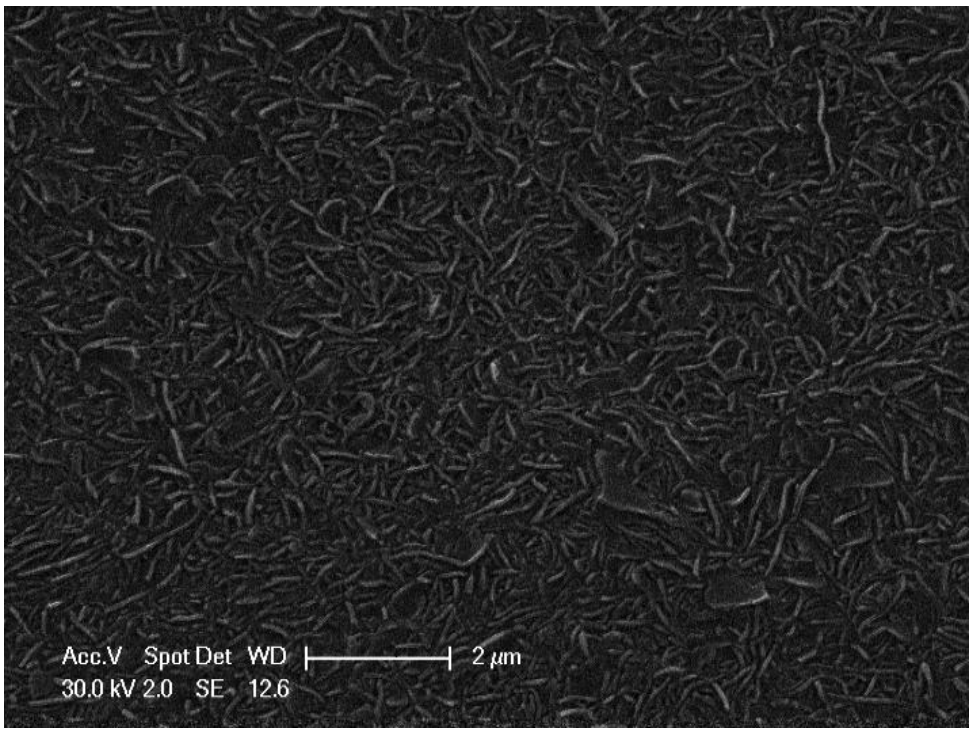

Figure 4-15: SEM image with poor resolution and contrast, taken using a Philips L30CP.

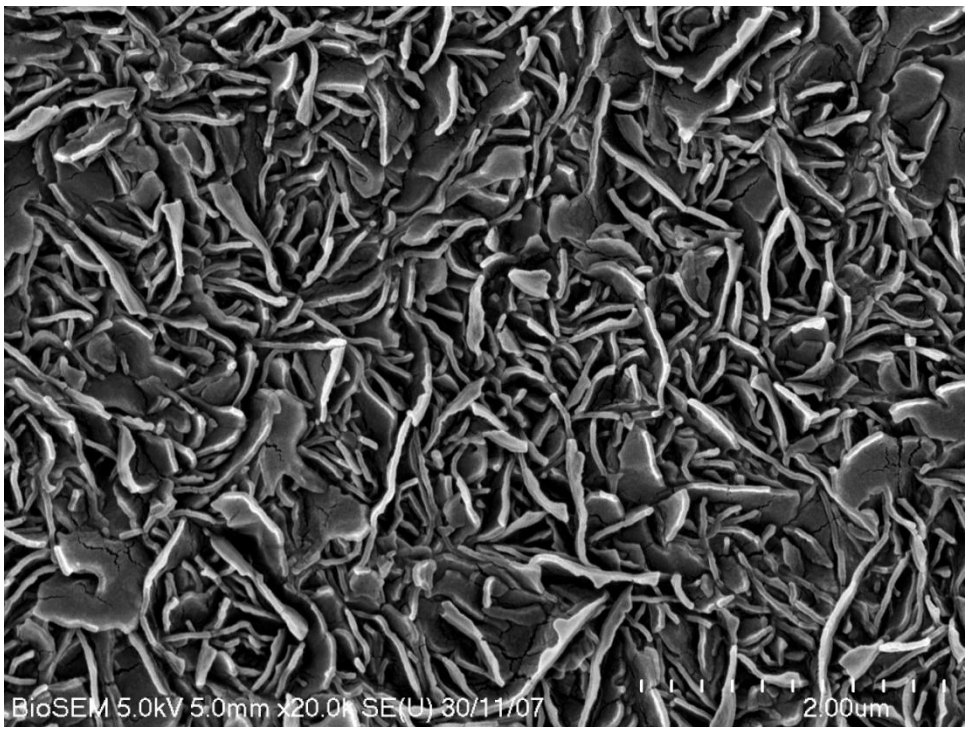

Figure 4-16: FE-SEM image with improved spatial resolution and good contrast, taken using a Hitachi S-5000.

To maximise the information attainable from one UHMWPE test pin under the electron microscopy, highly specific sample preparation methodologies were applied. Following three million wear cycles, worn pins were sectioned in half using a scalpel. This permitted separate imaging of topography and microstructure (Figure 4-17). Prior to imaging, all samples were washed ultrasonically in a Neutracon solution and wiped with acetone before being gold sputter coated to a depth of approximately 6nm.

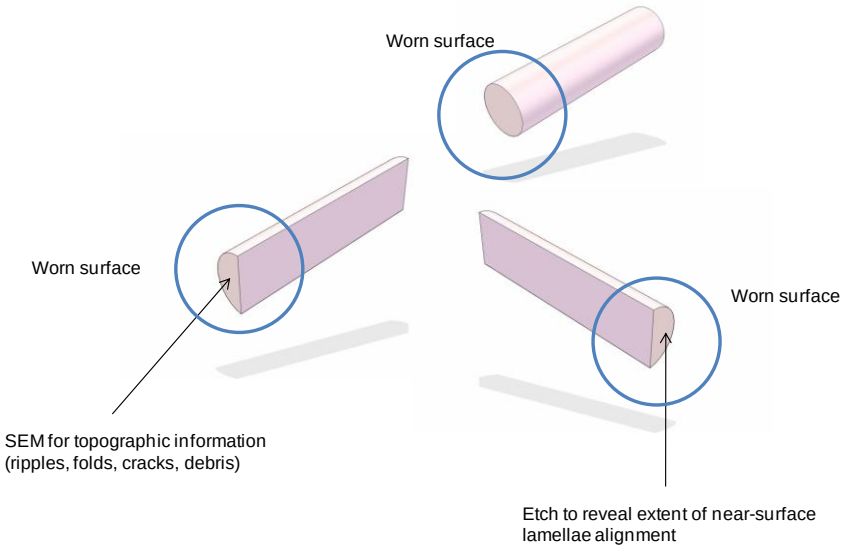

Figure 4-17: Worn pin surfaces were sectioned longitudinally to permit topography and morphology studies.

To reveal the lamellae microstructure, oxidising acids have historically been used to etch the chemically resistant semi-crystalline polyethylene surface[69]. The acid preferentially diffuses into and attacks the disordered less tightly packed amorphous domains, leaving the crystalline tightly packed chains within the lamellae proud of the surface[175]. A less oxidizing acid permanganic etchant has been since shown to reveal lamellar structures with more detail[176, 177].

Despite the ability to image crystal domains and produce informative microstructural images from SEM, acidic etching of worn polymer surfaces has been used by few groups. The majority of etched UHMWPE work has been conducted in the Medical Polymers Group, the University of California at Berkeley[70-72].

A pilot study on the development of UHMWPE microstructure in response to plastic strain was carried out jointly with researchers in the Medical Polymers Group, the University of California at Berkeley (Appendix 11: Lamellar Orientation in Strained UHMWPE). The Berkeley studies served to complement further characterisation work on etchant behaviour at increasing levels of UHMWPE strain. Tensile test dogbone specimens of GUR 1020 were uniaxially strained at 0%, 25%, 100%, 240%, 400% engineering strain to failure, the gauge sections removed, then subject to a number of analysis techniques; DSC, SEM and Fourier Transform Infrared spectroscopy. Etching was carried out according to the method of Olley and Bassett[176] and crystallinity of the gauge sections was determined from DSC.

In a separate study, the effect of etchant penetration on unstrained UHMWPE with respect to submersion period (10-60mins) was also investigated. The experimental protocol and etch recipe is detailed in Appendix 12: Potassium permanganate etch recipe. The results are presented in Section 5.4.

5 Results

Summary

A programmable multi-directional motion and dynamic load tribometer has been used to investigate wear induced ultra-structural change in both unirradiated (-PE) and highly crosslinked (100kGy) UHMWPE (+PE).

To validate the machine, three orthopaedic polymers of clinical relevance; polytetrafluoroethylene, polyacetal, and UHMWPE were subjected to linear-reciprocating and novel elliptical motion paths under a Paul-type load profile. All three polymers showed higher wear factors under elliptical motion by up to 2 orders of magnitude, in agreement with values found in explanted acetabular sockets. The UHMWPE elliptical wear factor was comparable to that reported for clinical, where $k_{elliptical} = 1.56x10^{-6}$ mm^3/Nm. Wear rankings concurred with the ranking defined in the ASTM standard; PTFE>>POLYACETAL≥ UHMWPE. However, only under elliptical motion were the wear rate ratios comparable in magnitude to published clinical data.

To investigate surface anisotropy in -PE and +PE, linear-reciprocating and elliptical wear paths were applied. Following three million elliptical cycles, crosslinking reduced wear by up to 92%. Under reciprocating motion, mean steady state wear of -PE and +PE groups was not significantly different (t-test p=0.65). Raman spectra indicated a de-crystallisation zone in the near surface region of -PE and +PE reciprocating pins. This was attributed to large strain development in conjunction with slow lamellar removal and renewal of new surface material in the lower wearing specimens. SEM images of fragmented lamellae supported this observation.

5.1 Overview of Chapter

Results are presented in the order they appear in the previous chapter. The validation study results are presented first. Secondly, Raman crystallinity results are compared with differential scanning calorimetry enthalpy curves and the Raman z-depth resolution is determined experimentally from a polymer laminate study. Finally, wear rates of -PE and +PE are compared along with surface morphology and sub-surface microstructure images.

5.2 The Validation Wear Study

5.2.1 Polytetrafluoroethylene

The effect of motion path on wear rate is seen in Figure 5-1. Sliding motion significantly influenced the rate of wear; elliptical motion resulted in faster material removal than pins subjected to linear reciprocating motion. Little or no wear-in was observed under either motion path. All PTFE pins exhibited an approximately linear relationship between wear volume and sliding distance. The average wear volume of the four load and motion specimens for both motion groups showed good linear correlation between sliding distance and wear volume; R^2=0.91 and R^2=0.98 for linear and elliptical wear respectively.

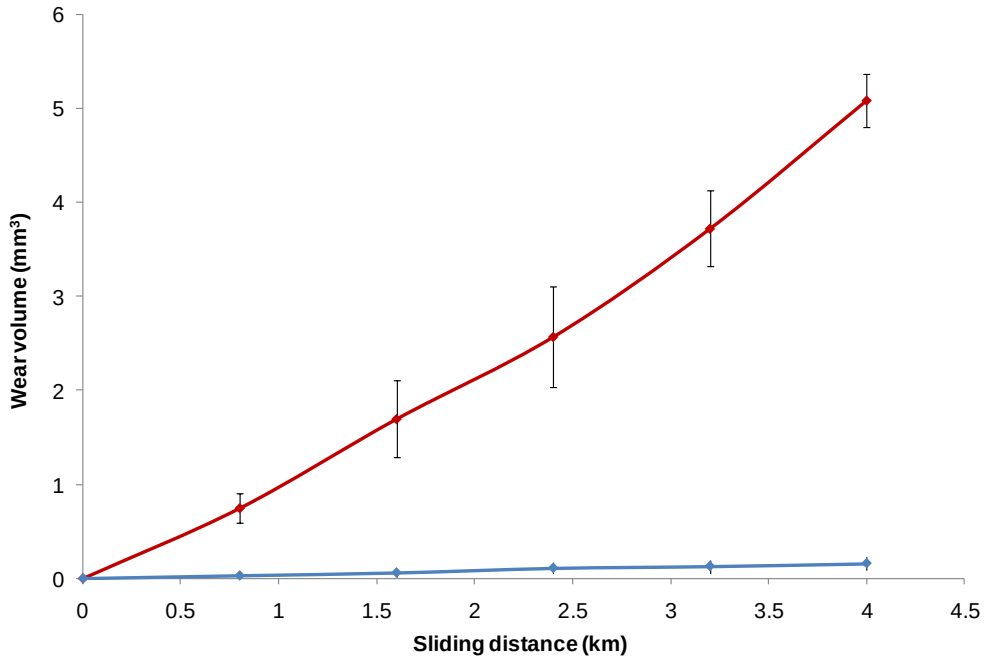

Figure 5-1: Mean PTFE wear in response to elliptical motion (red) and linear reciprocating motion (blue). Lines are shown as smoothed point-to-point. Error bars represent one standard deviation.

The linear relationship permitted average steady-state wear to be extrapolated and presented as volume of material lost per million cycles (mm^3/million). One million cycles was not run experimentally as the high wear experienced under multi-directional motion would quickly

result in the stainless-steel pin holder sliding against the cobalt-chrome plate. A wear rate (± S.D) of 3.41±2.94mm^3/million and 63.58±3.55mm^3/million under linear-reciprocating and elliptical motion respectively was calculated.

To normalise the wear volume with respect to applied load and total sliding distance, a steady-state wear factor was calculated (Section 2.4.2.5). The wear factor under elliptical motion, 33.84±1.19x10^{-6}mm^3/Nm, was an order of magnitude greater than the reciprocating wear factor, 1.84±1.60x10^{-6}mm^3/Nm.

Linear penetration rates are calculated according to Section 2.6.4. Elliptical motion produced penetration rates an order of magnitude greater than that under linear-reciprocating motion; 3.17±0.18mm/million and 0.17±0.15mm/million respectively. The pin holder restricted the free length of polymer to 2mm (the unworn 20mm PTFE pin protruded 2mm beyond the stainless steel holder). Consequently, the maximum number of sliding cycles for pins to be worn back to the level of the holder under elliptical motion can be approximated as 628930 cycles (2/3.17x1000000). This is equivalent to a sliding distance of 31km, using a cycle sliding distance of 50mm (628930x50) and is in good agreement with the maximum predicted sliding distance of 26.5km based on a wear factor of 30x10^{-6}mm^3/Nm (Section 4.4.1).

Wear under linear reciprocating motion was lower than expected. Two CoCrMo plates in this group showed evidence of polymer transfer (Figure 5-2). The low wear behaviour may be attributed to PTFE sliding on a thin layer of PTFE. Table 5-1 summarises the PTFE wear results.

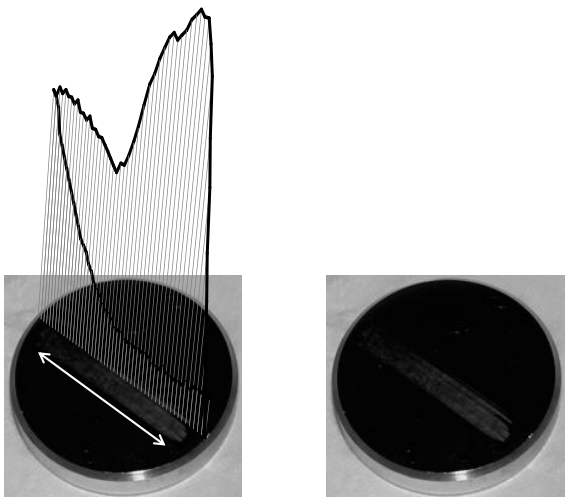

Figure 5-2: Photograph of PTFE transfer film with; (a) superimposed load profile indicating the film to be particularly evident under the heel-down portion of the dynamic load cycle; (b) the raw image, plate diameter 36mm.

	Linear	Elliptical
Volumetric wear (mm^3/million) (±S.D)	3.41±2.95	63.58±3.55
Linear penetration (mm/million) (±S.D)	0.17±0.15	3.17±0.18
Wear factor x 10^{-6} (mm^3/Nm) (±S.D)	1.84±1.60	33.84±1.19

Table 5-1: PTFE steady-state wear behaviour.

5.2.2 Polyacetal

Under linear reciprocating sliding the average wear factor during wear-in (a steeper average wear gradient was apparent during the first15km of sliding) was an order of magnitude larger than the steady-state wear factor; $22.04\pm10.79\text{x}10^{-6}mm^3/Nm$ and $0.23\pm0.29\text{x}10^{-6}mm^3/Nm$ respectively. Linear penetration was calculated according to the method used in Section 5.2.1. The initial wear rate produced an average linear penetration rate 94-fold higher than that under steady-state conditions; 1.87±1.13mm/million cycles and 0.02±0.02mm/million cycles respectively.

Elliptical sliding results are discussed in greater detail than the reciprocating cohort due to the discovery of third body debris in the test lubricant (Figure 5-3). Initial wear of all four pins was negligible. Following the first downtime where pins were removed, cleaned, dried and weighed, the wear rate of three pins increased substantially (Figure 5-3(i)). Lubricant replenishment during the second downtime revealed metallic debris in three of the open-topped chambers, corresponding to the high-wear pins. Metallic debris was generated by fretting wear (micro-motion) between the stainless steel pin-holder and the aluminium loading arm. Micro-movement of the pin holder was caused by friction at the pin-plate interface. This induced a moment which encouraged motion to develop within the sliding tolerance of the pin holder barrel and loading arm bore. Debris entered the test chambers from above, providing an explanation for the dramatic increase in wear in three of the four pins. Further micro-motion between pin-holder and loading arm was prevented using a second lock-nut to secure the height adjustment screws more tightly. Subsequent to this small revision no debris was observed in the test lubricant. Note that the wear rate of pin one remained approximately constant throughout the test duration.

Following the second downtime, two of the three break-away pins returned to a lower wear rate, similar to the initial wear rate and remained at this steady-state for the remainder of the test (the wear gradients were similar to the unaffected pin). The return to steady-state wear was attributed to the second pin and plate cleaning protocol which removed debris that had previously remained on the samples or in the chamber following the first downtime. However, one pin remained in a breakaway state of high wear, only receding after a sliding distance of 34km; the wear rate decreased to a steady-state value approaching those of the

remaining three specimens (Figure 5-3(ii)). For the "high wear" pin it seems logical to explain the delayed return to low steady-state wear by the continued presence of metallic debris particles; finally removed after the fourth gravimetric downtime.

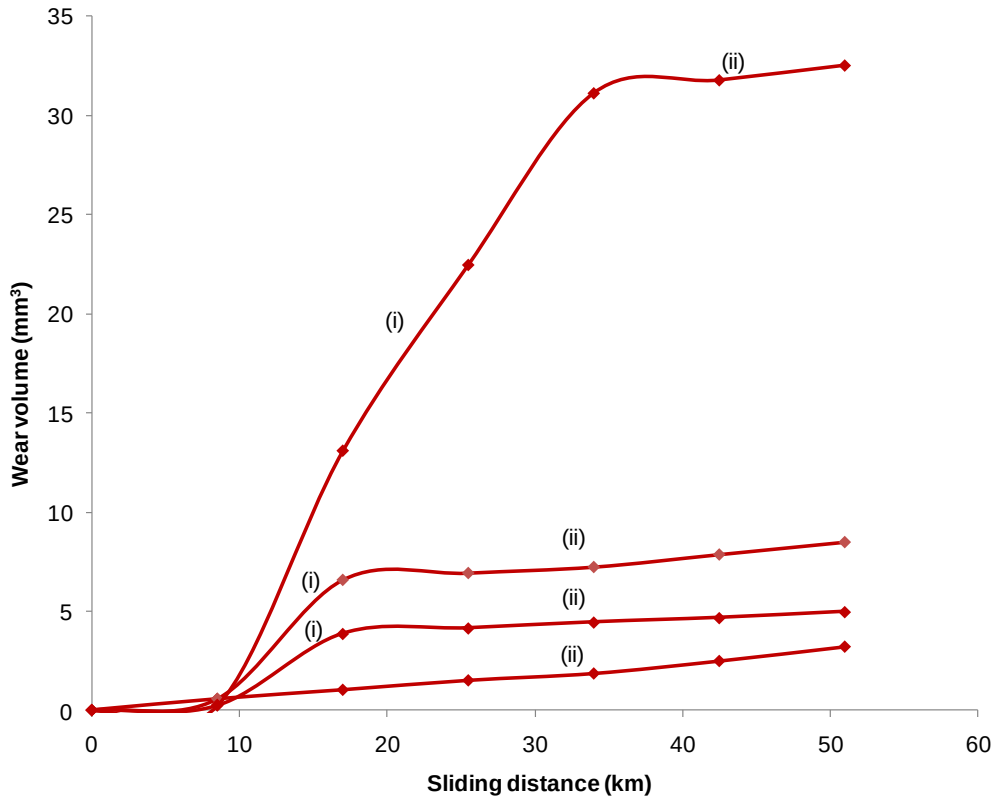

Figure 5-3: Wear graphs of the four polyacetal pins under elliptical motion where; (i) accelerated wear attributed to metallic debris in the contact zone; (ii) pin wear returned to that of the steady-state wear rate once the debris had been removed. Lines are shown as smoothed point-to-point. Error bars are absent due to the close grouping of gravimetric readings for each pin at each weighing interval.

The average steady-state volumetric wear was calculated from the mass of material removed excluding the high-wear regions. A value of 3.84±0.71mm^3/million was extrapolated. This was an order of magnitude greater than the equivalent steady-state rate under linear reciprocating motion (0.43±0.55mm^3/million). The average wear factor calculated during the initial sliding period (within the first 8.5km of sliding) was similar to the steady-state value; 1.27±0.58x10^{-6}mm^3/Nm and 1.28±0.33x10^{-6}mm^3/Nm respectively. Linear penetration under elliptical motion was an order of magnitude greater than under linear reciprocating motion. Polyacetal wear behaviour is summarised in Table 5-2.

	Linear	Elliptical
Volumetric wear (mm^3/million) (±S.D)	0.43±0.55	3.84±0.71
Linear penetration (mm/million) (±S.D)	0.02±0.02	0.19±0.04
Wear factor x 10^{-6} (mm^3/Nm) (±S.D)	0.23±0.29	1.28±0.33

Table 5-2: Polyacetal steady state wear behaviour.

5.2.3 Ultrahigh Molecular Weight Polyethylene

The effect of motion path on wear is seen in Figure 5-4. The blue plots represent wear under linear reciprocating motion (n=4), red lines represent elliptical wear (n=4). Linear motion produced little discernable wear, 0.09±0.04mm^3/million cycles. The steady-state wear factor for the group was 0.038±0.004x10^{-6}mm^3/Nm. The irregular accelerated wear rates at (i) and (ii) are a result of low lubricant levels. Wear factors associated with these breakaway periods were two orders of magnitude greater than the steady-state lubricated sliding wear factor; 2.34x10^{-6}mm^3/Nm and 1.46x10^{-6}mm^3/Nm at (i) and (ii) respectively.

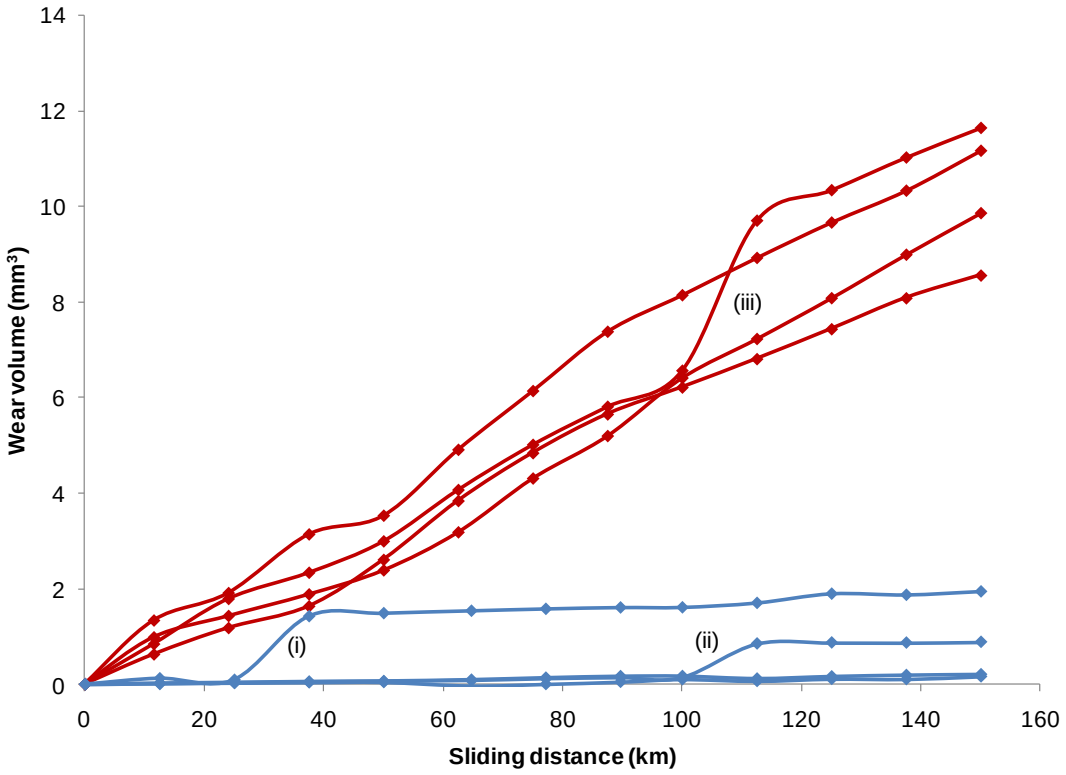

Figure 5-4: Wear graphs of the four UHMWPE pins under elliptical (red) and linear reciprocating motion (blue). Lines are shown as smoothed point-to-point. Error bars are absent due to the close grouping of gravimetric readings for each pin at each weighing interval.

The introduction of a secondary motion axis caused greater material removal. The average volumetric wear rate (±S.D) was 3.44±0.46mm^3/million elliptical cycles. The steady state wear factor was 1.56±0.21x10^{-6}mm^3/Nm; two orders of magnitude greater than that under reciprocating motion. At Figure 5-4(iii), a breakaway occurred and the pin specimen wore more rapidly. This was caused by a drop in lubricant level, the result of a faulty sensor. A larger than average wear factor of 5.6x10^{-6}mm^3/Nm was calculated during this high-wear period. Replacing the sensor and restoring the serum level returned the wear gradient to that of the other three pins and the wear factor returned to within the steady-state range.

Both groups showed good linear correlation between sliding distance and average wear volume, R^2=0.99 and R^2=0.92 for elliptical and linear wear respectively (Figure 5-5). The occurrence of constant UHMWPE wear has been suggested important when evaluating the clinical relevance of an *in vitro* test[178]. The constant wear rates observed herein serves to support the tribological conditions applied by the Edinburgh tribometer.

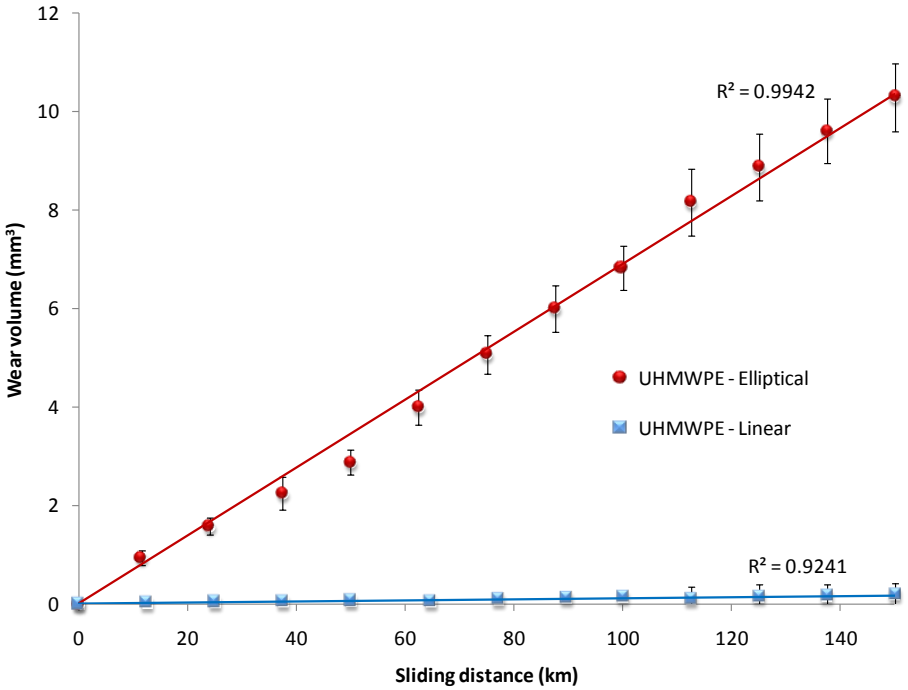

Figure 5-5: Each wear graph is plotted using the mean wear rate of the four pins shown in Figure 5.4. Both groups showed good linear correlation between sliding distance and wear volume. Error bars represent one standard deviation. Note, the directional dependence of UHMWPE wear is stark.

Furthermore, ASTM F732-00 states a UHMWPE clinically relevant linear penetration range should fall between 0.07–0.2mm/million cycles[145]. Under elliptical motion the mean linear penetration rate was found to be 0.17±0.03mm/million which is in good agreement. The linear wear removal of pin material over the test period is seen in Figure 5-6.

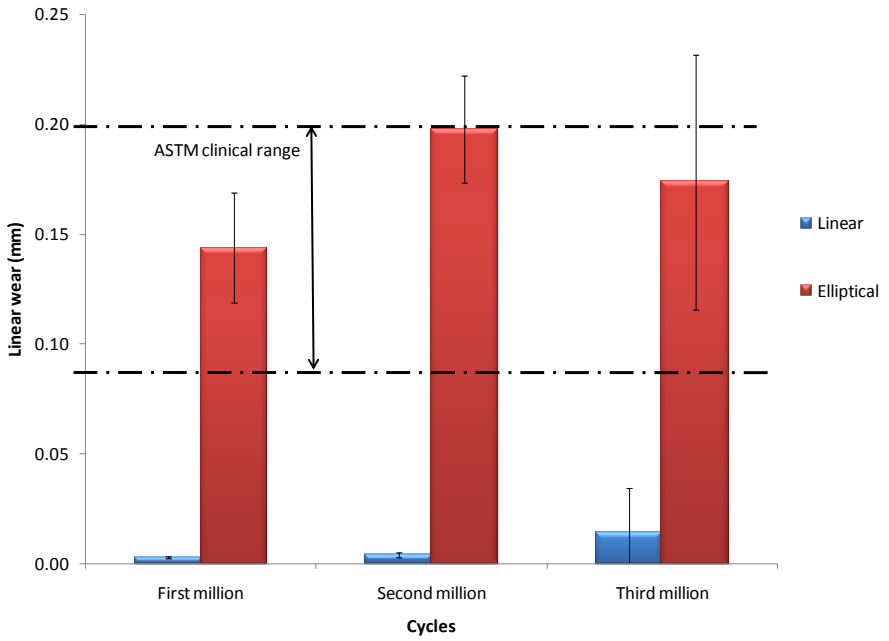

Figure 5-6: Linear removal of UHMWPE test pins attributed to each one million cycle period. Error bars represent one standard deviation.

Optical microscopy revealed worn linear reciprocating surfaces to be consistently characterised by highly textured abrasive mechanisms such as ploughing and scratching parallel to the sliding direction (Figure 5-7a). Surfaces subjected to elliptical motion appeared to be more highly polished and burnished (Figure 5-7b). Machine marks remained clearly visible on load-soak pins (Figure 5-7c).

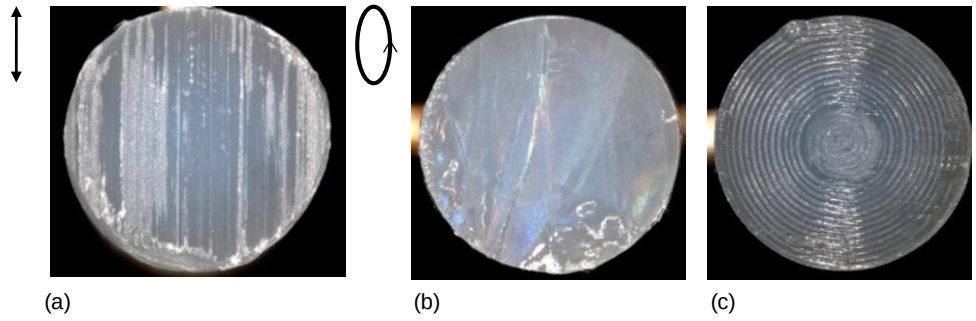

Figure 5-7: Optical images of 5mm diameter UHMWPE pins following 3 million cycles of (a) linear reciprocating wear; (b) elliptical wear; (c) load-soak control. Wear path schematics shown where appropriate.

Parallel ripples of wavelength typically between 1-2µm and amplitude ~30nm were imaged on the more rapidly wearing elliptically worn pins (Figure 5-8). Elliptically worn surfaces were found to have an arithmetic mean surface roughness approximately, S_a 0.11µm.

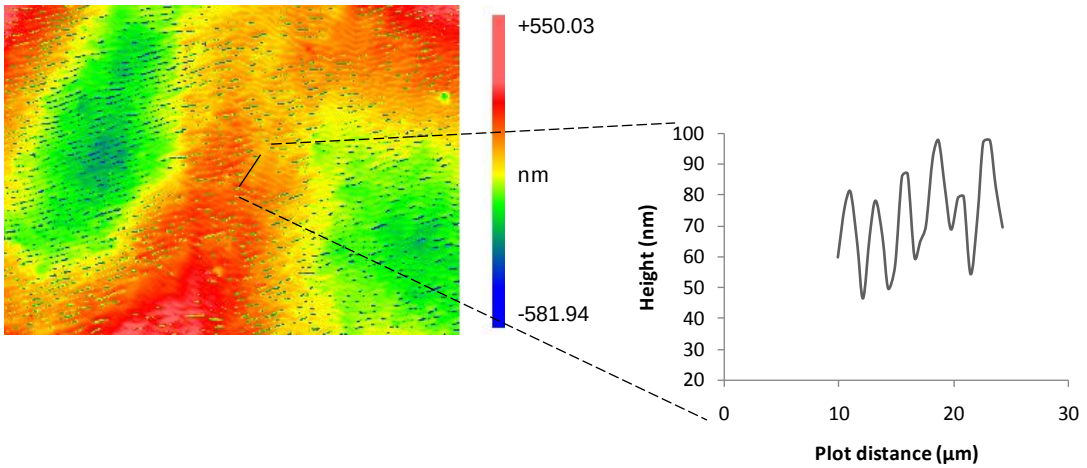

Figure 5-8: Zygo contour plot showing ripple morphology observed on -PE surfaces worn in an elliptical manner; scan area 176µm x 134µm. The line plot represents a 2D profile with wavelength typically between 1-2µm and amplitude ~30nm.

The ripple morphology imaged readily under multi-directional motion was absent on the low-wearing reciprocating surfaces. Instead, ploughing and cutting marks tended to support the abrasive mechanisms first observed at low magnification (Figure 5-7a). Scratches and raised material adjacent to the scratches were consistently imaged parallel to the sliding direction (Figure 5-9). Despite the aggressive appearance of these features, the arithmetic mean surface roughness (S_a) 0.051µm, was an order of magnitude lower than the initial unworn mean, S_a, 0.83µm. This was attributed to the gradual removal of surface machining marks.

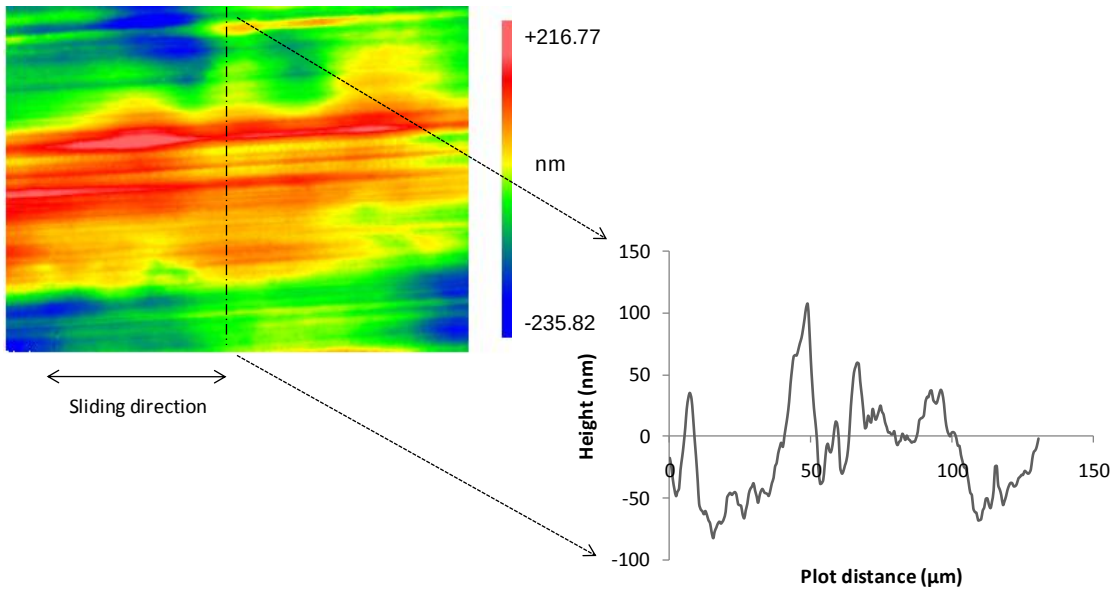

Figure 5-9: Zygo contour plot of -PE worn under linear reciprocating motion; scan area 176µm x 134µm. Surfaces typically showed abrasive markings parallel to the sliding direction.

5.2.4 Wear Ranking

The calculated wear factor for UHWMPE under reciprocating motion was two orders of magnitude lower than both elliptical and clinical (Table 5-3). This was consistent with previous literature findings. For PTFE and Delrin pins subjected to linear reciprocating motion, the wear factors were one and two orders of magnitude lower than those pins under elliptical motion.

	Wear factor (x 10^{-6} mm^3/Nm)		
Material	**Reciprocating**	**Elliptical**	**Clinical**
PTFE	1.1	36	37[164]
Polyacetal	0.069	1.4	5.4[179]
UHMWPE	0.029	1.6	2[116]

Table 5-3: Mean wear factors for PTFE, Polyacetal and unirradiated UHMWPE.

The ASTM recommended wear ranking of PTFE >> Polyacetal ≥ UHMWPE was achieved under both motion paths (Table 5-4). Only the elliptical path produced wear factors and penetration rates similar to published clinical studies supporting the importance of open wear paths in pin-on-plate studies.

	Mean penetration depth (mm/million cycles)		
Material	**Reciprocating**	**Elliptical**	**Clinical (range)**
PTFE	0.37	3.17	4 (2-6)[1]
Polyacetal	0.01	0.19	0.8 (0.1-3)[179]
UHMWPE	0.003	0.18	0.15[115]

Table 5-4: Mean penetration rates for PTFE, Polyacetal and unirradiated UHMWPE.

5.3 The Raman Microscope

5.3.1 Thermal Analysis

Crystallinity results from Raman spectroscopy and DSC are seen in Figure 5-10. For all polymer groups DSC showed consistently less spread about the mean values, although larger variation in Raman scattering was not statistically significant (t-test $p>0.05$). Good agreement between the two techniques is encouraging although the small sample size makes it difficult to call on statistical methods with certainty. The largest difference in mean crystallinity came from the analysis of powder 2; 37.32±1.77% and 34.09±3.55% using DSC and Raman respectively.

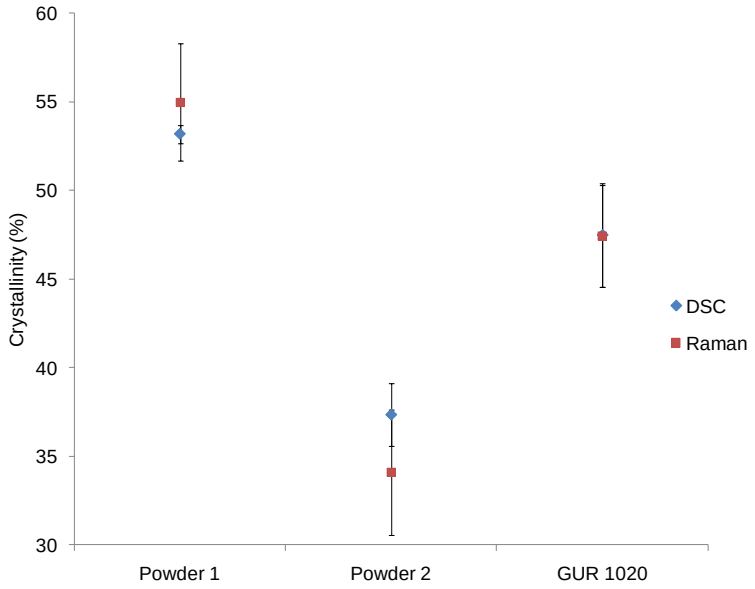

Figure 5-10: Mean polymer crystallinity measured using DSC and Raman spectroscopy. Error bars represent the standard deviation.

5.3.2 Scattering Depth

The reader is referred back to Section 4.3.2 for information regarding the polymer laminate sample nature. Raman spectra for pure PMMA and Delrin are seen in Figure 5-11. A composite spectrum consisting of Raman scattered from both polymers is shown in the middle scan. The composite spectrum is collected when the focusing depth of the system is greater than the thickness of the Delrin top layer. Spectra were collected from both standard and pseudo-confocal apertures using x20 and x50 objectives. Raman shift specific to PMMA at 811cm^{-1} (relating to CH_3 rocking[180]) and that for Delrin at 917cm^{-1} (relating to the symmetric O-C-O stretch) were normalised at each Delrin thickness (10µm-28µm) and compared to the intensity of pure PMMA.

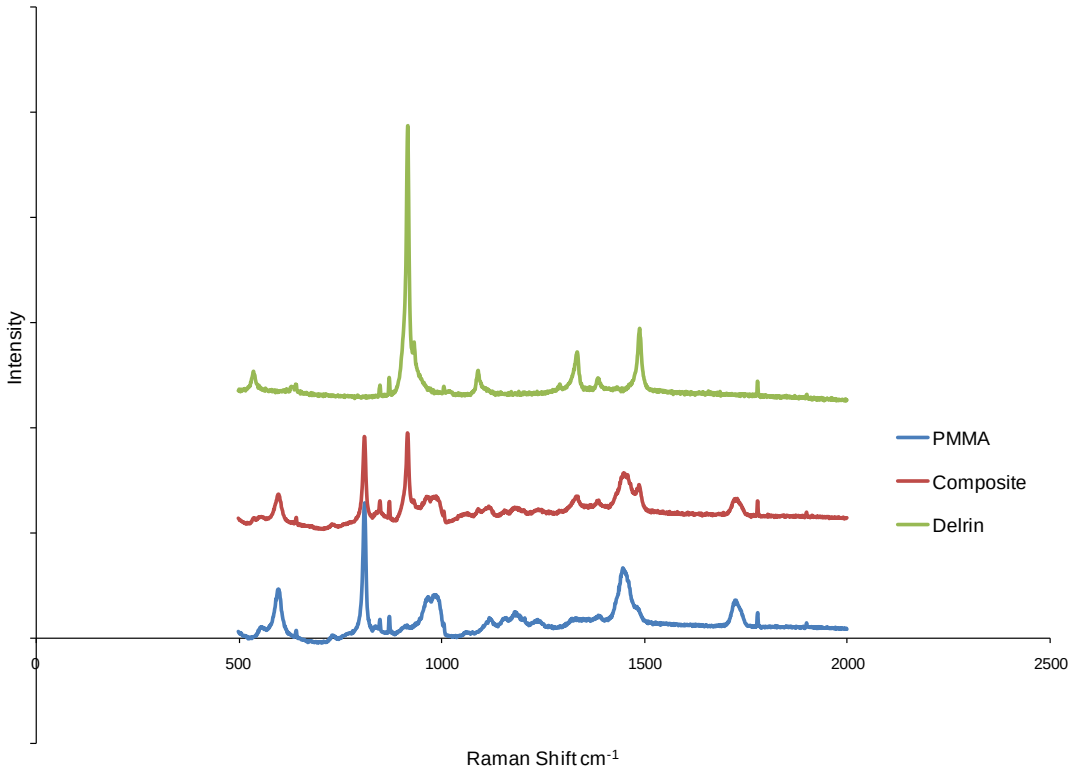

Figure 5-11: Raman spectra of pure PMMA (blue), Delrin (green) and a composite of both (red); spectra offset for clarity.

The Raman response of PMMA, normalised to the 811cm^{-1} peak is plotted in Figure 5-12; in the absence of Delrin the intensity of the PMMA peak is 1, values less than 1 indicate that the material within the laser spot is not composed entirely of PMMA. Spectra gathered using the x20 objective in both standard and pseudo-confocal modes showed no consistency. PMMA signal were detected throughout the depth of Delrin tested leading to the x20 objective being abandoned in favour of the x50 objective.

The x50 objective significantly decreased the sampling volume, increasing the z-depth resolution of the system. Pseudo-confocal mode was found to produce the smallest scattering volume; at Delrin sections greater than 10µm the contribution of PMMA was modest. Therefore, the depth of the scattering volume when using the x50 pseudo-confocal setup was approximated as 10µm. All further Raman studies were conducted using the x50 objective in pseudo-confocal mode.

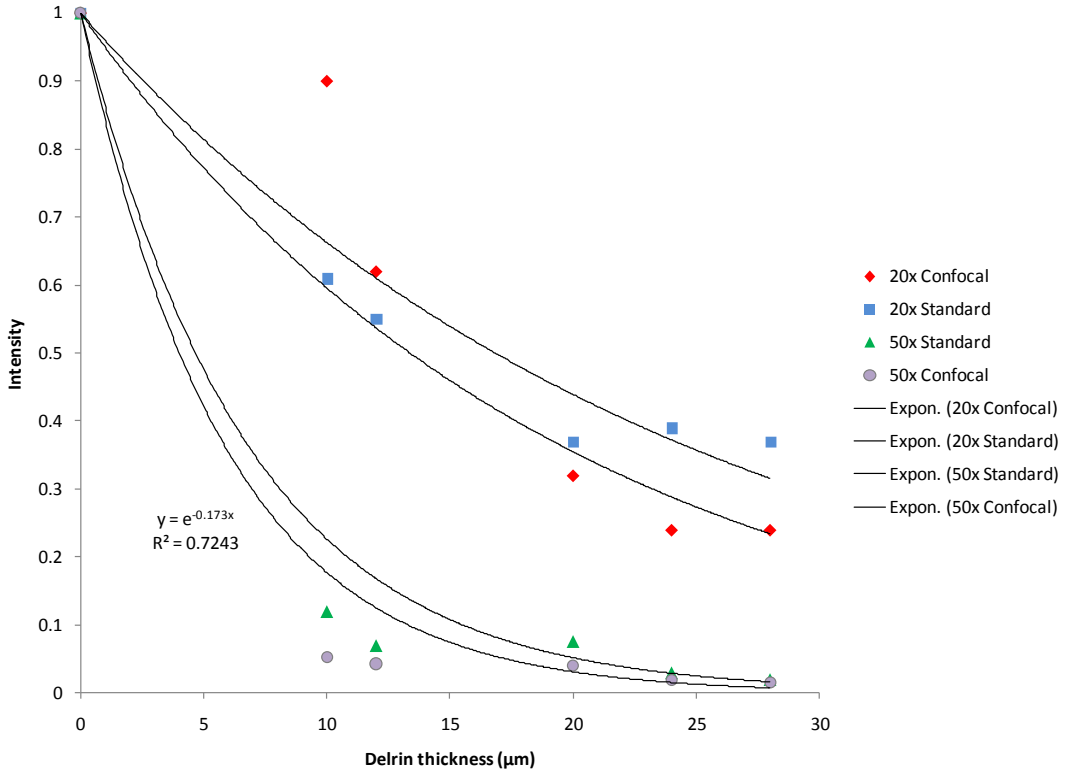

Figure 5-12: PMMA sampling measured using the normalised intensity of the 811cm^{-1} Raman peak. Experiments were carried out in both standard and pseudo-confocal mode with a x20 and x50 objective.

5.4 Etchant and Microstructural Detail

The efficacy of the etch protocol was assessed by etching an as-machined UHMWPE sample for varying times: 10, 20, 30 and 40 minutes. The etch depth was monitored by observing the removal of surface machining marks as shown by the low magnification images (x45 magn.) in Figure 5-13. The concentric patterns of the original machining marks were clearly visible after ten minutes (Figure 5-13(i)). Finer details were lost as the etch period increased; edges of the UHMWPE segments became more rounded and tool marks became ill-defined or were completely removed (Figure 5-13(iii) and Figure 5-13(iv)). These observations indicate more surface material was removed with increasing etch period.

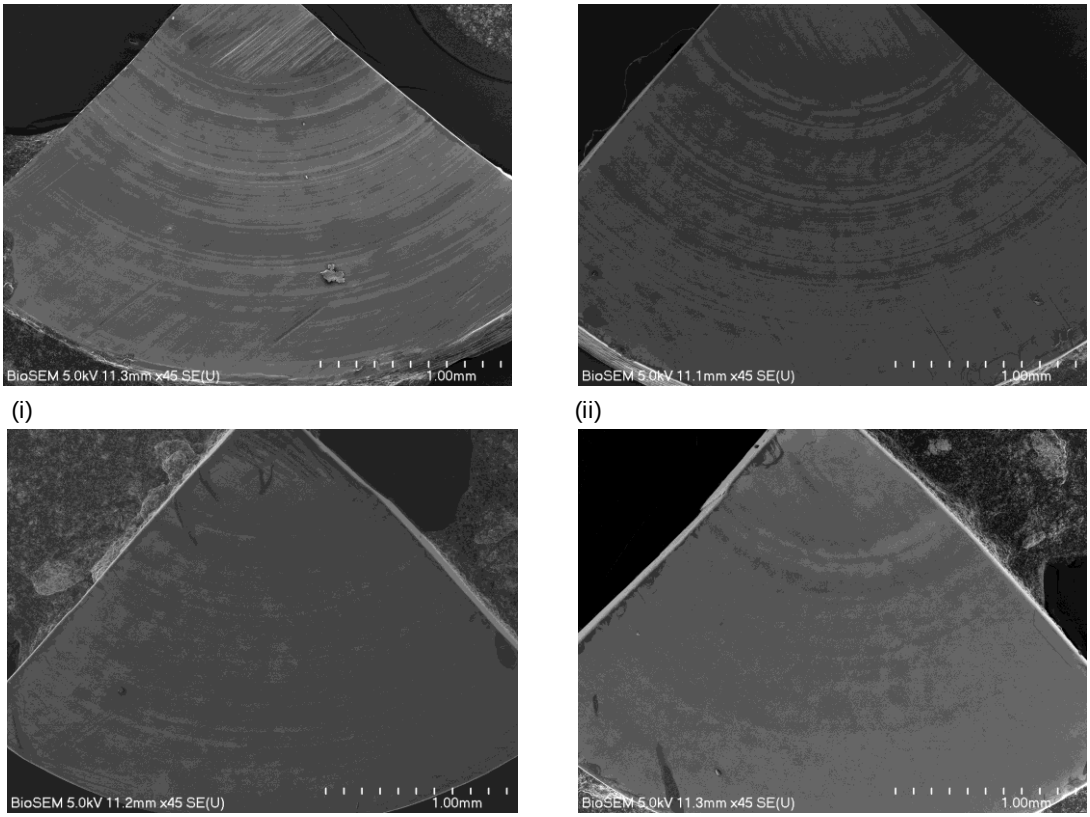

Figure 5-13: Low magnification FE-SEM images of UHWMPE segments after etching period; (i) 10mins; (ii) 20mins; (iii) 30mins; (iv) 40mins.

Higher magnification images (x5,000 magn.) revealed the extent of time-dependent detail between amorphous and crystalline domains. After ten minutes, a proportion of amorphous material had been etched revealing crystalline lamellae (Figure 5-14(i)). However, darker zones dominate the micrograph and within these areas the etchant is presumed to penetrate less. At shorter etch times the materials resistance to the etchant is inhomogeneous leaving areas of darker amorphous material.

Following twenty minutes, unetched material was still evident, identified by the darker less defined areas in Figure 5-14(ii). After a minimum of thirty minutes submerged in etchant micrographs showed uniformly etched surfaces (Figure 5-14(iii) and Figure 5-14(iv)). Unlike Figure 5-14(i) and Figure 5-14(ii) no distinguishable contrast between micro-domains was observed indicating deeper penetration of etchant and greater removal of amorphous material.

Although this study was brief it revealed microstructural contrast could be attained within a submersion period as short as ten minutes, shorter than previous studies have suggested[176] and implemented[79]. The etch period used in the current microstructural analysis of worn UHWMPE material was twenty minutes. This period was thought appropriate when considering the extent of material removed (Figure 5-13) and lamellae detail revealed (Figure 5-14).

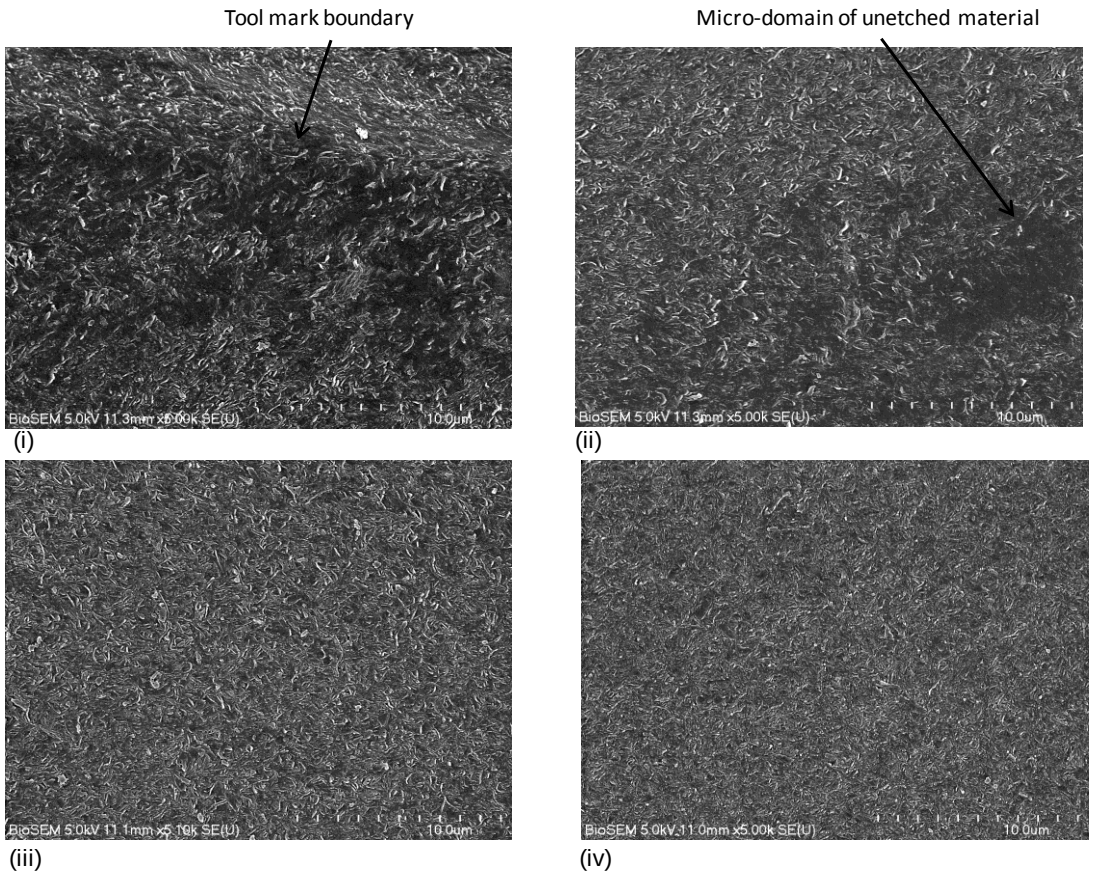

Figure 5-14: FE-SEM; UHMWPE microstructural detail within a machine mark after; (i) 10mins: (ii) 20mins; (iii) 30mins; (v) 40mins.

5.5 The Crosslinked Study

5.5.1 Crosslink Density

Swelling experiments clearly differentiated -PE from +PE. This can be seen in Figure 5-15 where the unirradiated material was found to swell up to tenfold that of the crosslinked material. The influence of crosslinking on swell ratio was attributed to two predominant factors. Firstly, the elevated crosslink levels reduced the number of possible chain conformations limiting the swell-ability, and secondly, the crosslinks improved the structural integrity of the polymer producing a network less prone to chain stretch and solvent absorption. From Flory-Rehner network swelling theory and the mean swell ratios, the average molecular weight between crosslinks was calculated; 238,080g/mole and 5,663g/mole for -PE and +PE respectively.

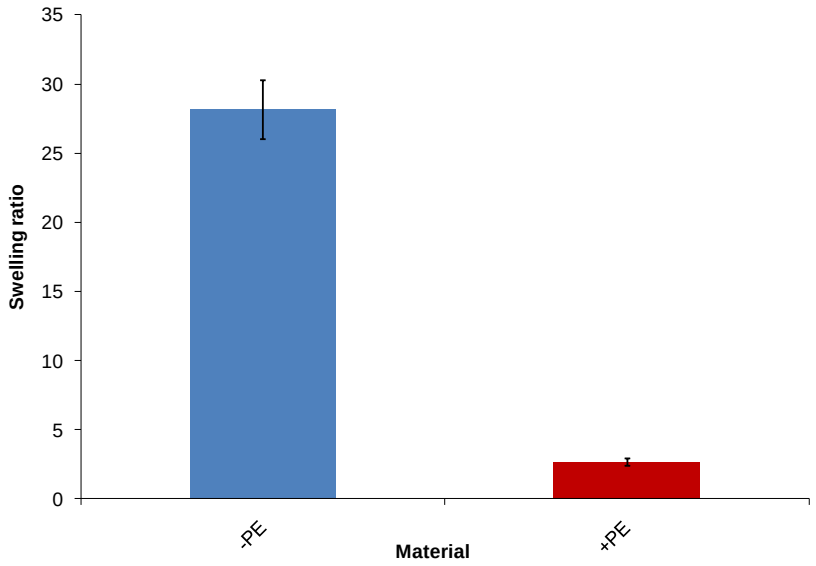

Figure 5-15: Effect of radiation dose on swelling ratio. Error bars represent one standard deviation.

5.5.2 Gravimetric Analysis

Wear of the four crosslinked pins with respect to linear reciprocating sliding distance can be seen in Figure 5-16 (red plots). The unirradiated wear data is re-plotted for comparison (blue plots). Both groups exhibited similar wear rates with the two exceptions previously noted in Section 5.2.3. In brief, the irregular accelerated wear of the unirradiated material at (i) and (ii) were caused by low lubricant levels. These regrettably circumstantial events were non-typical of the wear behaviour under controlled tribological conditions. As such, comparisons between the two material groups are made excluding these erratic periods.

In response to reciprocating motion, the difference in mean steady-state wear (±S.D) between crosslinked and unirradiated material was not significant; 0.06±0.02mm^3/million and 0.09±0.04mm^3/million respectively (t-test p=0.65).

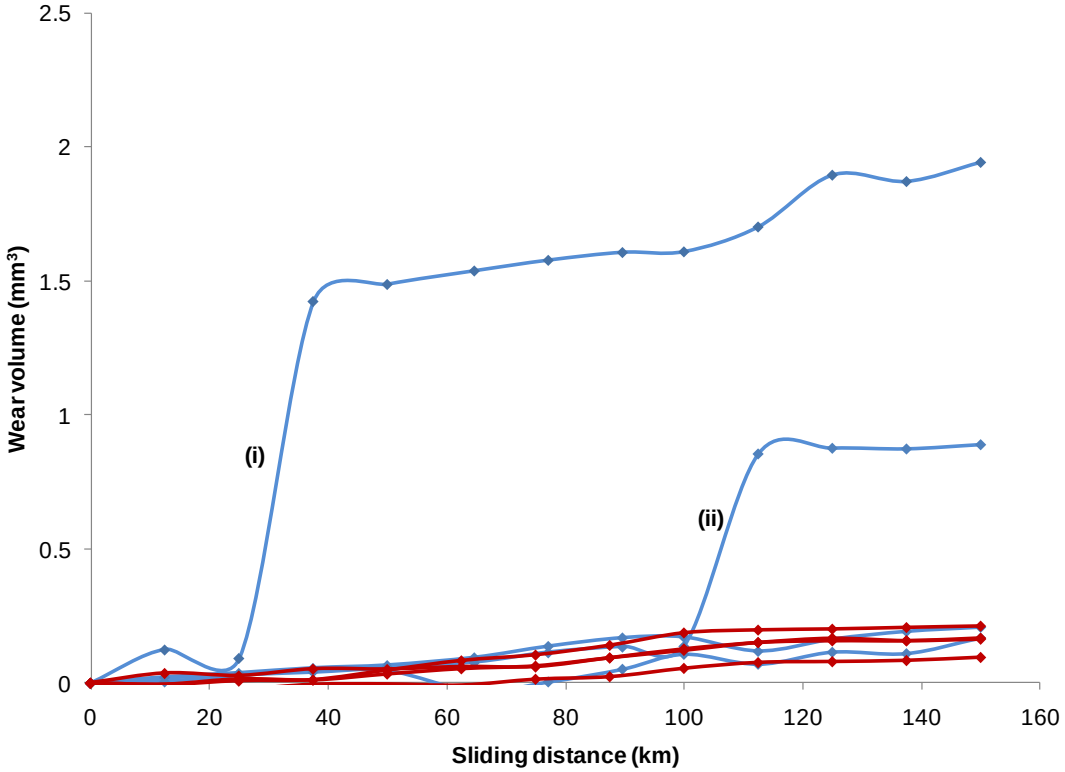

Figure 5-16: Wear graphs under linear reciprocating motion of unirradiated pins (blue) and crosslinked pins (red); at (i) chamber 1 ran dry and (ii) chamber 4 lubricant level ran low, both causing elevated wear rates. Note the initial wear rates return upon lubricant replenishment. Lines are shown as smoothed point-to-point.

The wear volume of crosslinked material with respect to multi-directional sliding distance is seen in Figure 5-17. Similarly, the equivalent wear of unirradiated material has been re-plotted for comparison. The mean steady-state wear volume for crosslinked and unirradiated material were 0.27±0.08mm^3/million and 3.44±0.46mm^3/million respectively which were shown to be statistically different (t-test $p<0.05$). This equates to a 92% reduction in wear at the completion of three million cycles. A summary of steady-state wear rates (mg/million) are seen in Figure 5-18. Both unirradiated and crosslinked material under linear reciprocating and elliptical motion are compared.

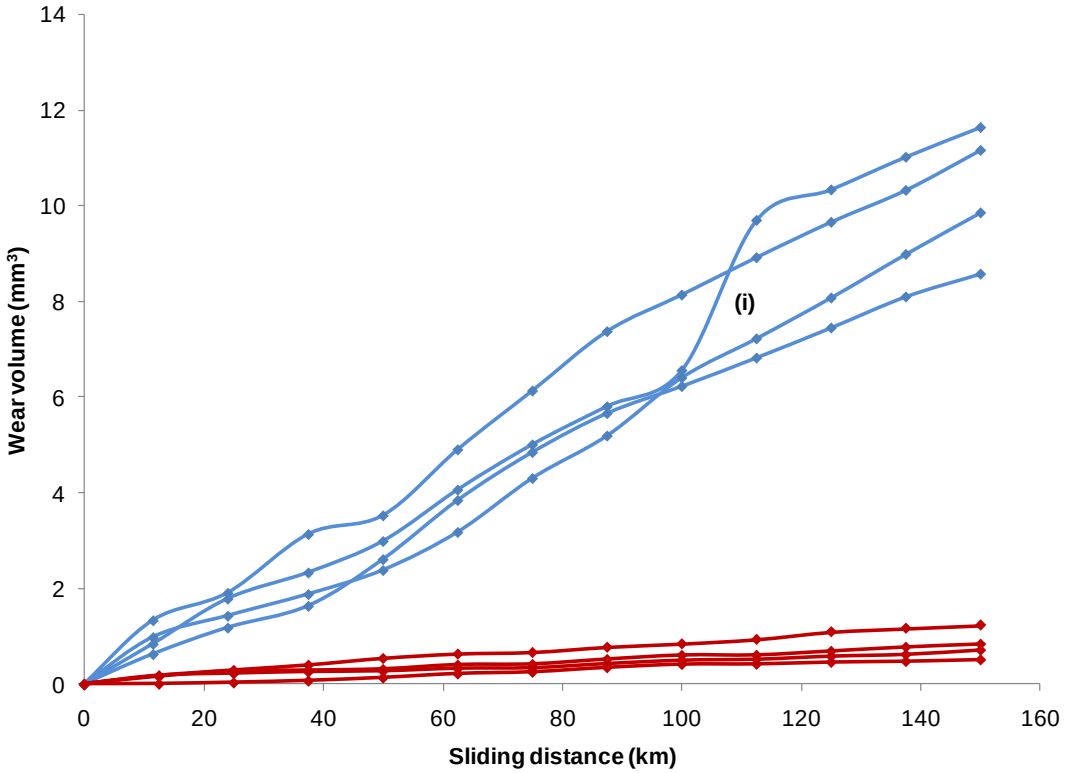

Figure 5-17: Wear graphs under elliptical motion of unirradiated pins (blue) and crosslinked pins (red); at (i) chamber 3 lubricant level ran low causing an increase in wear rate. Lines are shown as smoothed point-to-point.

Steady-state wear factors for both material groups subjected to reciprocating motion were two orders of magnitude lower than wear data calculated from retrieved or radiographic studies of conventional UHMWPE (Table 5-5). The elliptical +PE wear factor was an order of magnitude lower than that of the equivalent unirradiated group and an order of magnitude higher than either group under reciprocating wear.

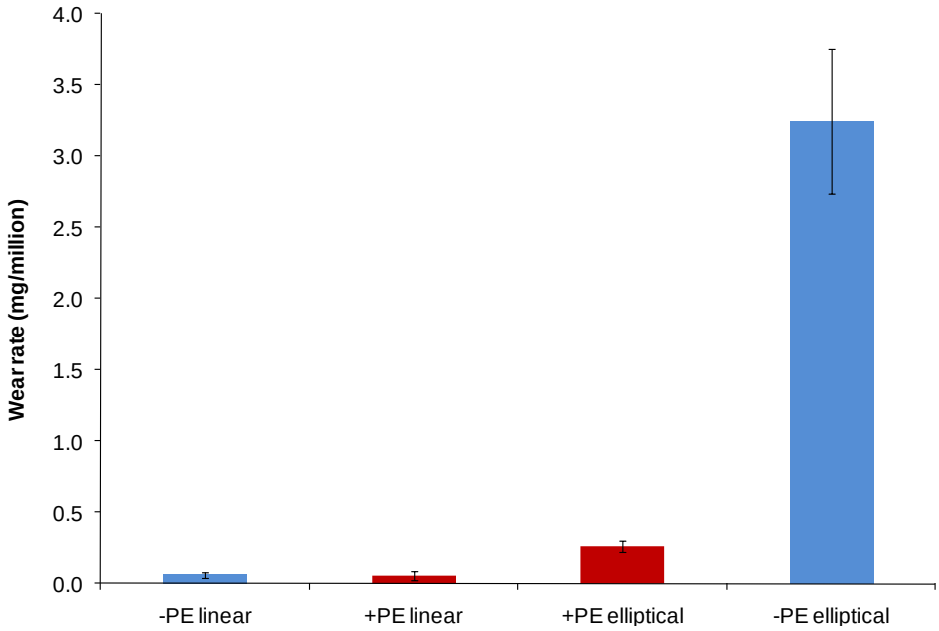

Figure 5-18: Comparison of the average wear rates of unirradiated and irradiated material under both linear reciprocating and elliptical sliding. Error bars represent one standard deviation.

The metallic plates were assessed for the presence of specific wear features such as scratching, ploughing, pitting and polymer transfer. Abrasive wear mechanisms were slight and infrequently observed along the direction of reciprocated sliding (Figure 5-19). This orientation of scratching has been shown to have minimal ploughing, cutting or adverse effects on accelerating the wear rate in the softer polymer bearing[56]. CoCrMo scratching has similarly been observed *in vivo*[44].

Material	Wear path	Wear factor (x 10^{-6} mm^3/Nm)	Penetration (mm/yr)
-PE	Reciprocating	0.03	0.003
+PE	Reciprocating	0.04	0.0026
-PE	Elliptical	1.6	0.18
+PE	Elliptical	0.13	0.01
Conventional	Clinical[116]	2	0.15

Table 5-5: Comparison of the wear factors and linear penetration rates calculated for unirradiated and highly crosslinked UHMWPE.

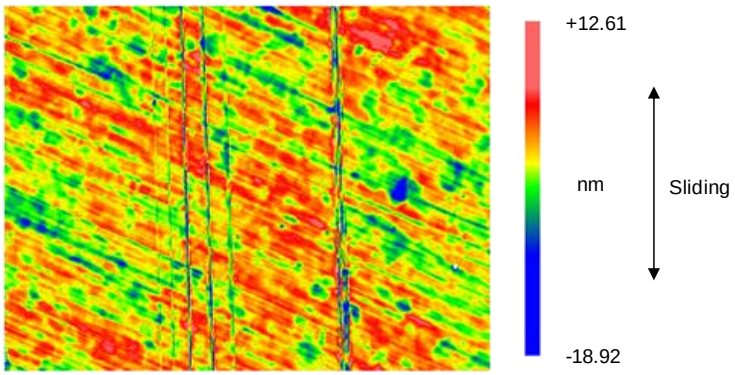

Figure 5-19: Contour plot of a lightly scratched CoCrMo linear reciprocating plate after 3 million +PE cycles; scan area 176µm x 134µm.

The final average surface roughness (±S.D), $S_{a,}$ 0.002±0.0004µm, was similar to the unworn polished plates (Table 4-1). No polymer transfer was observed on any of the CoCrMo plates.

+PE surfaces were assessed for the presence of wear features using low magnification optical microscopy and higher magnification interferometry. Polishing of the worn surfaces was observed in both linear and elliptical groups. Typical appearances can be seen in Figure 5-20a and Figure 5-20b, albeit the optical microscope proved poor in generating contrast across the smooth surfaces.

Removal of the machine marks was not unexpected. According to Figure 4-6, the machine marks protrude approximately 1.5µm above the mean surface centreline. Therefore, even pins in the lowest wearing group (+PE subject to linear reciprocating motion) with a mean penetration rate of ~3µm/million would wear through these surface features after approximately 500,000 cycles. Linear reciprocating surfaces were typically characterised with an arithmetic surface roughness (S_a) of 0.052±0.019µm.

Figure 5-20: Optical images after 3 million cycles for (a) +PE linear wear, light scratching; (b) +PE elliptical wear, highly burnished; (c) +PE load soak pin, machine marks clearly visible. Note the lack of definition on the very smooth worn surfaces.

The slow removal and renewal of +PE material under reciprocating motion suggests that sliding surfaces were subjected to large numbers of cycles before debris was released. The ripple morphology imaged in Figure 5-21 may support the proposal of a high-cycle fatigue regime and a surface prone to plastic deformation.

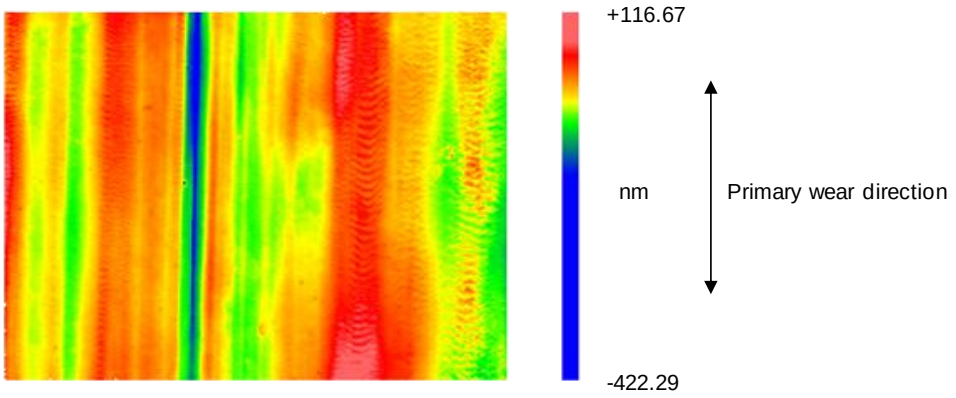

Figure 5-21: Zygo contour plot of a +PE reciprocating worn surface. Scratching and rippling were observed; scan area 176µm x 134µm.

The average penetration rate of +PE pins under multi-directional motion was three-fold higher than the equivalent reciprocating motion, 10µm/million cycles. The distinct ripple morphology imaged on unirradiated material (Figure 5-8) was less apparent on the highly crosslinked surfaces (Figure 5-22). Elliptically worn material was typically found to have an arithmetic surface roughness (S_a) similar to that of the reciprocating worn surfaces, 0.055±0.011µm.

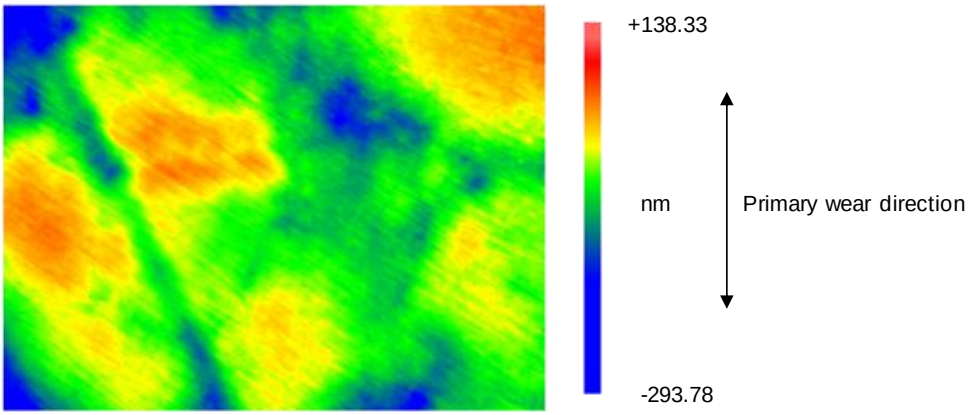

Figure 5-22: Zygo contour plot of +PE elliptically worn surface; scan area 176µm x 134µm.

5.5.3 Raman Crystallinity Study

5.5.3.1 Unirradiated UHMWPE

Changes in unirradiated crystallinity with respect to depth of Raman sampling can be seen in Figure 5-23. At each depth, the mean crystallinity from the worn groups were statistically compared to the load-only and microtomed control groups using analysis of variance (ANOVA) and the t-test. The group subjected to elliptical motion (Figure 5-23a) showed no significant difference in surface (t-test p=0.83) and sub-surface crystallinity when compared to the unworn control (Figure 5-23b). The mean load-soak crystallinity was found to have the least variation with depth, typically characterised at 50% (Figure 5-23c). Lower crystallinity in the linear reciprocating motion (Figure 5-23d) and load-only groups were consistently found up to the maximum recorded depth of sub-37.5µm.

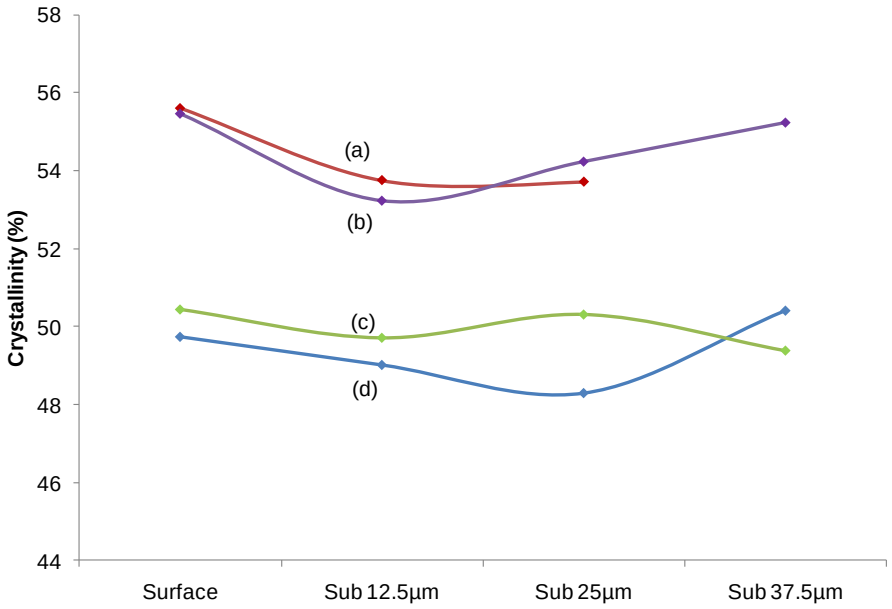

Figure 5-23: -PE crystallinity for (a) three million elliptical cycles; (b) control surface; (c) three million load only cycles; (d) three million linear reciprocating cycles. Lines are shown as smoothed point-to-point. Note, the x-axis defines the distance beneath the surface at which the Raman laser was focused.

Surface crystallinity data can be seen in Table 5-6. The average surface crystallinity of the reciprocating group, a value of 49.8% was 5% lower than either the unworn control or those surfaces worn in a multi-directional manner.

	N	Mean	Std. Deviation	Std. Error	95% Confidence Interval for Mean		Minimum	Maximum
					Lower Bound	Upper Bound		
Elliptical wear	30	55.60	3.04	0.56	54.46	56.73	49.64	62.30
Linear wear	30	49.73	5.96	1.09	47.50	51.96	37.24	65.49
Load soak	30	50.43	6.13	1.12	48.14	52.73	42.30	70.25
Unworn control	20	55.29	1.70	0.38	54.49	56.09	53.00	60.01
Total	110	52.53	5.46	0.52	51.50	53.56	37.24	70.25

Table 5-6: Unirradiated surface crystallinity following three million cycles and unworn bulk material.

No significant change was found in the surface crystallinity of the linear-reciprocating group when compared to the load-soak cohort (t-test p=0.57). However, the mean surface crystallinity between elliptical and linear-reciprocating groups was shown to be statistically different ($p<0.01$).

5.5.3.2 Highly Crosslinked UHMWPE

Changes in crosslinked crystallinity with respect to depth of Raman scattering can be seen in Figure 5-24. Surface crystallinity results are seen in Table 5-7. The microtomed control crystallinity was 53.16±1.92% within the first 37.5µm of material (Figure 5-24a). A gradual increase in crystallinity with increasing depth was observed in elliptical, linear-reciprocating and load-soak groups; Figure 5-24b, Figure 5-24c and Figure 5-24d.

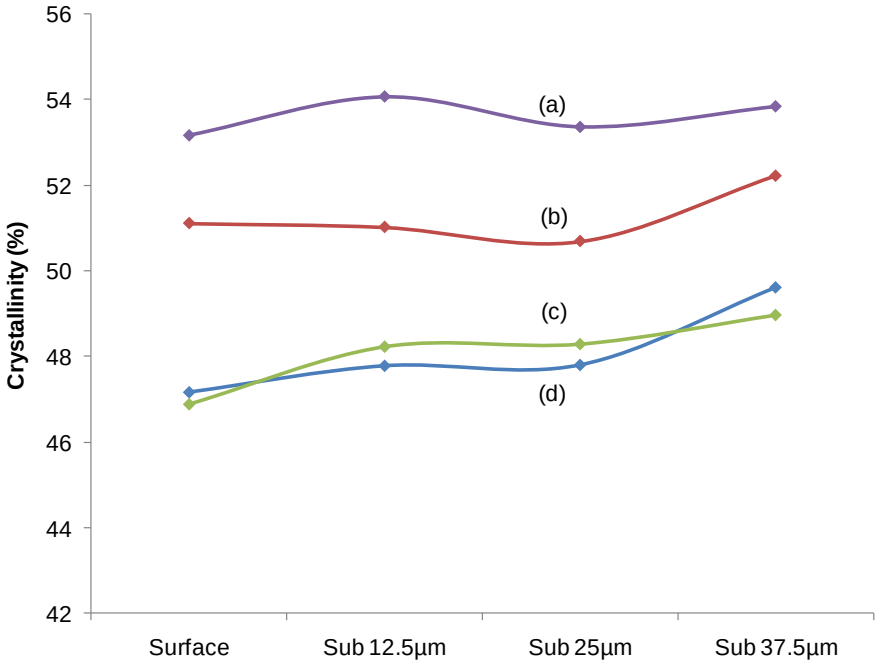

Figure 5-24: +PE crystallinity for (a) unworn control (b) three million elliptical cycles; (c) three million load only cycles; (d) three million linear reciprocating cycles. Lines are shown as smoothed point-to-point. Note, the x-axis defines the distance beneath the surface at which the Raman laser was focused.

Despite the unworn control group having the highest mean surface crystallinity, the elliptically worn surface was found to be statistically similar, 51.11±3.19% (ANOVA p=0.23).

	N	Mean	Std. Deviation	Std. Error	95% Confidence Interval for Mean		Minimum	Maximum
					Lower Bound	Upper Bound		
Elliptical wear	40	51.11	3.19	0.50	50.09	52.14	44.66	56.72
Linear wear	40	47.16	5.66	0.90	45.35	48.97	33.86	57.81
Load soak	20	46.89	6.21	1.39	43.98	49.80	37.32	54.47
Unworn control	10	53.16	1.92	0.61	51.79	54.53	50.24	55.90
Total	110	49.10	5.24	0.50	48.11	50.09	33.86	57.81

Table 5-7: +PE surface crystallinity following three million cycles and unworn material.

Mean surface crystallinity associated with the linear motion group, 47.16±5.66%, was statistically similar to the load soak cohort (ANOVA p=0.84). Both groups were shown to have lower crystallinity than the +PE control and elliptically worn surfaces (ANOVA $p<0.05$). Lower crystallinity values were consistently found in all crosslinked groups when compared with equivalent unirradiated groups.

5.5.4 Residual Strain

5.5.4.1 Unirradiated UHMWPE

The mean full width at half maximum (FWHM) of the 1129cm^{-1} peak (attributed to C-C stretching) in linear reciprocating, elliptical, load-only and microtomed groups were assessed. The FWHM magnitudes of the measured band at ~1129cm^{-1} can be seen in Figure 5-25. The values observed were in agreement with the crystallinity measurements; lower crystallinity groups showed broader Raman peaks indicative of greater residual damage. Under our existing set of conditions, a typical low wearing surface may be characterised as having a lower crystallinity and broader ~1129cm^{-1} peak.

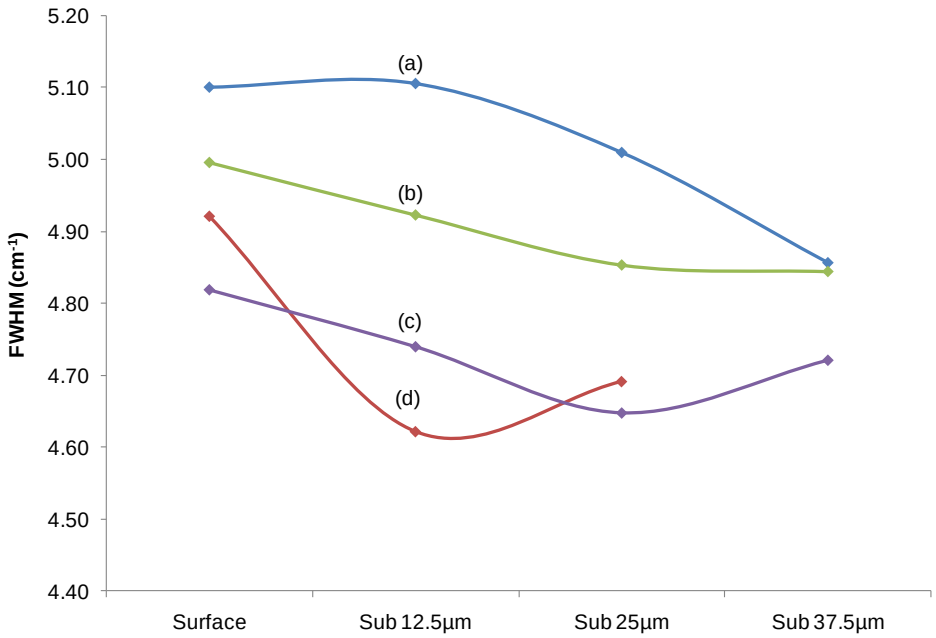

Figure 5-25: -PE Full width at half maximum (~1129cm^{-1}); (a) three million linear reciprocating cycles; (b) three million load-only cycles; (c) control surface; (d) three million elliptical cycles. Lines are shown as smoothed point-to-point. Note, the x-axis defines the distance beneath the surface at which the Raman laser was focused.

If we consider surface measurements, the control group possessed the narrowest band of 4.82±0.17cm^{-1} (Figure 5-25c). This was consistent with a surface microtomed to remove residual damage or strain. No statistical difference could be found between the elliptical (Figure 5-25d), load only (Figure 5-25b) and control surfaces. Greatest peak broadening was found in the linear reciprocating group, 5.10±0.24cm^{-1} (Figure 5-25a). This was found to be statistically different to the elliptical surface group, 4.92±0.25cm^{-1} (t-test p=0.02).

Load-soak surfaces had a mean FWHM ~1129cm^{-1} of 5.00cm^{-1}, gradually decreasing to 4.84cm^{-1} sub 37.5µm. The microtomed bandwidth also decreased with subsurface depth, but to a lesser extent falling to a minimum peak width of 4.72±0.09cm^{-1} at sub 37.5µm.

Despite the lack of statistically significant difference between control, elliptical and load-only groups, a common decreasing trend suggests that smaller levels of strain were found with increasing depth beneath the surface.

There was a statistically significant drop in ~1129cm^{-1} bandwidth in the elliptical group between surface and sub 12.5µm measurements; 4.92±0.25 and 4.62±0.05cm^{-1}, indicating a narrow near-surface band of elevated strain.

5.5.4.2 Highly Crosslinked UHMWPE

The largest mean FWHM ~1129cm^{-1} was consistently found in the load-soak group, where a decreasing trend with increasing depth was observed (Figure 5-26a). A similar trend was

observed in the linear reciprocating group. No statistical difference between these two cohorts was found. Peak broadness in both groups remained statistically higher than the control microtomed group (ANOVA $p<0.05$) despite this group showing greater variation sub-surface (Figure 5-26d). The presence of a broader ~1129cm^{-1} peak in both linear-reciprocating and load-soak groups suggests greater damage accumulation in the near-surface.

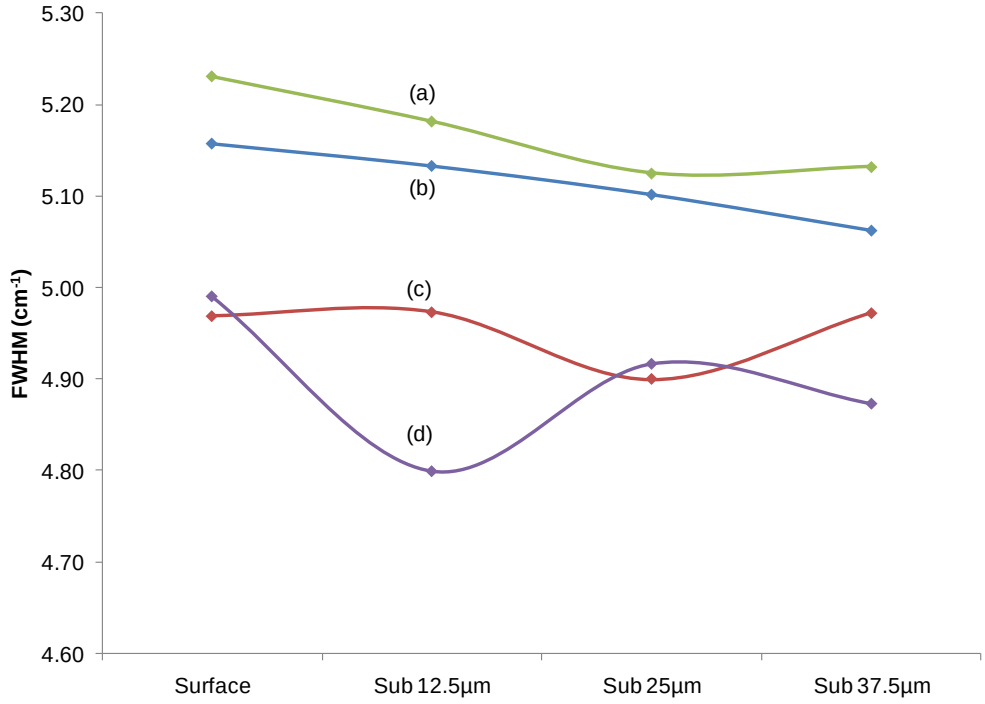

Figure 5-26: +PE Full width at half maximum (~1129cm^{-1}); (a) three million load only cycles; (b) three million linear reciprocating cycles; (c) three million elliptical cycles; (d) control surface. Lines are shown as smoothed point-to-point. Note, the x-axis defines the distance beneath the surface at which the Raman laser was focused.

The damage zone may extend further into the material than the maximum depth investigated. Had the near-surface affected zones been constrained to within the first 37.5µm of material a significant decreasing trend might have been expected with final peak widths similar to the microtomed control group.

Despite three-million elliptical cycles, equivalent to 150km of sliding, no statistical difference between the elliptical and microtomed control mean was found at any depth (Figure 5-26c). Mean surface values in the elliptical and control group were found to be 4.97±0.16 cm^{-1} and 4.99±0.17cm^{-1} respectively (t-test $p=0.79$). The elliptical and control group means sub-surface 37.5µm were 4.97±0.14 cm^{-1} and 4.87±0.17 cm^{-1} (t-test $p=0.13$).

5.5.5 Microstructural Change

5.5.5.1 Unirradiated UHMWPE

The microstructure of unworn, worn, and load-only material was assessed. A typical image of the control microtomed group is seen in Figure 5-27. This group was consistently characterised by random lamellae orientation and deep penetration of etchant between lamellae offering good contrast. When compared with the unworn control microstructure, the effects of elliptical wear seem negligible (Figure 5-28). Elliptically worn images exhibited similar characteristics to the control group; random lamellar orientation of similar size and breadth.

Distinct microstructural development was imaged in the reciprocating sliding group. This group was consistently characterised by large domains of lamellae imaged closely packed together offering some orientation along the direction of sliding motion (Figure 5-29). Subsequent FE-SEM at higher magnification provided evidence of lamellar break-up and fragmentation (Figure 5-30). This was substantiated with Raman data which confirmed lower crystallinity in the lower wearing linear reciprocating group (Section 5.5.3.1).

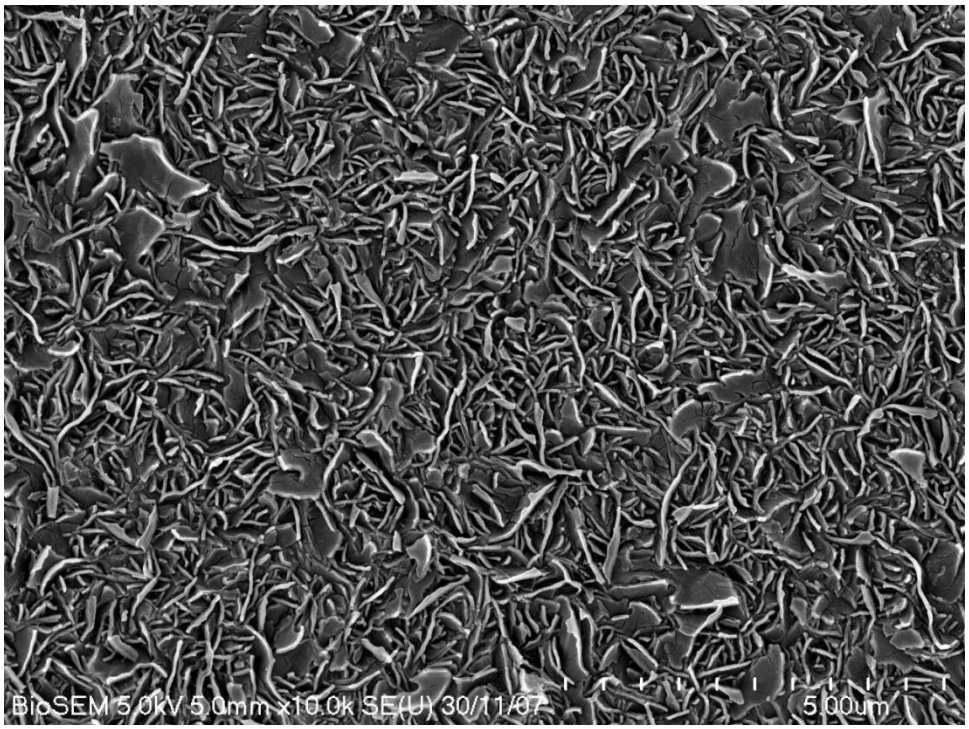

Figure 5-27: FE-SEM image of microtomed control microstructure. Note the random lamellae orientation.

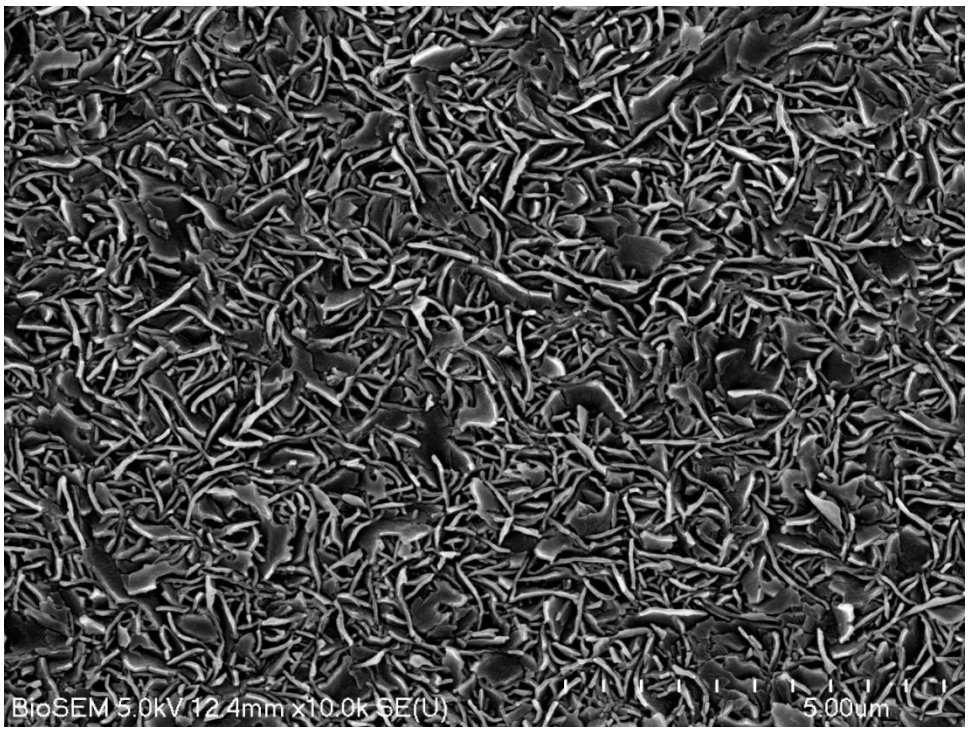

Figure 5-28: FE-SEM microstructural image of elliptically worn material following three million load and motion cycles (primary wear axis top to bottom). Note the random lamellae orientation.

Figure 5-29: FE-SEM microstructural image of –PE after three million load and linear reciprocating motion cycles (sliding direction left to right). In comparison to the control microstructure, the texture consists of more tightly packed and fragmented lamellae.

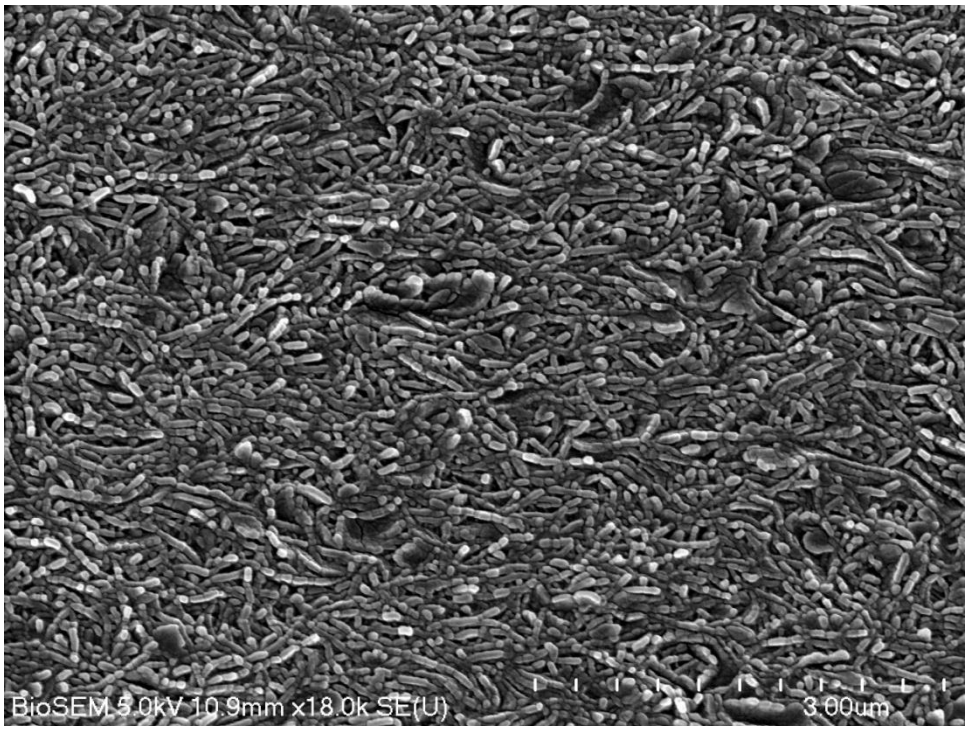

Figure 5-30: FE-SEM microstructural image of –PE after three million load and linear reciprocating motion cycles (sliding direction left to right). The higher magnification shows more clearly the close packing of lamellae, preferential orientation (left to right) and fragmented lamellae.

5.5.5.2 Highly Crosslinked UHMWPE

Figure 5-31 shows the post-irradiated unworn lamellar size, shape and distinct lack of preferential alignment in control material. In comparison to the unirradiated control microstructure seen in Figure 5-27, the lamellae appeared consistently smaller. This may be expected, a consequence of the CISM process. The process, described in Section 2.5.6, involves an above melt-anneal process. Upon cooling from the melt, chain mobility is restricted due to additional crosslinks. These limit the re-organisation and folding of chains producing a microstructure consisting of smaller lamellae.

The low wearing elliptical group (Figure 5-32) and reciprocating group (Figure 5-33) showed increasing signs of lamellar break-up and micro-domains of stack rotation and close packing. Both linear and elliptical groups showed a degree of lamellae orientation and mobility in response to wear. Overall this was less apparent in the elliptically worn group. Worn +PE material was consistently characterised by folded, bent and broken lamellae in response to frictional sliding forces. The differentiation between the effects of linear and elliptical motion on microstructural development was found to be less clear in crosslinked material.

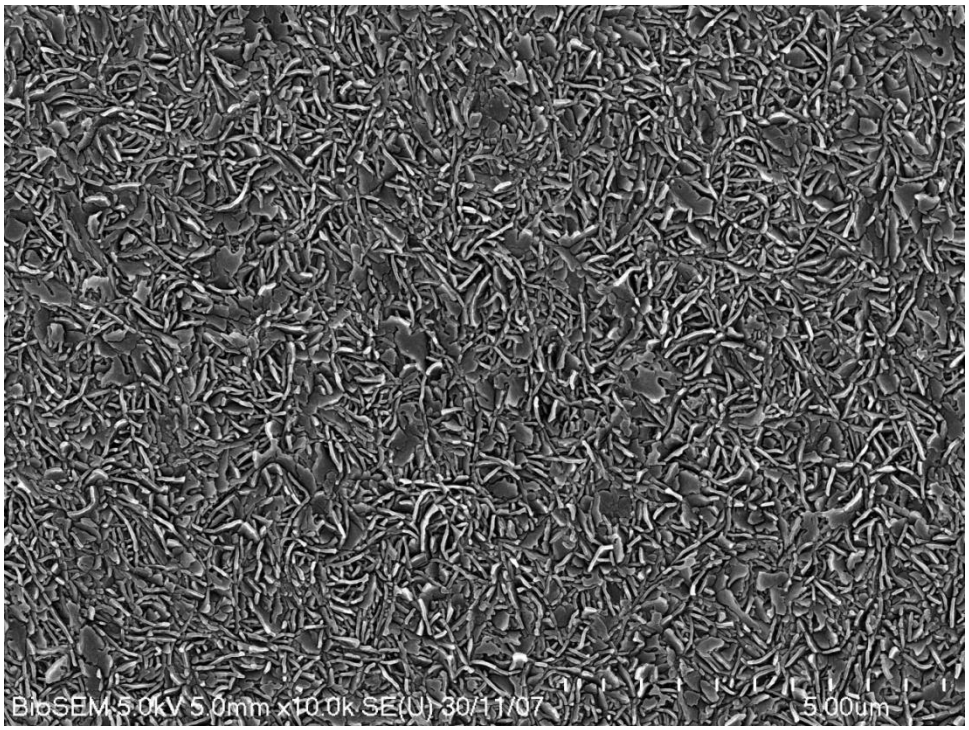

Figure 5-31: FE-SEM image of +PE microtomed control microstructure.

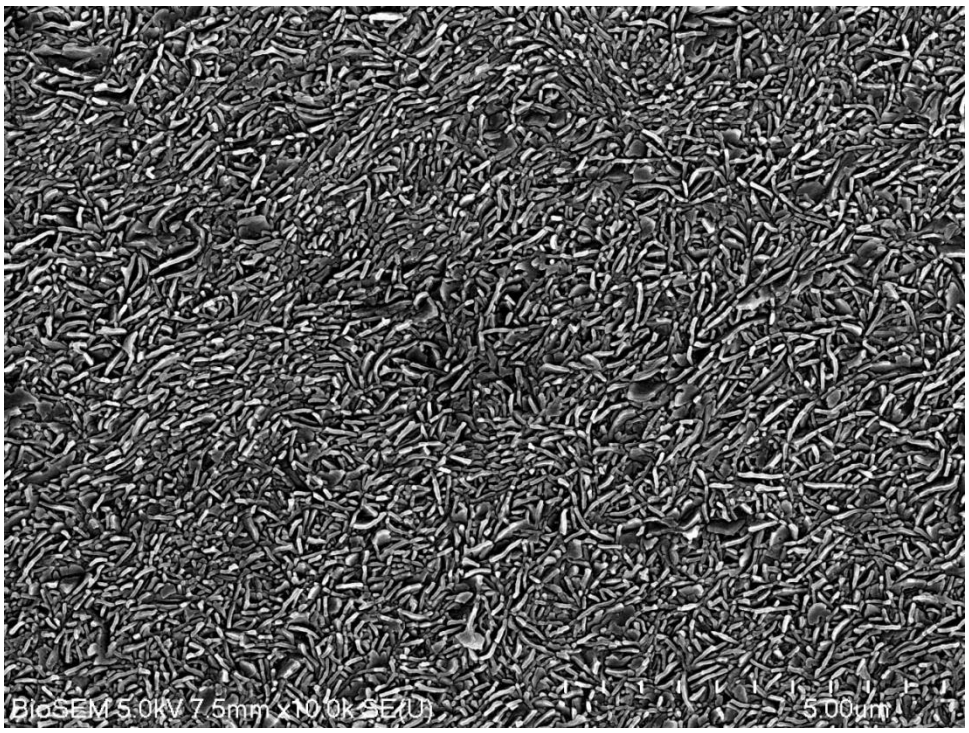

Figure 5-32: FE-SEM microstructural image of +PE following three million load and elliptical motion cycles (primary wear axis diagonal to page).

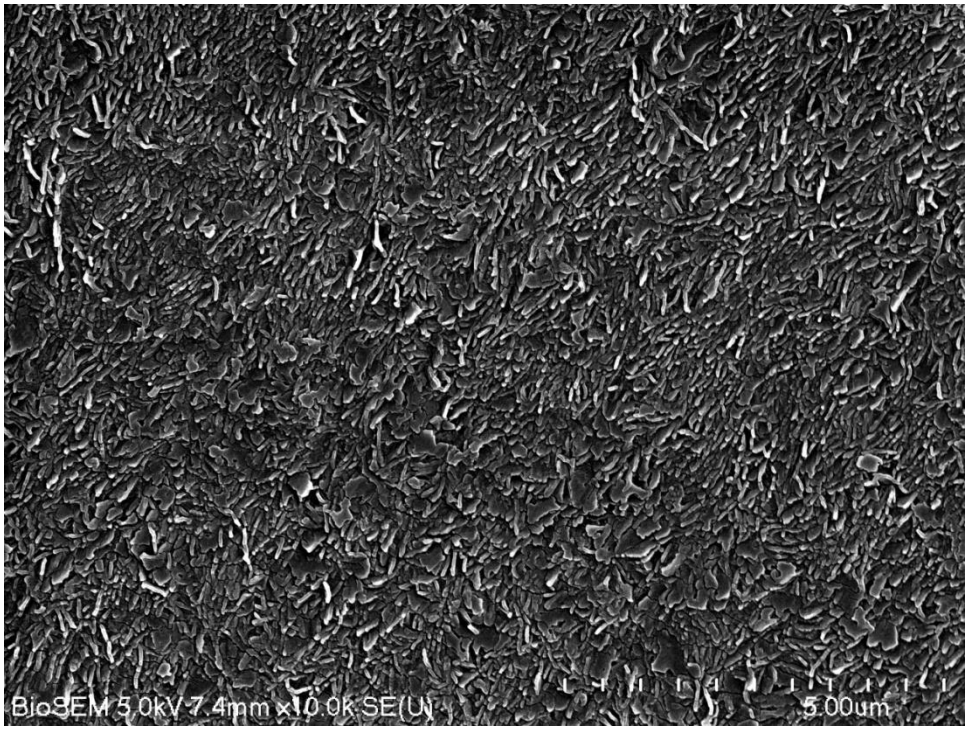

Figure 5-33: FE-SEM microstructural image of +PE following three million load and linear reciprocating motion cycles (diagonal to page). Domains of orientation were observed.

5.5.6 Morphological Surface Change

5.5.6.1 Unirradiated UHMWPE

Following three million linear reciprocating cycles, worn surfaces were found with light scratches in the direction of sliding motion. The edges of these scratches appeared to be plastically deformed and folded in such a way to produce fibrils running perpendicular to the motion path. Areas of -PE were re-organised into domains running parallel to the surface in the direction of wear (Figure 5-34). In areas where this formation was highly developed, elongated fibrils were observed extending from the surface (Figure 5-35).

Parallel ripples were imaged on the surface of the more rapidly wearing unirradiated pins under elliptical motion (Figure 5-36). Tearing, folding, cracking and fibrillar features were all imaged at higher magnification (Figure 5-37).

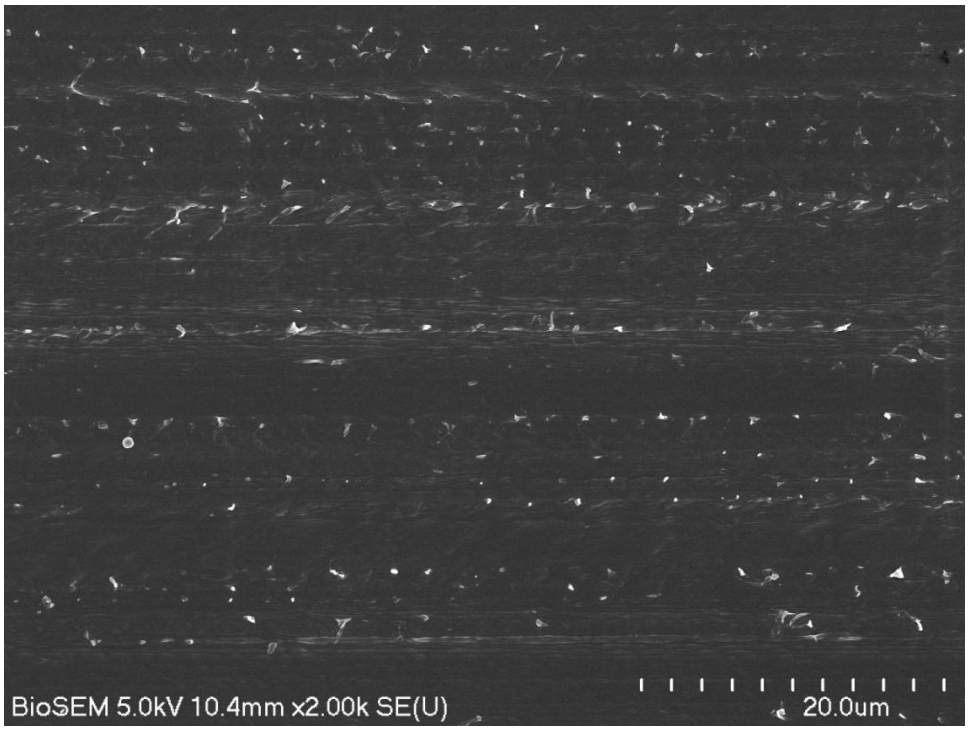

Figure 5-34: FE-SEM image of the unirradiated surface following three million load and linear reciprocating motion cycles (left-to-right). Note the light scratching in the direction of sliding and fibrillar tearing extending perpendicular to this.

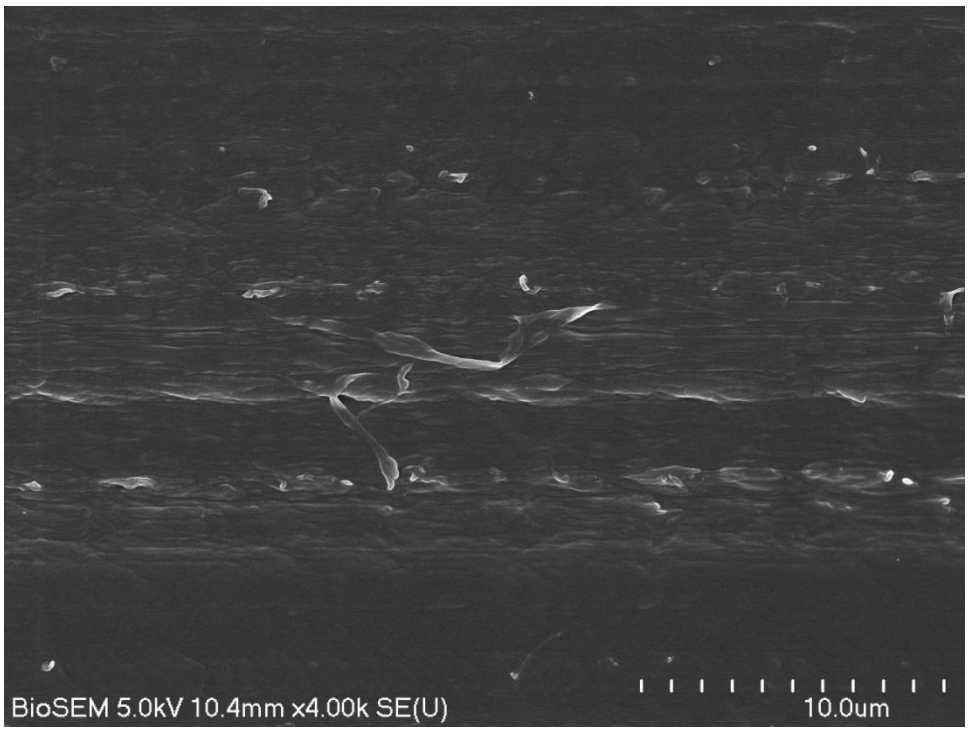

Figure 5-35: FE-SEM image of the unirradiated surface following three million load and linear reciprocating motion cycles (left-to-right). The image captures the origin of fibrillar debris, just before it detaches from the surface.

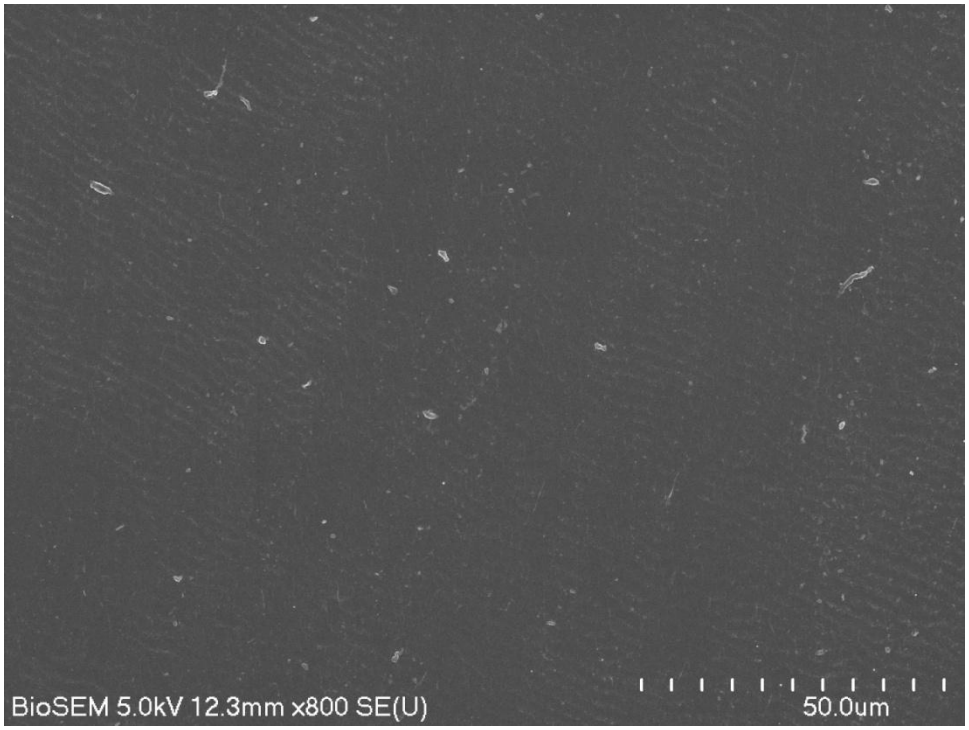

Figure 5-36: FE-SEM image of the unirradiated surface following three million load and elliptical motion cycles (primary wear axis top to bottom). Note the regular ripples running across surface.

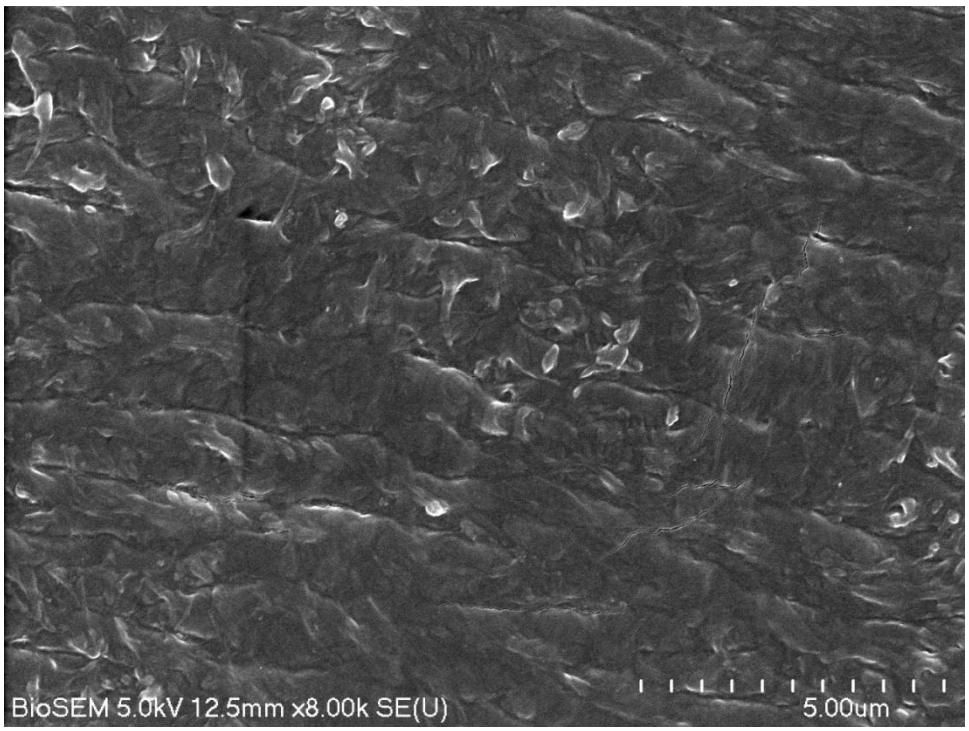

Figure 5-37: FE-SEM image of the unirradiated surface following three million load and elliptical motion cycles (primary wear axis top to bottom). Tearing, folding and opening of surface cracks were observed predominantly perpendicular to the primary wear axis.

5.5.6.2 Highly Crosslinked UHMWPE

Small parallel ripples were consistently imaged on +PE linear reciprocating surfaces (Figure 5-38). The peak-to-peak distance of these features were approximately 1μm, and were found transverse to the direction of sliding.

The micrographs of +PE surfaces worn under elliptical motion were highly smooth, indicated by the lack of contrast picked on the FE-SEM. Sub-micron debris was imaged on the surface (Figure 5-39). In other areas a granular texture was observed; the beads appeared on the order of 500nm in width (Figure 5-40). This texture was found highly developed in some regions; beads were drawn out into folded elongated strands running across the primary elliptical wear axis (Figure 5-41).

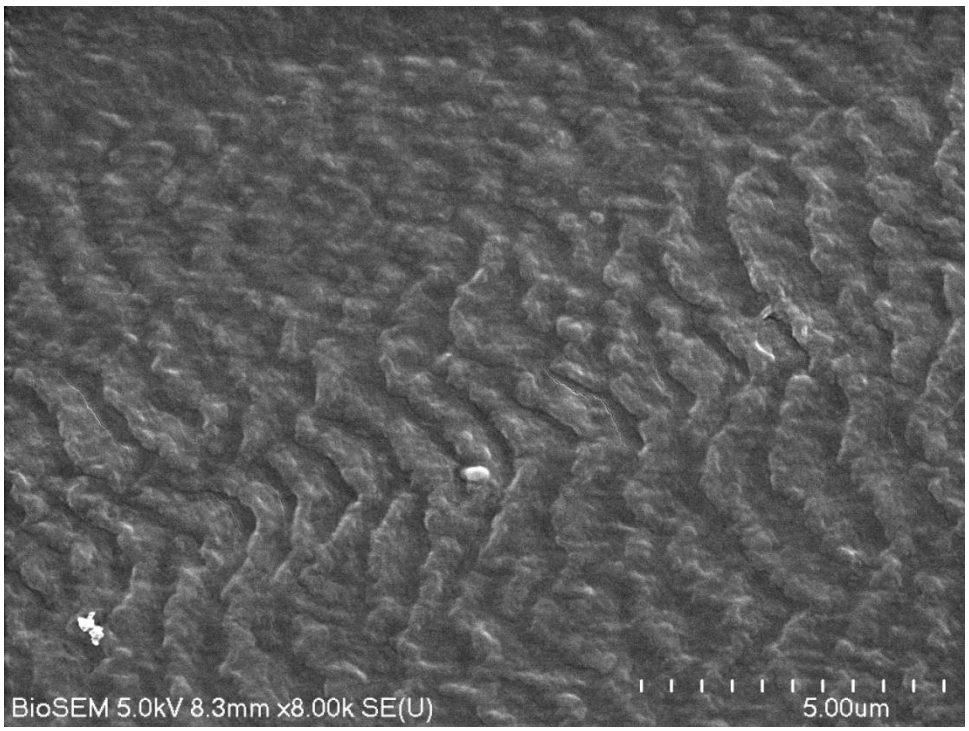

Figure 5-38: FE-SEM of the highly crosslinked surface following three million load and linear reciprocating motion cycles (sliding direction diagonal left-to-right). The ripples run perpendicular to the sliding motion.

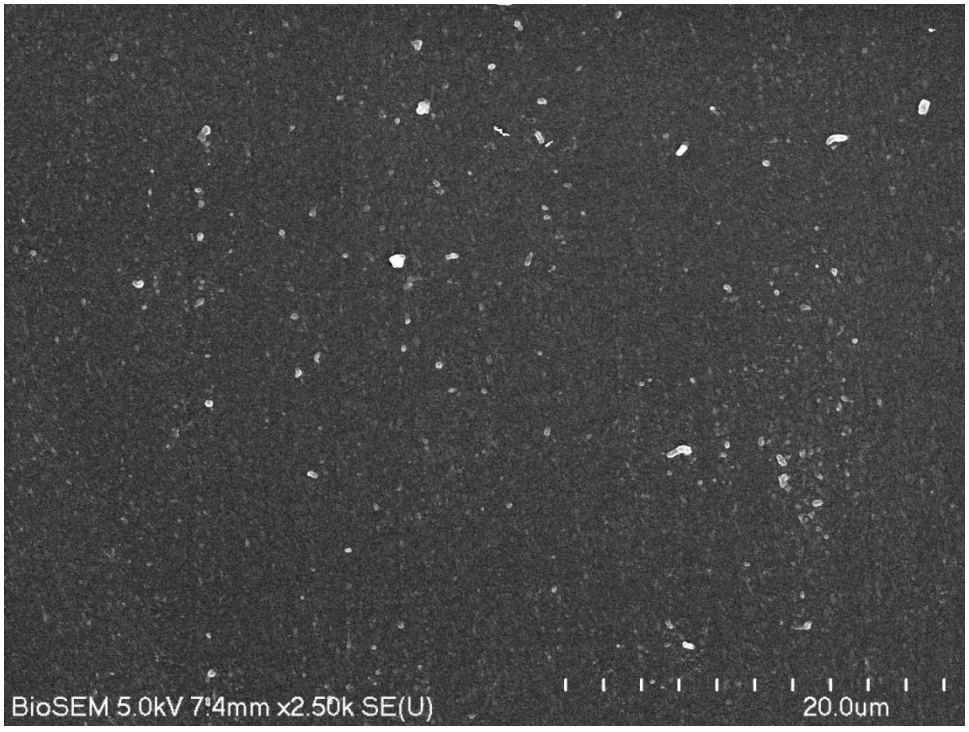

Figure 5-39: FE-SEM image of the highly crosslinked surface following three million load and elliptical motion cycles (primary wear axis left-to-right). Micron and sub-micron debris were observed on the otherwise highly smooth surface.

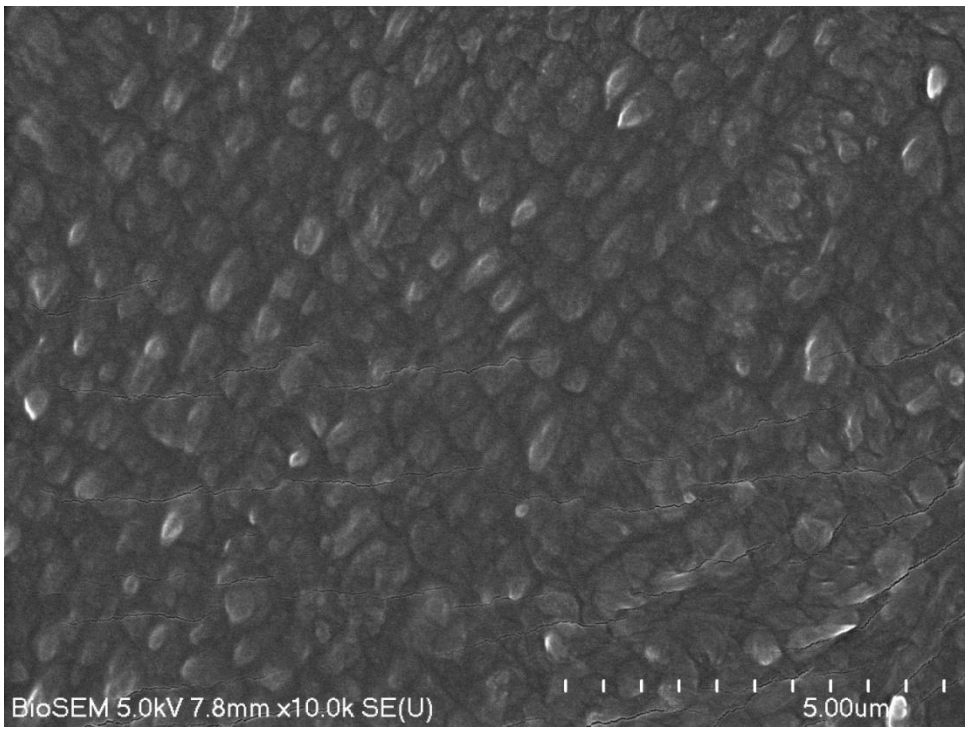

Figure 5-40: FE-SEM image of the highly crosslinked surface following three million load and elliptical motion cycles (primary axis left to right). Note the granular texture with a feature size diameter ~0.5µm.

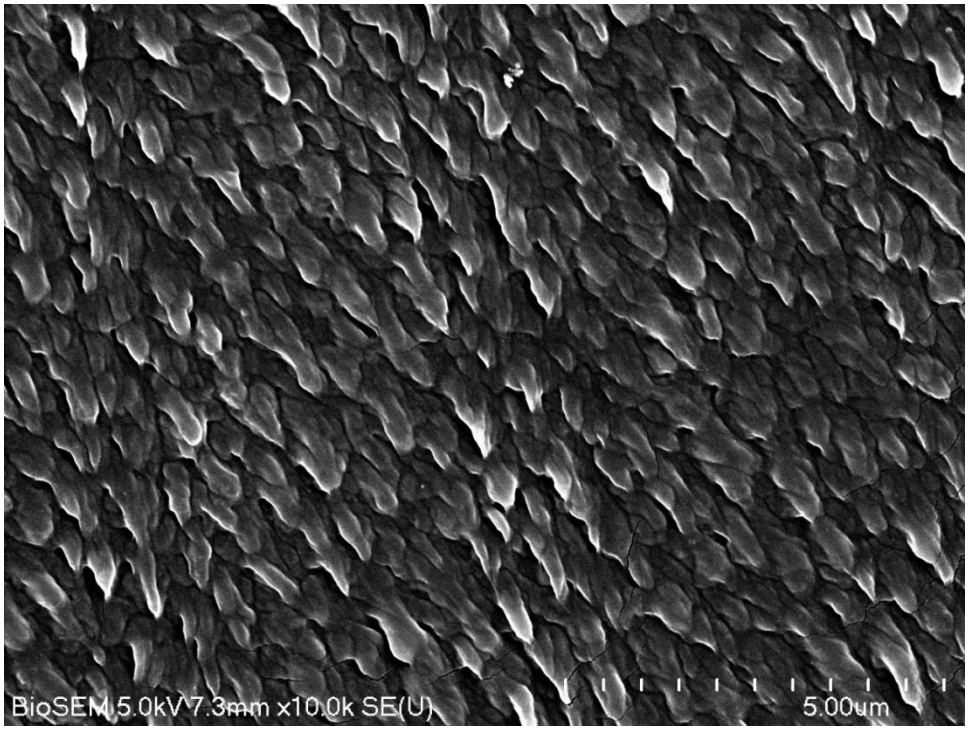

Figure 5-41: FE-SEM image of the highly crosslinked surface following three million load and elliptical motion cycles (primary axis left to right). Note the apparent adhesive drawing out from the initial granular texture shown above.

6 Discussion

Summary

Simplified tribometers have a valuable role in simple biomaterial screening tests prior to full joint simulation. To date, there are few pin-on-plate machines which can approximate more closely the physiological motion and loading profiles found in the hip; even fewer machines exist which are capable of producing a range of physiological loads and slide paths akin to those found within the hip joint. In response to areas which may be considered to be limitations in contemporary tribometer designs, a novel wear testing machine capable of better simulating physiological loads[8, 9], and motion paths[100, 101, 125] has been designed, built and validated.

The complexity of UHMWPE microstructural re-arrangement under clinical sliding requires that the contemporary pin-on-plate tribometer needs to expand upon early reciprocating or rotational motion paths (one degree of motion machines) to introduce multi-directional motion and varying cross-shear vectors at the sliding interface. Furthermore, the requirement to investigate the characteristic directional-dependence of UHMWPE wear is facilitated by tribometers that are capable of exerting uniform shear vectors across the pin surface[104, 106, 110]. Such machines are necessary to yield understanding of the influence of sliding motion and cross-shear on strain hardening and the wear rate of UHMWPE.

The experimental results presented herein confirm the notion that crosslinking reduces volumetric wear in UHMWPE when sliding takes the form of open motion tracks possessing a cross-shearing action. Linear-reciprocating motion, defined as having zero cross-shear[111], did not exhibit a statistically significant difference in the mean steady-state wear rates between the two material groups.

6.1 Tribometer appraisal

In the following section the Edinburgh tribometer is discussed in the context of existing approaches to wear testing. Before comparing wear data, a number of interesting observations can be made from a simple comparison of kinematics with those machines introduced in Section 2.6.3.

Durham, Leeds and Berkeley research groups have all revised their machines to create wear conditions more closely matched to those experienced *in vivo*. Modifications to the Durham and Leeds pin-on-plate machines include rotation of the pin in addition to the standard reciprocation of the test plate. Durham opted for a constant angular velocity of the pin achieved with direct electric motor drive via belt drive[105]. In contrast, the Leeds machine adopts an oscillating pin rotation driven through a gear linkage from the translation drive and hence inherently synchronous [113]. Both machines introduce some form of multi-directional motion but lack the programmability to study a range of motion paths. Furthermore, the kinematics associated with this type of machine complicate the ability to quantify the effects of motion path on wear rate, see Section 0, and Figure 2-28. Both machines employ a static load onto the test pin.

Reciprocating motion has been added to the Berkeley pin-on-disc tribometer[122]. Continuous disc rotation has been replaced using an electric motor and crank arm arrangement, similar to the Durham and Leeds adapted machines. This enables the pin to slide back and forth along an oscillating 90º circular arc. The adapted motion of this machine is too simplistic to introduce multi-directional shear, as demonstrated by the very low wear rates reported, but the start/stop kinematics are more likely to limit the degree to which hydrodynamic lubrication contributes to the load transfer at the pin/plate interface.

A pin-on-disc machine in which the pin is subject to constant sliding velocity is the circularly translating pin-on-disk device (CTPOD)[106]. However, unlike a simple pin-on-disc device the pin in the CTPOD is exposed to continuously changing shear vectors as the plate is circularly translated underneath. The CTPOD machine is a static load machine and is limited to circulatory motion unless a significant mechanical modification is made in order to generate elliptical wear paths[181].

More modern wear testers, such as the commercially available AMTI OrthoPOD and custom designed machines[104], have the ability to translate the pin discrete distances in the x and y direction. Shear vectors, rather than constantly changing, are controlled along the direction of motion. These studies rely on simple rectangular motion paths in order to define a primary and secondary sliding direction[112].

The Edinburgh tribometer conforms to the traditional pin-on-plate wear testing configuration. The components used to transfer motion on adapted machines provide multi-directional sliding but limit the range of motion. Restricted functionality is avoided in the Edinburgh machine using programmable computer controlled linear slides to translate the pin along two axes (Table 6-1). The machine is neither limited to circular nor rectangular motion paths; it can be programmed to produce a specific set of tribological motion conditions.

The pin remains fixed relative to the plate creating a uniform shear vector condition across the pin surface. These shear vectors are controlled and the direction is known to act along the sliding direction. As such, each pin surface worn on the Edinburgh tribometer is quantifiable with respect to sliding conditions because each point on the pin surface is worn in an identical manner. This arrangement is suited to investigation of the microstructural modification during UHMWPE wear. In contrast, oscillating pin-on-plate devices are more suited to rank the wear of bearing couples under constant load and sinusoidal velocity due to the anisotropic nature of the worn pin surface.

Group[reference]	**Bearing surface articulation**	**Uniform shear vector on pin surface**	**load curve**	**Slide track**
Bragdon 2001[104]**.**	Two translations	yes	Double peak	rectangular 5mmx10mm
Galvin 2006[113]**.**	Reciprocating / Translating	no	Constant	Stroke 28mm, pin rotation 60°
Gevaert 2005[120]**.**	Two translations	yes	Constant	5-pointed star, each length 20mm
Joyce 2000[105]**.**	Reciprocating / Translating	no	Constant	stroke 26mm, pin rotates
Saikko "100 station" 2005[123]**.**	Rotating, pin stationary	yes	Constant	circular, diameter 10mm
Saikko "12 station" 1998[106]**.**	Rotating, pin stationary	yes	Constant	circular, diameter 10mm
This study[182]	*Two translations*	*yes*	*Double peak*	*Elliptical (20mm x 10mm)*
Turell 2003[112]**.**	Two rotations	no	Constant	rectangular 3mmx7mm

Table 6-1: Pin on flat comparison.

The effects of nominal stress and contact area on UHMWPE wear have been much debated. The ASTM F732-00 (2006) on satisfactory clinical wear testing recommends a peak contact stress between 2MPa and 10MPa, and an average nominal contact stress of 3.54MPa. In this study our peak contact stress of 4.8MPa falls within the ASTM range, yet our mean contact stress of 1.9MPa is lower than the ASTM standard but similar in magnitude to Joyce *et al.*[105]

and higher than Saikko, who used a value of 1.1MPa suggesting that contact pressures in the hip may be lower than the ASTM indicates[123].

In one study, the effects of contact stress were investigated by keeping the applied load constant and varying the pin diameter[151]. Pin diameters ranged from 8-23mm resulting in a range of contact stresses between 23.9–2.8MPa respectively. The highest wear rate was found at 10.6MPa over a 12mm diameter pin. At diameters either side of this the wear rate decreased. The peak in wear factor was explained in terms of fluid replenishment. At smaller diameters, the contact surface would be sufficiently lubricated with proteins and hence even though a high stress is imposed the entre contact surface would be protected, reducing the wear rate. At larger diameters, because the stress is sufficiently low, lubrication starvation is not likely and fluid flow will occur between the plastic asperities and the metal surface. It is worth noting that a higher percentage of flakes (larger debris) were found at higher stresses (smaller diameters) than at lower contact stresses. The higher stresses could lead to a greater probability of crack propagation, causing larger flakes to be produced[183].

Dynamic loading has been shown to affect the wear rate of both conventional UHMWPE [150] and highly crosslinked UHMWPE[124]. Barbour *et al.* found that under simple cyclic loading the wear factor increased by 30% over that for UHMWPE under a constant load of similar magnitude. Despite this, many contemporary orthopaedic pin-on-plate research groups continue to use machines which impose a static load onto the pin[71, 72, 105, 106, 112, 113, 122, 123, 184]. Cyclic loading at the articulating interface is suggested to affect a number of tribological factors including the nature of the lubrication regime and degree of lubricant replenishment during the swing phase[104], the degree of protein absorption[185], the debris "dwell" time in the contact zone[150] and the degree of plasticity and fracture propagation; since a crack cannot propagate when it is fully closed[186]. Under static load the pin is permanently compressed onto the bearing surface. Continual compression may prevent debris from escaping the contact zone, unlike contacts which undergo periods of relief allowing surfaces to marginally separate. It is hypothesised that under static load, trapped particles may act to protect the polymer surface from the counter-bearing asperities, causing low misleading wear rates [187]. In addition, constant compressive stresses may further retard surface and near-surface microcrack growth. In order for cracks to propagate in mode 1 (tensile crack opening), new surfaces formed from crack growth must be able to move apart. Under a constant compressive load the ability to separate is limited, deterring this mechanism.

Some researchers suggest the addition of dynamic loading does not appear necessary[105, 123], where the added complication of the dynamic load arrangement may detract from the

simplistic nature of the pin-on-plate device. A varying load, through the simple Archard relationship, implies that the wear factor will also vary throughout each cycle (since the wear volume is proportional to the normal load). Under such conditions it becomes necessary to discretise the load and motion in order to describe the tribological conditions at any point in the wear cycle. In practice, this becomes difficult, since the amount of material lost per cycle must also be discretised. For simplicity, all wear factors in the Edinburgh study were calculated using the mean nominal load and sliding distance per cycle. Furthermore, sliding conditions, such as the UHMWPE friction coefficient, have been found to change with the magnitude of nominal stress; an increase in stress from 1MPa to 6MPa has been shown to cause a two-fold reduction in friction coefficient[111, 188]. As such, the introduction of dynamic load may better approach physiological conditions, but in doing so, the controlled conditions associated with static pin-on-plate machines may be compromised.

Articulation of metal-on-polymer artificial hip joints is considered to occur under both boundary and mixed lubrication regimes. Certainly one might have imagined lower wear rates from the Edinburgh machine since only 50% of each cycle is loaded. One might further postulate that the minimum film thickness between contacts will occur under the highest load and slowest velocity. The peak load occurs 0.11sec into each cycle. Under peak loading the relative velocity between the pin and plate is an appreciable 49.5mm/s. The mean composite surface roughness of the CoCrMo and UHMWPE surfaces used in this study is 0.83μm. By approximating the flat-on-flat with a sphere-on-flat such that the contact half-width of the sphere is similar in size to the radius of the pin, a film thickness of ~0.14μm is calculated using EHL theory under peak loading at 49.5mm/s. During the "swing" or lightly loaded phase of the cycle the film thickness increases to ~0.23μm. Although this is a crude approximation, it seems unlikely that a film thickness exceeding this will develop, resulting in a sliding regime dominated by boundary lubrication. Scholes *et al.* also predict boundary lubrication, a film thickness of 0.09μm occurring in their 28mm diameter CoCrMo ball and UHMWPE socket with a radial clearance of 0.2mm[27]. The smaller film thickness can be attributed to the higher load and a larger reduced radius of curvature.

Similar wear rates under static loading may be achieved by coincidence, but the type of wear mechanisms acting may be different to those that occur *in vivo* under dynamic loading. For this reason dynamic loading is often employed in more physiologically accurate hip simulator studies as required by the ASTM for full joint simulator testing[145]. However, in hip simulators, the nature of the flexion-extension and abduction-adduction make it difficult to correlate relationships between simple tribological conditions such as the effects of load profile on UHMWPE wear rate[127]. By introducing dynamic loading at the pin-on-plate

interface, the Edinburgh machine is capable of a more practically simple investigation of UHMWPE wear than simulators, whilst achieving a closer tribological match than previous pin-on-plate wear testers.

The use of dynamic loading in pin-on-plate studies has been adopted by few investigators. The literature reports one pin-on-plate study carried out on conventional UHMWPE[104] and one study on highly crosslinked material[135]. The machine used in both these studies is unable to account for load-soak specimens, instead relying on separate pre-soaked pins to establish the amount of fluid absorption. However, dynamic loading has been shown to significantly affect the amount of fluid absorption of UHWMPE. In one study, cyclically loaded crosslinked acetabular soak-control liners were found to gain as much as 19.26mg in weight compared to 1.24mg in the no-load soak cups over the same period[124]. This has important implications in gravimetric testing protocols, especially when the amount of mass loss attributed to wear can often be less than 10mg. Unloaded soak specimens may be inadequate in compensating for UHMWPE mass loss under dynamic-load wear studies. To provide the most accurate correction for fluid absorption the Edinburgh machine accommodates two dedicated load-soak stations which expose the control specimens to near identical conditions as the wear specimens.

The longest individual tests carried out on the Edinburgh wear tester were those that involved both -PE and +PE; conducted to 3 million cycles with 12 intermediate wear measurements. This exceeds the minimum two million test duration specified by the ASTM and the recommended minimum of four measurements subsequent to the initial measurement[145]. The cumulative number of cycles completed by the machine to date is approaching 10 million cycles; over this period the machine has proved reliable. With advances towards more wear resistant treatments such as crosslinking, or highly wear resistant polymers such as polyether-ether-ketone (PEEK), it seems likely that longer tests will be needed to generate and accurately record polymer wear.

Reliability is due to careful design in specifying and installing suitable components. Stepper motors and loading actuators were specified with sufficient size and power to operate well below the manufacturer's duty cycles, ensuring overloading and/or overheating was minimised. Each slide has good repeatability, ±0.02mm, providing accurate tracing of wear paths throughout the test duration. Limit switches and sensors ensure test variables are controlled and intermittently recorded to assess stability and accuracy. For example, each loading cycle was recorded periodically throughout each test and remained consistently

within 7% of its initial cycle. On average the loading cycles for the six stations remained within 3.2% during testing.

6.2 The Validation study

Laboratory studies have historically been used to wear rank bearing couples under simplified motion and loading. The aim of these experiments was often to approximate the modes of wear and wear rates found in the body on quick and simple screening devices under controlled conditions. This has led to a large spread in wear data; from those machines which approach clinical wear factors to those which do not. Any new tribometer should first be validated to confirm its suitability for carrying out further clinically pertinent studies.

The objective of the validation study was to measure polymer wear rates against orthopaedic grade CoCrMo under two motion types, in doing so verifying the need for multi-directional motion and the clinical relevance of the new machine. Of the three clinically relevant polymers wear tested in the current study, UHMWPE is the only material still used in load-bearing joint replacement today, so its wear behaviour is the most important to consider in these set of tests.

6.2.1 Polytetrafluoroethylene

Polytetrafluoroethylene (PTFE) was the initial polymer of choice for Charnley's hip arthroplasty due to its favourable properties of low friction and chemical inertness; desirable qualities for an implantable material. PTFE acetabular cups experienced high wear *in vivo* and were soon replaced by UHMWPE cups. Charnley found that femoral heads were penetrating into the 22mm diameter joint PTFE cups, following a linear trajectory, on average 0.2mm/month, equivalent to 2.26mm/year. Maximum penetration occurred under smaller diameter heads; hence smaller contact areas, higher stresses, and slower sliding velocities[1]. We report an average linear penetration rate of 0.17mm/million and 3.17mm/million cycles for PTFE under reciprocating and elliptical motion respectively (Table 5-1). Walking steps per year has been reported as ranging from 0.9million cycles to 1.6million cycles[189]. Converting mm/million to mm/year based on sliding distance per cycle would equate to a PTFE linear penetration rate of 2.8-5.1mm/year respectively. This is in good agreement with Charnley's published clinical range of 2-6mm/year[1]. Further, a clinical wear factor of $37x10^{-6}mm^3/Nm$ has been reported[164]. Our wear factor under elliptical motion is in good agreement, $36x10^{-6}mm^3/Nm$.

Very low PTFE wear rates have been observed in both water-lubricated hip simulator sliding and water-lubricated reciprocating pin-on-plate studies. In the hip simulator study the wear rate of PTFE was compared by sliding in water and bovine serum[190]. Wear in water produced extremely low wear rates, on average a four-fold reduction in comparison to Charnley's original data. In addition to low wear, water based sliding was found to produce a three-

phase wear plot, which introduced three different nominal wear rates throughout the duration of the test. In comparison, sliding in bovine serum was found to produce near constant wear rates.

In one pin-on-plate study, both linear-reciprocating motion and rotating pin-on-reciprocating plate motion produced very low wear factors in water lubricated sliding; $1.5x10^{-6}mm^3/Nm$ and $0.1x10^{-6}mm^3/Nm$ respectively[191].

In the present study, linear-reciprocating motion produced a wear factor of $1x10^{-6}mm^3/Nm$. This was an order of magnitude lower than the wear factor produced under elliptical motion and is similar in magnitude to the water lubricated sliding in the Joyce *et al*. study[191]. However, all sliding experiments were conducted in dilute newborn calf serum (28g/l protein concentration) so the low wear behaviour cannot be attributed to water-based sliding. Furthermore, the wear rate remained reasonably constant throughout the test, supporting previous observations of constant wear in a proteinacious environment. Despite ambiguity in the linear-reciprocating test, our multi-directional elliptical motion data is in very close agreement with the Joyce *et al*. study who report a wear factor of $37x10^{-6}mm^3/Nm$ using bovine calf serum diluted to a similar protein concentration of 25g/l.

6.2.2 Polyacetal

The wear behaviour of Polyacetal has been much discussed throughout its relatively short period of use in the manufacture of acetabular components. Polyacetal was suggested as a load-bearing polymer, due to its superior creep-resistance and hardness[156]. Polyacetal is approximately five-times harder than UHMWPE and was predicted to better resist the abrasive action of bone chips and acrylic cement should these enter the articulating zone. It was used in the Christiansen prosthesis from 1969, the majority implanted in Scandinavia. This design relied on a larger 37mm diameter head (in relation to Charnley's smaller joint sizes) and a second Polyacetal component; a trunnion bearing that permitted rotation between the femoral ball and stem, Figure 6-1.

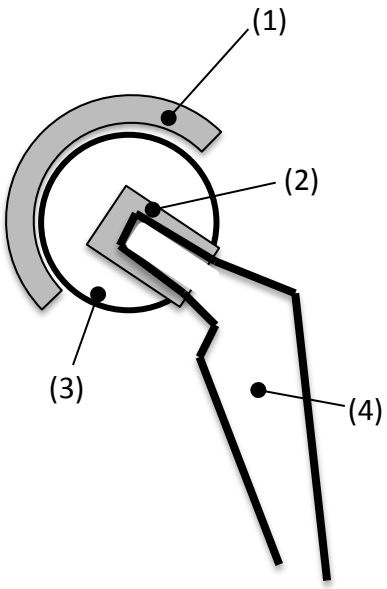

Figure 6-1: Christiansen hip prosthesis; 1) Polyacetal acetabular insert; 2) Polyacetal bearing insert; 3) CoCr femoral head; 4) CoCr femoral stem.

During normal gait the majority of rotation was designed to occur between the ball and stem, leaving the femoral head relatively stationary inside the cup. This design was thought to minimise loosening of the socket by reducing frictional torque transmitted to the bone/stem interface. Despite the trunnion, high revision rates *in vivo* led to the abandonment of polyacetal as an acetabular component after a period of 14 years. In one study, at 5-8 year follow up, 31% of Christiansen's prostheses had been revised in comparison with 4% of Charnley joints[192]. From anterior/posterior radiographic studies, socket penetration rates have been reported at approximately 0.4mm/year[193]. In the current study, under elliptical motion a steady-state linear penetration wear rate of 0.19mm/million cycles was found (Table 5-2). Elliptical motion resulted in similar wear factors for both UHMWPE and Polyacetal. This is consistent with the ASTM standard which ranks the wear rates of Polyacetal ≥ UHMWPE.

Using the steady-state linear penetration rate of 0.19mm/million and assuming one million cycles is approximately equivalent to one year of *in vivo* use, a 5mm thick acetabular component would take 42 years to wear through. However, during testing a brief run-away period of high wear was observed caused by metallic debris in chambers 2-4. Tests were stopped and pins and plates cleaned before further testing. The volumetric wear during the "high-wear" period was 33.73mm^3/million, equivalent to a penetration rate of 1.69mm/million, taking the 5mm cup approximately 3 years to wear out. This shows closer agreement with the Sudmann *et al.* 5-8 year follow-up study in which high wear areas are reported for explanted polyacetal components and in two cases the polyacetal components

had worn through[192]. A two-year follow-up study reported a 9% failure rate in the polyacetal Christiansen prosthesis as opposed to a 1% failure rate in the ultra-high molecular weight polyethylene Charnley prosthesis[194]. Both the literature and our findings confirm that in some conditions polyacetal is capable of providing a low-wear sliding surface, yet it is also susceptible to incoherent high third-body wear. This unpredictable behaviour is further substantiated by Mathiesen *et al.* who found that the frictional characteristics of polyacetal changed as the material aged *in vivo*[195]. UHMWPE sockets were found to exhibit steady friction coefficients.

6.2.3 UHMWPE

6.2.3.1 Clinical Comparison

Retrieved UHMWPE cups have been reported by Elfick *et al.* as having a mean wear factor of $2x10^{-6}mm^3/Nm$[116]. This was calculated from the average wear volume of sixty-five 32mm joint size cups, the average patient weight, and the approximated sliding distance based on an empirical formula suggested by Dowson and Wallbridge[164]. The estimated number of cycles during the median implantation period of 7.3years was calculated to be 12million cycles, equivalent to 1.6million cycles/year. Average sliding distance per cycle has been linked to femoral head diameter from computer models and gait analysis. Wang *et al.* propose that the average sliding distance per cycle of the ball in socket is approximately two-thirds that of the diameter[110]. This is supported by the previously mentioned retrieval study, where the average sliding distance per cycle of the 32mm diameter cohort was found to be 21.4mm/cycle[116]. Taking this into consideration, the sliding distance/year can be approximated as 34.24km/year ($1.6x10^6$ cycles of 21.4mm). In comparison, the elliptical sliding distance in this study is 50mm/cycle which means the equivalent number of cycles on our machine to achieve a clinical sliding distance per year would be 684,800 cycles. Under elliptical motion we report an average volumetric wear rate of $3.44mm^3$/million cycles. Using the linear relationship between sliding distance and wear volume, our wear volume/million cycles adjusted for the discrepancy between clinical and pin-on-plate sliding distances can be approximated as 3.44 x (684800/1000000), or $2.36mm^3$/year. Applying Elfick *et al's.* wear factor and median patient mass of 71.5kg, a wear volume of $48mm^3$/year can be back calculated. To a first approximation, using Archard's wear equation, the wear volume is said to be proportional to the nominal load. Our test pins are subject to an average nominal force of 39N/cycle. Under such circumstances we would expect the equivalent tribometer wear volume/year based on Elfick *et al.*'s study to be $2.67mm^3$/year (39N x $48mm^3$/701N). Our actual wear volume of $2.36mm^3$/year is in good agreement.

Finally, the ASTM states a clinically relevant linear wear range between 0.07–0.2mm/million cycles should be achieved for UHMWPE[145]. Under elliptical motion the mean linear penetration rate (mm/million cycles) was found to be 0.17mm/million which concurs with ASTM requirements and is in good agreement with post-creep penetration rates of 0.14mm/year[196] and larger penetration rates between 0.15-0.18mm/year for conventional material[115, 197]

Under elliptical motion the machine has produced UHMWPE and PTFE wear factors in the clinical range. However, because PTFE wears more quickly than UHMWPE, some researchers suggest that correctly ranking the polymers in order of wear is too trivial and is not a satisfactory measure of how close a tribometer approximates *in vivo* wear. Instead, the correct wear ranking should also be supported by clinically relevant wear ratios between PTFE and UHMWPE[34, 198]. Early retrieval work by Charnley on both PTFE and UHMWPE acetabular liners showed the PTFE cups to have worn at least 13 times higher[1, 115]. Under elliptical motion a wear ratio of 18 agrees well with clinically published data. The wear ratio of PTFE/UHMWPE under linear reciprocating motion was 123.

6.2.3.2 Pin-on-Plate Comparison

Before considering the importance of multi-directional motion on the wear rate of UHMWPE, a brief retrospective account of linear reciprocating motion is required. Linear reciprocating was the first mode of long duration testing carried out on the Edinburgh tribometer and teething issues were expected. On two occasions, two chambers ran dry between weighing intervals (Figure 5-4). Adjustments were made to the machine to prevent recurrence of this behaviour but regrettably, the opportunity to complete another 3 million cycle test did not exist. Despite this, wear results excluding these brief run-away periods were similar to those expected and found from other wear testers, giving confidence in the ability of the machine to produce relevant values. Wear rates remained reasonably constant throughout the duration of the test, similar to wear data reported by Cooper *et al.* who previously ran linear-reciprocating tests on smooth counterfaces lubricated with bovine serum[23]. They report a constant wear factor of $12 \times 10^{-9} mm^3/Nm$, smaller than our reported steady-state wear factor of $29 \times 10^{-9} mm^3/Nm$. The obvious difference between the two tests is the nature of our dynamic load replacing their static 80N load which produced a nominal contact stress of 12MPa onto their pins. This is higher than our average contact stress of 1.9MPa. In a more recent pin-on-plate study, higher stresses were shown to result in lower wear factors[150] which may explain the smaller wear factor reported by Cooper *et al.*. Finally, no details on the protein concentration of the bovine serum used in the Leeds study were given.

The remainder of this section is based on those machines which exert multi-directional motion at the bearing interface. Joyce *et al.* validated an adapted pin-on-plate machine which incorporates multi-directional motion at the pin-plate interface[105]. The modification includes the addition of rotation to the test pins in addition to the standard reciprocation of the test plates. Test pins used in this machine are machined from cylinders to an external diameter of 5mm. A stroke length of 26mm is achieved through a crank and connecting rod mechanism powered by an electric motor. Plates translate and pins rotate at 1Hz under a constant load of 40N, or nominal contact pressure of 2MPa. A comparison of the Edinburgh machine to the Durham machine is obvious. Both machines use 5mm diameter test pins, both have similar sliding distances per cycle and both have similar average contact pressures over a test cycle. There are two significant differences between the tribological setup of the one used in the present study and the Durham rig. The first is the addition of dynamic loading, with higher peak contact pressures than the constant pressure seen on the Durham machine. The swing phase of the Edinburgh loading cycle has been programmed to account for 50% of the cycle time. Secondly, the Edinburgh tribometer has been designed to ensure uniform shear vectors across the whole pin surface, unlike the Durham wear setup, where the rotating pin results in complex, varying, wear paths across the surface. Bearing in mind these tribological differences, Joyce reports a UHMWPE wear rate of 2.3mm^3/million cycles and a wear factor of 1.1x10^{-6}mm^3/Nm. The addition of simple cyclic loading has been reported to increase the wear factor by 30% over that calculated for UHMWPE under a constant load of similar magnitude[150]. Hence, were the Durham machines to adopt a simple square-wave load profile we might predict a 30% increase in their current wear factor. This predicted wear factor of 1.43x10^{-6}mm^3/Nm is in closer agreement with our wear factor of 1.60x10^{-6}mm^3/Nm.

The two-axis stepper driven system built and applied by Bragdon *et al.* is capable of producing a rectangular wear path (10x5mm) with a dynamic load profile (peak contact stress 4.8MPa) applied onto 8mm diameter pins[104]. From this study a wear rate of 10.4mg/million cycles is reported for UHMWPE sliding against a smooth cobalt chrome counterface (R_a 0.05µm). This is over three-times the wear rate of 3.25mg/million cycles generated on our machine under elliptical motion. Bragdon *et al.'s* pins slide 30km/million cycles as opposed to our 50km/million. However, because both machines employ different diameter pins and dynamic loading profiles, the range of resultant lubrication regimes during each respective wear cycle make it difficult to compare wear rates. Furthermore, no wear factors are reported from the Bragdon study. The open wear path of our model does obviate the sinusoidal velocity profile inherent over each side of a rectangular path[104, 112], producing a closer gait-matched tribological setup. They do, however, find UHMWPE pins under

simple reciprocating motion to wear two orders of magnitude lower than pins worn under the rectangular path. A similar reduction was observed in this study.

Galvin *et al*. applied both a ±10 deg or ±30 deg rotation about the long axis of their UHMWPE pins as they were loaded onto stainless steel plates that reciprocate over a stroke length of 28mm[113]. Tests on smooth counterfaces (R_a ~0.01µm) produced wear factors of $0.17x10^{-6}mm^3/Nm$ and $0.22x10^{-6}mm^3/Nm$ for the ±10deg and ±30deg rotation respectively. The increase in cross shear angle at the pin/plate interface resulted in a larger wear factor. This further demonstrates Wang's proposal[111] that increasing the angle of cross-shear, up to a maximum of 90deg at the articulating interface, generates larger amounts of frictional work used to release a greater amount of debris (Equation 2-6). Both wear factors generated from the Leeds machine are an order of magnitude lower than our elliptical wear factor. However, the different wear paths generated across the worn surface as the pin reciprocates and the plate translates makes it difficult to make a direct comparison.

The Clemson group "MAX-Shear Wear Testing System" is a highly capable machine on which stainless steel spheres form the upper bearing material and a UHMWPE plate forms the lower bearing surface[120]. The spheres are loaded in a constant manner onto the translating polymer plate. This is similar to conditions approaching those found in total knee joint replacement bearing systems, rather than the polymer pin dynamically loaded onto a cobalt-chrome plate in the current study; a closer tribological match to the hip joint. Within the Clemson study a five-pointed star test pattern was used in conjunction with surface profilometry to assess the ratio of wear volume normalised to sliding distance (mm^3/mm) calculated from the linear segments and the cross-shear points of the star. It is difficult to compare the findings of this machine with setups in which the sacrificial specimen undergoes constant sliding and is loaded either constantly or dynamically throughout each cycle. A summary of some contemporary UHMWPE pin-on-plate wear results is shown in Table 6-2.

Group	Wear path motion	Pin diameter (mm)	Wear rate (mg/million)	Wear factor x 10^{-6} (mm^3/Nm)	Linear wear rate (mm/million)
Bragdon *et al.*[104]	Two translations	9	10.10	-	-
Galvin *et al.*[113]	Reciprocating pin / Translating plate	8	-	0.22	-
Joyce *et al.*[105]	Reciprocating pin / Translating plate	5	~2.2	1.10	0.12
Saikko[106]	Rotating, pin stationary	3mm chamfered at 60°	1.69	0.80	0.13
This Study	***Two translations***	***5***	***3.25***	***1.60***	***0.17***
Turell *et al.*[112]	Two rotations	9	~8.9	2.50	-

Table 6-2: Pin-on-flat UHMWPE wear rates and wear factors.

6.3 The Crosslinked Wear Study

6.3.1 Swelling

The significant difference in swelling ratio found herein and by others indicates a profound alteration to the UHMWPE microstructure following exposure to high dosages of irradiation. An explanation of these molecular differences has been used in-part to describe the wear performance gain using highly crosslinked acetabular cups rather than conventional material. This has been reviewed in Section 2.7.2.

Swelling experiments have been used by several research groups to infer the crosslink density of UHMWPE although there is reservation as to whether this relationship holds true for semi-crystalline polymers. Some researchers suggest the association between swelling and crosslink density does not apply to UHMWPE because the majority of crosslinking occurs in the amorphous domain rather than occurring homogenously throughout the microstructure[199].

In one study the swelling ratio of UHMWPE was found to reach a constant value at irradiation doses greater than 27kGy[70]. An alternative study found the swelling ratio to continuously decrease with increasing irradiation dose, up to the maximum investigated dose of 150kGy[111]. Unfortunately, it is not possible to confirm which relationship best describes UHMWPE under our test conditions because only unirradiated and 100kGy material was investigated.

According to Edidin *et al.* a dramatic increase in the wear performance of UHMWPE occurred when the irradiation dose level was increased from 25kGy to 90kGy. Despite this, the swell ratio was found to reach a constant after 27kGy. Should the Flory-Rehner relationship between swell ratio and crosslink density, shown in Equation 4-4, hold true then this would indicate a constant crosslink density above 27kGy. As such, crosslink density could not be used to explain the increased wear performance at higher irradiation doses.

However, contemporary theoretical wear models explain the improved wear resistance in crosslinked material by exploiting the idea of increasing crosslink density at higher irradiation doses; increasing irradiation dose increases the crosslink density which in turn increases the number of chemical bonds between adjacent molecular chains making it more difficult to split one molecule from another[111]. This appears consistent with clinical findings; conventional material is often sterilised at dosages higher than 27kGy but is known to wear faster than highly crosslinked material, attributed to fewer crosslinks in the conventional material to prevent rupture and limit the amount and ease of debris released. As such, a

difference in swell ratio and crosslink levels in materials irradiated between 27–106kGy might have been expected.

The lack of relationship between swell ratio and wear resistance in the Edidin study would suggest that either swelling is an inadequate technique for accurately determining the crosslink density, or wear resistance is only in-part dependent on the degree of crosslinking. Despite this uncertainty, Edidin *et al.* report a swell ratio of 2.87±0.13 at 100kGy which is in good agreement with the swelling ratio of 2.8 reported herein. To corroborate this, McKellop *et al.* report a swell ratio between 2.5-2.8 for 95kGy material[136].

Unlike Edidin *et al.*, Wang reports the swelling ratio of UHMWPE to continually decrease as the polymer is subject to increasing irradiation dose between 25-150kGy, suggesting an increase in crosslink density at higher doses[111]. In agreement with Edidin *et al.*, UHMWPE sockets were found to offer improved wear resistance when irradiation was increased from 25kGy to 75kGy. The sensitivity of UHMWPE *in vitro* wear at these irradiation levels agrees well with clinical studies. Significant wear reductions in highly crosslinked material (75-100kGy) are observed *in vivo* when compared with conventional material typically sterilised at 25-40kGy, see Section 6.3.2.

Using swelling data and Flory-Rehner theory, Wang extrapolates a line of best fit between a plot of average molecular weight between crosslinks and wear rate. A theoretical zero wear condition was proposed should the molecular weight between crosslinks in the UHMWPE material be less than or equal to 4258g/mol. The linear relationship is described in Equation 6-1 where, k, is the wear factor and M_c, is the average molecular weight between crosslinks:

$$k = [(0.0003M_c) - 4258] \times 10^{-6}$$

Equation 6-1: Empirical relationship between wear factor and average molecular weight between crosslinks.

Let us apply the same Flory-Rehner theory, which approximates the average molecular weight between crosslinks for our 100kGy material to be 5663g/mol. Using Equation 6-1 a theoretical wear factor of 0.42×10^{-6} mm^3/Nm is calculated. Our actual experimental elliptical wear factor was 0.13×10^{-6}mm^3/Nm. The difference may be attributed to the difference in surface roughness of the metal components used in the two studies. In Wang's tests the femoral heads were polished to an average centreline surface roughness of 0.015µm, an order of magnitude greater than the mean arithmetic surface roughness of our plates, 0.0015µm. The increased roughness might be expected to increase the relative wear of the crosslinked material which is reportedly more susceptible to counter-bearing roughness than

conventional material[200]. We would therefore expect a steeper regression line in Wang's initial study which would account for the larger theoretical wear factor.

Unirradiated material was close to dissolving after the 24hr swelling period, only recoverable due to the mesh cage which contained the gel. The average unirradiated swelling ratio was found to be 28. Similar observations and swelling ratios have been published by DiMaio *et al.*[201] and Edidin *et al*[70], who confirm high swelling ratios in unirradiated material of 30 and 25 respectively.

6.3.2 Clinical Comparison

A 92% reduction in crosslinked wear was found under our elliptical motion study. Similar wear performance gains have been reported in short-term radiographic follow-up studies[137, 138]. Heisel *et al*. compared linear head penetration in GUR1150 non-crosslinked cups sterilised by gamma irradiation in air and GUR1050 cups machined from ram extruded bar. The crosslinked cohort were previously subjected to 50kGy gamma irradiation, re-melted at 155ºC for 24hours and sterilised with gas plasma prior to implantation. Despite the modest level of crosslinking irradiation, an 81% reduction in wear rate was found in the crosslinked group. The annual linear wear rates of the conventional and crosslinked material was 0.13mm/year and 0.02mm/year respectively.

Dorr *et al.* report a 45% reduction in annual linear wear rate in cross-linked liners when compared to conventional material at five years implantation. The annual wear rate of liners manufactured from 25-40kGy conventional material and 95kGy crosslinked material was 0.065mm/year and 0.029mm/year respectively. The crosslinked pins worn on the Edinburgh tribometer were found to wear at an average rate of 0.014mm/million cycles under multi-directional motion. This is approximately 50% lower than that found in the Dorr study, but almost 50% higher than the 0.008mm/year reported by Harris for similar crosslinked material[196]. Harris reports a 94% wear reduction in joints articulating against highly crosslinked rather than conventional cups.

6.3.3 Pin-on-Plate Crosslinked UHMWPE Studies

Linear-reciprocating motion, defined as having zero cross-shear[111], did not exhibit a statistically significant difference in mean steady-state wear rates between unirradiated (-PE) and highly crosslinked (+PE) material groups. These observations support earlier findings by Wang *et al.* who investigated UHMWPE motion dependent behaviour by wear testing UHMWPE exposed to 0–100kGy on both knee and hip simulators[143]. The tibial components, tested on a knee simulator with limited cross-shear, were found to undergo similar wear rates, independent of radiation dosage. In contrast, acetabular components tested on a hip

simulator displayed an exponentially decreasing wear trend with increasing radiation dose, supporting the motion dependent wear response of crosslinked polyethylene.

The use of dynamic loading in pin-on-plate crosslinked studies has been adopted by few investigators. Muratoglu *et al.* used a dynamically loaded (Paul-type, ~445N peak 1, 290N peak 2), bi-directional (10x5mm rectangular wear path) tribometer to investigate the wear behaviour of unirradiated and 100kGy crosslinked material[135]. They report wear rates for the unirradiated material as 9.8mg/million cycles reducing to 1.6mg/million cycles for irradiated; an 84% reduction in wear rate. The wear rate of +PE subjected to elliptical motion in our study was found to be 0.26mg/million cycles, substantially lower than that of Muratoglu *et al*.. Unfortunately, wear factors were not reported for the bi-directional tests, so a direct comparison between the tribological conditions with respect to sliding distance and nominal load is not possible. However, the sliding distance per cycle of the ellipse used in this work is ~50mm in comparison to the total rectangular sliding path length of 30mm. This equates to the pins used in this study sliding an additional 20km per million cycles. The increased sliding distance would be expected to produce higher not lower wear rates per million cycles. Furthermore, Muratoglu *et al*. employed 9mm diameter pins onto which a heel-strike peak contact stress of ~7MPa was applied equating to a peak force of ~445N; higher than the peak force of 94.3N used in the present study. The effect of dynamic loading on the wear rate is likely to be complex as additional modes of lubrication may be experienced between different load profiles and over statically loaded instruments.

Galvin *et al.* report a 73% wear reduction using 100kGy material instead of unirradiated material sliding against a smooth counterface[113]. The reduced wear benefit of crosslinking may result from the variable tribological conditions inherent in Galvin *et al's*. adapted pin-on-plate tribometer. The rotating pin-on-oscillating plate design results in a continuously variable wear path along the radius of the face of the pin. Those points on the pin surface nearer the centre will travel in a more linear fashion, be subjected to limited multi-directionality and trace paths with higher aspect ratios. High aspect ratio wear paths have been found to cause lower wear rates in conventional UHMWPE[112, 181] which may explain the reduced difference between wear of non-crosslinked and crosslinked material on this machine. Galvin *et al.* report a wear factor of $0.06 \times 10^{-6} mm^3/Nm$ for 100kGy material experiencing 60 degrees of pin rotation against a smooth counterface. This is an order of magnitude lower than the elliptical wear factor of $0.13 \times 10^{-6} mm^3/Nm$ found in the current study. However, they also report a wear factor of $0.2 \times 10^{-6} mm^{3/}Nm$ for their unirradiated material which is an order of magnitude lower than the value reported herein and that reported from clinical studies.

Hip simulator studies have also shown significant wear savings in crosslinked material[136, 202]. Mckellop *et al.* report an 87% reduction in wear rate of UHMWPE gamma irradiated at 95kGy compared to cups machined from bulk material irradiated at 33kGy. Ries *et al*. report a 96% reduction in wear using 100kGy irradiated cups when measured against conventional UHMWPE cups. Both these are in good agreement with the 92% decrease in wear rate of 100kGy material reported in this study. The modest level of crosslinking achieved at conventional sterilization doses do not provide the dramatic wear resistance offered by heavily irradiated UHMWPE. Our non-crosslinked material would therefore be expected to show similar wear behaviour to clinical data. This level of agreement between the advanced pin-on-plate tribometer described in this study and multi-directional joint simulators confirms the value of the further developments in tribometer design during the past decade.

6.4 The Crystallinity Study

Contemporary pin-on-plate studies are conducted on machines with more realistic motion and loading, shifting emphasis from the description of UHMWPE bulk wear behaviour to in-depth microstructural characterisation. The remainder of this discussion is focused around microstructural development observed throughout the current study.

The process of microstructural change is of great influence on the wear properties of UHMWPE. The modified sub-surface zone observed in worn UHMWPE acetabular cups has been labelled the plasticity-induced damage layer[70]. Edidin *et al.* classified this sliding-induced, altered layer by the discovery of oriented crystal lamellae within the near-surface. The TEM images they present show micro-domains of lamellae orientation up to a critical sub-surface depth of 8μm in unirradiated material and 4μm in highly crosslinked material. At these depths the images appear similar to images taken of the unworn bulk microstructure. The TEM micrographs show no evidence of lamellae fragmentation within the sliding induced damage layer.

To further characterise the microstructure and depth to which the sliding affected sub-surface layer extends, we conducted depth profiling using a pseudo-confocal Raman microscope. The Raman crystallinity results presented herein represent the percentage of crystalline material in –PE (Figure 5-23) and +PE (Figure 5-24) found at the surface and sub-surface following three million linear and elliptical wear cycles.

6.4.1 Unirradiated UHMWPE

Unirradiated material, worn under elliptical motion was characterised with similar percentage crystallinity to the unworn control up to the investigated depth of 25μm. This implied that in response to multi-directional motion, deformation mechanisms within unirradiated UHMWPE were constrained to the amorphous domain. Such behaviour would leave the majority of lamellae undamaged and crystallinity ratio unchanged from the bulk material.

This proposed damage model exploits the deformation order in polyethylene (Section 2.7.1), where interlamellar (amorphous) mechanisms are thought to precede intralamellar (crystalline) deformation mechanisms[131]. FE-SEM images support this hypothesis, showing the elliptically worn microstructure to be similar (in terms of lamellae size, breadth and orientation) to the unworn control. Furthermore, the absence of lamellae fragmentation under multi-directional motion is in support of the TEM images published by Edidin *et al.*[70].

If we accept that crystalline lamellae in unirradiated material remain largely undamaged under multi-directional motion then previous wear theories may be scrutinised on this basis.

In broad agreement, current theories suggest only amorphous regions in the semi-crystalline UHMWPE are modified during wear[71, 111]. Tearing and/or crack propagation through the amorphous material at critical strain forms the basis for debris generation. However, both have idiosyncrasies which should be addressed.

Klapperich *et al.*, through uni-directional pin-on-disc wear testing found UHMWPE to undergo preferential lamellae alignment in the direction of sliding[71]. They suggest this development reduces the strength of the material; randomly oriented lamellae might better deflect cracks than an orientated microstructure and, as such, offer greater resistance to crack growth. However, this model does not lend itself to the wear of THA. The experimental conditions they use offer problems for comparison to our study. The simple continuous rotation of the disc and higher nominal contact pressures (minimum 16.2MPa) would produce worn surfaces quite different from those found herein. One could further argue that uni-directional motion, which is known to produce lower wear factors, would therefore strengthen the material rather than weaken it as suggested in the Klapperich study. Furthermore, our finding of lamellae fragmentation under simplified linear-reciprocating motion, kinematics which are closer to the Klapperich wear study, questions the basis of deformation mechanisms occurring exclusively in the amorphous domain.

Contrary to Klapperich *et al.*, Wang eludes the obvious question over the applicability of uni-directional motion by developing a multi-directional wear theory. Ignoring wear in the primary direction he solely acknowledges wear debris to originate from secondary motion; tearing pre-aligned molecules from one another[111]. The assumptions used seem somewhat idealistic; our lack of lamellae re-alignment under elliptical motion questions the basis of microstructural orientation being a precursor to wear in the UHMWPE acetabular cup.

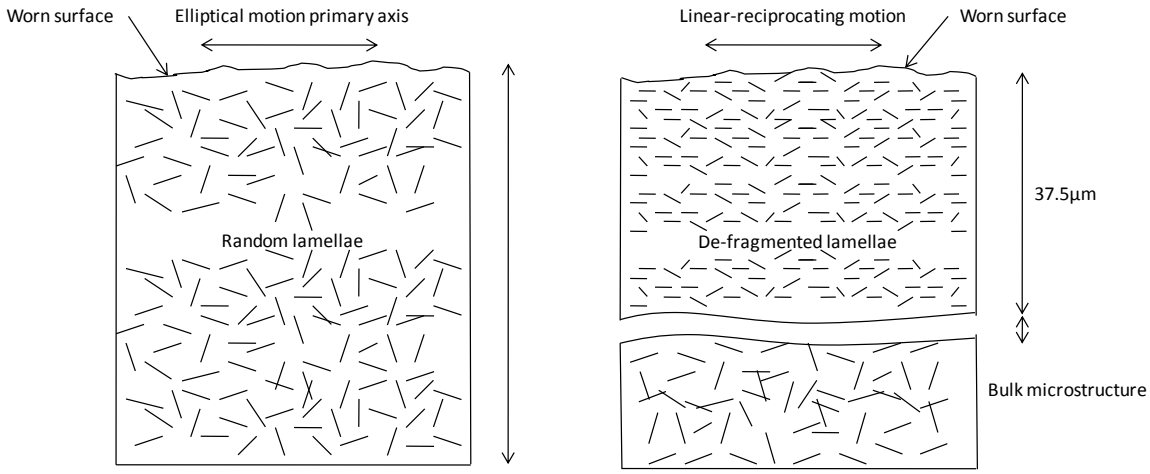

Figure 6-2: Schematic of worn elliptical and linear-reciprocating unirradiated UHMWPE microstructures. Under elliptical motion the worn microstructure remained similar to bulk material, implying deformation mechanisms were constrained to the amorphous domains. Under reciprocating motion smaller and broken, de-fragmented, lamellae were observed.

In contrast, the lower wearing –PE surfaces under linear reciprocating motion were found to undergo intralamellar deformation mechanisms leading to de-crystallisation. This was attributed to strain induced microstructural amorphous and crystalline degradation mechanisms. FE-SEM images yielded evidence of crystalline fragmentation, with the appearance of smaller broken lamellae in the worn microstructure (Figure 5-30). The potential for considerable accumulation of damage on, and beneath, the slower wearing surface may have caused a transfer of the deformation mechanisms from acting preferentially within the amorphous domain to occurring, in addition, within the crystalline domains. Deformation within the crystalline lamellae may be the wear mechanism responsible for crystalline chain slip and lamellae break-up. Schematics of unirradiated directional dependent worn microstructures under our existing set of conditions are seen in Figure 6-2.

Although lower crystallinity was found in the reciprocating cohort (in comparison to the unworn control and elliptically worn surfaces), we observed no statistical difference in mean crystallinity between the surface and sub-surface of this group. This suggests that the de-crystallisation zone may extend further that the maximum sampled depth of 37.5µm. Had the extent of sub-surface damage been constrained to less than this, an increase in crystallinity with increasing depth should have been observed as the microstructure returned to its native configuration being no longer affected by the frictional forces and de-crystallisation phenomenon at the surface.

In an earlier study, Davey *et al.* conducted polarised Fourier-transform infrared spectroscopy (FTIR) on retrieved UHMWPE acetabular components[203]. Cylindrical cores were taken perpendicular to the worn surface and then sectioned on a microtome into 200μm thick slices. They found the greatest amount of lamellar orientation occurring in the first 200μm beneath the surface, although microstructural re-arrangement was also apparent up to 400μm. The Raman technique employed within this study indicated a sub-surface damage layer consisting of a de-crystallisation zone extending to a depth greater than 37μm. The only material and wear path combination that showed no observable change in surface crystallinity under sliding was the unirradiated material worn under elliptical motion.

The following two references are used to explore the idea that near-surface UHMWPE crystallinity may either increase or decrease depending on the sliding conditions. The purpose here is not to compare the following studies with our own; they are markedly different both in terms of wear test motion, and dry compared to lubricated sliding. However they do serve to illustrate the dependence of microstructural development on tribological test conditions. As such, care should be taken when attempting to model *in vivo* wear accurately.

In the first study a steel ring was rotated against a flat UHMWPE specimen. Under such conditions an increase in crystallinity of the worn UHMWPE surface was reported[204]. The nature of the wear test created unidirectional shear forces on the surface and sub-surface of the UHMWPE sample. The tests were performed without lubrication. Crystallinity was assessed through use of DSC. Samples were sliced from the worn and unworn regions. The increase in crystallinity was attributed to annealing of the surface material due to increased surface temperatures at the sliding surface. Prolonged elevated temperatures experienced at the worn surface were thought sufficient to allow UHMWPE molecules to re-arrange, becoming more ordered in the form of larger crystals. Crystallinity within the worn surface was calculated at 59.20%, compared to the bulk crystallinity of 49%.

In the second study, a larger de-crystallised sub-surface zone extending up to and exceeding 200μm beneath the surface was found[205]. Dryzek *et al.* conducted pin-on-disk studies rubbing 10mm diameter pellets of UHMWPE onto a stainless steel disk with nominal loads of 100N and 150N. Again, sliding was conducted in the absence of lubricant. X-ray diffraction indicated 100m of sliding was enough to cause a de-crystallised surface and sub-surface layer, well beyond 200μm into the material. Clearly, the likely transfer-film formation and heat build-up experienced in Dryzek *et al.'s* study disallow a direct comparison. However, it does serve to illustrate that the uni-directional nature of the pin-on-disk will, just like the linear-reciprocating motion applied herein, cause strain hardening and

preferential lamellar alignment at substantial depths beneath the surface beyond those expected from a consideration of the contact mechanics. Under these simplified tribological conditions we also found a de-crystallised worn surface and sub-surface layer in UHMWPE.

6.4.2 Highly Crosslinked UHMWPE

Edidin *et al.* suggest that crosslinking may constrain the ability of the crystalline lamellae to re-orient, resulting in a smaller plasticity induced damage layer and lower wear rates[70]. In the current study crosslinking was found to cause noticeable reductions in wear rate under elliptical motion. Unlike the unirradiated group, Raman spectroscopy indicated lower surface and sub-surface crystallinity in both +PE motion groups when compared to the +PE unworn control (Figure 5-24). This finding was supported by FE-SEM micrographs showing evidence of fragmented lamellae in response to elliptical (Figure 5-32) and linear-reciprocating (Figure 5-33) motion. Similarly to the unirradiated test, the linear motion group were found to have the lowest +PE crystallinity.

Crosslinked material worn under linear or elliptical motion exhibited a trend of increasing crystallinity with depth beneath the surface, suggesting the extent of surface stresses and strains diminished as the distance beneath the surface increased. This is in agreement with contact mechanics theorems e.g. Hertz. However, sub 37.5µm neither group, linear reciprocating (49.6%) or elliptical (52.2%) reached the crystallinity ratio of the unworn control material (53.8%). This may be explained through a de-crystallised damage layer extending further than the maximum depth of 37.5µm explored in this study.

It is difficult to describe the sub-surface deformation conditions occurring in the current test due to the flat-on-flat contact geometry. This makes the application of Hertzian contact within the scope of elastic stress fields beneath the +PE surface difficult. By approximating the flat-on-flat with a sphere-on-flat such that the contact half-width of the sphere is similar in size to the radius of the pin, Hertzian contact gives the depth at which the maximum shear stress occurs as >1.4mm. Although this is a crude approximation it seems likely that sliding induced shear stresses will far exceed the 4µm plasticity induced damage layer first proposed by Edidin *et al.*. This supports the notion of a larger than measured +PE damage zone proposed in our study.

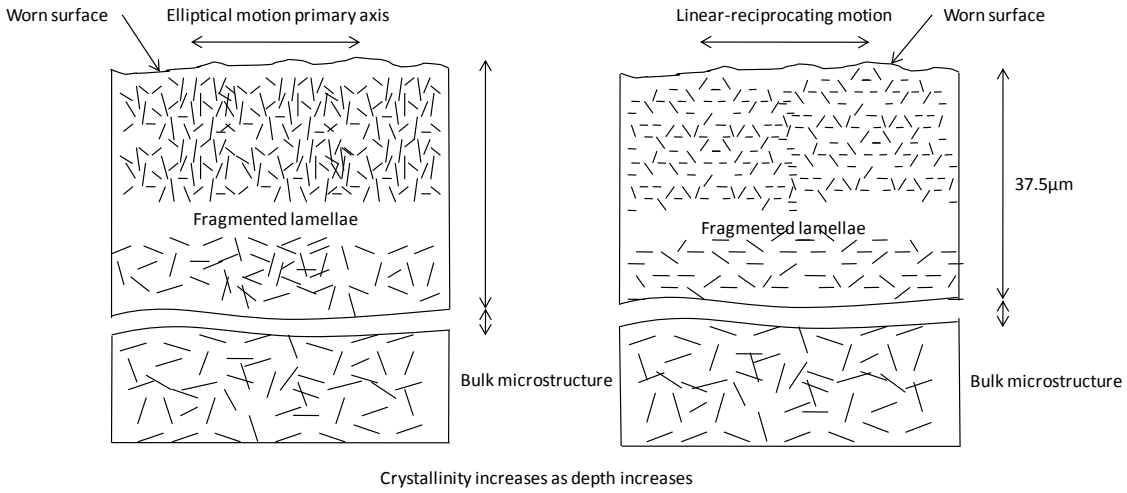

Figure 6-3: Schematic of worn elliptical and linear-reciprocating highly crosslinked microstructures. Under both types of motion alignment and fragmented lamellae were observed. Alignment was more significant under reciprocating wear.

The results presented herein indicate that +PE experiences a sub-surface damage layer which contains in-part re-oriented and fragmented lamellae regardless of motion path. Under both types of motion, a de-crystallisation zone was found to extend more than 37.5µm beneath the surface. This is shown schematically in Figure 6-3; smaller/broken lamellae were thought to be found closer to the worn surface in accordance with the increasing crystallinity with depth trend from the Raman spectra. Microstructural re-orientation was more obvious in the linear-reciprocating cohort.

The addition of irradiation controlled crosslinking produced a more wear resistant surface under multi-directional motion. These lower wearing surfaces appeared to accumulate higher levels of residual damage due to the increased period taken for a given amount of material to be removed. In brief, this resulted in a greater accumulation of residual damage in crosslinked rather than unirradiated surfaces. Furthermore, the slower wearing surfaces exhibited lower crystallinity following the completion of each wear test. This confirmed the hypothesis that a transition from amorphous to crystalline deformation mechanisms exists at higher levels of damage. Broken lamellae, particularly in the highly wear resistance crosslinked material may finally be released as sub-micron sized debris.

6.5 Microstructural Damage

The limited series of experiments (Section 4.4.4) regarding the ~1129cm^{-1} (symmetric C-C stretch mode) peak broadening of uniaxial strained UHMWPE Raman spectra may best be described as a preliminary study. It was not the intention of these experiments to correlate uniaxial strain with sliding induced damage, but rather to acknowledge the finding of Kyomoto *et al.*; ~1129cm^{-1} peak broadening occurs in response to damage and/or strain accumulation in UHMWPE material[173]. The Raman pilot study provided a method of qualitatively indicating relative amounts of damage between material groups.

6.5.1 Tooling Damage

The starting microstructure (consisting of machined surfaces) did not influence steady-state UHMWPE wear rates. This has been described in detail as part of the validation discussion; wear factors were similar in magnitude to previous tribometer studies and clinical reports. However, damage imposed into the near-surface during machining (prior to sliding) was identified by Raman peak broadening.

A damage zone caused by machining appeared to exceed 37.5µm beneath the surface. This was apparent on all pin surfaces, regardless of motion type or irradiation treatment, confirmed by the broader 1129cm^{-1} peak in both the unirradiated (Figure 5-25) and crosslinked (Figure 5-26) pins when compared to the respective microtomed control specimens. As such, all pins commenced sliding with residual "tool" strain.

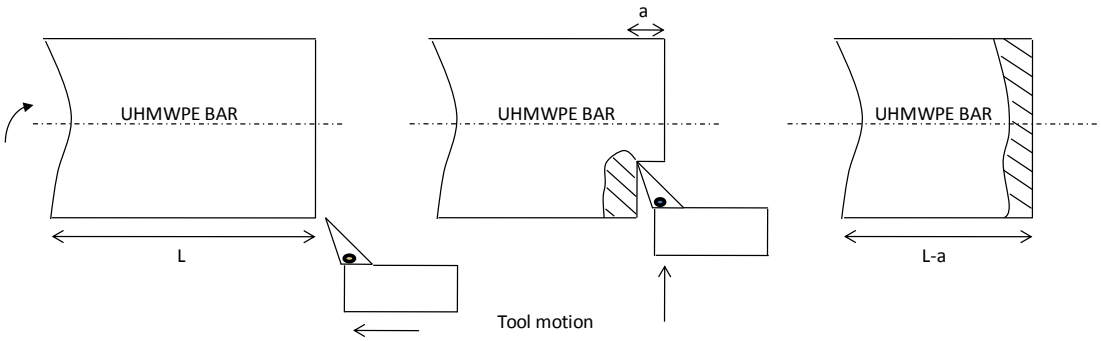

Figure 6-4: Machining process induced a near-surface damage zone due to the friction of the cutting tool across the face of the UHMWPE bar.

Let us consider this in more detail; as the tool-piece cuts across the surface of the material, surface and sub-surface microstructural damage will be imparted into the finished specimen. A schematic of this process is seen in Figure 6-4. Damage, necessary for the near-surface de-crystallisation observed under the Raman microscope could be introduced in this way. The residual stresses and strains may become important when considering those manufacturing

methods which machine to final dimensions after heat-treatment, thereby degrading the near-surface microstructure prior to implantation.

Higher wear in ram extruded and machined cups over direct compression moulded (DCM) cups has been reportedly linked to better consolidation and fewer fusion defects under compression moulding[84]. Our results also advocate the presence of a degraded surface and near-surface zone when UHMWPE is manufactured through machining. This may further explain the poorer wear performance of ram extruded and machined cups. To minimise the damage zone an additional post-machining below melt-annealing step is proposed.

The notion that microtomed material contains minimal residual damage is supported by Raman spectra indicating this group, independent of crosslinking, to have the narrowest 1129cm^{-1} band. This justifies the decision to use the microtomed group as the control group, against which microstructural development in response to sliding motion and dynamic loading is compared.

6.5.2 Unirradiated UHMWPE

For the group of unirradiated UHMWPE pins subjected to linear reciprocating motion, peak broadening was statistically larger (ANOVA $p<0.05$) than the load-soak pins up to the sub-surface depth of 37.5µm (ANOVA $p=0.84$); suggesting that this sliding motion introduced additional strain into the already tool-damaged near-surface. Such microstructural restructuring supports strain accumulation wear models[65, 140, 206].

Under simplified linear-reciprocating motion, linear penetration attributed to wear was calculated to be ~9µm. It follows that the final worn surfaces remain within the initial "tool-damaged" domain; this was likely to be greater than 37.5µm as discussed in Section 6.5.1. Hence, upon leaving the additional near-surface damage zone caused by sliding, Raman peak broadening should diminish to those values found within the load-only machined material. This appeared to occur as seen in Figure 5-25, suggesting the first 37.5µm of sub-surface material to be the maximum depth influenced by linear-reciprocating motion.

Under elliptical sliding, unirradiated UHMWPE showed similar Raman peak widths to that of the control group, symptomatic of a surface and sub-surface microstructure with similar constituents and strain levels to the unworn material. Peak broadening in the elliptical group, although not statistically significant to the load-only group was found to be greater than the unworn control peak widths. This was attributed to the additional 150km of sliding wear. However, peaks narrowed dramatically after the first 12.5µm of material, and looked to approach a steady value similar to the control group subsequent to this depth. This was attributed to a narrow near-surface region of lightly strained material.

On average, elliptical group pins were found to wear ~0.18mm/million cycles, equivalent to a total linear penetration loss of ~540µm after 3million wear cycles. The extent and depth of "tool-strain" in the pins remains unclear, our measurements were only taken to a maximum 37.5µm beneath the surface and at this depth there was no obvious indication of peak widths falling to those of the microtomed group. However, due to the lack of residual strain in the elliptically worn surfaces, it appears that the tool-damaged zone was completely worn through and the final worn microstructure was solely due to the nature of multi-directional wear.

Multi-directional motion, in causing higher wear rates, prevented surface material from accumulating larger damage levels, such as those found under slower wearing linear reciprocating motion; mean FWHM peaks from both the microtomed control and elliptical groups were statistically similar (t-test p=0.336).

6.5.3 Highly Crosslinked UHMWPE

Similar trends to those observed in the unirradiated material were seen in the highly-crosslinked material. In brief, unworn control and elliptically worn microstructures were found with a higher proportion of crystalline phase than either linear-reciprocating or load-only groups. Whereas, linear-reciprocating and load-only groups were found to have statistically broader FWHM ~1129cm^{-1} peaks than either the elliptical or unworn groups.

Despite three-million linear-reciprocating and elliptical cycles, load-only material was found with the broadest 1129cm^{-1} FWHM peaks at each surface and sub-surface depth recorded. No statistical significant difference (ANOVA $p>0.05$) was found between linear-reciprocating and load-only group means. This relationship applied throughout the depth of sub-surface measurements, suggesting no additional damage to the residual tool damage was introduced from reciprocating sliding wear.

Similar reasoning to that proposed for the unirradiated reciprocating wear may be applied to the reciprocating crosslinked study. Upon completion of the 3million cycle test, the group had undergone ~9µm of linear wear such that "final" worn surfaces remained within the pre-worn tool-damaged zone. It follows that final linear-reciprocating Raman peak widths did not approach those of the microtomed control group (Figure 5-26).

Under elliptical motion, FWHM peaks were found to be within (±S.D) 4.95±0.04cm^{-1} throughout the first 37.5µm of material. No statistical difference to the microtomed group could be found. This implied that despite the addition of crosslinks known to reduce the wear factor in this study by an order of magnitude under elliptical motion; 1.6x$10^{-6}$$mm^3$/Nm vs.

$0.1x10^{-6}mm^3/Nm$, additional damage caused by sliding in the slower wearing near-surface was negligible when compared to the unworn microtomed control group.

This finding may help confirm the hypothesis that multi-directional motion prevents strain hardening. Such a notion was found to be independent of crosslinking. The average linear penetration rate of the elliptically worn +PE group was ~0.01mm/million cycles, equivalent to a total mean linear wear removal of 30μm. Therefore, the average elliptically worn sub-surface might be expected to be influenced by the initial "tool-strain". This would be confirmed by Raman peaks taken on the worn surface approaching that of the load-only group. However, this was not found, instead a specific sub-surface, more lightly strained microstructure in response to multi-directional motion was discovered (Figure 5-26). Unfortunately, it is difficult to state with certainty the extent to which this lightly strained sub-surface extended because the extent of the load-only microstructure was unknown.

6.6 Wear Mechanisms

In this section we discuss UHMWPE wear theories in light of observations made during the current study. Where differences arise, an attempt to expand upon these models will be undertaken. Finally, a mode of wear will be developed based on our existing set of contact conditions.

There are numerous explanations for the observed wear behaviour of UHMWPE. Most theories commonly involve one or more of the following concepts: plastic-strain accumulation at the near-surface[65, 70, 206], molecular chain orientation under articulation[101, 108], strain hardening and cross-shear[100, 143] and intergranular weakness[46, 83, 207]. It seems likely that all may contribute, at some level, to the development of the worn surface and to the generation of wear debris.

The discussion of sub-surface damage development commonly involves the terms "strain" and "plastic deformation". Before further reading the reader is familiarised with these concepts. Strain, is a non-dimensional parameter used to describe the elongation of a material. When describing wear, it is the microstructural development or damage incurred for a given level of strain which is equally, or arguably more important than discussing strain accumulation in itself. Plastic deformation refers to permanent deformation, hence topographic or sub-surface features which remain once sliding is complete are said to involve an element of plastic behaviour. To enter plastic deformation, one must first exhaust the elastic component. Elastic deformation is fully recoverable and occurs from the stretching of bonds. Because the elastic limit of UHMWPE is much lower than its ultimate elongation at break the majority of microstructural behaviour will involve plastic deformation (see Section 2.7.1).

The most noticeable difference between linear reciprocating and elliptically worn pins was the creation of a very highly polished appearance on elliptically worn surfaces. Similar observations are reported in mature acetabular cups, where the head wears into the cup producing highly burnished regions. The primary wear mechanism is thought to be microscopic asperity scale wear, causing adhesive/fatigue mechanisms[208]. Cooper *et al.*, propose a strain dependent sub-surface wear model; intermittent periods of high and low wear are attributed to plastic strain accumulation. At some critical level of residual strain, macroscopic failure occurs and the removal of larger surface material is responsible for the increase in wear rate. Instead, we observed nominally constant wear which is commonly reported under serum lubricated conditions[28]. The pin-on-plate tests Cooper *et al.* conducted were, however, carried out under water-based sliding which is found to underestimate the

wear and produce larger debris particles than under serum based sliding[25]. Despite these differences, the notion of strain development is now a commonly accepted paradigm of the early stages of wear.

Gravimetric results can be thought of as a summation of all wear events, but one might imagine at small length scales a multitude of different wear mechanisms occurring, each specific to the region of wear on the surface of the acetabular cup. At small scales, a discretised asperity wear process would be favorably represented by the critical strain model. A period of strain accumulation in load-bearing asperities would appear as slow microadhesive wear resulting in failure of critically strained asperities causing faster macroscopic wear.

A later wear model based on asperity-asperity contact (Equation 6-2), builds on the critical strain criterion after which debris is produced[65]. Where V is the volumetric wear rate, N is the applied load, R_a is the surface roughness, σ_{UTS} is the ultimate tensile strength and ε_{UTS} is the strain at failure.

$$\Delta V \; \alpha \; N^{\frac{3}{2}} \; R_a{}^{\frac{3}{2}} \quad \frac{1}{\sigma_{UTS}{}^{\frac{3}{2}} \epsilon_{UTS}}$$

Equation 6-2: Theory of wear based on asperity contacts; critical strain criterion.

The equation implies that the tensile rupture energy or toughness (defined as the product of σ_{UTS} and ε_{UTS}) of UHMWPE may determine the volumetric wear rate. A similar relationship was first proposed by Lancaster and Ratner (Equation 2-2), whereby a material with higher ultimate tensile strength and elongation at rupture was found more resistant to abrasive wear. This equation may adequately describe the mechanical behaviour and wear of non-crosslinked polymers[198], but the relationship involving highly crosslinked polyethylene (XLPE) toughness against wear performance remains less clear. Mechanical tensile tests on XLPE confirm a decrease in toughness in comparison to conventional material[135, 159]. As such, Equation 6-2 incorrectly predicts crosslinked material should be more susceptible to wear. The large increase in XLPE multi-directional wear resistance when sliding against a smooth counterface (S_a <0.05μm) shows this model to be flawed (Figure 5-17). The disagreement can be broadly attributed to two features. The first is the importance of sliding induced shear stress and its influence on microstructural rearrangement. This undoubtedly determines the polymer response to an extent not accounted for in Equation 6-2. Secondly, Dowson *et al.* have shown a metal counterface with scratches perpendicular to the sliding direction negate the effects of a strain hardening UHMWPE surface[56]. Therefore, one can imagine when ploughing and scratching occurs under an abrasive dominant regime, the

conditions are too severe for XLPE to fully benefit at the microscale over conventional UHMWPE re-arrangement. As all our sliding experiments were conducted against smooth surfaces, it seems logical to concentrate on those wear models which exploit similar conditions. As such, the focus falls heavily on microstructural re-arrangement, a process more challenging to quantify than those relationships involving mechanical properties.

The wear models introduced so far show no attempt to involve the effects of cross-shear or the importance of multi-directional motion. To account for high *in vivo* wear under complex sliding paths (Section 2.6.3.2), a strain-softening adhesive model was proposed[110]. This model assumes UHMWPE articulates against a smooth metal counterface, allowing the polymer both time and the ability to orientate under sliding induced friction forces. The release of debris occurs via the following method; a multi-directional stress field must be present on the UHMWPE surface, where the principal stress occurs in the flexion/extension direction (direction of largest sliding distances) causing preferential molecular orientation in this direction.

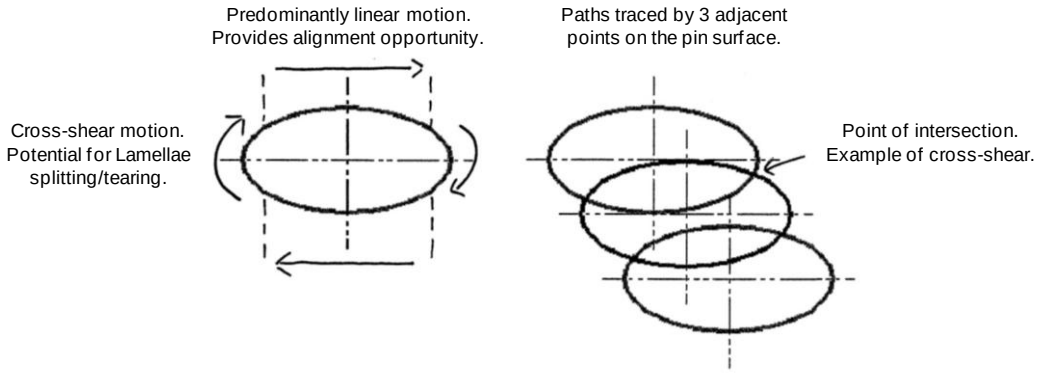

Figure 6-5: Elliptical track split into linear and crossing motion. The majority of wear is proposed to occur during sliding through the apex of the ellipse.

The principal stress vectors cause the aligned molecules to stretch but not rupture. Subsequently, this leads to material softening and a greater susceptibility to wear in the direction of the secondary stress component, acting perpendicular to the principal, in the adduction/abduction direction. This causes rupture in the aligned molecules and the formation of fibrillar wear particles. Figure 6-5 shows a schematic of our elliptical path annotated according to Wang's proposal. Note in this theoretical prediction, uni-directional sliding would cause molecular alignment and extension in the principal stress direction but zero wear debris. Under test, both –PE and +PE lost material under linear-reciprocating motion.

In measured support of this proposal we found evidence of lamellae alignment and Raman peak broadening in unirradiated material subjected to $3x10^6$ linear-reciprocating cycles. Field-emission scanning electron microscopy, in conjunction with a potassium permanganate etchant, confirmed microstructural re-arrangement along the principal stress direction. Furthermore, evidence of ~1129cm^{-1} peak broadening indicates molecular extension and strain accumulation, supporting the strain hardening phenomenon on which Wang's proposal is based[29]. The findings herein support the initial steps of the strain-softening model, the caveat being that Wang's model represents multi-directional wear and so far our findings in support of Wang's theory are taken from simplified linear-reciprocating motion. The multi-directional data is somewhat more contradictory, due to the observed lack of microstructural alignment. The absence of preferential orientation would lessen the susceptibility to wear in the secondary direction, questioning Wang's explanation for increased clinical wear rates. Nevertheless, larger wear factors in the clinical range were associated with our UHMWPE worn under multi-directional motion. Raman spectroscopy on –PE elliptically worn surfaces further supported the lack of sliding induced damage; band widths were similar to unworn microtomed surfaces.

At first glance, these analytical findings question strain accumulation models and the basis of orientation being a precursor to accelerated wear. In order to expand the theory of molecular wear under multi-directional motion the case of simplified LR motion is considered in more detail. In both –PE (Figure 5-29) and +PE (Figure 5-33) microstructures we observed preferential alignment and very similar wear factors. FE-SEM images from both cohorts were similar, showing preferential lamellar alignment and crystalline deformation mechanisms. There were two immediate differences between the materials. Firstly, swell tests revealed elevated crosslinking in +PE amorphous domains, and secondly, FE-SEM showed the +PE microstructure was composed of smaller lamellae. The insignificant benefit using +PE under simplified motion may be a combination owing to higher mechanical properties and fracture toughness of -PE offset against the poorer mechanical properties, slower strain hardening response and lower fracture toughness of +PE. Had studies only been conducted under linear-reciprocating motion, the significant difference in multidirectional wear performance between these two material grades might have been in danger of being overlooked, adding further importance to physiologically matched motion for pin-on-plate wear machines.

The lack of preferential alignment observed in elliptically worn unirradiated material does not rule-out the ability of the microstructure to re-orientate. On the contrary, the possibility of microstructural re-arrangement is heightened when one considers the potential for

increased mobility in a microstructure without crosslinking. The response of UHMWPE molecules to sliding appears reasonably quick[209]. Re-alignment of molecules under linear-reciprocating sliding motion has been found to occur within 2,000cycles. This response can be considered swift when compared to the useful operating lifetime of the component ($x10^7$cycles). Sambasivan *et al's* slide path had a stroke length of 25mm, equating to just 100m of sliding needed to cause significant microstructural development (50mm x 2,000cycles). Their UHMWPE material was gamma irradiated in nitrogen ~37kGy allowing one to postulate even swifter orientation in unirradiated material such as that tested herein. Taking into account the apparent ease of molecular mobility in Sambasivan's study and the extended length of tests in our study, an alternative interpretation for the apparent random microstructure under elliptical wear is made.

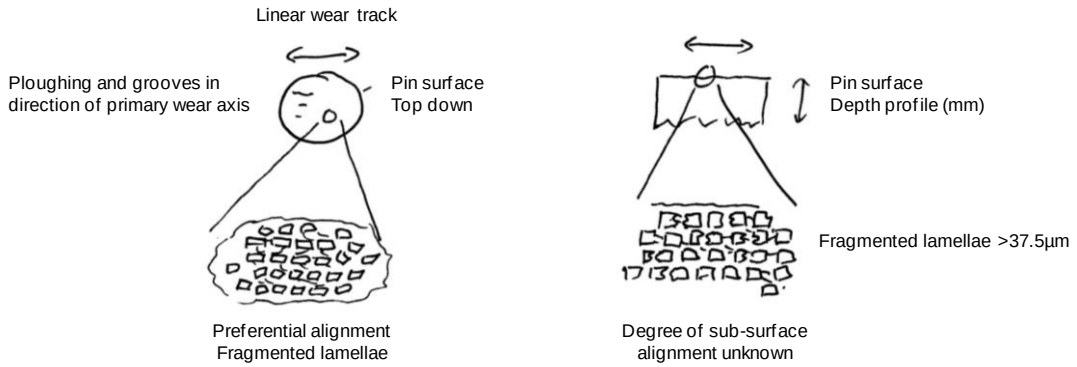

Figure 6-6: Schematic of preferential alignment under linear reciprocating sliding.

Consider that the faster wear rate and surface turn-over in unirradiated elliptically worn material prevented both Raman spectroscopy from identifying de-crystallised material and FE-SEM from imaging significant lamellae orientation. A faster wearing surface will leave less time for large strains to develop, leaving a worn surface void of preferential orientation or fragmented lamellae. If we entertain the possibility of lamellae re-arrangement, the mechanism by which wear would happen is illustrated in Figure 6-7. The relatively small change in sliding direction when motion is primarily along the elliptical long axis induces a degree of molecular alignment according to the slide path seen in Figure 6-5. In this intermediate state, surface molecules become susceptible to molecular tearing and splitting perpendicular to the primary wear axis. Evidence of these wear features can be seen in Figure 5-37. The majority of this damage would occur during the apex, at each end of the elliptical track, where the largest changes in sliding direction and cross-shear occur. Surface lamellae unable to be released would remain elevated above the micro-domains of neighbouring un-aligned, newly uncovered lamellae. Load would then be transferred to these older micro-domains where further re-orientation and tearing occurs until the elevated

domains are worn back and load is transferred elsewhere. This uneven wear process may contribute to the development of the topographic rippling feature imaged on the worn surface under elliptical sliding (Figure 5-36); a tribological setup resulting in the highest degree of cross-shear and surface turn-over.

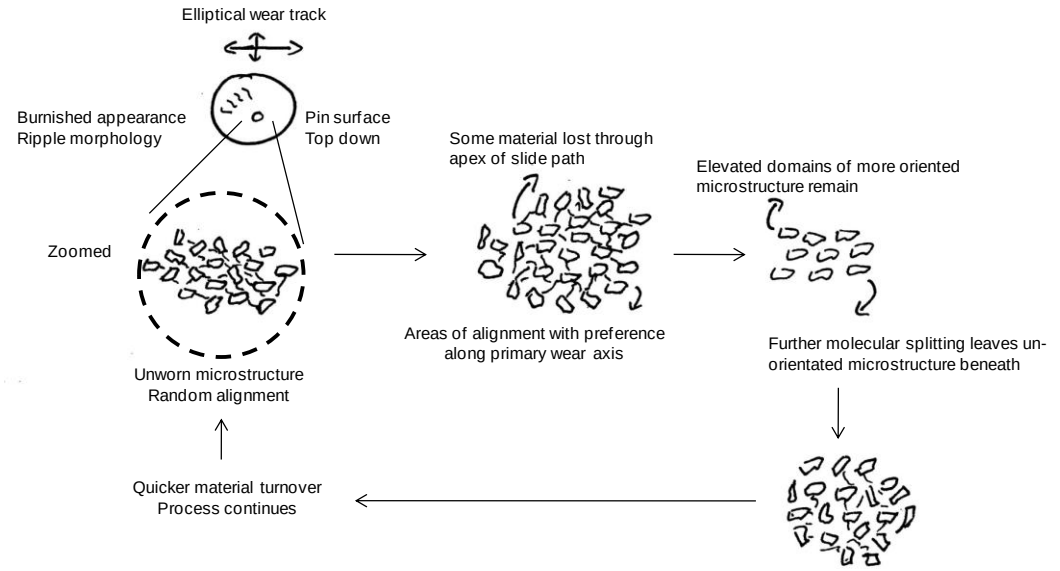

Figure 6-7: Schematic of elliptical wear process in unirradiated material.

Similar ripples of wavelengths ~1-2μm have been imaged on the surface of high wear areas of explanted UHMWPE cups[47, 68]. These were commonly imaged at the pole of the cup where maximum stresses have since been found[10]. Ripples have been postulated to be a viscoelastic plastic response of UHMWPE to cyclic stress[67] and more recently have been attributed to the plastic flow of near-surface material[122]. The limitation of the rippled morphology to occur only in areas of the cup exhibiting high wear and high hip joint contact stress may suggest high degrees of cross-shear in the presence of adhesive or fatigue type wear is a prerequisite for such a feature. Our ripples typically occurred every 1-2μm with a peak-to-trough amplitude ~30nm, similar to previous observations and in fitting with typical lamellae dimensions as seen in Figure 4-16.

The aspect ratio (AR) of the slide track has been shown to have a significant effect on the wear of UHMWPE. Saikko *et al*. have worn UHMWPE using elliptical slide tracks with AR's ranging from 1 to 388[181], where an AR of 1.0 was a circle and 388 was approximately linear reciprocating. AR's less than 5.5 were found to produce wear factors clinical in magnitude. An approximate five-fold increase in AR from 1.0 to 5.5 produced a 1.8-fold increase in wear factor, $1.0–1.8 \times 10^{-6} mm^3/Nm$.

Turell *et al.* conducted a similar study, instead using rectangular slide paths with varying AR[112]. Of the discrete number of paths chosen in their study (where each path was cycled 1million times) only rectangular paths with an AR<4 produced wear factors in what is considered the UHMWPE clinical range (1-2x$10^{-6}$$mm^3$/Nm). It was when using these AR's that discrepancies in the orientation softening model[111] were found i.e. theoretical predictions of wear factor were found to underestimate the experimental wear factor. Criticism may also be directed at the Turell *et al.* study; the decision to terminate at 1 million cycles may have produced misleading higher wear factors, unfairly skewed by wearing-in behaviour.

Clinical aspect ratios from one gait study are reported to range between 2.08±0.93 to a maximum of 5.36±1.59, resulting in an average physiological aspect ratio of 3.33[128]. In the current study a low aspect ratio was chosen to represent the more open wear paths of those found *in vivo*. An AR 2.0 (20mm and 10mm primary and secondary axes of the ellipse) seems a realistic value in comparison to the alternative linear reciprocating motion.

The lack of alignment observed under low aspect ratio wear has been reported elsewhere[203]. Davey *et al.* failed to find significant alignment in explanted cups subject to slide paths with average AR's <3.4, in good agreement with the AR 2.0 ellipse in this study. In a further study, Davey *et al.* go on to report a positive correlation between acetabular cup wear and the inverse of the mean AR[128]. By combining the two studies it is possible to hypothesise that cups showing little preferential alignment are accompanied by higher wear rates, in agreement with our results.

Zhou *et al.* identified the surface ripple dimensions (size and wavelength) to be dependent on irradiation dose[122]. More highly irradiated material was observed to have smaller ripple wavelengths, implying the development and extent of near-surface microstructure was reduced or limited by additional crosslinks restricting lamellae mobility. A similar reduction in a plasticity induced damage layer was found in highly crosslinked material[70].

The lack of a strain affected zone beneath the surface of unirradiated material questions the basis of this plasticity induced damage layer. However, this could be due to poor inter-molecular communication in the non-crosslinked material proving inefficient at strain transfer sub-surface. This would prove increasingly difficult when one considers the faster material turn-over. A similar wear test and analysis conducted on conventional gamma-sterilised material would further this hypothesis. It seems logical that the mechanism and ease of material release will affect the damage inherent in the remaining surface and near surface. For example, the lack of crosslinks in unirradiated material allow debris to be teased from the surface more easily (due to fewer bonds and ties to the bulk material) leaving

behind a less damaged surface than would be expected on an equivalent highly crosslinked bearing.

For the case of crosslinked wear, evidence of orientation supports the ability of lamellae to partially align when sliding vectors change little along a primary wear axis. It seems logical to propose that the crosslinked microstructure develops in a similar manner to unirradiated material as they possess similar wear factors under linear reciprocating motion. Were the mechanisms to be divergent, one might have imaged a larger difference in wear behaviour under the extremes of simplified motion. We propose the following wear scenario founded on the above wear paradigm for unirradiated material (Figure 6-8). Partially aligned material begins to elongate in the primary wear axis as amorphous domains re-organise to accommodate plasticity induced damage. For molecular splitting to occur, (the wear path provides the opportunity during the apex of the elliptical track) higher levels of strain energy are required due to the increased crosslink density. Hence, more friction induced damage and larger numbers of sliding cycles allows the aging surface more opportunity to stretch and re-orientate along the primary axis. Eventually, predominantly amorphous deformation transfers to intra-crystalline, producing fragmented lamellae (accompanied by a decrease in crystallinity) and further microstructural alignment of micro-domains. At some critical level, sliding friction overcomes the remaining taut tie-molecules causing lamellae to fracture and/or deform outwards from the bulk (Figure 5-41). These are then gradually teased away from the surface before finally being released as debris.

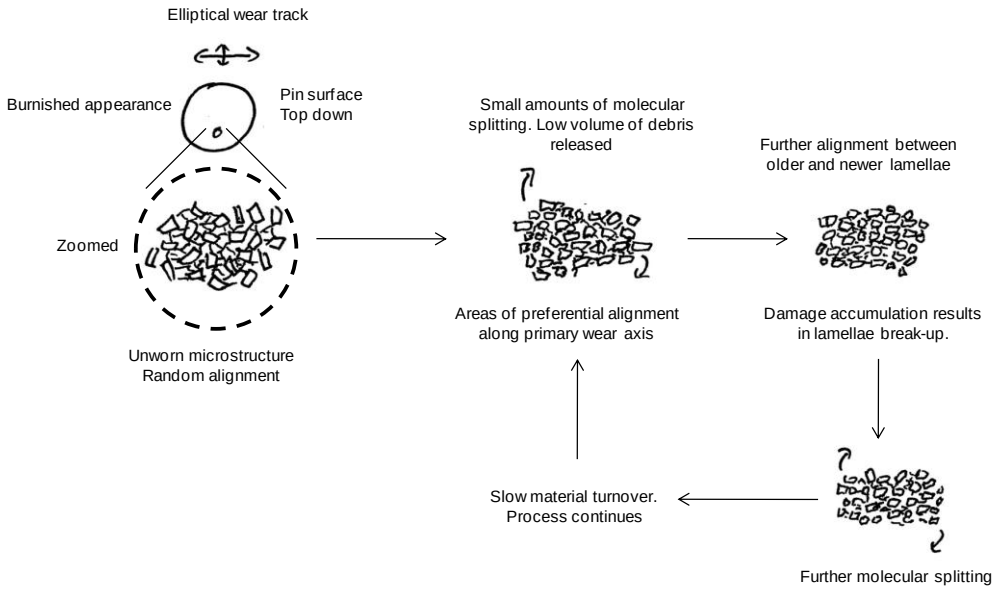

Figure 6-8: Schematic of elliptical wear process in highly crosslinked material.

The novel multi-directional tribometer has provided a platform to investigate the nuances of multi-directional wear specific to unirradiated and highly crosslinked material. The principal difference between the two proposed wear processes is shown by the difference in return path in the schematic diagrams of Figure 6-7 and Figure 6-8. In brief, fewer crosslinks allow unirradiated material to organise and be released quicker, in doing so periodically leaving a surface free from extended fibrils and a fresher randomly orientated sub-surface microstructure. In the case of the more wear resistant crosslinked material, the additional crosslinks prevent quick material turnover due to slower molecular splitting and tearing and in doing so, the worn surface always contains a large proportion of fragmented lamellae amongst newly exposed crystallites.

Furthermore, the tribometer has shown that current wear theories, which assume the majority of deformation mechanisms occur in the amorphous domains, may be adequate at explaining conventional material wear under multi-directional motion but are less applicable to highly crosslinked material. With increasing numbers of acetabular implants being manufactured from highly crosslinked material, the inherent attributes of low wear come at the price of increased microstructural damage as wear mechanisms are increasingly transferred to the stiffer lamellae. Under physiological hip stresses, accumulated strain may not be relieved from the surface as debris, as would be in conventional material, but rather transferred from amorphous to crystalline domains increasing the time it takes to generate debris particles. From an osteolytic potential, a decrease in wear volume is favourable. However, the potential for fragmented lamellae to provide the basis for nanoscale wear debris still provides the basis for a pathogenic cellular response[49].

Research concerned with tailoring the UHMWPE microstructure to optimise the wear performance has shown an emerging trade-off between increased crack resistance offered by larger crystallites[79] yet better wear resistance by smaller crystallites[210, 211]. As such, the importance of a tribometer offering a closer approximation of *in vivo* wear should not be underrated; such a machine could offer more accurate wear results across a range of polymer grades under controlled conditions. The current novel tribometer distills the operation of the complicated simulator, yet retains the importance of physiological conditioning, offering a considerable improvement over existing machines.

7 Conclusions

A novel six-station programmable load and motion wear machine has been designed and manufactured to further the tribological investigation into wear and sub-surface plasticity of UHMWPE. For the first time in orthopaedic wear studies, the pin-on-plate machine combined a physiologically relevant elliptical motion path with advanced dynamic loading.

Built to surpass the capability of previous pin-on-flat machines, the following design features were incorporated to facilitate the study of UHMWPE wear:

- A double peak Paul-type dynamic load was used to better simulate the heel-strike, stance-phase, toe-off, and swing-phase of the gait cycle;
- A programmable motion control system was able to approximate more closely the wear paths simulated to occur across the femoral head during *in vivo* operation; use of the machine confirmed the importance of multi-directional motion in pin-on-plate studies;
- The orientation specific pin and plate mounting arrangement ensured consistent microstructural development such that the polymer surface remained fixed with respect to the primary wear axis during advanced multi-directional testing;
- A fixed polymer surface relative to the plate created a homogeneous shear condition across the entire face of the pin. This provided a basis for non-destructive analysis techniques to characterise microstructure development in response to wear path.

The tribometer has been shown to perform well in terms of the efficacy of the motion path, load profile, lubrication and sliding conditions. This was established through the clinically indicated wear ranking of PTFE>>POLYACETAL≥UHMWPE achieved in the validation study. Further clinical relevance was provided by calculated wear factors in good agreement with those reported from *ex vivo* studies.

Linear-reciprocating and elliptical wear paths clearly showed the extent of improved UHMWPE wear resistance in response to simplified motion, where all sliding occurred against smooth counterfaces. This supports the perception that to induce molecular re-orientations and wear factors similar to those found *in vivo*, pin-on-plate machines must be capable of producing closer gait-matched wear paths.

Prior to wear testing, all UHMWPE pins commenced sliding with as-machined surfaces. The machining process was found to produce a band of near-surface material with lower crystallinity and higher levels of residual strain; this was present in both non-crosslinked and highly crosslinked material.

Microtomed surfaces were characterised with higher crystallinity and minimal residual strain when compared to worn and load-soak surfaces. This confirmed that the microtoming protocol successfully removed the tool-damaged, more highly strained near-surface, justifying the belief that microtomed surfaces were suitable control microstructures.

A potassium permanganate etch recipe was used successfully to reveal the surface lamellae at shorter etch times than previously implemented. The minimal etch time was shown to be important to preserve the true nature of the worn microstructure.

Raman spectroscopy was used for the first time in UHMWPE pin-on-plate testing, allowing the effects of slide track on crystallinity and residual damage to be jointly investigated. The non-destructive technique showed good agreement with conventional differential scanning calorimetry. The depth of sampling volume was characterised at 10μm and provided suitable resolution to investigate near-surface development.

The microstructure of unirradiated UHMWPE worn under elliptical motion appeared markedly similar to that of the unirradiated control material; lamellae remained randomly orientated and of similar size and form. An explanation for the failure to observe alignment and de-crystallisation was attributed to faster lamellae removal and renewal of new surface material obscuring the origins of preferential alignment and microstructural wear.

The microstructure of unirradiated UHMWPE worn under linear reciprocating motion proved highly distinct from that of the unirradiated elliptically worn group. Domains of crystalline lamella were found aligned in a preferential manner, coinciding with the sliding direction. Orientation was also accompanied by lamellae break-up, frequently observed on potassium permanganate etched worn surfaces.

Raman spectroscopy indicated a statistically significant drop in the mean surface crystallinity of unirradiated material worn under linear reciprocating motion when compared to the elliptically worn group.

Crosslinking dramatically improved on the wear resistance of unirradiated UHMWPE under advanced multi-directional motion. The use of simplified linear-reciprocating motion could not distinguish between the two material cohorts. The hypothesis that crosslinking does not inhibit lamellar mobility was supported through FE-SEM images that revealed re-orientation under sliding in both grades of UHMWPE.

Similar wear reductions in crosslinked material have been reported in multi-directional simulator trials. This level of agreement confirms the value of the further developments

instilled in the current tribometer design; by bridging the gap between conventional tribometers and more complicated simulators, studies may be carried out in a more cost-effective manner, without compromise to the relevance of the physiological testing environment.

A typical low wearing surface was characterised with having reduced crystallinity and higher residual strain in the surface and sub-surface zones than unworn control UHMWPE. This was found to be independent of crosslink density. The occurrence of fragmented lamellae in crosslinked material and unirradiated material worn under simplified motion indicated similar microstructural failure. This has been attributed to greater damage accumulation over longer periods of time, in conjunction with slow lamellar removal and renewal of new surface material providing a mechanism for crystalline fragmentation.

A wear paradigm, based on the orientation softening model, was proposed which accounted for the reduction in near-surface crystallinity. The dominant mechanism transits from the rupture of tie-molecules within the amorphous phase under faster wearing conditions to the intra-crystalline slip and rupture of lamellae under slower wearing circumstances and in highly crosslinked material.

Despite crosslinked UHMWPE offering a substantial increase in wear resistance under more physiologically accurate hip-joint motion, the potential for fragmented lamellae to provide the basis for nanoscale wear particles may still induce a pathogenic response in surrounding tissue.

8 References

1. Charnley, J., Kamangar, A., and Longfield, M. D., The Optimum Size of Prosthetic Heads in Relation to the Wear of Plastic Sockets in Total Replacement of the Hip. Medical & Biological Engineering, 1969. 7(1): pp. 31-39.
2. Burns, A. W. R. and Bourne, R. B., (vi) Economics of revision total hip arthroplasty. Current Orthopaedics, 2006. 20(3): pp. 203-207.
3. Charnley, J., Total Hip Replacement by Low-Friction Arthroplasty. Clinical Orthopaedics and Related Research, 1970(72): pp. 7-21.
4. McCutchen, C. W., Sponge-Hydrostatic and Weeping Bearings. Nature, 1959. 184(4695): pp. 1284-1285.
5. Katta, J., Jin, Z., Ingham, E., and Fisher, J., Biotribology of articular cartilage--A review of the recent advances. Medical Engineering & Physics, 2008. 30(10): pp. 1349-1363.
6. Cooke, A. F., Dowson, D., and Wright, V., The rheology of synovial fluid and some potential synthetic lubricants for degenerate synovial joints. Proceedings of the Institution of Mechanical Engineers Part H-Journal of Engineering in Medicine, 1978. 7(2): pp. 66-72.
7. Charnley, J., The Lubrication of Animal Joints in Relation to Surgical Reconstruction by Arthroplasty. Annals of the Rheumatic Diseases, 1960. 19(1): pp. 10-19.
8. Paul, J. P., Forces transmitted by joints in the human body. Proceedings of the Institution of Mechanical Engineers Part H-Journal of Engineering in Medicine, 1966. 181: pp. 8-15.
9. Bergmann, G., Graichen, F., and Rohlmann, A., Hip joint loading during walking and running, measured in two patients. Journal of Biomechanics, 1993. 26(8): pp. 969-990.
10. Brown, T. D. and Shaw, D. T., In vitro contact stress distributions in the natural human hip. Journal of Biomechanics, 1983. 16(6): pp. 373-384.
11. Ratner, B. D., Hoffman, A. S., Schoen, F. J., and Lemons, J. E., Biomaterials Science; An Introduction to Materials in Medicine. 2nd Edition ed. 2004, San Diego: Elsevier Academic Press.
12. Amstutz, H. C. and Grigoris, P., Metal on metal bearings in hip arthroplasty. Clinical Orthopaedics and Related Research, 1996(329): pp. S11-S34.
13. Unsworth, A., Effects of Lubrication in Hip-Joint Prostheses. Physics in Medicine and Biology, 1978. 23(2): pp. 253-268.
14. Stachowiak, G. W. and Batchelor, A. W., Engineering Tribology. Third Edition ed. 2005, Oxford: Elsevier Butterworth-Heinemann.
15. Reynolds, O., On the Theory of Lubrication and Its Application to Mr. Beauchamp Tower's Experiments, Including an Experimental Determination of the Viscosity of Olive Oil. Proceedings of the Royal Society of London, 1886. 40: pp. 191-203.
16. MacConaill, M. A., The function of intra-articular fibrocartilages, with special reference to the knee and inferior radio-ulnar joints. Journal of Anatomy, 1932. 66: pp. 210-227.
17. Bowden, F. P. and Tabor, D., Boundary Lubrication, in Friction and Lubrication. 1956, Methuen: London. pp. 107.
18. Hills, B., Boundary lubrication in vivo. Proceedings of the Institution of Mechanical Engineers, Part H: Journal of Engineering in Medicine, 2000. 214(1): pp. 83-94.
19. Walker, P. S., Dowson, D., Longfield, M. D., and Wright, V., Boosted Lubrication in Synovial Joints by Fluid Entrapment and Enrichment. Annals of the Rheumatic Diseases, 1968. 27(6): pp. 512-521.
20. Dowson, D. and Higginson, G. R., Elastohydrodynamic Lubrication. 1977, Oxford: Pergamon Press.
21. Hamrock, B. J. and Dowson, D., Ball Bearing Lubrication, The Elastohydrodynamics of Elliptical Contacts. 1981: John Willey and Sons.
22. Jalali-Vahid, D., Jagatia, M., Jin, Z. M., and Dowson, D., Prediction of lubricating film thickness in UHMWPE hip joint replacements. Journal of Biomechanics, 2001. 34(2): pp. 261-266.
23. Cooper, J. R., Dowson, D., and Fisher, J., The effect of transfer film and surface roughness on the wear of lubricated ultra-high molecular weight polyethylene. Clinical Materials, 1993. 14(4): pp. 295-302.
24. McKellop, H., Clarke, I. C., Markolf, K. L., and Amstutz, H. C., Wear characteristics of UHMW polyethylene: A method for accurately measuring extremely low wear rates. Journal of Biomedical Materials Research, 1978. 12(6): pp. 895-927.
25. Wang, A., Essner, A., Stark, C., and Dumbleton, J. H., Comparison of the size and morphology of UHMWPE wear debris produced by a hip joint simulator under serum and water lubricated conditions. Biomaterials, 1996. 17(9): pp. 865-871.
26. Lu, Z. and McKellop, H., Frictional heating of bearing materials tested in a hip joint wear simulator. Proceedings of the Institution of Mechanical Engineers, Part H: Journal of Engineering in Medicine, 1997. 211(1): pp. 101-108.
27. Scholes, S. C., Unsworth, A., Hall, R. M., and Scott, R., The effects of material combination and lubricant on the friction of total hip prostheses. Wear, 2000. 241(2): pp. 209-213.
28. McKellop, H., Clarke, I. C., Markolf, K. L., and Amstutz, H. C., Friction and wear properties of polymer, metal, and ceramic prosthetic joint materials evaluated on a multichannel screening device. Journal of Biomedical Materials Research, 1981. 15(5): pp. 619-653.

29. Pooley, C. M. and Tabor, D., Friction and Molecular Structure - Behavior of Some Thermoplastics. Proceedings of the Royal Society of London Series A-Mathematical and Physical Sciences, 1972. 329(1578): pp. 251-274.
30. Chandrasekaran, M., Wei, L. Y., Venkateshwaran, K. K., Batchelor, A. W., and Loh, N. L., Tribology of UHMWPE tested against a stainless steel counterface in unidirectional sliding in presence of model synovial fluids: part 1. Wear, 1998. 223(1-2): pp. 13-21.
31. Wang, A., Essner, A., and Schmidig, G., The effects of lubricant composition on in vitro wear testing of polymeric acetabular components. Journal of Biomedical Materials Research Part B: Applied Biomaterials, 2004. 68B(1): pp. 45-52.
32. Liao, Y. S., McNulty, D., and Hanes, M., Wear rate and surface morphology of UHMWPE cups are affected by the serum lubricant concentration in a hip simulation test. Wear: 14th International Conference on Wear of Materials, 2003. 255(7-12): pp. 1051-1056.
33. Clarke, I. C., Chan, F. W., Essner, A., Good, V., Kaddick, C., Lappalainen, R., Laurent, M., McKellop, H., McGarry, W., Schroeder, D., Selenius, M., Shen, M. C., Ueno, M., Wang, A., and Yao, J., Multi-laboratory simulator studies on effects of serum proteins on PTFE cup wear. Wear: 13th International Conference on Wear of Materials, 2001. 250(1-12): pp. 188-198.
34. Essner, A., Schmidig, G., and Wang, A., The clinical relevance of hip joint simulator testing: In vitro and in vivo comparisons. Wear, 2005. 259(7-12): pp. 882-886.
35. Lentner, C., Geigy scientific tables, Units of measurements, body fluids, composition of the body, nutrition. Vol. Volume 1. 1981, West Caldwell, NJ: Ciba-Geigy.
36. Briscoe, B. and Tabor, D., Friction and wear of polymers: The role of mechanical properties. British Polymer Journal, 1978. 10(1): pp. 74-78.
37. Briscoe, B. J. and Sinha, S. K., Wear of polymers. Proceedings of the Institution of Mechanical Engineers Part J-Journal of Engineering Tribology, 2002. 216(J6): pp. 401-413.
38. Briscoe, B. J. and Stolarski, T. A., Combined Rotating and Linear Motion Effects on the Wear of Polymers. Nature, 1979. 281(5728): pp. 206-208.
39. Young, R. J. and Lovell, P. A., Introduction to Polymers. Second Edition ed. 1991: CRC Press.
40. Dunn, A. C., Steffens, J. G., Burris, D. L., Banks, S. A., and Sawyer, W. G., Spatial geometric effects on the friction coefficients of UHMWPe. Wear, 2008. 264(7-8): pp. 648-653.
41. Cooper, R. A., McAllister, C. M., Borden, L. S., and Bauer, T. W., Polyethylene debris-induced osteolysis and loosening in uncemented total hip arthroplasty : A cause of late failure. The Journal of Arthroplasty, 1992. 7(3): pp. 285-290.
42. Willert, H. G., Bertram, H., and Buchhorn, G. H., Osteolysis in Alloarthroplasty of the Hip - the Role of Ultra-High-Molecular-Weight Polyethylene Wear Particles. Clinical Orthopaedics and Related Research, 1990(258): pp. 95-107.
43. Harris, W. H., The Problem Is Osteolysis. Clinical Orthopaedics and Related Research, 1995(311): pp. 46-53.
44. McKellop, H. A., Campbell, P., Park, S. H., Schmalzried, T. P., Grigoris, P., Amstutz, H. C., and Sarmiento, A., The Origin of Submicron Polyethylene Wear Debris in Total Hip-Arthroplasty. Clinical Orthopaedics and Related Research, 1995(311): pp. 3-20.
45. Campbell, P., Ma, S., Yeom, B., McKellop, H., Schmalzried, T. P., and Amstutz, H. C., Isolation of predominantly submicron-sized UHMWPE wear particles from periprosthetic tissues. Journal of Biomedical Materials Research, 1995. 29(1): pp. 127-131.
46. Shanbhag, A. S., Jacobs, J. J., Glant, T. T., Gilbert, J. L., Black, J., and Galante, J. O., Composition and Morphology of Wear Debris in Failed Uncemented Total Hip-Replacement. Journal of Bone and Joint Surgery-British Volume, 1994. 76B(1): pp. 60-67.
47. Elfick, A. P. D., Smith, S. L., Green, S. M., and Unsworth, A., A re-appraisal of wear features of acetabular sockets using atomic force microscopy. Wear, 2002. 253(7-8): pp. 839-847.
48. Schmalzried, T. P., Jasty, M., and Harris, W. H., Periprosthetic Bone Loss in Total Hip-Arthroplasty - Polyethylene Wear Debris and the Concept of the Effective Joint Space. Journal of Bone and Joint Surgery-American Volume, 1992. 74A(6): pp. 849-863.
49. Green, T. R., Fisher, J., Matthews, J. B., Stone, M., and Ingham, E., Effect of size and dose on bone resorption activity of macrophages by in vitro clinically relevant ultra high molecular weight polyethylene particles. Journal of Biomedical Materials Research Part B: Applied Biomaterials, 2000. 53(5): pp. 490-497.
50. Lubrication (tribology) education and research. ('Jost Report'). 1966, Department of Education and Science, HMSO.
51. Dowson, D. and Wright, V., Bio-tribology. In: Proceedings of the conference on the rheology of lubrication., 1973: pp. 81-89.
52. Dowson, D., History of Tribology. 2nd Edition ed. 1998: Wiley-Blackwell.
53. Burwell, J. T. and Strang, C. D., On the Empirical Law of Adhesive Wear. Journal of Applied Physics, 1952. 23(1): pp. 18-28.
54. Hutchings, I. M., Tribology; Friction and Wear of Engineering Materials. 2nd Edition ed. 2001, Oxford: Butterworth-Heinemann.

55. What are the Wear Mechanisms and What Controls Them?, in Implant Wear in Total Joint Replacement "American Society of Orthopaedic Surgeons". 2001.
56. Dowson, D., Taheri, S., and Wallbridge, N. C., The Role of Counterface Imperfections in the Wear of Polyethylene. Wear, 1987. 119(3): pp. 277-293.
57. Research Group on Wear of Engineering Materials, Glossay of Terms and Definitions in the Field of Friction, Wear and Lubrication. Tribology O.E.S.D.Publications, 1969.
58. Lancaster, J. K., Abrasive Wear of Polymers. Wear, 1969. 14(4): pp. 223-239.
59. Lancaster, J. K., Relationships between Wear of Polymers and Their Mechanical Properties. Industrial Lubrication and Tribology, 1969. 21(7): pp. 214.
60. Turell, M. E., Friedlaender, G. E., Wang, A., Thornhill, T. S., and Bellare, A., The effect of counterface roughness on the wear of UHMWPE for rectangular wear paths. Wear, 2005. 259: pp. 984-991.
61. Elfick, A. P. D., Hall, R. M., Pinder, I. M., and Unsworth, A., The influence of femoral head surface roughness on the wear of ultrahigh molecular weight polyethylene sockets in cementless total hip replacement. Journal of Biomedical Materials Research, 1999. 48(5): pp. 712-718.
62. Godet, M., The third-body approach: A mechanical view of wear. Wear, 1984. 100(1-3): pp. 437-452.
63. Isaac, G. H., Wroblewski, B. M., Atkinson, J. R., Dowson, D., Kennedy, K. D., and Smith, M. R., The Causes and Effects of In vivo Femoral-Head Roughening of Charnley Hip Prostheses. Journal of Bone and Joint Surgery-British Volume, 1988. 70(3): pp. 496-496.
64. Morscher, E. W., Hefti, A., and Aebi, U., Severe osteolysis after third-body wear due to hydroxyapatite particles from acetabular cup coating. The Journal of Bone and Joint Surgery, 1998. 80-B(2): pp. 267-272.
65. Wang, A., Sun, D. C., Stark, C., and Dumbleton, J. H., Wear Mechanisms of UHMWPE in Total Joint Replacements. Wear, 1995. 181: pp. 241-249.
66. Archard, J. F., Contact and Rubbing of Flat Surfaces. Journal of Applied Physics, 1953. 24(8): pp. 981-988.
67. Rostoker, W., Chao, E. Y. S., and Galante, J. O., Appearances of Wear on Polyethylene - Comparison of *In vivo* and *In vitro* Wear Surfaces. Journal of Biomedical Materials Research, 1978. 12(3): pp. 317-335.
68. Dowling, J. M., Atkinson, J. R., Dowson, D., and Charnley, J., Characteristics of Acetabular Cups Worn in Human-Body. Journal of Bone and Joint Surgery-British Volume, 1978. 60(3): pp. 375-382.
69. Olley, R. H., Hodge, A. M., and Bassett, D. C., A permanganic etchant for polyolefines. Journal of Polymer Science: Polymer Physics Edition, 1979. 17(4): pp. 627-643.
70. Edidin, A. A., Pruitt, L., Jewett, C. W., Crane, D. J., Roberts, D., and Kurtz, S. M., Plasticity-induced damage layer is a precursor to wear in radiation-cross-linked UHMWPE acetabular components for total hip replacement. The Journal of Arthroplasty, 1999. 14(5): pp. 616-627.
71. Klapperich, C., Komvopoulos, K., and Pruitt, L., Tribological properties and microstructure evolution of ultra-high molecular weight polyethylene. Journal of Tribology, Transactions of the ASME, 1999. 121(2): pp. 394-403.
72. Zhou, J., Chakravartula, A., Pruitt, L., and Komvopoulos, K., Tribological and Nanomechanical Properties of Unmodified and Crosslinked Ultra-High Molecular Weight Polyethylene for Total Joint Replacements. Journal of Tribology, 2004. 126(2): pp. 386-394.
73. Hamrock, B. J., Fundamentals of Fluid FiIm Lubrication. 1994, Singapore: McGraw-Hill International Editions.
74. Keller, A., Polymer Crystals. Reports on Progress in Physics, 1968. 31: pp. 623-704.
75. Lin, L. and Argon, A. S., Structure and plastic deformation of polyethylene. Journal of Materials Science, 1994. 29(2): pp. 294-323.
76. Bunn, C. W. and Alcock, T. C., The Texture of Polythene. Transactions of the Faraday Society, 1945. 41(6): pp. 317-325.
77. Kurtz, S. M., Muratoglu, O. K., Evans, M., and Edidin, A. A., Advances in the processing, sterilization, and crosslinking of ultra-high molecular weight polyethylene for total joint arthroplasty. Biomaterials, 1999. 20(18): pp. 1659-1688.
78. Bassett, D. C., Principles of Polymer Morphology. 1st Edition ed. 1981, London: Cambridge University Press.
79. Simis, K. S., Bistolfi, A., Bellare, A., and Pruitt, L. A., The combined effects of crosslinking and high crystallinity on the microstructural and mechanical properties of ultra high molecular weight polyethylene. Biomaterials, 2006. 27(9): pp. 1688-1694.
80. Lewis, G., Polyethylene wear in total hip and knee arthroplasties. Journal of Biomedical Materials Research, 1997. 38(1): pp. 55-75.
81. Kurtz, S. M., The UHMWPE Handbook. 2004, San Diego: Elsevier Academic Press.
82. Benson, L. C., DesJardins, J. D., and LaBerge, M., Effects of in vitro wear of machined and moulded UHMWPE tibial inserts on TKR kinematics. Journal of Biomedical Materials Research, 2001. 58(5): pp. 496-504.

83. Pienkowski, D., Jacob, R., Hoglin, D., Saum, K., Kaufer, H., and Nicholls, P. J., Low-Voltage Scanning Electron-Microscopic Imaging of Ultrahigh-Molecular-Weight Polyethylene. Journal of Biomedical Materials Research, 1995. 29(10): pp. 1167-1174.
84. Bankston, A. B., Keating, E. M., Ranawat, C., Faris, P. M., and Ritter, M. A., Comparison of Polyethylene Wear in Machined Versus Molded Polyethylene. Clinical Orthopaedics and Related Research, 1995(317): pp. 37-43.
85. James, S. P., Lee, K. R., Beauregard, G. P., Rentfrow, E. D., and McLaughlin, J. R., Clinical wear of 63 ultrahigh molecular weight polyethylene acetabular components: Effect of starting resin and forming method. Journal of Biomedical Materials Research, 1999. 48(3): pp. 374-384.
86. Bellare, A. and Cohen, R. E., Morphology of rod stock and compression moulded sheets of ultra-high molecular-weight polyethylene used in orthopaedic implants. Biomaterials, 1996. 17(24): pp. 2325-2333.
87. Pruitt, L., The Effects of Radiation on the Structural and Mechanical Properties of Medical Polymers, in Radiation Effects on Polymers for Biological Use. 2003. pp. 63-93.
88. McGovern, T. F., Ammeen, D. J., Collier, J. P., Currier, B. H., and Engh, G. A., Rapid polyethylene failure of unicondylar tibial components sterilized with gamma irradiation in air and implanted after a long shelf life. Journal of Bone and Joint Surgery-American Volume, 2002. 84A(6): pp. 901-906.
89. Edidin, A. A., Jewett, C. W., Kalinowski, A., Kwarteng, K., and Kurtz, S. M., Degradation of mechanical behavior in UHMWPE after natural and accelerated aging. Biomaterials, 2000. 21(14): pp. 1451-1460.
90. Li, S. and Burstein, A. H., Ultra-high molecular weight polyethylene. The material and its use in total joint implants. The Journal of Bone and Joint Surgery, 1994. 76: pp. 1080-1090.
91. Wannomae, K. K., Bhattacharyya, S., Freiberg, A., Estok, D., Harris, W. H., and Muratoglu, O. K., In Vivo Oxidation of Retrieved Cross-linked Ultra-High-Molecular-Weight Polyethylene Acetabular Components with Residual Free Radicals. The Journal of Arthroplasty, 2006. 21(7): pp. 1005-1011.
92. Ries, M. D. and Pruitt, L., Effect of cross-linking on the microstructure and mechanical properties of utra-high molecular weight polyethylene. Clinical Orthopaedics and Related Research, 2005(440): pp. 149-156.
93. Baker, D. A., Bellare, A., and Pruitt, L., The effects of degree of crosslinking on the fatigue crack initiation and propagation resistance of orthopedic-grade polyethylene. Journal of Biomedical Materials Research Part A, 2003. 66A(1): pp. 146-154.
94. Greenwald, A. S., Bauer, T. W., and Ries, M. D., New polys for old: Contribution or caveat? Journal of Bone and Joint Surgery-American Volume, 2001. 83A: pp. 27-31.
95. Muratoglu, O. K., Bragdon, C. R., O'Connor, D. O., Jasty, M., and Harris, W. H., A novel method of cross-linking ultra-high-molecular-weight polyethylene to improve wear, reduce oxidation, and retain mechanical properties: Recipient of the 1999 HAP Paul Award. The Journal of Arthroplasty, 2001. 16(2): pp. 149-160.
96. Galante, J. O. and Rostoker, W., Wear in Total Hip Prostheses - Experimental Evaluation of Candidate Materials. Acta Orthopaedica Scandinavica, 1973(145): pp. 1-46.
97. Rostoker, W. and Galante, J., Wear Studies in Materials for Joint Replacement. Journal of Bone and Joint Surgery-American Volume, 1975. A 57(4): pp. 582-582.
98. Rostoker, W. and Galante, J. O., Contact pressure dependence of wear rates of ultra high molecular weight polyethylene. Journal of Biomedical Materials Research, 1979. 13(6): pp. 957-964.
99. Wright, K. W. J., Dobbs, H. S., and Scales, J. T., Wear Studies on Prosthetic Materials Using the Pin-on-Disc Machine. Biomaterials, 1982. 3(1): pp. 41-48.
100. Ramamurti, B. S., Bragdon, C. R., O'Connor, D. O., Lowenstein, J. D., Jasty, M., Estok, D. M., and Harris, W. H., Loci of movement of selected points on the femoral head during normal gait: Three-dimensional computer simulation. The Journal of Arthroplasty, 1996. 11(7): pp. 845-852.
101. Bragdon, C. R., O'Connor, D. O., Lowenstein, J. D., Jasty, M., and Syniuta, W. D., The importance of multidirectional motion on the wear of polyethylene. Proc Inst Mech Eng [H], 1996. 210(3): pp. 157-65.
102. Amstutz, H. C., Polymers as bearing materials for total hip replacement: A friction and wear analysis. Journal of Biomedical Materials Research, 1969. 3(4): pp. 547-568.
103. Rose, R. M., Cimino, W. R., Ellis, E., and Crugnola, A. N., Exploratory investigations on the structure dependence of the wear resistance of polyethylene. Wear, 1982. 77(1): pp. 89-104.
104. Bragdon, C. R., O'Connor, D. O., Lowenstein, J. D., Jasty, M., Biggs, S. A., and Harris, W. H., A new pin-on-disk wear testing method for simulating wear of polyethylene on cobalt-chrome alloy in total hip arthroplasty. The Journal of Arthroplasty, 2001. 16(5): pp. 658-665.
105. Joyce, T. J., Monk, D., Scholes, S. C., and Unsworth, A., A multi-directional wear screening device and preliminary results of UHMWPE articulating against stainless steel. Bio-Medical Materials and Engineering, 2000. 10(3-4): pp. 241-249.
106. Saikko, V., A multidirectional motion pin-on-disk wear test method for prosthetic joint materials. Journal of Biomedical Materials Research, 1998. 41(1): pp. 58-64.

107. Ramamurti, B. S., Estok, D. M., Jasty, M., and Harris, W. H., Analysis of the kinematics of different hip simulators used to study wear of candidate materials for the articulation of total hip arthroplasties. Journal of Orthopaedic Research, 1998. 16(3): pp. 365-369.
108. Wang, A., Stark, C., and Dumbleton, J. H., Mechanistic and morphological origins of ultra-high molecular weight polyethylene wear debris in total joint replacement prostheses. Proceedings of the Institution of Mechanical Engineers, Part H-Journal of Engineering in Medicine, 1996. 210(H3): pp. 141-155.
109. Charnley, J., Wear of Plastics Materials in Hip-Joint. Plastics and Rubber, 1976. 1(2): pp. 59-63.
110. Wang, A., Sun, D. C., Yau, S. S., Edwards, B., Sokol, M., Essner, A., Polineni, V. K., Stark, C., and Dumbleton, J. H., Orientation softening in the deformation and wear of ultra-high molecular weight polyethylene. Wear, 1997. 203-204: pp. 230-241.
111. Wang, A., A unified theory of wear for ultra-high molecular weight polyethylene in multi-directional sliding. Wear, 2001. 248(1-2): pp. 38-47.
112. Turell, M., Wang, A., and Bellare, A., Quantification of the effect of cross-path motion on the wear rate of ultra-high molecular weight polyethylene. Wear, 2003. 255(7-12): pp. 1034-1039.
113. Galvin, A., Kang, L., Tipper, J., Stone, M., Ingham, E., Jin, Z. M., and Fisher, J., Wear of crosslinked polyethylene under different tribological conditions. Journal of Materials Science-Materials in Medicine, 2006. 17(3): pp. 235-243.
114. Marrs, H., Barton, D. C., Jones, R. A., Ward, I. M., Fisher, J., and Doyle, C., Comparative wear under four different tribological conditions of acetylene enhanced cross-linked ultra high molecular weight polyethylene. Journal of Materials Science: Materials in Medicine, 1999. 10(6): pp. 333-342.
115. Charnley, J. and Halley, D. K., Rate of Wear in Total Hip-Replacement. Clinical Orthopaedics and Related Research, 1975(112): pp. 170-179.
116. Elfick, A. P. D., Hall, R. M., Pinder, I. M., and Unsworth, A., The effect of socket design, materials and liner thickness on the wear of the porous coated anatomic total hip replacement. Proceedings of the Institution of Mechanical Engineers Part H-Journal of Engineering in Medicine, 2001. 215(H5): pp. 447-457.
117. Hall, R. M., Unsworth, A., Siney, P., and Wroblewski, B. M., Wear in retrieved Charnley acetabular sockets. Proc. Inst. Mech. Engr., 1996. 210(3)(0954-4119 (Print)): pp. 197:207.
118. AMTI, Ortho-POD Pin-On-Plate Wear-testing Machine. www.amti.biz.
119. Hamilton, M. A., Sucec, M. C., Fregly, B. J., Banks, S. A., and Sawyer, W. G., Quantifying Multidirectional Sliding Motions in Total Knee Replacements. Journal of Tribology, 2005. 127(2): pp. 280-286.
120. Gevaert, M. R., LaBerge, M., Gordon, J. M., and DesJardins, J. D., The quantification of physiologically relevant cross-shear wear phenomena on orthopedic bearing materials using the MAX-shear wear testing system. Journal of Tribology-Transactions of the ASME, 2005. 127(4): pp. 740-749.
121. Wang, A., Polineni, V. K., Essner, A., Sokol, M., Sun, D. C., Stark, C., and Dumbleton, J. H., Significance of nonlinear motion in the wear screening of orthopaedic implant materials. Journal of Testing & Evaluation, 1997. 25(2): pp. 239-245.
122. Zhou, J. and Komvopoulos, K., Wear Mechanisms of Untreated and Gamma Irradiated Ultra-High Molecular Weight Polyethylene for Total Joint Replacements. Journal of Tribology, 2005. 127(2): pp. 273-279.
123. Saikko, V., A hip wear simulator with 100 test stations. Proceedings of the Institution of Mechanical Engineers Part H-Journal of Engineering in Medicine, 2005. 219(5): pp. 309-318.
124. Yao, J. Q., Laurent, M. P., Gilbertson, L. N., and Crowninshield, R. D., The effect of minimum load on the fluid uptake and wear of highly crosslinked UHMWPE total hip acetabular components. Wear "13th International Conference on Wear of Materials", 2001. 250(1-12): pp. 140-144.
125. Bennett, D. B., Orr, J. F., and Baker, R., Movement loci of selected points on the femoral head for individual total hip arthroplasty patients using three-dimensional computer simulation. The Journal of Arthroplasty, 2000. 15(7): pp. 909-915.
126. Saikko, V. and Calonius, O., Slide track analysis of the relative motion between femoral head and acetabular cup in walking and in hip simulators. Journal of Biomechanics, 2002. 35(4): pp. 455-464.
127. Barbour, P. S., Fisher, J., and Stone, M. H., A Hip Joint Simulator Study using Simplified Loading and Motion Cycles Generating Physiological Wear Pathsand Rates. Proceedings of the I MECH E Part H Journal of Engineering in Medicine, 1999. 213: pp. 455-467.
128. Davey, S. M., Orr, J. F., Buchanan, F. J., Nixon, J. R., and Bennett, D., The effect of patient gait on the material properties of UHMWPE in hip replacements. Biomaterials, 2005. 26(24): pp. 4993-5001.
129. Bennett, D., Orr, J., Beverland, D., and Baker, R., The influence of shape and sliding distance of femoral head movement loci on the wear of acetabular cups in total hip arthroplasty. Proceedings of the Institution of Mechanical Engineers, Part H: Journal of Engineering in Medicine, 2002. 216(6): pp. 393-402.
130. Bartczak, Z., Argon, A. S., and Cohen, R. E., Deformation Mechanisms and Plastic Resistance in Single-Crystal-Textured High-Density Polyethylene. Macromolecules, 1992. 25(19): pp. 5036-5053.

131. Bartczak, Z., Galeski, A., Argon, A. S., and Cohen, R. E., On the plastic deformation of the amorphous component in semicrystalline polymers. Polymer, 1996. 37(11): pp. 2113-2123.
132. Bowden, P. B. and Young, R. J., Deformation Mechanisms in Crystalline Polymers. Journal of Materials Science, 1974. 9(12): pp. 2034-2051.
133. Li, D., Garmestani, H., Kalidindi, S. R., and Alamo, R., Crystallographic texture evolution in high-density polyethylene during uniaxial tension. Polymer, 2001. 42(11): pp. 4903-4913.
134. Boontongkong, Y., Cohen, R. E., Spector, M., and Bellare, A., Orientation of plane strain-compressed ultrahigh-molecular-weight polyethylene. Polymer, 1998. 39(25): pp. 6391-6400.
135. Muratoglu, O. K., Bragdon, C. R., O'Connor, D. O., Jasty, M., Harris, W. H., Gul, R., and McGarry, F., Unified wear model for highly crosslinked ultra-high molecular weight polyethylenes (UHMWPE). Biomaterials, 1999. 20: pp. 1463-1470.
136. McKellop, H., Shen, F., Lu, B., Campbell, P., and Salovey, R., Development of an extremely wear-resistant ultra high molecular weight polythylene for total hip replacements. Journal of Orthopaedic Research, 1999. 17(2): pp. 157-167.
137. Dorr, L. D., Wan, Z. N., Shahrdar, C., Sirianni, L., Boutary, M., and Yun, A., Clinical performance of a durasul highly cross-linked polyethylene acetabular liner for total hip arthroplasty at five years. Journal of Bone and Joint Surgery-American Volume, 2005. 87A(8): pp. 1816-1821.
138. Heisel, C., Silva, M., dela Rosa, M. A., and Schmalzried, T. P., Short-term in vivo wear of cross-linked polyethylene. Journal of Bone and Joint Surgery-American Volume, 2004. 86A(4): pp. 748-751.
139. Dumbleton, J. H., Shen, C., and Miller, E. H., Study of Wear of Some Materials in Connection with Total Hip-Replacement. Wear, 1974. 29(2): pp. 163-171.
140. Jasty, M., Goetz, D. D., Bragdon, C. R., Lee, K. R., Hanson, A. E., Elder, J. R., and Harris, W. H., Wear of polyethylene acetabular components in total hip arthroplasty - An analysis of one hundred and twenty-eight components retrieved at autopsy or revision operations. Journal of Bone and Joint Surgery-American Volume, 1997. 79A(3): pp. 349-358.
141. Deboer, J., Vandenberg, H. J., and Pennings, A. J., Crosslinking of Ultrahigh Molecular-Weight Polyethylene in the Oriented State with Dicumylperoxide. Polymer, 1984. 25(4): pp. 513-519.
142. Kurtz, S. M., Pruitt, L. A., Jewett, C. W., Foulds, J. R., and Edidin, A. A., Radiation and chemical crosslinking promote strain hardening behavior and molecular alignment in ultra high molecular weight polyethylene during multi-axial loading conditions. Biomaterials, 1999. 20(16): pp. 1449-1462.
143. Wang, A., Essner, A., Polineni, V. K., Stark, C., and Dumbleton, J. H., Lubrication and wear of ultra-high molecular weight polyethylene in total joint replacements. Tribology International, 1998. 31(1-3): pp. 17-33.
144. Joyce, T. J., Vandelli, C., Cartwright, T., and Unsworth, A., A comparison of the wear of cross-linked polyethylene against itself under reciprocating and multi-directional motion with different lubricants. Wear, 2001. 250(1-12): pp. 206-211.
145. ASTM F732-00(2006), Standard Test Method for Wear Testing of Polymeric Materials for Use in Total Joint Prostheses. ASTM international, 2006.
146. SMAC, SMAC Actuator LAL-95-015 / LAC-1 Controller.
147. Dowling, N. E., Mechanical Behaviour of Materials. Third Edition ed. 2007, Upper Saddle River, NJ: Pearson Prentice Hall.
148. Callister, W. D., Materials science and engineering: an introduction. Fifth ed. 2000, New York; Chichester: Wiley.
149. Saikko, V., Effect of lubricant protein concentration on the wear of ultra-high molecular weight polyethylene sliding against a CoCr counterface. Journal Of Tribology-Transactions Of The Asme, 2003. 125(3): pp. 638-642.
150. Barbour, P. S. M., Barton, D. C., and Fisher, J., The influence of stress conditions on the wear of UHMWPE for total joint replacements. Journal of Materials Science: Materials in Medicine, 1997. 8(10): pp. 603-611.
151. Sathasivam, S., Walker, P. S., Campbell, P., and Rayner, K., The effect of contact area on wear in relation to fixed bearing and mobile bearing knee replacements. Journal of Biomedical Materials Research, 2001. 58(3): pp. 282-290.
152. Buehler, www.buehler.com.
153. Bunn, C. W. and Howells, E. R., Structures of Molecules and Crystals of Fluoro-Carbons. Nature, 1954. 174(4429): pp. 549-551.
154. Biswas, S. K. and Vijayan, K., Friction and wear of PTFE -- a review. Wear, 1992. 158(1-2): pp. 193-211.
155. Makinson, K. R. and Tabor, D., Friction and Transfer of Polytetrafluoroethylene. Nature, 1964. 201(491): pp. 464-466.
156. Dumbleton, J. H., Delrin as a material for joint prosthesis - a review. ASTM STP 684, Corrosion and Degradation of implant materials, 1979.
157. Barbour, P. S. M., Barton, D. C., and Fisher, J., The influence of contact stress on the wear of UHMWPE for total replacement hip prostheses. Wear, 1995. 181-183(1): pp. 250-257.

158. Poleunis, C., Rubio, C., Compere, C., and Bertrand, P., Role of salts on the BSA adsorption on stainless steel in aqueous solutions. II. ToF-SIMS spectral and chemical mapping study. Surface and Interface Analysis, 2002. 34(1): pp. 55-58.
159. Pruitt, L. A., Deformation, yielding, fracture and fatigue behavior of conventional and highly cross-linked ultra high molecular weight polyethylene. Biomaterials, 2005. 26(8): pp. 905-915.
160. Glotin, M. and Mandelkern, L., A Raman spectroscopic study of the morphological structure of the polyethylenes. Colloid & Polymer Science, 1982. 260(2): pp. 182-192.
161. Mandelkern, L., Alamo, R. G., and Kennedy, M. A., Interphase Thickness of Linear Polyethylene. Macromolecules, 1990. 23(21): pp. 4721-4723.
162. Strobl, G. R. and Hagedorn, W., Raman spectroscopic method for determining the crystallinity of polyethylene. Journal of Polymer Science: Polymer Physics Edition, 1978. 16(7): pp. 1181-1193.
163. Wunderlich, B. and Cormier, C. M., Heat of Fusion of Polyethylene. Journal of Polymer Science Part A-2-Polymer Physics, 1967. 5(5pa2): pp. 987-988.
164. Dowson, D. and Wallbridge, N. C., Laboratory Wear Tests and Clinical Observations of the Penetration of Femoral Heads into Acetabular Cups in Total Replacement Hip Joints .1. Charnley Prostheses with Polytetrafluoroethylene Acetabular Cups. Wear, 1985. 104(3): pp. 203-215.
165. ASTM D2765-01 (2006), Standard Test Methods for Determination of Gel Content and Swell Ratio of Crosslinked Ethylene Plastics. ASTM international, 2006.
166. Rodriguez, F., Cohen, C., Ober, C. K., and L.A., A., Principles of Polymer systems. 5th ed. 2003, London: Taylor and Franciss.
167. Flory, P. J., Principles of Polymer Chemistry 1953, Ithaca, NY: Cornell University Press.
168. Shen, F. W., McKellop, H. A., and Salovey, R., Irradiation of chemically crosslinked ultrahigh molecular weight polyethylene. Journal of Polymer Science Part B: Polymer Physics, 1996. 34(6): pp. 1063-1077.
169. Affatato, S., Bersaglia, G., Emiliani, D., Foltran, I., Taddei, P., Reggiani, M., Ferrieri, P., and Toni, A., The performance of gamma- and EtO-sterilised UHMWPE acetabular cups tested under severe simulator conditions. Part 2: wear particle characteristics with isolation protocols. Biomaterials, 2003. 24(22): pp. 4045-4055.
170. Affatato, S., Bersaglia, G., Rocchi, M., Taddei, P., Fagnano, C., and Toni, A., Wear behaviour of cross-linked polyethylene assessed in vitro under severe conditions. Biomaterials, 2005. 26(16): pp. 3259-3267.
171. Affatato, S., Bordini, B., Fagnano, C., Taddei, P., Tinti, A., and Toni, A., Effects of the sterilisation method on the wear of UHMWPE acetabular cups tested in a hip joint simulator. Biomaterials, 2002. 23(6): pp. 1439-1446.
172. Bertoluzza, A., Fagnano, C., Rossi, M., Tinti, A., and Cacciari, G. L., Micro-Raman spectroscopy for the crystallinity characterization of UHMWPE hip cups run on joint simulators. Journal of Molecular Structure, 2000. 521(1-3): pp. 89-95.
173. Kyomoto, M., Miwa, Y., and Pezzotti, G., Strain in UHMWPE for orthopaedic use studied by Raman microprobe spectroscopy. Journal of Biomaterials Science, Polymer Edition, 2007. 18: pp. 165-178.
174. Pezzotti, G., Stress microscopy and confocal Raman imaging of load-bearing surfaces in artificial hip joints. Expert Review of Medical Devices, 2007. 4: pp. 165-189.
175. Sawyer, L. C. and Grubb, D. T., Polymer Microscopy. 2nd ed. 1987, New York: Chapman and Hall Ltd.
176. Olley, R. H. and Bassett, D. C., An improved permanganic etchant for polyolefines. Polymer, 1982. 23(12): pp. 1707-1710.
177. Shahin, M. M., Olley, R. H., and Blissett, M. J., Refinement of etching techniques to reveal lamellar profiles in polyethylene banded spherulites. Journal of Polymer Science Part B: Polymer Physics, 1999. 37(16): pp. 2279-2286.
178. Clarke, I. C., Good, V., Anissian, L., and Gustafson, A., Charnley wear model for validation of hip simulators - Ball diameter versus polytetrafluoroethylene and polyethylene wear. Proceedings of the Institution of Mechanical Engineers Part H-Journal of Engineering in Medicine, 1997. 211(1): pp. 25-36.
179. Havelin, L. I., Gjerdet, N. R., Lunde, O. D., Rait, M., and Sudmann, E., Wear of the Christiansen hip prosthesis. Acta Orthop Scand, 1986. 57(5): pp. 419-22.
180. Dybal, J. and Krimm, S., Normal-mode analysis of infrared and Raman spectra of crystalline isotactic poly(methyl methacrylate). Macromolecules, 2002. 23(5): pp. 1301-1308.
181. Saikko, V., Calonius, O., and Keränen, J., Effect of slide track shape on the wear of ultra-high molecular weight polyethylene in a pin-on-disk wear simulation of total hip prosthesis. Journal of Biomedical Materials Research, 2004. 69B(2): pp. 141-148.
182. Kilgour, A. and Elfick, A., Design and test of novel tribometer: investigation into wear performance of materials used in total hip replacements. Tribology - Materials, Surfaces & Interfaces, 2008. 2: pp. 161-168.
183. Suh, N. P., The Delamination Theory of Wear. Wear, 1973. 25: pp. 111-124.

184. Barbour, P. S. M., Stone, M. H., and Fisher, J., A study of the wear resistance of three types of clinically applied UHMWPE for total replacement hip prostheses. Biomaterials, 1999. 20(22): pp. 2101-2106.
185. Yao, J. Q., Blanchet, T. A., Murphy, D. J., and Laurent, M. P., Effect of fluid absorption on the wear resistance of UHMWPE orthopaedic bearing surfaces. Wear "14th International Conference on Wear of Materials", 2003. 255(7-12): pp. 1113-1120.
186. Pruitt, L., Hermann, R., and Suresh, S., Fatigue Crack-Growth in Polymers Subjected to Fully Compressive Cyclic Loads. Journal of Materials Science, 1992. 27(6): pp. 1608-1616.
187. Torrance, A. A. and Zhou, F., Fracture Modes in Wear Particle Formation, in Dissipative processes in tribology: proceedings of the 20th Leeds-Lyon Symposium on Tribology, D. Dowson, et al., Editors. 1994, Elsevier Science Publishers: Amsterdam.
188. Saikko, V., Effect of contact pressure on wear and friction of ultra-high molecular weight polyethylene in multidirectional sliding. Proceedings of the Institution of Mechanical Engineers Part H- Journal of Engineering in Medicine, 2006. 220: pp. 723-731.
189. Schmalzried, T. P., Szuszczewicz, E. S., Northfield, M. R., Akizuki, K. H., Frankel, R. E., Belcher, G., and Amstutz, H. C., Quantitative assessment of walking activity after total hip or knee replacement. Journal of Bone and Joint Surgery-American Volume, 1998. 80A(1): pp. 54-59.
190. Good, V. D., Clarke, I. C., and Anissian, L., Water and bovine serum lubrication compared in simulator PTFE/CoCr wear model. 1996. pp. 275-283.
191. Joyce, T. J., Thompson, P., and Unsworth, A., The wear of PTFE against stainless steel in a multi-directional pin-on-plate wear device. Wear: 14th International Conference on Wear of Materials, 2003. 255(7-12): pp. 1030-1033.
192. Sudmann, E., Havelin, L. I., Lunde, O. D., and Rait, M., The Charnley Versus the Christiansen Total Hip-Arthroplasty - a Comparative Clinical-Study. Acta Orthopaedica Scandinavica, 1983. 54(4): pp. 545-552.
193. Ohlin, A. F. and Persson, P. G., Failed Christiansen total hip arthroplasty. A radiographic and histologic study. The Journal of Arthroplasty, 1989. 4: pp. 207-215.
194. Josefsson, G., Eriksson, B., Fagerlund, M., Gudmundersson, G., Helgasson, H., Karlsson, O., Nordstrom, B., Olnas, B. O., and Wijkstrom, S., Non-Septic Loosenings in a Multi-Center Study of 1686 Thr. Acta Orthopaedica Scandinavica, 1981. 52(6): pp. 696-696.
195. Mathiesen, E. B., Lindgren, U., Reinholt, F. P., and Sudmann, E., Wear of the Acetabular Socket - Comparison of Polyacetal and Polyethylene. Acta Orthopaedica Scandinavica, 1986. 57(3): pp. 193-196.
196. Harris, W. H. Current status of highly crosslinked polyethylenes. in Thirty-Second Open Scientific Meeting;The Tenth Combined Open Meeting Hip Society and AAHKS. 2004. San Francisco, California.
197. Pedersen, D. R., Callaghan, J. J., Johnston, T. L., Fetzer, G. B., and Johnston, R. C., Comparison of femoral head penetration rates between cementless acetabular components with 22-mm and 28-mm heads. The Journal of Arthroplasty, 2001. 16(8, Supplement 1): pp. 111-115.
198. Edidin, A. A. and Kurtz, S. M., Influence of mechanical behavior on the wear of 4 clinically relevant polymeric biomaterials in a hip simulator. The Journal of Arthroplasty, 2000. 15(3): pp. 321-331.
199. Premnath, V., Bellare, A., Merrill, E. W., Jasty, M., and Harris, W. H., Molecular rearrangements in ultra high molecular weight polyethylene after irradiation and long-term storage in air. Polymer, 1999. 40(9): pp. 2215-2229.
200. McKellop, H., Shen, F. W., DiMaio, W., and Lancaster, J. G., Wear of gamma-crosslinked polyethylene acetabular cups against roughened femoral balls. Clinical Orthopaedics and Related Research, 1999(369): pp. 73-82.
201. DiMaio, W., G,, Saum, K. A., Lilly, W. B., and Moore, W. C., Effect of radiation dose on the physical properties of crosslinked UHMWPE. . In: Transactions of the 45th Annual Meeting of the Orthopaedic Research Society, 1999(Anaheim, CA, USA, February 1–4, 1999. p. 100).
202. Ries, M. D., Scott, M. L., and Jani, S., Relationship Between Gravimetric Wear and Particle Generation in Hip Simulators: Conventional Compared with Cross-Linked Polyethylene. Journal of Bone and Joint Surgery-American Volume, 2001. 83(2_suppl_2): pp. S116-122.
203. Davey, S. M., Orr, J. F., Buchanan, F. J., Nixon, J. R., and Bennett, D., Measurement of molecular orientation in retrieved ultra-high-molecular-weight polyethylene (UHMWPE) hip sockets using Fourier-transform infrared spectroscopy. Strain, 2004. 40(4): pp. 203-210.
204. Gongde, L., Yingzi, C., and Huilin, L., A study on sliding wear mechanism of ultrahigh molecular weight polyethylene/polypropylene blends. Wear, 2004. 256(11-12): pp. 1088-1094.
205. Dryzek, E. and Dryzek, J., Measurement of subsurface zone in UHMWPE after sliding against stainless steel using the new experimental method DSIP. Radiation Physics and Chemistry, 2007. 76(2): pp. 157-159.
206. Cooper, J. R., Dowson, D., and Fisher, J., Birefringent Studies of Polyethylene Wear Specimens and Acetabular Cups. Wear, 1991. 151(2): pp. 391-402.

207. Elfick, A. P., Hall, R. M., Unsworth, A., and Pinder, I. M., Surface topography of retrieved PCA acetabular liners: proposal of a novel wear mechanism. Journal of Materials Science Letters, 1998. 17(13): pp. 1085-1088.
208. Cooper, J. R., Dowson, D., and Fisher, J., Macroscopic and microscopic wear mechanisms in ultra-high molecular weight polyethylene. Wear, 1993. 162-164(Part 1): pp. 378-384.
209. Sambasivan, S., Fischer, D. A., Shen, M. C., and Hsu, S. M., Molecular orientation of ultrahigh molecular weight polyethylene induced by various sliding motions. J Biomed Mater Res, 2004. 70B(2): pp. 278-85.
210. Furman, B. D., Maher, S., Morgan, T. G., and Wright, T. M., Elevated Crosslinking Alone Does Not Explain Polyethylene Wear Resistance, in Crosslinking and Thermally Treated Ultra High Molecular Weight Polyethylene for Joint Replacements, S.M. Kurtz, R.A. Gsell, and J. Martell, Editors. 2004, ASTM International: West Conshohocken.
211. Van Citters, D. W., Kennedy, F. E., and Collier, J. P., Rolling sliding wear of UHMWPE for knee bearing applications. Wear, 2007. 263: pp. 1087-1094.

Appendix 1: Tribometer Start-up Protocol

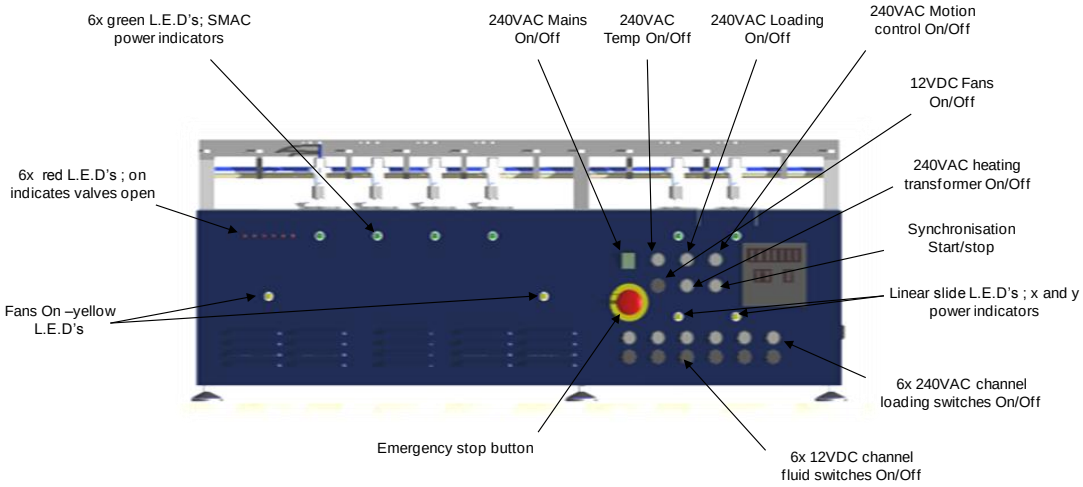

Checklist

1. Check all switches are in the off position.
2. Turn on the computer.
3. Check the serial expander
    - **number 4 – com 3** (smac loading, RJll-serial converter).
    - **number 1 – com 4** (Omega temperature control, blue 9-way D plug).
    - **number 2 – com 5** (Trio motion, grey 9-way D plug).
4. Check loading arms are exempt of pin holders.
5. Check slide travel is unobstructed.
6. Check for fluid spillage in the run-off trays.
7. Check digital I/0 channels on MC206
    - **Channel 8 – Start/stop** switch on front panel.
    - **Channel 9 – Reed relay** and smac channel 1 (pulls to ground).
    - **Channel 10 – Limit switch** input on axis (0) Top slide.
    - **Channel 12 – Limit switch** input on axis (1) Bottom slide.
8. Check de-ionised water level in both tanks.
9. Check the condition of the level sensors and thermocouples.
10. Switch on temperature circuit
    - Check the consistency of the thermocouple readings across all six channels. They should all read room temperature.
11. Check operation of the solenoid valves
    - Switch on the mains transformer.
    - Switch on each valve; check each red LED lights as water discharges.
    - Check for third body particles in the flow.
    - Check each valve and corresponding LED. These should switch-off upon current flowing between the sensing probes.

Start-up Protocol

1. Switch on mains 240Vac supply.
2. Turn on computer.
3. Switch on MC206 transformer, check for green light and red status light.
4. Load "Motion Perfect" software (check communication with MC206 in com 5) click "ok"
5. Click "drives enabled" (check the red "status" light goes off on MC206)
6. Switch on stepper drive PSU, and slides. Check status LED's. Three green on PSU indicates okay.
7. Check digital I/0 channels on MC206
    - Open digital I/0 window, click to enable channel 8. Check "start/stop" button disables channel)
8. Run program "*Simple*", check for axis errors. Re-enable drives if necessary.
9. Run Program "*Datum_D2*" (this program was written to perform a slide datuming sequence, always to an absolute position, front left corner *(0,0)*). Check BASE, SPEED, and MOVE values.
10. Check MPOS/DPOS are zero for both slides. This can be viewed within the "Motion Perfect" software in the "*axis parameters*" window.
11. Insert chambers 1-4 (leave heating leads unconnected).
12. Pipette 20ml of diluted Newborn calf serum solution into each chamber.
13. Run Program "*Start_D1*" (This program was written to position the slides at the beginning of the wear track). Ensure the program is first highlighted in "selected program" window.
14. Connect up heaters (will take approx 25mins to reach 37°C at approx 0.72°C/min).
15. Switch on heating transformer and temperature controller (Set to 37°C).
16. Load "CN616" software. Check channels in "*set points*" and zone scan on controller. Check PID settings read as follows (N.b. values displayed exactly as displayed on the controller):
    - Cycle time 02.0secs.
    - Hysteresis 02 deg.
    - Proportional band 0004 deg.
    - Reset 0.60 repeat/min.
    - Rate 00.00min.
17. Check individual channel control by turning on/off each zone and taking note of orange heating LED (load change – return run-check zone display on temperature controller).
18. Carefully, using tweezers, place test pins into their respected pin holders.
19. Connect up fluid level sensors. Switch on channels 1-6 and 12Vdc fluid control board supply.
20. Check fluid "*top-up*" LED's are off when the platinum probes are mounted in the chamber (ensures the water level system is set to 20ml/chamber). This also confirms the conductivity of the lubricant is sufficient to work with the sensors.
21. Place thermocouples in holders and ensure tip is reading temperature of fluid (not air, or counter-surface). Compare the temperature variation across all six channels for errors.
22. Switch on 24Vdc solenoid valve transformer.
23. Bring each pin down onto the plate using the height adjuster. The Loading arms should be horizontal. If not then adjust the SMAC collar.
24. Load up HyperTerminal software "*SMAC.trm*"
25. Set the SMAC "black box" to channel 1.

26. Switch on SMAC 1, a curser should appear on the software window, type "*MF*" for motor off. Check for two green LED's on LAC-1 controller.
27. Switch all six SMAC controllers on, "MF"
28. Check previous program stored in controllers by typing "TM-2". This will depend on which SMAC channel is currently selected by the "black box".
29. "RM" reset macros if necessary.
30. Check values stored in registers of each controller
    - 10-12 Initial sq values.
    - 13-16 time intervals.
    - 17-20 current gains.
    - 21 cycle counter.
    - 30 gradient taken from calibration curve.
    - 31 intercept taken from calibration curve.
31. Load "*Double peak*" Program.
32. Check channel inputs and communication between Trio MC206 and the LAC-1 controllers.
33. Load up motion perfect program "Linear wear" or "Elliptical wear".
34. Start loading cycle "MS" (waits for communication from MC206).
35. Start wear path (software now waits for a trigger from the user. This is activated by the "start" switch).
36. Switch on the cooling duct fans.
37. Press start….
38. At gravimetric intervals, stop loading and motion with the "start/stop" button. Stop the programs in software.
39. Remove pin holders, place on tray ready for initial rinse with tap water. Make sure test pins do not touch anything.
40. Disconnect heating resistors, fluid level probes and thermocouples.
41. Run "Datum_D2".
42. Decant lubricant into individual bottles ready for freezing.
43. Remove chambers, place on tray ready for initial rinse with tap water.

To load new gradient and intercept values into the controller registers

- Load up relevant calibration values onto registers (see SMAC programs).
- Switch off SMAC 1 and switch on SMAC 2. Select SMAC 2 using the "black box", "MF" for motor off.
- Load up relevant register values.
- Repeat steps for each of the SMAC units.

Appendix 2: Torque Calculations

This appendix calculates the minimum torque required of the lower linear slide stepper motor. The stepper motor must be capable of moving the "stacked" linear slide, chambers, heating components, worktop surfaces and additional normal and perpendicular loads created from the loading actuators. Based on the sum of the torque required to move the mass above, the torque required to overcome friction within the system and finally the torque required to accelerate the mass, the total torque is calculated. Friction to overcome within the system is generated by both the ball-screw and at the pin/plate interface.

1. Inputs

Define units: $rpm := rad \cdot s^{-1}$

1.1 Linear slide variables

Length of Slide: $Length := 390mm$

Mass per unit length: $M_{length} := 15.2 \cdot kg \cdot m^{-1}$

Pitch of screw thread: $Pitch := 5 \cdot mm$

Efficiency of Ball screw: $\eta := 0.8$

Diameter of ballscrew: $d := 12 \cdot mm$

Density of spindle (aluminium): $\rho := 2750 kg \cdot m^{-3}$

Typical coefficient of friction for ball screw: $\mu_{screw} := 0.1$

1.2 Loading Variables

Maximum dynamic load in gait cycle: $Load_{max} := 100 N$

Number of load and motion chambers: $Pins_{moving} := 4$

1.3 Motor Variables

Inertia of motor (input zero if not known): $J_{motor} := 0 \cdot kg \cdot m^2$

Speed in rpm: $n := 400 rpm$

Time to accelerate load: $t := 0.1 \cdot sec$

2.Load acting perpendicular to motion

The lower linear stage stepper motor must be capable of moving the "stacked" linear slide, chambers "base" plate, chambers, heating components and the additional normal and perpendicular forces created from the four load actuators.

2.1 Mass of "stacked" slide (Unimatic LF5)

Mass of linear slide: $M_{slide} := M_{length} \cdot Length$

2.2 Dynamic Load

In addition to this load (acting perpendicular to directions of motion), there is a dynamic load applied from the electric/pneumatic actuators:

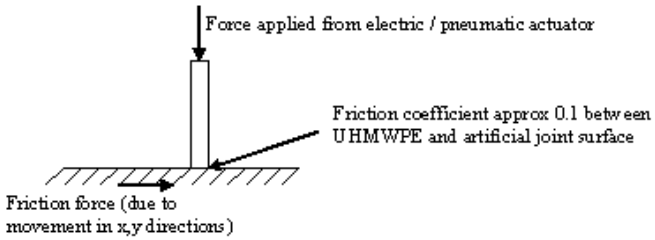

Peak maximum load from test pins: $Peak_{load} := Load_{max} \cdot Pins_{moving}$

3.Torque required to move the total load

3.1 Maximum Load acting perpendicular on lower slide

Total load: $Total_{load} := Peak_{load} + (M_{slide} \cdot g)$

Torque required to move the mass: $T_{load} := \frac{Total_{load} \cdot Pitch}{2 \cdot \pi \cdot \eta}$

4.Torque required to overcome friction within slide and from pins

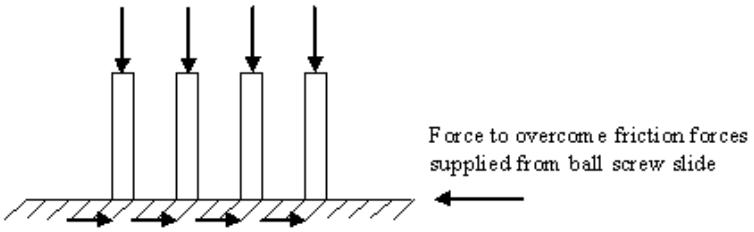

4.1 Torque to overcome friction

$$T_{friction} := \frac{Total_{load} \cdot Pitch \cdot \mu_{screw}}{2 \cdot \pi \cdot \eta}$$

5. Inertia of Ballscrew components

5.1 Inertia of Mass on screwthread

$$J_{load} := \frac{Total_{load}}{g} \cdot \left(\frac{Pitch}{2 \cdot \pi}\right)^2$$

5.2 Inertia of ballscrew spindle

$$J_{ballscrew} := \frac{\pi}{32} \cdot \rho \cdot Length \cdot d^4$$

5.3 Total inertia

$$J_{total} := \begin{cases} J_{load} + J_{ballscrew} & \text{if } J_{motor} = 0 \cdot kg \cdot m^2 \\ J_{load} + J_{ballscrew} + J_{motor} & \text{otherwise} \end{cases}$$

6. Torque required to accelerate the load

6.1 Angular speed

Angular speed: $\omega := \frac{2 \cdot \pi}{60} \cdot n$

6.2 Angular acceleration

Angular acceleration: $\alpha := \frac{\omega}{t}$

6.2 Acceleration torque

Torque: $T_{accelerate} := J_{total} \cdot \alpha$

7. Total Torque Required

The total torque required is the sum of the torque required to move the mass, the torque required to overcome friction within the system and finally the torque required to accelerate the mass

$$T_{total} := T_{load} + T_{friction} + T_{accelerate}$$

8. Outputs

Mass of linear Slide: $M_{slide} = 5.928\,kg$

Max load induced by four test pins: $Peak_{load} = 400\,N$

Total load acting perpendicular to motion: $Total_{load} = 458.134\,N$

Torque required to move the load: $T_{load} = 0.456\,N \cdot m$

Torque required to overcome friction within the system: $T_{friction} = 0.046\,N \cdot m$

Inertia of mass on screwthread: $J_{load} = 2.958 \times 10^{-5}\,kg \cdot m^2$

Inertia of ballscrew spindle: $J_{ballscrew} = 2.183 \times 10^{-6}\,kg \cdot m^2$

Inertia of motor: $J_{motor} = 0$

Total Inertia of system: $J_{total} = 3.177 \times 10^{-5}\,kg \cdot m^2$

Angular velocity: $\omega = 41.888\,rad \cdot s^{-1}$

Angular acceleration: $\alpha = 418.879\,rad \cdot s^{-2}$

Torque required to accelerate load: $T_{accelerate} = 0.013\,N \cdot m$

Total torque of system: $T_{total} = 0.515\,N \cdot m$

Appendix 3: Load Profile Calculations

The workbook was written to convert actuator output current into force and nominal stress at the pin-plate interface. Current values were related to force using a predetermined linear calibration curve. The following working was used to characterise actuator one, used in station one of the six station tribometer.

1. Import Servo Output

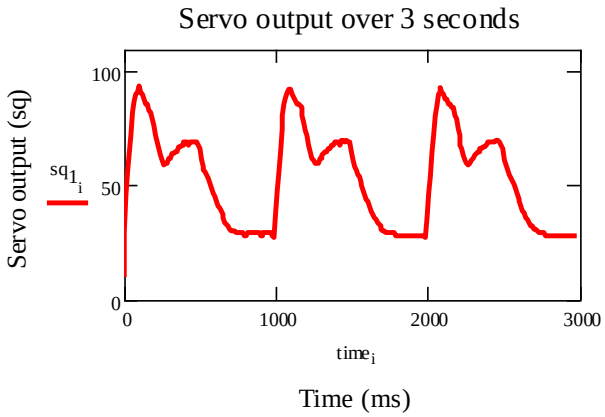

Load profile still in SMAC actuator units and is converted to force (N) using calibration curves.

2. Force Calibration

Linear output response from calibration plot: $y = 1.2459x - 27.151$

$$Force_i := 1.2459 \cdot N \cdot sq1_i - 27.151 \cdot N$$

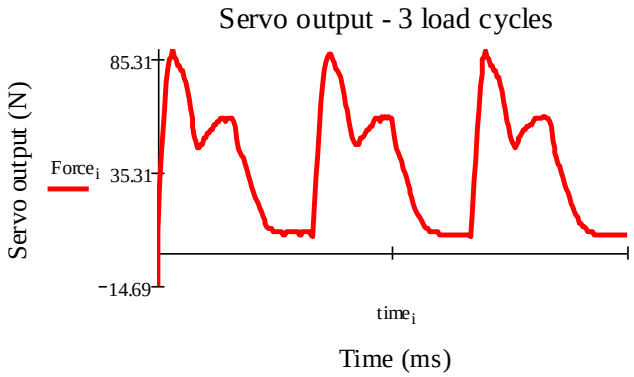

Isolate one cycle:

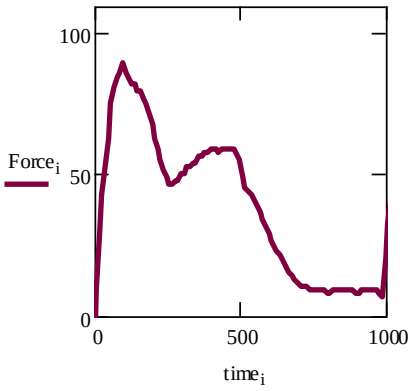

3. Contact Forces and Stresses

Average force per cycle (N): $Force_{av} := \frac{\sum_{i=200}^{298} Force_i}{100}$

Average force over stance phase (N): $Force_{av\_stance} := \frac{\sum_{i=200}^{258} Force_i}{58}$

Contact area (mm^2): $area := 20 \cdot mm^2$

Average nominal contact stress per cycle (MPa): $\sigma_{av} := \frac{Force_{av}}{area}$

Average nominal contact stress per stance phase (MPa): $\sigma_{av\_stance} := \frac{Force_{av\_stance}}{area}$

Maximum force (heel strike) (N): $F_{max} := max(Force)$

Relative minimum force (N): $F_{min} := Force_{26}$

2nd maximum force (toe-off) (N): $F_{2nd} := Force_{47}$

Max contact stress - heel strike (MPa) $\sigma_{max} := \frac{max(Force)}{area}$

Relative min contact stress (MPa): $\sigma_{relative\_min} := \frac{Force_{29}}{area}$

2nd max contact stress - toe-off (N): $\sigma_{2nd} := \frac{Force_{54}}{area}$

4. Outputs

Nominal contact area (mm^2): $area = 20mm^2$

Average force per cycle (N): $Force_{av} = 39.23N$

Average force per stance phase (N): $Force_{av\_stance} = 59.62N$

Maximum force (heel strike) (N): $F_{max} = 89.96N$

Relative minimum force (N): $F_{min} = 46.36N$

2nd maximum force (toe-off) (N): $F_{2nd} = 58.82N$

Max contact stress - heel strike (MPa) $\sigma_{max} = 4.5MPa$

Relative min contact stress (MPa): $\sigma_{relative\_min} = 2.38MPa$

2nd max contact stress - toe-off (N): $\sigma_{2nd} = 2.13MPa$

Average nominal contact stress per cycle (MPa): $\sigma_{av} = 1.96MPa$

Average nominal contact stress over stance phase (MPa): $\sigma_{av\_stance} = 2.98MPa$

Appendix 4: Main Shaft Design Calculations

The workbook was written to approximate the maximum bending moment, longitudinal stress, deflection and maximum slope of the tribometers main shaft. The shaft was supported at either end, which the workbook assumes to be pinned-pinned. This simplifies the moments about the supports and adds a conservative approach to the calculation. The shaft may deflect due to the loads induced upon it by the loading arms and reaction forces at the pin-plate interfaces. Only the longest unsupported span length was considered, over which 4 loading arms were mounted.

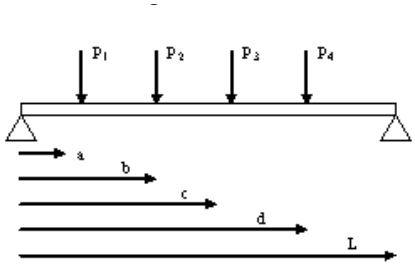

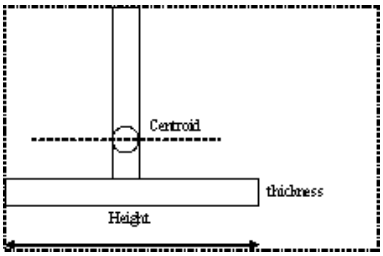

1. Inputs

1.1 Shaft Parameters

Length of shaft:		$L_{total} := 500mm$
If a solid bar then enter "no" and enter outer radius only:		tube := "no"
Outer radius of shaft:		$r_o := 6 \cdot mm$
Inner radius of shaft tubing:		$r_i := 0 \cdot mm$
Distance from N.A to outer most fibre:		$y := 6 \cdot mm$
Loading point distances spanwise across the shaft from L.H.S (dimensions taken from Solid Edge draft drawings):		$a := 100mm$
		$b := 200mm$
		$c := 300mm$
		$d := 400mm$
Youngs Modulus:	Aluminium=69GPa Stainless steel=200GPa	$E := 200 10^9 \cdot Pa$
Yield Strength:	Aluminium=55MPa Stainless steel=250MPa	$\sigma_y := 250 \cdot 10^6 Pa$

1.2 Loading Arm Parameters

Length of loading arm:	$L_{arm} := 320mm$

Height of arm: $height := 20 \cdot mm$

Density of Aluminium: $\rho_{alu} := 2750 \cdot kg \cdot m^{-3}$

Mass of individual housed pedestal bearing (SKF from RS): $M_{bearing} := 0.250 kg$

1.3 T-section Parameters

Height of section: $h := 38 \cdot mm$

Section thickness: $t := 6 \cdot mm$

Youngs Modulus: Aluminium=69GPa Stainless steel=200GPa $E := 69 \cdot GPa$

2. Calculations

2.1 Mass of Loading arm

Cross sectional area: $A_{cross} := width \cdot height$

Volume of Material used in loading arms: $V_{arm} := A_{cross} \cdot L_{arm}$

Mass of individual loading arm: $M_{arm} := \rho_{alu} \cdot V_{arm}$

2.2 Mass acting at each point along shaft

The P's represent the combined bearing and loading arm masses

With factor of safety (1.7):

$$P_1 := 1.7\left[g \cdot \left(M_{arm} + M_{bearing}\right)\right] + 100\,N$$

$$P_2 := 1.7\left[g \cdot \left(M_{arm} + M_{bearing}\right)\right] + 100\,N$$

$$P_3 := 1.7\left[g \cdot \left(M_{arm} + M_{bearing}\right)\right] + 100\,N$$

$$P_4 := 1.7\left[g \cdot \left(M_{arm} + M_{bearing}\right)\right] + 100\,N$$

2.3 Support Reactions

Summing vertical equilibrium: $P_{total} := P_1 + P_2 + P_3 + P_4$

Vertical support reaction: $V_A := \frac{P_{total}}{2}$

2.4 First moments of area of T-section

$$A_1 := h \cdot t$$

$$A_2 := (h - t) \cdot t$$

$$y_{centroid} := \frac{A_1 \cdot \frac{t}{2} + A_2 \cdot \left(\frac{h - t}{2} + t\right)}{A_1 + A_2}$$

2.5 Second Moments of Area

Second moments of area of shaft:

$$M_{max} := M\left(\frac{L_{total}}{2}\right)$$

$$I_{xx\_bar} := \begin{cases} \frac{\pi \cdot \left(r_o^4 - r_i^4\right)}{4} & \text{if tube = "yes"} \\ \frac{\pi \cdot r_o^4}{4} & \text{otherwise} \end{cases}$$

Second moments of area of T-section:

Using parallel axis theorem:

$$depth := h - y_{centroid}$$

$$I_{xx1} := \frac{t \cdot depth^3}{3}$$

$$depth_2 := y_{centroid} - t$$

$$I_{xx2} := \frac{t \cdot depth_2^3}{3}$$

$$y_3 := 3 \cdot mm$$

$$h_{centroid} := y_{centroid} - y_3$$

$$A_3 := h \cdot t$$

$$I_{xx3} := \frac{h \cdot t^3}{12} + A_3 \cdot h_{centroid}^2$$

$$I_{xx\_section} := I_{xx1} + I_{xx2} + I_{xx3}$$

Total second moments of area:

$$I_{xx} := I_{xx\_bar} + I_{xx\_section}$$

2.6 Maximum Bending Moment

Bending moment as a function of spanwise position x from L.H.S:

$$M(x) := \begin{cases} V_A \cdot x & \text{if } 0 \cdot m \le x \le a \\ V_A \cdot x - P_1 \cdot (x-a)^1 & \text{if } a < x \le b \\ V_A \cdot x - P_1 \cdot (x-a)^1 - P_2 \cdot (x-b)^1 & \text{if } b < x \le c \\ V_A \cdot x - P_1 \cdot (x-a)^1 - P_2 \cdot (x-b)^1 - P_3 \cdot (x-c)^1 & \text{if } c < x \le d \\ V_A \cdot x - P_1 \cdot (x-a)^1 - P_2 \cdot (x-b)^1 - P_3 \cdot (x-c)^1 - P_4 \cdot (x-d)^1 & \text{otherwise} \end{cases}$$

Check bending moments at supports:

$$M_{support} := \begin{cases} \text{"Good"} & \text{if } M(0 \cdot m) = 0 \cdot N \cdot m \\ \text{"check"} & \text{otherwise} \end{cases}$$

$$M(0 \cdot m) = 0\ N \cdot m$$

$$M\left(L_{total}\right) = -3.553 \times 10^{-15}\ N \cdot m$$

Maximum bending moments occurs at centre of shaft:

$$M\left(\frac{L_{total}}{2}\right) = 33.451\ N \cdot m$$

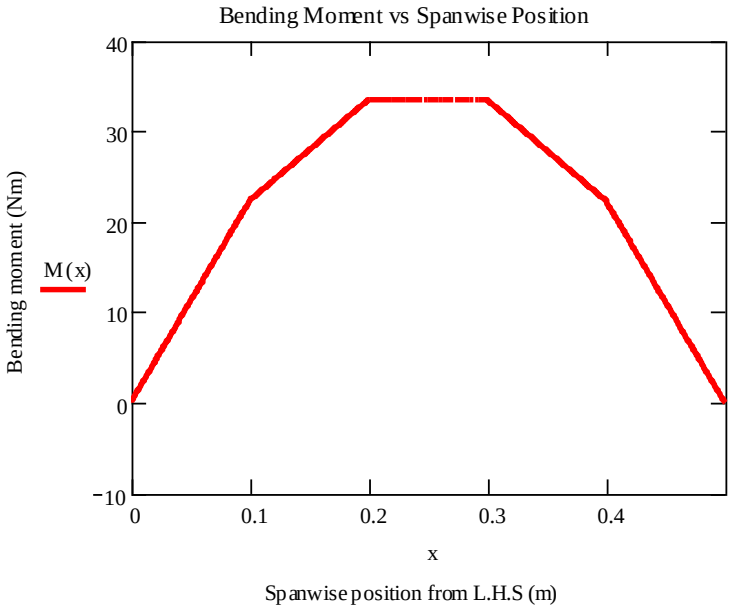

2.7 Maximum Longitudinal Stress

Longitudinal stress in shaft as a function of spanwise positon x from L.H.S:

$$\sigma(x) := \frac{M(x) \cdot y}{I_{xx}}$$

Where y is distance from neutral axis to outer most fibre of cross section

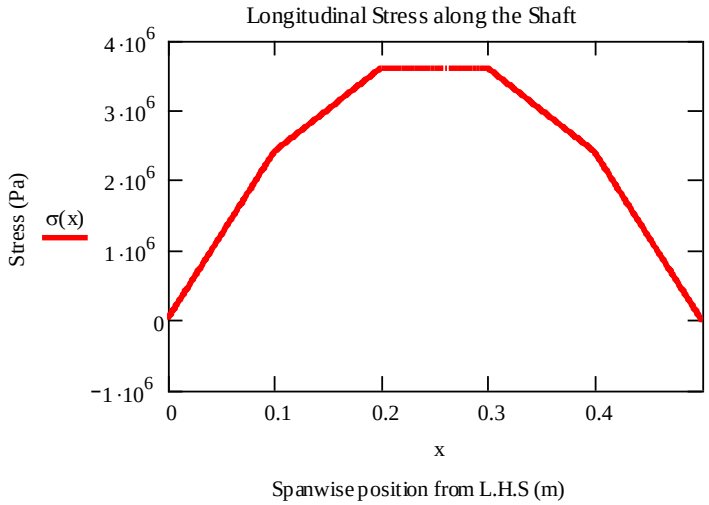

Check for yield:

$$\sigma\left(\frac{L_{total}}{2}\right) = 3.603\ \text{MPa}$$

$$yield := \begin{cases} \text{"shaft below yield"} & \text{if } \sigma\left(\frac{L_{total}}{2}\right) < \sigma_y \\ \text{"plastic deformation"} & \text{otherwise} \end{cases}$$

2.8 Spanwise Deflection

From boundary conditions (pinned-pinned):

$$C_1 := \frac{V_A \cdot L_{total}^2}{6} - \frac{P_1 \cdot (L_{total} - a)^3}{6 \cdot L_{total}} - \frac{P_2 \cdot (L_{total} - b)^3}{6 \cdot L_{total}} - \frac{P_3 \cdot (L_{total} - c)^3}{6 \cdot L_{total}} - \frac{P_4 \cdot (L_{total} - d)^3}{6 \cdot L_{total}}$$

Expression for spanwise deflection along shaft:

$$y(x) := \begin{cases} \frac{-V_A \cdot x^3}{6 \cdot E \cdot I_{xx}} + \frac{C_1 \cdot x}{E \cdot I_{xx}} & \text{if } 0 \cdot m \le x < a \\ \frac{-V_A \cdot x^3}{6 \cdot E \cdot I_{xx}} + \frac{P_1 \cdot (x - a)^3}{6 \cdot E \cdot I_{xx}} + \frac{C_1 \cdot x}{E \cdot I_{xx}} & \text{if } a \le x \le b \\ \frac{-V_A \cdot x^3}{6 \cdot E \cdot I_{xx}} + \frac{P_1 \cdot (x - a)^3}{6 \cdot E \cdot I_{xx}} + \frac{P_2 \cdot (x - b)^3}{6 \cdot E \cdot I_{xx}} + \frac{C_1 \cdot x}{E \cdot I_{xx}} & \text{if } b < x \le c \\ \frac{-V_A \cdot x^3}{6 \cdot E \cdot I_{xx}} + \frac{P_1 \cdot (x - a)^3}{6 \cdot E \cdot I_{xx}} + \frac{P_2 \cdot (x - b)^3}{6 \cdot E \cdot I_{xx}} + \frac{P_3 \cdot (x - c)^3}{6 \cdot E \cdot I_{xx}} + \frac{C_1 \cdot x}{E \cdot I_{xx}} & \text{if } c < x \le d \\ \frac{-V_A \cdot x^3}{6 \cdot E \cdot I_{xx}} + \frac{P_1 \cdot (x - a)^3}{6 \cdot E \cdot I_{xx}} + \frac{P_2 \cdot (x - b)^3}{6 \cdot E \cdot I_{xx}} + \frac{P_3 \cdot (x - c)^3}{6 \cdot E \cdot I_{xx}} + \frac{P_4 \cdot (x - d)^3}{6 \cdot E \cdot I_{xx}} + \frac{C_1 \cdot x}{E \cdot I_{xx}} & \text{otherwise} \end{cases}$$

Check deflection values at supports: $y(0 \cdot m) = 0\,m$ $\quad y(L_{total}) = 0\,m$

Maximum deflection of shaft occurs at centre: $y\left(\frac{L_{total}}{2}\right) = 0.228\,mm$

$$y_{max} := y\left(\frac{L_{total}}{2}\right)$$

2.9 Maximum Slope of Shaft

Initial guess for slope: $\theta := 1 \cdot deg$

Given

angle of slope from horizontal: $\sin(\theta) = \frac{y(0.2 \cdot m) - y(0 \cdot m)}{0.1 \cdot m}$

$\theta := \text{Find}(|\theta|)$

3. Outputs

Cross section of loading arm: $A_{cross} = 500\,mm^2$

Volume of loading arm: $V_{arm} = 1.6 \times 10^5\,mm^3$

Mass of individual loading arm: $M_{arm} = 0.44kg$

Vertical support reaction: $V_A = 223.006N$

Bending moment support check: $M_{support} = \text{"Good"}$

Maximum bending moment in shaft: $M_{max} = 33.451N \cdot m$

Yield Stress of material: $\sigma_y = 250MPa$

Maximum stress in shaft: $\sigma\left(\frac{L_{total}}{2}\right) = 3.603\,MPa$

Check shaft has yielded: $yield = \text{"shaft below yield"}$

Maximum deflection of shaft occurs at centre: $y_{max} = 0.228mm$

Maximum Slope of Shaft (with reference to horizontal): $\theta = 0.125deg$

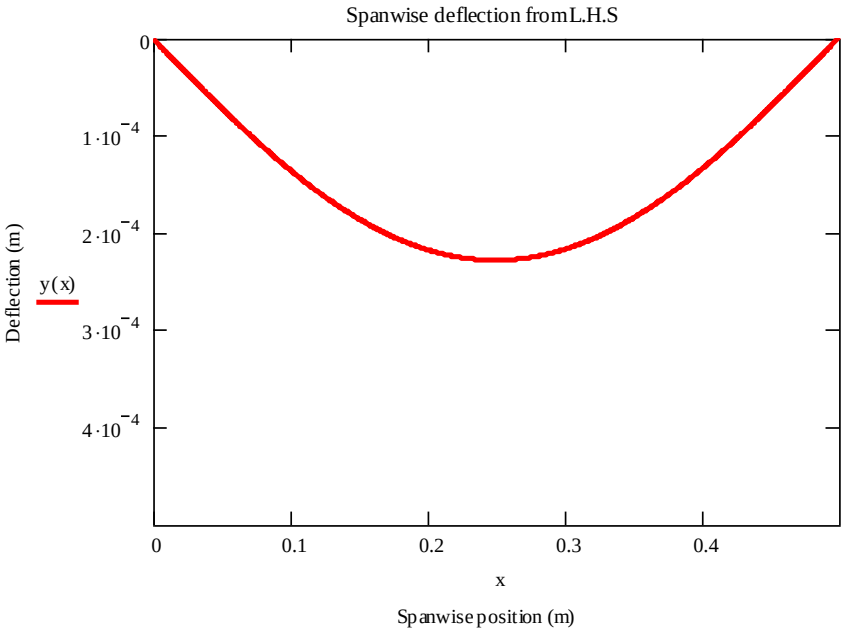

Appendix 5: Pin Deflection

This MathCAD workbook was written to approximate the lateral tip deflection of an unsupported test pin. The pin-plate interface was replaced by a point load representing the frictional force. Moments at the base of the pin and second moments of area were calculated from user inputs. The differential equation of flexure was integrated twice to represent the pin deflection as a function of spanwise position.

1. Inputs

1.1 Test Pin Variables

Length: $Length := 20 \cdot mm$

Diameter: $d := 5 \cdot mm$

Assume Young's Modulus of UHMWPE: $E := 690\,10^{6} \cdot Pa$

Maximum dynamic axial load in test cycle: $Load_{max} := 100\,N$

Assume friction coefficient at point of contact: $\mu := 0.1$

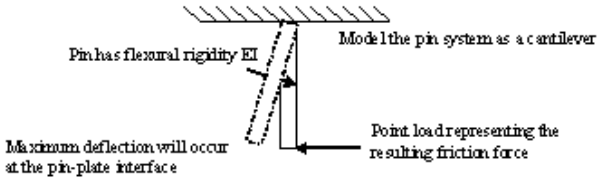

2. Calculations

2.1 Calculating friction force

Maximum point load acting on test pin: $V_A := \mu \cdot Load_{max}$

2.2 Support moments at test pin holder

Support Moments from the pin holder: $M_{pin} := -V_A \cdot Length$

2.3 Second moments of area of test pin

Second moments of area of test pin $I := \frac{\pi d^4}{64}$

2.4 Test pin deflection as a function of spanwise position

From differential equation of flexure: $y(x) := \frac{-M_{pin} \cdot x^2}{2 \cdot E \cdot I} - \frac{V_A \cdot x^3}{6 \cdot E \cdot I}$

3. Outputs

Support Moments from the pin holder: $M_{pin} = -0.2\,N\cdot m$

Second moments of area of pin: $I = 30.68\,mm^4$

Maxmimum dynamic axial load on pin: $Load_{max} = 100\,N$

Maximum lateral load (due to friction): $V_A = 10\,N$

Deflection of the test pin at the point of contact: $y(Length) = 1.26\,mm$

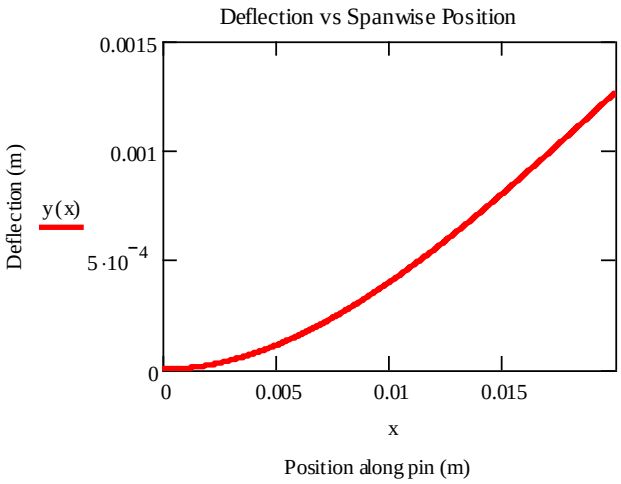

Appendix 6: Pin Buckling

The following workbook is based on the derivation of Leonhard Euler (1757) who calculated the maximum axial load that could be supported by a column before buckling. In this application the pin is assumed to behave as the column and the critical normal force to induce buckling is calculated.

1. Inputs

1.1 Test Pin Properties

Length of test pins: $Length := 20 \cdot mm$

Diameter of test pins: $d := 5 \cdot mm$

Young's Modulus of test pin: $E := 690\,10^{6} \cdot Pa$

Maximum dynamic load in gait cycle: $Load_{max} := 100\,N$

Boundary condition: $B_c := "Fixed\text{-}Free"$

Input either "Fixed-Fixed", "Fixed-Pinned", Pinned-Pinned" or "Fixed-Free"

2. Critical Loads for ideal columns

2.1 Second moments of area

Second moments of area: $I_{xx} := \frac{\pi d^4}{64}$

2.2 Critical Load

Critical Loads for ideal columns:

$$P_{critical} := \begin{cases} \frac{\pi^2 \cdot E \cdot I_{xx}}{Length^2} & \text{if } B_c = "Pinned\text{-}Pinned" \\ \frac{\pi^2 \cdot E \cdot I_{xx}}{4 \cdot Length^2} & \text{if } B_c = "Fixed\text{-}Free" \\ \frac{4 \cdot \pi^2 \cdot E \cdot I_{xx}}{Length^2} & \text{if } B_c = "Fixed\text{-}Fixed" \\ \frac{2.046 \cdot \pi^2 \cdot E \cdot I_{xx}}{Length^2} & \text{if } B_c = "Fixed\text{-}Pinned" \end{cases}$$

2.3 Stability of pins

Check stability of test pins:

$$Euler\_Buckling := \begin{cases} "Test\ pins\ are\ stable" & \text{if } Load_{max} \le P_{critical} \\ "Test\ pins\ are\ unstable" & \text{otherwise} \end{cases}$$

3.0 Outputs

Second moments of area: $I_{xx} = 30.68\,mm^4$

Critical buckling Load: $P_{critical} = 130.581\,N$

Stability of test pins through cycle: $Euler\_Buckling = "Test\ pins\ are\ stable"$

Appendix 7: Load Profile Program

To achieve a double peak dynamic load profile the following program was developed for the SMAC electric actuators. Communication between actuator and PC is through hyper-terminal and RS-232. For a full list of SMAC functionality visit www.smac-mca.com.

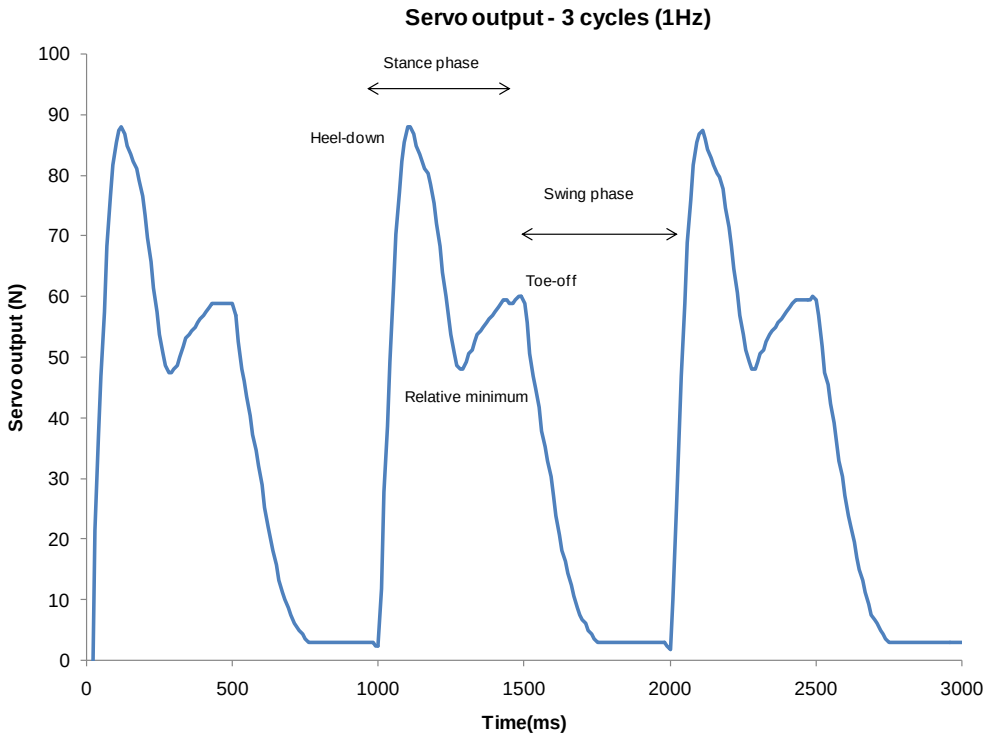

; MOTOR OFF, RESET MACROS, SET CHANNEL 6 ACTIVE IN LOW STATE

;(MS1) - SET DEBOUNCE TIME TO ZERO, WHEN CHANNEL 6 GOES "ON" JUMP TO MACRO 2.

;(MS2) - LOAD PID VALUES

;(MS3) - LOAD SQ VALUES INTO REGISTERS 10-12

;(MS4) - CALIBRATED SQ VALUE FROM REGISTER 10 NOW IN REGISTER 40

;(MS5) - CALIBRATED SQ VALUE FROM REGISTER 11 NOW IN REGISTER 41

;(MS6) - CALIBRATED SQ VALUE FROM REGISTER 12 NOW IN REGISTER 42

;(MS7) - LOAD TIME INTERVALS (MS) IN REGISTERS 13-16

;(MS8) - SET CURRENT GAIN IN REGISTERS 17-20

;(MS9) - INITIALISE COUNTER IN REGISTER 21 AND SET TO 1

;(MS10) - SET DEBOUNCE TIME TO ZERO, WHEN CHANNEL 1 GOES "ON" JUMP TO MACRO 11

;(MS11) - SET 1MS REALTIME REGISTER CLOCK TO ZERO

;(MS12) - ENABLE OVER TEMPERATURE VECTOR AND LOAD INTO REGISTER 22

;(MS13) - TELL REGISTER 21, MOTOR ON, START LOADING CYCLE

```
;(MS21) - READ REGISTER 21, ADD 1, RE-LOAD TO REGISTER 21, IF 250000 CYCLES OR GREATER, DATA DUMP, MACRO JUMP 21, ELSE MACRO JUMP 23
;(MS22) - PRINT SELECTED TEXT STRING, RESET REGISTER 21 TO 1, MOTOR OFF, END PROGRAM
;(MS23) - PRINT SELECTED TEXT STRING,MOTOR OFF,END PROGRAM
;(MS24) - IF CHANNEL 6 IS "OFF" THEN MACRO JUMP TO 25, OTHERWISE REPEAT THIS COMMAND
;(MS25) - MACRO JUMP TO 10

MF,RM,CL6
MD1,ID0,IN6,NO,MJ2,RP
MD2,SG4000,SI1000,SD2200,IL5000,FR1,PH0,RI1,SA1000,SV30000,SQ32767,SS2,SE16383; SET PID VALUES
MD3,AL88,AR10,AL45,AR11,AL75,AR12; SET SQ VALUES INTO REGISTERS 10-12
MD4,RA10,AM@31,AR40,RA40,AS@33,AR40,RA40,AA@32,AR40,RA40,AD@30,AR40
;ADJUSTED SQ VALUE FROM REGISTER 10 NOW IN REGISTER 40
MD5,RA11,AM@31,AR41,RA41,AS@33,AR41,RA41,AA@32,AR41,RA41,AD@30,AR41
;ADJUSTED SQ VALUE FROM REGISTER 11 NOW IN REGISTER 41
MD6,RA12,AM@31,AR42,RA42,AS@33,AR42,RA42,AA@32,AR42,RA42,AD@30,AR42
;ADJUSTED SQ VALUE FROM REGISTER 12 NOW IN REGISTER 42
MD7,AL175,AR13,AL250,AR14,AL500,AR15,AL950,AR16; SET TIME INTERVALS (MS)
MD8,AL200,AR17,AL50,AR18,AL70,AR19,AL50,AR20; SET CURRENT GAIN
MD9,AL0,AR21; INITIALISE COUNTER, SET TO 0
MD10,ID0,IN6,NO,MJ11,RP
MD11,AL0,WL1830; SET REALTIME CLOCK TO ZERO
MD12,AL23,LV27,EV27
MD13,TR21,MN,QM1,DH,SQ@40,SC@17
MD14,RL1830,IG@13,NO,MJ15,RP
MD15,MN,QM1,SQ@41,SC@18
MD16,RL1830,IG@14,NO,MJ17,RP
MD17,MN,QM1,SQ@42,SC@19
MD18,RL1830,IG@15,NO,MJ19,RP
MD19,MN,QM1,SQ30,SC@20
MD20,RL1830,IG@16,NO,MJ21,RP
MD21,RA21,AA1,AR21,IG250000,no,MJ22,MJ24
MD22,MG"250000 LOAD CYCLES COMPLETED",AL1,AR21,MF,EP
MD23,MG"OVER TEMPERATURE ALERT",MF,EP
MD24,IF6,SQ15,MJ25,RP
MD25,MJ10
```

Appendix 8: Linear Motion Program

In the following appendix the LR program, complete with nested loops, is written using TRIO MOTION® programming code.

'Linear reciprocating motion. Bottom slide (axis 1) reciprocates over 25mm
'Program waits for physical switch triggered by operator (channel 8)
‘Ensures lubricant temperature is within acceptable bounds ±2°C
'Initially SMAC channel 1 is "off" in the active "off" state
The user inputs the number of cycles. Once completed, slides will stop at their initial coordinates.
‘Slides will stop if interrupted by the start/stop switch, if activated cycles will return to zero.
'Software limits are set, if exceeded subsequent moves and SMAC loading will be cancelled

MERGE=OFF
BASE(1) 'The following parameters are applied to axis 1 - bottom slide
UNITS=400*16/5 'from stepper drive "bit setting". Sets units of mm and seconds
SPEED=77.25'mm/s
CREEP=1 'mm/s
ACCEL=450 'mm/s/s
DECEL=450 'mm/s/s

'label I/O channels
play=8 'start/stop switch on front panel
smac=9 'associated with channel 6 on smac I/0 interface, pulls to ground
INVERT_IN(play,ON) 'for standard switch convention

limits:
FS_LIMIT=26'set firward software limit (mm)
RS_LIMIT=-1'set revers software limit (mm)
FE_LIMIT=2 'mm, maximum allowable following error (not connected to watchdog
GOTO start

start:
x=250000 'set number of cycles between gravimetric analysis
DEFPOS(0) 'set initial position to zero
OP(play,ON)'sets channel 8 on/active
OP(smac,OFF) 'Ensure input channel 1 is high
WAIT UNTIL IN(play)=ON 'activated by user
WAIT UNTIL IN(0)=ON 'Lubricant temperature within limits
GOTO main

main:
TICKS=0' set millisecond counter to zero
FOR a=1 TO x 'Set the number of cycles

```
MOVE(25) 'mm
WAIT LOADED
OP(smac,ON) 'smac channel 1 is set to "high/on" at beginning of first move
IF (AXISSTATUS AND 512)>0 THEN
PRINT "in forward software limit"
OP(smac,OFF)
CANCEL(2)
ENDIF
MOVE(-25) 'mm
IF (AXISSTATUS AND 1024)>0 THEN
PRINT "in reverse software limit"
OP(smac,OFF)
CANCEL(2)
ENDIF
WAIT IDLE 'Ensures next command is initiated upon completion of previous command
OP(smac,OFF) 'smac channel 1 is set to "low/off" at end of previous move
WA(20) 'wait 20ms to ensure both programs start in sync
PRINT ABS(TICKS/1000) 'print the cycle time in seconds
IF IN(play)=OFF THEN GOTO start 'all motion will stop when user operate switch
IF IN(0)=OFF THEN GOTO finish ‘input channel 0 off if under/over temp alarm triggered
IF a=x THEN GOTO finish ELSE NEXT a ‘ stop program when cycles completed
GOTO start 'ensures that smac channel 1 in "off" and motion is waiting to start

finish:
CANCEL(1)
CANCEL(1)
WAIT UNTIL IN(play)=OFF
GOTO start
STOP
```

Appendix 9: Elliptical Motion Program

In the following appendix the elliptical program, complete with nested loops, is written using TRIO MOTION® programming code.

```
BASE(0) 'The following parameters are applied to axis 0 - top slide
UNITS=400*16/5 'from stepper drive "bit setting". Sets units of mm and seconds
SPEED=20'mm/s
CREEP=1 'mm/s
ACCEL=450 'mm/s/s
DECEL=450 'mm/s/s

BASE(1) 'The following parameters are applied to axis 1 - bottom slide
UNITS=400*16/5 'from stepper drive "bit setting". Sets units of mm and seconds
SPEED=20'mm/s
CREEP=1 'mm/s
ACCEL=450 'mm/s/s
DECEL=450 'mm/s/s
MERGE=ON' set seamless integration of moves

'label I/O channels
play=8 'start/stop switch on front panel
smac=9 'associated with channel 1 on smac I/0 interface, pulls to ground
INVERT_IN(play,ON) 'for standard switch convention

start:
DEFPOS(0) 'set initial position to zero
OP(play,ON)'sets channel 8 on/active
OP(smac,OFF) 'Ensure input channel 1 is high
WAIT UNTIL IN(play)=ON 'activated by user
WAIT UNTIL IN(0)=ON 'Lubricant temperature within limits
GOTO table_points

table_points:
' create the table points for axis 0
points = 101
FOR i = 0 TO (points - 1)
 x = i / (points - 1)
TABLE(0+i,10*SIN(2*PI*x))
NEXT i
' set the variables
tablestop = 0 + points - 1
' create the table points for axis 1
tablepoints = 301
```

```
FOR a = 200 TO (tablepoints - 1)
 x = a / (points - 1)
TABLE(0+a,5*COS(2*PI*x))
NEXT a
' perform the move
GOTO main

main:
x=250000’ set number of cycles between gravimetric analysis
TICKS=0
FOR a=0 TO x 'Set the number of cycles
BASE(0)
SPEED=20
BASE(1)
SPEED=20
OP(smac,ON)'SMAC channel 1 is set to "high/on" at beginning of cycle
CAM(0,100,1280,20) AXIS(0)'Generate movement on axis 0 according to table value
CANCEL(1)'Clears the buffered move leaving the presently executing move
CAM(200,300,1280,20) AXIS(1)'Generate movement on axis 1 according to table
CANCEL(1)'Clears the buffered move leaving the presently executing move
WAIT LOADED 'Switch SMAC off upon completion of a cycle
OP(smac,OFF)'SMAC channel 1 is set to "low/off" at end of cycle
PRINT ABS(TICKS/1000) 'print the cycle time in seconds
'WAIT LOADED
CANCEL(1)'Clears the buffered move leaving the presently executing move
CANCEL(1)'Clears the buffered move leaving the presently executing move
WA(10)'Wait 10ms after each cycle

IF IN(play)=OFF THEN GOTO finish 'all motion will stop when user operates switch
IF IN(0)=OFF THEN GOTO finish
IF a=x THEN GOTO finish ELSE NEXT a

finish:
WAIT LOADED
BASE(0)
SPEED=5’slide travels at half speed through final cycle, to reduce backlash on the ball screw
BASE(1)
SPEED=5’ slide travels at half speed through final cycle, to reduce backlash on the ball screw
WAIT UNTIL IN(play)=OFF
GOTO start' ensures that smac channel 1 in "off" and motion is waiting to start
```

Appendix 10: Pin and plate cleaning protocols[8]

Test chambers, pin holders (stainless steel components) and cobalt chrome test specimens

1. Clean in a 2% weight aqueous Neutracon solution (non-ionic detergent) for 2hrs.
2. Rinse with de-ionised water.
3. Further clean in methanol in an ultrasonic bath for 1hr.
4. Rinse with de-ionised water.
5. Ensure the cleaning of specimens produces a surface free of any particles, oils, greases, or other contaminants that might influence the wear process.
6. Dry with lint free tissue (non abrasive, highly absorbent) .

Method for cleaning of bio-polymer specimens

1. Rinse with tap water to remove bulk contaminants.
2. Wash in an ultrasonic bath in a 1% weight aqueous Neutracon solution for 15mins.
3. Rinse in a stream of de-ionised water.
4. Rinse in an ultrasonic bath in de-ionised water for 5mins.
5. Rinse in a stream of de-ionised water.
6. Dry with lint free tissue.
7. Immerse in methyl alcohol (methanol) for 3mins (PTFE, Polyacetal, and UHMWPE).
8. Dry with lint free tissue.
9. Air-dry in a dust free environment at room temperature for 30mins.
10. During storage, newly cleaned samples are wrapped in lint-free tissue.

Method for weighing bio-polymer specimens

1. Remove the wear and load-soak specimens at desired intervals.
2. Wash, rinse, clean, and dry the specimens (see "Method for cleaning of bio-polymer specimens").
3. Handle the pin specimens with clean tweezers using the alignment dowel for purchase.
4. Move specimens between holder and balance only.
5. Upon completion of the specified drying time weighing can begin.
6. Place the pin on the balance and wait for the balance to settle. Wait a further ten seconds before recording the mass.
7. Carefully place the specimen back in the holder and weigh the next pin.
8. Pins are weighed and recorded sequentially until the mass of each pin has been recorded four times.
9. For each consecutive gravimetric downtime, start the weighing procedure on the subsequent pin.

[8] Based on the ASTM F732-00(2006), Standard Test Method for Wear Testing of Polymeric Materials for Use in Total Joint Prostheses. ASTM international, 2006.

Appendix 11: Lamellar Orientation in Strained UHMWPE

Evolution of lamellar alignment in plastically strained UHMWPE

Sara A. Atwood[a], Alastair Kilgour[b], Mike Hoang[a], Jevan Furmanski[a], Lisa Pruitt[a]
[a]Department of Mechanical Engineering, University of California Berkeley
[b]Institute of Materials and Processes, University of Edinburgh

Introduction

Ultra-high molecular weight polyethylene (UHMWPE) is a common bearing material in total joint replacements. Wear of polyethylene is a primary cause of late-stage failure. It has been proposed that plasticity-induced alignment of the crystalline lamellae parallel to the sliding direction is a precursor to wear [1, 2]. However, limited work has been done to understand the micromechanisms responsible for lamellar alignment.

Furthermore, lamellar orientation and size have been shown to affect crack propagation resistance [3]. Crosslinked UHMWPE was introduced in hip replacements due to its observed decrease in wear, thought to result from the crosslinked network restricting lamellar alignment [4, 5]. However, crosslinking decreases the fatigue crack propagation resistance and lowers mechanical properties such as ultimate tensile strain and elastic modulus relative to conventional UHMWPE [6, 7].

This work seeks to elucidate plasticity-induced lamellar alignment in conventional UHMWPE. A better understanding of this process will serve to establish the relationship between lamellar alignment, wear, and fatigue mechanisms in total joint replacements.

Method

Uniaxial tensile tests (8871 Instron) performed on uncross-linked UHMWPE dog-bone specimens (ASTM type IV)

Strained to 25, 100, 240, 400%, failure (5 mm/min, RT compressed air cooling)

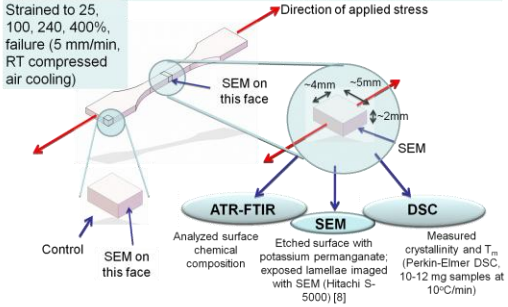

Results

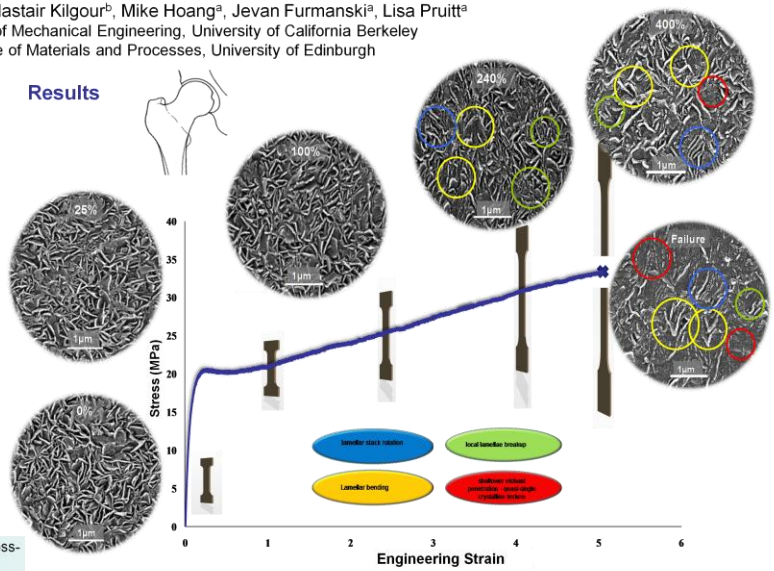

DSC Thermal Analysis Results

Engineering strain (%)	0%	25%	100%	240%	400%	Fail
Crystallinity (%) Mean ± S.D. (n=3)	47.0 ± 1.2	46.9 ± 0.7	45.9 ± 1.2	45.2 ± 1.3	42.3 ± 0.3	40.7 ± 1.7
Melting Temp (°C) Mean ± S.D. (n=3)	139.3 ± 0.9	139.2 ± 1.4	139.5 ± 1.0	137.4 ± 1.8	137.5 ± 0.3	137.7 ± 1.5

Discussion

The shallower penetration of etchant above 240% strain suggests a loss of free volume as the stretched amorphous chains draw together and form a weak pseudo-crystalline phase between the lamellae [9]. Evidence of lamellar stack rotation accompanied by smaller lamellae at these strains indicate interlamellar shear and possible chain pull-out. The homogeneous nature at ultimate strain indicates the evolution of a quasi-single crystalline nature, supported by a decreasing trend in melting temperature and crystallinity due to lamellae break-up.

The ability of lamellae to orient in response to applied plastic strains may be an important mechanism for wear and fatigue resistance. As such it is postulated that crosslinking inhibits lamellar alignment by forming a network of chains in the amorphous phase [4]. Extending this investigation to crosslinked UHMWPE is critical to understanding microstructural orientation and its influence on plastic deformation and wear in clinically relevant orthopaedic materials.

References
1. Edidin, A.A., et al. *Journal of Arthroplasty* 14(5): 616-627, 1999.
2. Wang, A., et al. *Proc Inst Mech Eng [H]* 210(3): 141-55, 1996.
3. Pruitt, L. and L. Bailey *Polymer* 39(8-9): 1545-1553, 1998.
4. McKellop, H., et al. *J Ortho Research* 17(2): 157-167, 1999.
5. Muratoglu, O.K., et al. *Biomaterials* 20(16): 1463-70, 1999.
6. Baker, D.A., et al. *J Biomed Mater Res A* 66(1): 146-54, 2003.
7. Ries, M.D. and L. Pruitt *Clin Orthop Relat Res* 440: 149-56, 2005.
8. Simis, K.S., et al. *Biomaterials* 27(9): 1688-94, 2006.
9. Bartczak, Z., et al. *Polymer* 37(11): 2113-2123, 1996.
10. Lin, L. and A.S. Argon *J Mat Sci* 29(2): 294, 1994.

SECOND INTERNATIONAL CONFERENCE ON MECHANICS OF BIOMATERIALS & TISSUES
DECEMBER 9-13, 2007 LIHUE, KAUAI HAWAII, USA

Acknowledgements
The Electron Microscope Lab, The University of California, Berkeley

Appendix 12: Potassium permanganate etch recipe[9]

1. Weigh 1.34g of potassium permanganate onto weighing paper.
2. Measure 6.7ml distilled water. Add to 150ml beaker containing glass coated stirrer bar.
3. Measure 66.7ml of sulphuric acid. Add to beaker with distilled water.
4. Measure 26.7ml of ortho-phosphoric acid. Add to same beaker.
5. Place beaker on stirrer plate and slowly add the weighed potassium permanganate. This is a volatile mixture so care should be taken.
6. Gently cover beaker with Parafilm and leave on stirrer plate for 60minutes to ensure complete dissolution.
7. Carefully add polymer samples. Leave for 30minutes.
8. Fill four 50ml beakers with one of the following; Sulphuric acid, 30% hydrogen peroxide, distilled water and acetone.
9. Place all four beakers in an ice bath and allow to cool for 15 minutes.
10. Using tweezers carefully remove polymer samples and place in the chilled sulphuric acid. Agitate gently for 90 seconds.
11. Move samples to beaker containing hydrogen peroxide and leave for 90 seconds.
12. Move samples to beaker containing distilled water and leave for 90 seconds.
13. Finally, move samples to beaker containing acetone and leave for 90 seconds.
14. Place samples on Lint free cloth to dry.
15. Care should be taken not to touch the etched surface of interest.
16. Platinum or gold sputter coat (~6nm) before viewing under an SEM.

[9] Adapted from Shahin *et al*. 1999 and the protocol used by the Medical Polymers Group, University of California, Berkeley.

Appendix 13: Publications

1. Atwood, S.A., Kilgour, A., Hoang, M., Furmanski, J., Pruitt, L.A., Lamellar orientation of plastically strained ultra-high molecular weight polyethylene, (Poster) presented at: Second International Conference on Mechanics of Biomaterials and Tissues, Lihue, Kaua'l Hawaii, USA, Dec. 2007.

2. Kilgour, A. and Elfick, A.P., Design and test of novel tribometer: investigation into wear performance of materials used in total hip replacements. Tribology - Materials, Surfaces & Interfaces, 2008. 2: p. 161-168.

3. Kilgour, A. and Elfick, A.P., Investigation of Polyethylene structure and its bearing on wear of joint replacements. (Abstract). Oral presentation In: World Biomaterials Congress. Amsterdam, 2008.

4. Kilgour, A. and Elfick, A.P., Influence of Crosslinked Polyethylene Structure on Wear of Joint Replacements. (Abstract). Oral presentation In: 35th Leeds-Lyon Symposium on Tribology, Leeds, 2008.

5. Kilgour, A. and Elfick, A.P., Influence of crosslinked polyethylene structure on wear of joint replacements. Tribology International, 2009. 42(11-12): p. 1582-1594.